



ARL-TR-7503 • OCT 2015



Modeling Turbulence Generation in the Atmospheric Surface and Boundary Layers

by David H Tofsted

Approved for public release; distribution is unlimited.

NOTICES

Disclaimers

The findings in this report are not to be construed as an official Department of the Army position unless so designated by other authorized documents.

Citation of manufacturer's or trade names does not constitute an official endorsement or approval of the use thereof.

Destroy this report when it is no longer needed. Do not return it to the originator.



Modeling Turbulence Generation in the Atmospheric Surface and Boundary Layers

by David H Tofsted

Computational Information Sciences Directorate, ARL

REPORT DOCUMENTATION PAGE				Form Approved OMB No. 0704-0188	
<p>Public reporting burden for this collection of information is estimated to average 1 hour per response, including the time for reviewing instructions, searching existing data sources, gathering and maintaining the data needed, and completing and reviewing the collection information. Send comments regarding this burden estimate or any other aspect of this collection of information, including suggestions for reducing the burden, to Department of Defense, Washington Headquarters Services, Directorate for Information Operations and Reports (0704-0188), 1215 Jefferson Davis Highway, Suite 1204, Arlington, VA 22202-4302. Respondents should be aware that notwithstanding any other provision of law, no person shall be subject to any penalty for failing to comply with a collection of information if it does not display a currently valid OMB control number.</p> <p>PLEASE DO NOT RETURN YOUR FORM TO THE ABOVE ADDRESS.</p>					
1. REPORT DATE (DD-MM-YYYY) October 2015		2. REPORT TYPE Final		3. DATES COVERED (From - To) May 2013–October 2014	
4. TITLE AND SUBTITLE Modeling Turbulence Generation in the Atmospheric Surface and Boundary Layers				5a. CONTRACT NUMBER	
				5b. GRANT NUMBER	
				5c. PROGRAM ELEMENT NUMBER	
6. AUTHOR(S) David H Tofsted				5d. PROJECT NUMBER AH71	
				5e. TASK NUMBER	
				5f. WORK UNIT NUMBER	
7. PERFORMING ORGANIZATION NAME(S) AND ADDRESS(ES) US Army Research Laboratory ATTN: RDRL-CIE-D White Sands Missile Range, NM 88002-5501				8. PERFORMING ORGANIZATION REPORT NUMBER ARL-TR-7503	
9. SPONSORING/MONITORING AGENCY NAME(S) AND ADDRESS(ES)				10. SPONSOR/MONITOR'S ACRONYM(S)	
				11. SPONSOR/MONITOR'S REPORT NUMBER(S)	
12. DISTRIBUTION/AVAILABILITY STATEMENT Approved for public release; distribution is unlimited.					
13. SUPPLEMENTARY NOTES primary author's email: <David.H.Tofsted.civ@mail.mil>.					
14. ABSTRACT <p>Optical turbulence effects in the earth's atmosphere are greatest on systems operating in the surface-layer atmosphere. To estimate the performance of systems operating in such environments, direct measurement of current local conditions is always possible, but a common approach used for planning purposes involves estimating the distribution of optical turbulence strength for a given locale through the connections provided by flux-profile relations (Monin–Obukhov similarity theory) between the sensible heat flux generated in the surface-layer atmosphere and the refractive index structure parameter.</p> <p>This report examines various alternative methods for handling various energy-budget components especially important for nocturnal energy-budget calculations. Fluxes considered include radiative and ground flux components, solar direct and diffuse radiation, foliage-cover effects, and a detailed discussion of gravity-wave influences. The discussion and conclusions sections highlight options for extending the model to fluctuating inputs either based on measured data or through use of statistical fluctuations, as well as testing recommendations for a program of model validation.</p>					
15. SUBJECT TERMS surface energy budget, boundary layer, flux profile method					
16. SECURITY CLASSIFICATION OF:			17. LIMITATION OF ABSTRACT UU	18. NUMBER OF PAGES 210	19a. NAME OF RESPONSIBLE PERSON David H Tofsted
a. REPORT Unclassified	b. ABSTRACT Unclassified	c. THIS PAGE Unclassified			19b. TELEPHONE NUMBER (Include area code) 575-678-3039

Contents

List of Figures	vi
List of Tables	ix
Acknowledgments	x
1. Overview of the Turbulence Problem	1
1.1 Boundary- and Surface-Layer Atmospheres	2
1.2 Turbulence Structure in the Atmosphere	6
1.3 Turbulence Spectrum	11
1.4 Outer-Scale Effects on the Refractive Index Spectrum	14
1.5 Inner-Scale Effects on the Refractive Index Spectrum	20
2. Introduction to the Surface Energy Budget	25
2.1 Turbulence Prediction using Surface Energy Budget	25
2.2 The Surface Energy Budget	28
2.3 Flux-Profile Characterization of the Sensible Heat Flux	31
2.4 Surface and Atmospheric Inertia Effects	35
2.5 History of Surface Energy Budget Model	35
3. Surface Energy Budget Model Inputs	37
3.1 Soil Properties	38
3.2 Foliage Properties	41
3.3 Surface-Layer Atmosphere Characteristics	42
3.4 Cloud-Cover Information	43
3.5 Site and Time Information	44
3.6 Model Execution	44
4. Diurnal Ground Heat Flux Model	46
4.1 Model Assumptions Used	47
4.2 Laplace Analysis of Ground Impulse Response Function	49
4.3 Fourier Analysis of a Diurnal Response	54
4.4 Conclusions and Observations	56

5. Effects of Vegetation on Convective Surface Fluxes	58
5.1 General Discussion	58
5.2 Sensible Heat Flux Calculation for a Vegetated Surface	60
5.3 Barren Soil's Resistance Factor	63
5.4 Vegetated Terrain's Resistance Factor	66
5.5 Transfer Efficiency for Intermediate Cases	68
5.6 Latent Heat Flux for Foliated-Terrain Conditions	71
6. Boundary-Layer Thermal Accounting	74
6.1 Vertical Temperature Profile Models	74
6.2 Decomposition of the Sensible Heat	77
6.3 Extended Surface- and Boundary-Layer Heating Equations	81
6.4 Perturbed Daytime-Temperature Profile Function	85
6.5 Simplified Unstable Layer Vertical Model	88
6.6 Stable Layer Vertical Structure Model	92
7. Cloud and Surface Radiative Effects Modeling	101
7.1 Review of Standard Radiation Models	101
7.2 Shapiro's Cloud Model	103
7.3 Foliage Layering Model	105
7.4 Foliage Sublayer Reflectivity and Emissivity Model	111
7.5 Foliage and Surface Aggregate Radiation Properties	120
8. Atmospheric Infrared Radiative Fluxes	132
8.1 Review of Deardorff's Long-Wave Radiation Model	133
8.2 Downward Long-wave Radiation Calculation Re-evaluation	134
8.3 Numerical Radiative-Transfer Calculation	134
8.4 Spectral Absorptivity Data Collection	140
8.5 Atmospheric Temperature and Pressure Model	142
8.6 Atmospheric-Radiation Calculations	148
8.7 Atmospheric-Radiation Results	150
9. Further Developments	154
9.1 Diabatic Wind Modeling	154

9.2	Nocturnal Low-Level Jet Development	158
9.3	Small-Scale Nocturnal Turbulence Generation	159
9.4	Gravity-Wave Turbulence in the Stable Surface Layer	163
9.5	Gravity-Wave Equation Set	164
9.6	Vertical Wind Perturbation Equation	170
9.7	Vertical Wind Structure	178
9.8	Gravity-Wave Breakdown	181
10.	Conclusions	186
	References	189
	List of Symbols, Abbreviations, and Acronyms	194
	Glossary	196
	Distribution List	197

List of Figures

Fig. 1	Typical diurnal behavior of boundary layer due to vertical growth, and modifications due to energy changes	3
Fig. 2	Intercomparison of Kaimal-frequency maximum data (f_m) versus dimensionless height parameter $\zeta = z/L_{Ob}$ and plot of Eq. 1.41	18
Fig. 3	Intercomparison of digitized Kaimal data with 1-D curve of Ψ_{nG} using original Kaimal $B = 0.16$ and $B = 0.19$, and Ψ_{nR} based on $B = 0.19$.	18
Fig. 4	Empirical inner-scale relationship to observed wind speed versus theoretical inner-scale wind dependence for neutral stability case	21
Fig. 5	Dissipation curve of Belen'kii function	22
Fig. 6	Intercomparison of different inner-scale-affected bump spectra	23
Fig. 7	Expanded decomposition of surface-energy fluxes in the presence a foliated layer	30
Fig. 8	Dimensionless function $G(u)$ produced from Laplace analysis of the heat equation	52
Fig. 9	Foliated layer's displacement-height and roughness-length offsets	62
Fig. 10	Ratio $Z_T/ Z_K $ of surface-layer characteristic thickness (Z_T) to absolute value of Obukhov length ($ Z_K $) (red line), and ratio $Z_A/ Z_K $ (dashed blue line), as functions of N_I	89
Fig. 11	Inversion-layer-temperature structure for $dT/dZ = 1^\circ\text{C/m}$ at 2 m AGL and a layer thickness of 200 m	97
Fig. 12	Various models of N_F dependence on σ_F comparing Deardorff constant Υ_F dependence versus multilayer model dependencies and infinite-layer dependence	110
Fig. 13	Scaled and normalized reflection function $P_{\text{scat}}(\psi)/[2/(3\pi)]$	116
Fig. 14	Upward- and downward-integrated scattering-probability plots as functions of incident radiation's zenith angle; green line shows sum of upward and downward components.	118
Fig. 15	Normalized hemispherical reflection curves, given scattering occurs into the upward (red) and downward (blue) hemispheres.....	119
Fig. 16	Diffuse radiation absorption and reflection results obtained for varying soil albedo, α_G , and foliage fraction, σ_F , for foliage reflectivity, $\alpha_F = 0.325$, and transmissivity, $\gamma_F = 0.175$. Red curves denote fractional energy absorbed by the ground, A_G ; green curves, A_F , show fractions absorbed by foliage; blue curves, α_S , show sky-reflection fractions....	125

Fig. 17	Behavior of surface-layer reflectivity of foliated layers of different surface fractions σ_F as functions of ground reflectivity α_G and as a function of the solar altitude in degrees	128
Fig. 18	Direct-radiation transmission factors to the ground (red lines), foliage (green lines), and sky-reflected (blue lines) for variable σ_F at a range of solar-zenith positions parameterized by Y , for constant $\alpha_G = 0.00$...	128
Fig. 19	Diffuse IR-radiation absorption and reflection results equivalent to the cases plotted in Fig. 16, but using altered foliage-albedo value $\alpha_{F(IR)} = 0.13$ ($\epsilon_F = 0.87$)	129
Fig. 20	Diffuse IR-radiation absorption and emission results similar to the cases plotted in Fig. 16, but using altered foliage albedo $\alpha_{F(IR)} = 0.13$ ($\epsilon_F = 0.87$) for ground-emitted radiation and plotting sky emissivity, E_S , rather than reflectivity, R_S	130
Fig. 21	Diffuse IR-radiation absorption and reflection results equivalent to cases plotted in Fig. 18, using foliage albedo $\alpha_F = 0.13$ ($\epsilon_F = 0.87$); radiation originates in foliage layer	130
Fig. 22	Four extinction-coefficient curves based on MODTRAN output: blue curve is for water vapor at 0.46% relative humidity, red curve plots CO ₂ extinction at 404 ppm, purple curve is methane, and green curve plots remaining dry-air gas effects; also, superposed are blackbody curves at 233 K (red), 273 K (green), and 313 K (blue).	147
Fig. 23	Four extinction-coefficient curves based on MODTRAN output: same data as Fig. 22 shown, except water-vapor content (blue curve) is plotted as its Standard Atmosphere value, and CO ₂ content (red curve) has been doubled (to 808 ppm); green plots the remaining dry-air contents and the purple line is the same methane effect as in Fig. 22, along with the same blackbody curves.	148
Fig. 24	Fluxes oriented toward the surface-interface layer (SI)	150
Fig. 25	Fluxes oriented toward the surface layer (SL).....	150
Fig. 26	Fluxes oriented toward the remainder of the boundary layer (BL).....	151
Fig. 27	Two scatterplots comparing computed emissivity values (abscissa, x-axis component) versus Staley and Jurica's (red) or Seller's (green) analytic emissivity expressions (ordinate components)	151
Fig. 28	Two scatterplots comparing computed emissivity values (abscissa, x-axis component) versus Staley and Jurica's (red) or Seller's (green) analytic emissivity expressions (ordinate components) for a series of neutral-atmosphere cases	152
Fig. 29	First 4 vertical wind modes, $W(z)$, for typical inversion scenario	180

Fig. 30	Computed frequency versus wave number for first 2 modes: Mode 1 plotted in red, Mode 2 in green, dashed line is $\omega = \kappa/3$	180
Fig. 31	First 4 horizontal wind modes, $U(z)$, for typical inversion scenario....	181
Fig. 32	Breakdown times (minutes) for a series of 4 gravity-wave modes, illustrating breakdown times from initiation of wave motion as functions of height.....	184

List of Tables

Table	Baseline dry-soil properties	39
-------	------------------------------------	----

Acknowledgments

This report would not have been possible without the support of Drs Darryl Sanchez and Thomas Farrell of the US Air Force Research Laboratory's Starfire Optical Range. This work also owes much to various researchers in this field who contributed to the author's understanding of this problem many years ago, including Mr Frank Hansen and Dr Kenneth Kunkel.

1. Overview of the Turbulence Problem

The field of optical engineering represents a unique combination of physics, mechanical engineering, and electrical engineering. Over the past 100 years the field has expanded from telescope design to range-gated imagers and digital systems. In the late 1960s, visual-imaging systems were augmented by infrared detectors. Digital cameras have also largely replaced film-recording systems and now feature high-resolution image capture capabilities. As systems improved, the desire to see farther and more accurately lead to an increasing awareness of the influence of optical turbulence on image quality, particularly in ground-to-ground observation scenarios. This recognition began with studies of turbulence effects on visual systems, but with the advent of third-generation forward looking infrared (FLIR) systems operating in the far infrared band (8–12 μm), turbulence-distortion effects are acknowledged as a critical limitation on a wide range of imaging conditions.

The 1960s also saw the advent of lasers. Coherent radiation faces its own set of unique challenges. Unlike passive systems where scintillation effects are largely negated by aperture averaging of the effect, coherent photons perturbed by turbulent fluctuations tend to interfere with one another, producing (at times) large scintillations, resulting in loss of focus of beams (turbulent beam spread), beam wander, and (for laser communications) unwanted data dropouts or reduced bandwidth.

To describe these effects, propagation modelers construct simulations based on turbulence strength measured through the refractive-index structure parameter, C_n^2 [$\text{m}^{-2/3}$], and 2 length scales, the inner and outer scales of turbulence, ℓ_o and L_o , that characterize the large-scale (L_o) and small-scale (ℓ_o) limits of the inertial subrange, the portion of the refractive-index power spectrum that obeys the Kolmogorov turbulence $\kappa^{-11/3}$ spectral power law dependence.

In turn, C_n^2 , ℓ_o , and L_o are typically modeled through correlations that have been measured between predicted atmospheric properties in the boundary-layer atmosphere and properties characterizing the turbulence itself. In the atmospheric surface layer (that layer where sensible heat and momentum fluxes are roughly constant with height), it is common to model C_n^2 as a function of height, the sensible heat flux, and the Monin–Obukhov (or simply Obukhov) length scale, L_{Ob} . This latter scale is related to the ratio of convective energy to mechanical energy and is mainly valid for daytime-atmosphere applications.

Various rules are employed to model C_n^2 in the surface layer, but a key question is how to extend this estimation technique into the lower boundary layer above the surface layer and, perhaps more problematically, what to do about nighttime predictions where the daytime assumption of fully mixed turbulence does not hold.

While the current effort does not provide a final answer to these questions, it is hoped that the techniques developed here for dealing with surface fluxes, radiation effects, and gravity-wave influences on nocturnal turbulence will lead this endeavor toward better surface-layer, boundary-layer, and nocturnal-layer evaluation of turbulence. Complementing these improvements efforts to incorporate intermittency effects using more detailed wind-flow models and thermal mixing to better characterize temperature fluctuations could be combined with the present study to better model point-turbulence fluctuations.

1.1 Boundary- and Surface-Layer Atmospheres

To set the stage for the Chapter 2 discussion, let us begin by overviewing the atmosphere to be modeled. The *boundary layer* generally constitutes that portion of the atmosphere that is influenced by the drag effects of the earth's surface. In this layer, the wind velocity at the exact surface itself is modeled as being exactly zero (a no-slip condition). The velocities of horizontal winds increase with height above the surface until at the top of the boundary layer the wind speed matches the geostrophic wind. This is the situation during the daytime. At night a nocturnal jet layer can result in wind speed considerably faster than the geostrophic speed, but the wind then reduces above the jet to match the geostrophic wind speed at the top of the nighttime boundary layer as well. Typically the layer grows vertically throughout daylight hours and exhibits modifications due to failing solar energy at sunset. This behavior is illustrated graphically in Fig. 1.

From Fig. 1, prior to dawn, an inversion condition typically persists from the previous day's cooling, as denoted by the **1** along the time track. Then, starting at dawn, energy enters the base of the boundary layer due to solar loading. This sunlight warms the surface and eventually breaks the surface-based inversion from the surface upward. Time point **2** highlights the morning growth of the mixed layer and an entrainment zone at the top of the warming boundary layer.

During the day, between the base and top of the boundary layer, the intervening atmosphere circulates air vertically through substitutions of air *parcels* that translate

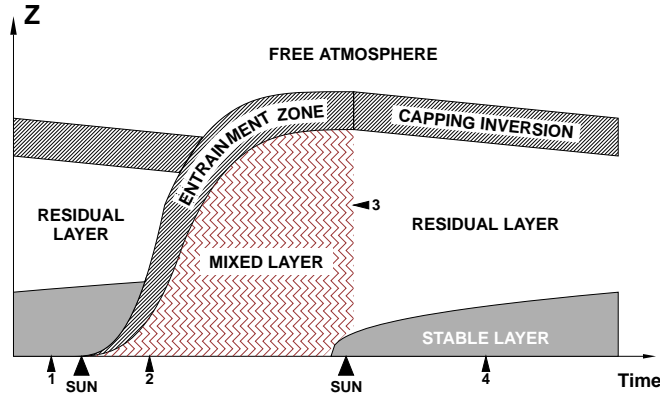


Fig. 1 Typical diurnal behavior of boundary layer due to vertical growth, and modifications due to energy changes

drag effects throughout the layer from the ground up. Simultaneously, air parcels arising from a given level produce temperature perturbations at a different level, degrading optical propagation.

As indicated previously, at the bottom of the boundary layer is the atmospheric surface layer in which the vertical sensible heat flux varies by less than 10% throughout the layer. The structure above the surface layer is described in different terms depending on the overall state of the boundary layer, as a function of the time of day. Starting from local noon, let us consider a typical sunny mid-latitude day. The layer immediately above the surface layer under these conditions is described as the *free convection layer* or the *convective boundary layer* (CBL). The CBL generally extends up to half the height of the full boundary layer. It is a daytime-only effect, where the name connotes the dominant effect of the convective heat flux arising from the surface. The bulk of the full boundary layer is termed (during the daytime) the *mixed layer*, connoting that region of the boundary layer where air is being both convectively and mechanically mixed due to drag interactions with the surface. At the top of the boundary layer there typically exists a capping inversion layer (or elevated inversion) where temperature becomes an increasing function of height.

This inversion appears to be driven by 3 mechanisms. First, cold air tends to sink relative to warmer air (being denser). So, one might expect colder air to be present near the surface despite the daily warming of the air by the surface. Second, and related, as warm air moves away from the equator toward more temperate

latitudes, the warm air tends to ride on top of cooler air at those latitudes, producing inversions. Third, under clear-sky conditions the layer atop the boundary layer often previously contained moist air that rained out; this leaves the upper air dry and the boundary layer moister (due to evaporation at the surface). Once this condition sets up, the moist air in the boundary layer becomes a more efficient radiator of heat than the air above the boundary layer. The boundary layer thus is constantly cooling due to radiation, while the upper layer retains more heat since it is less efficient as an infrared radiator (even with CO₂ present).

In daytime the above scenario, involving a surface layer, CBL, mixed layer, and elevated inversion layer, is common. Of course, modifications to this model are necessary to account for the presence of cloud cover, frontal passages, and precipitation, when present. The present model has not been developed to consider either weather fronts or precipitation effects, only variations in solar radiation due to cloud cover.

Let us next consider the transitional period to the nocturnal boundary layer. As the sun sinks toward sunset, the atmosphere experiences a deterioration from the daytime atmospheric structure to a neutral period in which the potential temperature is approximately constant with height. The sensible heat flux that had previously warmed the full boundary layer becomes sufficient to heat the surface layer plus a portion of the boundary layer. The upper portion of the boundary layer becomes disconnected from the surface layer and is redesignated the *residual layer*. (This transition is denoted by the **3** on the time track in Fig. 1.) Mechanical mixing of near-surface air will still yield intermittent temperature fluctuations in the layer, but not the strong fluxes of the CBL and mixed layers.

Eventually, the solar heating of the surface is insufficient to match the net thermal radiation lost due to the warm surface, and the surface begins to cool. At this point the atmosphere transitions from the *unstable* daytime atmospheric state to the *stable* nighttime atmosphere through an evening *neutral event*. This event begins in the surface layer where the atmosphere becomes temporarily isothermal (actually where the vertical gradient of the potential temperature is zero). In this case there are no turbulence fluctuations because there no longer is mixing of different temperature air.

The neutral event begins at the surface, therefore affecting the surface layer first. It then quickly spreads vertically into what was the CBL and then into the mixed

layer. There is some hysteresis to this effect since some upper level may not have responded to the neutral event before the cooling at the surface has caused the surface layer to transition into its next state: the surface-based inversion (denoted by the 4 in Fig. 1).

Once the surface-based inversion appears, the surface layer enters what is termed a *stable* state. Here the terms *stable* and *unstable* are used in relation to the motions of vertically displaced parcels of air during inversion and lapse conditions. Under an inversion condition, if a parcel of air is displaced vertically—all other things being equal—the parcel will tend to attempt to return to the vertical level of its origin. When displaced downward it becomes warmer (and therefore more buoyant) than its surroundings and attempts to move upward. When displaced upward it becomes colder than its surroundings (therefore less buoyant) and attempts to displace back downward. Parcels are therefore stable under vertical displacements.

This behavior is in contrast to unstable vertical air motions. Again, all other things being equal, if during the daytime (warm surface) a parcel of air is displaced vertically, it will always find itself out of balance (buoyancy-wise) with its surroundings: A parcel displaced downward becomes denser than its surroundings and tends to fall farther. A parcel displaced upward becomes warmer than its surroundings and remains buoyant. Daytime atmospheres thus enhance vertical mixing of air. This in turn affects the net effective drag of the surface on the geostrophic winds, and a deeper layer develops because a greater amount of air is involved in vertical motions. Conversely, because stable motions tend to block mixing, the nocturnal layer features less vertical mixing and a shallower overall layer. Nocturnal atmospheres also tend to become layered and unmixed.

Hence, the air nearest the ground becomes colder than the air above due to radiative cooling of the surface and cooling of the near-surface air to the surface via convection. The result is a stable inversion layer that grows slowly from the surface layer upward. Above the surface-based inversion the remainder of the boundary layer continues on as the residual layer, but odd (dynamically unstable) effects begin to occur in this layer as the nocturnal atmosphere unfolds. We shall leave these discussions for later sections, but suffice to say that the stable layer, while stable in terms of vertical parcel displacements, is unstable dynamically due to nonlinear processes such as Kelvin–Helmholtz instabilities and gravity-wave growth and collapse.

1.2 Turbulence Structure in the Atmosphere

The structure of the diurnal energy forcings in the boundary layer provide the source for temperature fluctuations, but these are large-scale effects. However, it is the structure of the turbulence at small scales that affects the performance of optical devices and propagation within the boundary layer. We thus address, in general terms, the structure of the turbulence in the boundary layer. We follow Appendix C of Volume 2 of Ishimaru's (1978) study of wave propagation in random media. Ishimaru follows Kolmogorov's (1941) original statistical description of turbulence based on scaling arguments, essentially following the description given in English mathematician Lewis Richardson's (1922) famous poem that describes how turbulence *cascades* from large-scale perturbations downward to the smallest scale elements that are destroyed by viscous forces:

*Big whirls have little whirls that feed on their velocity,
And little whirls have lesser whirls and so on to viscosity.*

Kolmogorov's theory considered the characterization of fully mixed turbulence at high Reynolds numbers. This number, Re , is a dimensionless quantity defined as vl/ν , where v and l are *characteristic* velocity and length scales associated with turbulent fluctuations of a certain size, and ν is the kinematic viscosity (m^2/s) of air, $\nu = \mu/\rho_a$. Here, μ is the dynamic viscosity, and ρ_a is the air density:

$$\mu = \mu_0 \left(\frac{T_\mu + C}{T + C} \right) \left(\frac{T}{T_\mu} \right)^{3/2}, \quad (1.1)$$

where $\mu_0 = 1.8325 \times 10^{-5} \text{ kg}/(\text{m}\cdot\text{s})$, $T_\mu = 296.16 \text{ K}$, and $C = 120 \text{ K}$ is Sutherland's constant. For dry air,

$$\rho_a = 0.34838 P/T, \quad (1.2)$$

where P is the air pressure in millibars, and T is the air temperature in Kelvin (K). At standard temperature (288 K) and pressure (1013 mbar), the kinematic viscosity is $1.79 \times 10^{-5} \text{ m}^2/\text{s}$. Stull (1988) observes, "The Reynolds number can be interpreted as the ratio of inertial to viscous forcings."

Under most length-scales and corresponding velocity scales, the atmosphere exhibits a very large Reynolds number due to the small viscosity. Only when

considering length scales of a few millimeters, and the corresponding velocity fluctuations at such scales, does one approach $Re \approx 1$ where viscous forces become dominant. Of course, computations at such millimeter scales in combination with typically meaningful propagation-scenario domain sizes on the order of kilometers—requiring on the order of 10^{18} computational cells—would be practically impossible given even today’s supercomputing resources. Thus, compromises are necessary. One method is to simply ignore viscous effects, or to treat such influences only due to a parameterized surface-drag effect. However, to estimate the turbulence strength itself, typically the structure of small-scale turbulence is parameterized using the approximations developed by Kolmogorov.

Having assumed the turbulence is well mixed, Kolmogorov’s next step involved estimating the rate of production of kinetic energy per unit mass in the flow, as well as the rate of dissipation of such kinetic energy. Let us consider that for length-scales of the order of l_f of the flow itself, the velocity perturbations of such scales are on the order of the mean velocity of the flow (v_f). A characteristic time scale within the flow may thus be estimated as $\tau_f = l_f/v_f$ for eddies (organized turbulent fluctuations within the flow) that are of the characteristic length-scale of the flow itself. The rate of kinetic-energy production of these elements per unit mass per unit time may then be estimated as

$$K_{P(f)} \sim v_f^2/\tau_f = v_f^3/l_f. \quad (1.3)$$

On the other hand, the rate of dissipation of turbulence from the flow should be relatively small at the largest spatial scales since the Reynolds number is so large and since turbulence at large scales is generally sustained. This suggests a dissipation rate for the largest spatial scales of the order

$$\epsilon_f \sim \nu v_f^2/l_f^2. \quad (1.4)$$

Kolmogorov’s analysis to this point is consistent with Stull’s interpretation of the Reynolds number since when the ratio of $K_{P(f)}$ to ϵ_f is formed, one obtains just the Reynolds number of this flow: $Re_f \sim v_f l_f/\nu$.

Because of the difference between the magnitude of the mean energy and the dissipation rate, based on the kinematic viscosity, it is clear dissipation processes

are not significant for large-scale flows. Rather, dissipative effects only become significant at smaller scales where kinematic influences (and therefore viscous effects) become important. These influences begin at millimeter scales.

Kolmogorov designated a cutoff point in his flow model that he characterized as an outer scale, designated here by L_o . This scale is the largest length-scale below which the flow can be considered fully mixed. And, there appears to be a strong correlation between this concept of full mixing and a related concept regarding isotropy of the turbulence. Klipp (2014) has studied the nature of the scale at which turbulence transitions from a (roughly) 2-dimensional structure to becoming isotropic, and this scale is of the same length as the outer scale. Above the outer scale the flow appears to exhibit anisotropies. Below this scale, in the inertial subrange the flow becomes isotropic. For flows close to the earth's surface the outer scale is a function of the height above the surface (varying from a few meters to perhaps several dozen meters [Tofsted 2000]), and has been shown to vary as a function of time of day (Tofsted et al. 2009, Fig. 21).

In connection with L_o , let us identify V_o as the corresponding characteristic velocity fluctuation at this scale. Since the dissipation rate of eddies of this size is negligible, if one assumes a steady state of the flow, then production at this scale must match the rate of transfer of energy from this scale to smaller eddy scales in a spectral *cascade* of energy to smaller turbulence scales. This cascade is, nevertheless, based on inertial mixing, not viscous effects. At successively smaller turbulence scales the same process occurs. Energy cascades downward to smaller and smaller length-scales while viscous forces gradually grow. Eventually energy is removed at some smallest length-scale, ℓ_o , termed the inner scale, where viscous forces become dominant, and the bulk of the kinetic energy is removed from the flow.

Let V_1, V_2, \dots, V_n be the velocities of eddies of scales L_1, L_2, \dots, L_n , where $L_o > L_1 > L_2 > \dots > L_n$. Then, due to the transfer of kinetic energies to smaller length-scales, the kinetic energies per unit mass per unit time for eddies of all length-scales (an equipartition argument) will tend to be approximately equivalent:

$$V_o^3/L_o \approx V_1^3/L_1 \approx V_2^3/L_2 \approx \dots V_n^3/L_n. \quad (1.5)$$

That is, when the flow is in a steady state, the amount of energy flow into a given length-scale range from the next-larger length-scale will equal the rate of kinetic-energy flow from that length-scale to the next smaller scale.

As the length-scales decrease, the dissipation rate, $\nu V_n^2/L_n^2$, tends to increase until the inner scale is reached, at which point the dissipation rate is of the same order as the rate of kinetic-energy flux into that length-scale:

$$V_\epsilon^3/L_\epsilon \approx V_\epsilon^3/\ell_o \approx \nu V_\epsilon^2/\ell_o^2 \approx \epsilon. \quad (1.6)$$

At this length-scale, practically all of the kinematic energy is dissipated into heat so that no eddies of scale smaller than ℓ_o remain in the flow. Only molecular thermal energy remains.

Two important properties emerged from this analysis. First, Kolmogorov recognized that $V_1^3/L_1 \approx \dots \approx V_n^3/L_n \approx B$, a constant, such that the velocity fluctuations could be written as a function of the length scale, $V_n \approx (B L_n)^{1/3}$. From this Kolmogorov deduced a form for the velocity structure function:

$$D_v(r) = C_v^2 (\epsilon r)^{2/3}, \quad \ell_o < r < L_o, \quad (1.7)$$

which is related to the square of the mean velocity difference at separation scale r . Here, C_v^2 is a constant, the velocity structure parameter. The structure function is considered isotropic, which follows naturally from the properties of the flow at length-scale L_o .

In general, one may define a structure function for any property, p , as

$$D_p(r) = \left\langle [p(\vec{x} + \vec{r}) - p(\vec{x})]^2 \right\rangle, \quad (1.8)$$

where $r = |\vec{r}|$.

Second, from the form of the velocity structure function, Kolmogorov was able to make the conceptual link to temperature fluctuations by assuming that temperature perturbations are carried along by the wind flow as a conserved property. That is, eddies, characterized by velocity $\vec{v}(\vec{r})$, will transport with them a characteristic temperature $T(\vec{r})$, since mixing effects are ignored at large scales.

Such perturbations, termed *conservative passive additives* (CPAs), persist within the flow down through the cascade process until such point as small-scale mixing causes the remaining perturbations to be dissipated out of the flow, as was the case with the wind field. Similarly, the temperature structure function follows the same power law as other CPAs.

However, we should add a few caveats when it comes to temperature. Thermal perturbations will tend to radiate differently depending on the temperature. Therefore, they are not exactly conservative. Also, because different temperatures exhibit different buoyancies relative to the background mean vertical temperature structure, they are not exactly passive, either. But, for the sake of simplicity, both of these assumptions are commonly used.

We focus on the temperature effects because of their direct relation to refractive index. In the boundary layer, atmospheric temperature fluctuations are primarily responsible for the variations in refractive index at ultraviolet through far-infrared wavelengths. While there is a pressure dependence that is nontrivial, in general pressure gradients are a relatively slowly varying function of height:

$$\frac{dP}{dz} = -\rho_a g/100, \quad (1.9)$$

where the 100 factor converts the dimension from Pascals (the natural MKSA dimension) to millibars (the units used commonly for meteorological measurements). From this relation, the total dry-air-density fluctuation can be written,

$$d\rho_a = 0.34838 \left(\frac{dP}{T} - \frac{P}{T} \frac{dT}{T} \right) = -\frac{\rho_a}{T} (0.034 dz + dT). \quad (1.10)$$

That is, thought of as a temperature gradient equivalent, the pressure effect is equivalent to a -0.034 K/m temperature drop.

Let us next introduce the formula used for converting pressure and temperature to the refractive index for dry air:

$$n \approx 1 + 78.2 \times 10^{-6} \frac{P}{T} = 1 + \aleph P/T = 1 + 224.5 \times 10^{-6} \rho_a. \quad (1.11)$$

The refractive index also features a humidity-dependent term, but this effect is a factor of roughly 100 weaker compared to the temperature effect. Similarly, there exists a spectral-dependent term in the refractive index formula that is second order. Finally, there is a humidity–temperature cross term that is approximately an order of magnitude weaker than the temperature effect; but, since turbulence strength can vary by orders of magnitude over a single diurnal cycle, and the uncertainty in the C_n^2 is roughly a factor of 2.0 or greater, due to intermittency effects, this 10% effect is ignored in practice.

To a good approximation one can compute a refractive index power spectrum knowing only the structure of the temperature fluctuations and using the above expression for the refractive index.

1.3 Turbulence Spectrum

We have now seen the refractive index structure parameter in at least one context. It appears in relation to the refractive index structure function,

$$\mathcal{D}_n(r) = \langle [n(\vec{x}) - n(\vec{x} + \vec{r})]^2 \rangle. \quad (1.12)$$

But a further refinement is often invoked. This one involves the assumption that the refractive index can be subdivided into a portion that is constant with position (n_0) and a perturbation term (n_1) that varies. In a real atmosphere this assumption is never technically true, since the mean refractive index must be a function height as it depends on vertically varying pressure and temperature. However, as long as length separations are not made *too long*, then it is approximately true. This is the implication of the concept of *stationary increments*.

With this assumption, the expression in Eq. 1.12 is modified such that n_1 's replace the n 's on the right-hand side (RHS). One may then write the structure function in terms of correlation functions:

$$\mathcal{D}_n(r) = 2 \Gamma_n(0) - 2 \Gamma_n(r), \quad (1.13)$$

where the Γ_n functions are covariance functions of n :

$$\Gamma_n(r) = \langle n_1(\vec{x}) n_1(\vec{x} + \vec{r}) \rangle. \quad (1.14)$$

This function is related to a power spectrum of the refractive index, $\Phi_n(\kappa)$, through a Fourier transform:

$$\Phi_n(\vec{\kappa}) = \left(\frac{1}{2\pi} \right)^3 \iiint_{-\infty}^{+\infty} \Gamma_n(\vec{r}) \exp(i \vec{\kappa} \cdot \vec{r}) d\vec{r}, \quad (1.15)$$

or via the following Fourier-transform pair if the turbulence is isotropic:

$$\Phi_n(\kappa) = \left(\frac{1}{2\pi} \right)^3 \int_0^\infty \Gamma_n(r) \frac{\sin(\kappa r)}{\kappa r} 4\pi r^2 dr, \quad (1.16)$$

$$\Gamma_n(r) = \int_0^\infty \Phi_n(\kappa) \frac{\sin(\kappa r)}{\kappa r} 4\pi \kappa^2 d\kappa, \quad (1.17)$$

by integrating first over the 2 angular variables.

Unfortunately, because the Kolmogorov refractive index structure function has no upper bound, only its $r^{2/3}$ dependence, and the cutoffs in r : $\ell_o < r < L_o$, when forming the refractive index spectrum one obtains a divergent integral ($\Gamma_n(0) = \infty$). This in turn indicates the Kolmogorov spectrum should diverge at the origin, which indeed it does, following the law,

$$\Phi_{nK}(\kappa) = \beta C_n^2 \kappa^{-11/3}, \quad (1.18)$$

where $\beta \approx 0.033$ is an integration constant:

$$\beta \equiv (5/36)[2^{2/3} \Gamma(5/6)]/[\pi^{3/2} \Gamma(2/3)] \approx 0.033. \quad (1.19)$$

We shall not dwell on the frequency spectrum, but we do note that the range of validity of the Kolmogorov spectrum is commonly expressed as

$$\frac{1}{L_o} < \kappa < \frac{1}{\ell_o}. \quad (1.20)$$

Hence, the inner and outer scales of turbulence appear again, this time as gatekeepers of sorts on the Kolmogorov *inertial subrange*, whereas previously the inner scale was shown to be related to the dissipation of kinetic energy and the outer scale to the source term of kinetic energy, in combination with the wind structure function.

Now, in terms of effects of the inner and outer scale on turbulence problems, we note 2 things. Outer scale is related to the amount of energy available in the turbulent fields, both wind and temperature fields. Therefore, in terms of modeling, the outer scale provides an important link between flux theories and turbulence calculations eventually used in propagation studies. On the other hand, the inner scale has a direct role in propagation studies of scintillation effects.

This inner-scale role appears because of the end of fluctuations at frequencies much higher than $1/\ell_o$, due to dissipation effects, and because of a particular feature of the wind dissipation itself. Emerging from Kolmogorov's analysis is the fact that

when the wind perturbations are dissipated at the size range around the inner scale, or the Kolmogorov scale, denoted η_o , where the 2 are related through Wyngaard's (1973) definition,

$$\ell_o \approx 7.4 \eta_o = 7.4 \left(\nu^3 / \epsilon \right)^{1/4}. \quad (1.21)$$

The distinction without a difference between these 2 measures is that the inner scale occurs roughly at the beginning of a *bump* in the refractive index spectrum, while η_o occurs in the middle of this spectral *bump* and typically measures less than a millimeter.

At this length-scale a secondary heating source appears due to the dissipated mechanical energy. This extra heating is intermittent, enhancing temperature fluctuations in its spectral vicinity and producing a *bump* in the temperature spectrum. This effect is termed the “Hill Bump” (Hill 1978; Hill and Clifford 1978).

This bump, though small, signals the end of the refractive spectrum (values zero at frequencies an order of magnitude greater than the bump frequency). The bump produces significant impacts on certain propagation effects, particularly those related to scintillations of beam-wave propagation of coherent light. For an optical path-length denoted S , and a monochromatic wavelength of radiation λ , a dimensionless parameter $\phi = (\lambda S) / \ell_o$ can be shown to parameterize the height of the resulting scintillation saturation curve as a function of integrated turbulence strength (e.g., Tofsted 1993).

The next section will introduce a more complete spectrum — but before leaving considerations of the basic spectrum, let us introduce a few useful relations that may be needed later. The first of these is the refractive index variance:

$$\sigma_n^2 = \int_0^\infty \Phi_n(\kappa) 4\pi \kappa^2 d\kappa. \quad (1.22)$$

The second is an integral that connects a 1-dimensional (1-D) spectrum such as would be sensed with a fixed sensor (a sonic anemometer for instance) with an equivalent 3-dimensional (3-D) spectrum used in propagation models.

$$F_n(\kappa_1) = 2 \int_0^\infty \Phi_n \left(\sqrt{\kappa_1^2 + \kappa_r^2} \right) 2\pi \kappa_r d\kappa_r, \quad (1.23)$$

where κ_1 is the transform dimension oriented along the direction of the mean wind, κ_r is a radial frequency in the plane transverse to the mean wind, and both F_n and

Φ_n are single-sided spectra (undefined for κ_r or κ less than zero). The inverse of this relation is

$$\Phi_n(\kappa) = -\frac{1}{4\pi\kappa} \frac{dF_n(\kappa)}{d\kappa}. \quad (1.24)$$

In the inertial subrange the 1-D spectrum evaluates as in Tofsted et al. (2007),

$$F_{nK}(\kappa_1) = (12\pi/5) \beta C_n^2 \kappa_1^{-5/3}, \quad (1.25)$$

the 1-D analog of the Eq. 1.18's 3-D Kolmogorov spectrum. However, it should be emphasized that these relations are based on the assumption of isotropic turbulence. When anisotropic turbulence is present at large length-scales, analysis has indicated (Tofsted et al. 2009) that at least in terms of wind turbulence the structure of the fluctuations produces a Reynolds stress tensor whose principle axes are not equal, meaning that at the largest length-scales the fluctuations are dominated by the horizontal-axis components. Interestingly enough, it is not the along-wind component that is the greatest horizontal term. Rather, due to the effects of meandering, it is the horizontal component that is transverse to the mean wind that is the largest component, followed closely by the along-wind component of the wind variance and then by the vertical component, in approximately a 6–4–1 ratio, but where the principal axes are tipped slightly forward and downward to account for the mean flux of momentum toward the ground.

1.4 Outer-Scale Effects on the Refractive Index Spectrum

It is not the purpose of the present work to develop models of the modifications of the turbulence spectrum due to the inner and outer scales of turbulence. For completeness and closure, however, this report presents model forms for both the outer- and inner-scale effects on the spectrum. In this way we will have a point of reference for viewing future impacts of the spectrum on propagation statistics as well as a model for describing moments of the turbulence when looking at energy content and source terms that particularly involve outer-scale effects.

The standard approach to dealing with the outer scale effects is to use the so-called von Kármán spectrum. We express this as

$$\Phi_{nV}(\kappa) = \beta C_n^2 \Upsilon_0(\kappa, \mathcal{L}_0), \quad \Upsilon_m(\kappa, \mathcal{L}) = \frac{\mathcal{L}^{11/3} (\kappa \mathcal{L})^{2m}}{[1 + (\kappa \mathcal{L})^2]^{(11+6m)/6}}. \quad (1.26)$$

Propagation scientists commonly identify \mathcal{L} directly with the outer scale L_o , and then define $L_o \approx k z$, where $k \approx 0.4$ is von Kármán's constant and z is the

height above the surface. But these associations appear rather arbitrary. Moreover, Hinze (1987) described the spectrum as including 3 regions: the *energy containing subrange*, the *inertial subrange*, and the *dissipation subrange*. Below the energy-containing range von Kármán (1948) indicated the spectral dependence should behave as κ^2 , not the constant spectral energy that reaches a maximum at zero frequency. A misinterpretation seems to have occurred somewhere such that the spectrum that bears his name does not behave as von Kármán himself intended. This was previously corrected in Tofsted (2000) and Tofsted et al. (2007).

In Tofsted (2000), forms Υ_1 and Υ_2 were combined to construct a κ^2 dependence at the lowest frequencies. However, this form did not strictly follow von Kármán's theory due to the presence of Υ_2 , yielding a κ^4 term. It also required one of the components to be negative. The 2007 paper corrected this deficiency through the use of 3 weighted Υ_1 functions:

$$\Phi_{nR}(\kappa) = \beta C_n^2 \sum_{i=0}^3 w_i \Upsilon_1(\kappa, \mathcal{L}_i), \quad (1.27)$$

where the nR subscript references the characterization of the energy-containing range of the spectrum, and where

$$\begin{aligned} w_1 &= 1/4, & \mathcal{L}_1 &= 0.8 L_o, \\ w_2 &= 1/2, & \mathcal{L}_2 &= 2.0 L_o, \\ w_3 &= 1/4, & \mathcal{L}_3 &= 5.0 L_o. \end{aligned} \quad (1.28)$$

These relations were chosen such that an outer scale could be defined relative to the rolloff of the Kolmogorov behavior at low frequency:

$$\Phi_{nR}(1/L_o)/\Phi_{nK}(1/L_o) \approx 0.5, \quad (1.29)$$

where $\kappa = 1/\lambda$ is used, consistent with Ishimaru (1978) and Andrews and Phillips (1998), as opposed to $\kappa = 2\pi/\lambda$ used by Clifford (1978) and Kopeika (1998). (The actual value on the RHS of Eq. 1.29, based on the coefficients of Eq. 1.28, is 0.506.)

This spectral form was designed to match data presented by, and the 1-D spectral model proposed by Kaimal et al. (1972). This 1-D model can be cast into a refractive index spectrum form as

$$F_{nG}(\kappa_1) = \sigma_n^2 \frac{B/\kappa_0}{1 + B(\kappa_1/\kappa_0)^{5/3}}. \quad (1.30)$$

This spectrum carries the appropriate asymptotic behaviors at low and high frequencies. At low frequencies it approaches a constant at maximum value. At high frequency it exhibits the $\kappa_1^{-5/3}$ behavior. The significance of this form is that the Kaimal group developed similarity-theory-based relations between the κ_0 constant and the ratio $\zeta = z/L_{Ob}$. However, we cannot use F_{nG} directly, for when we apply Eq. 1.24 to this functional form to generate the equivalent 3-D spectrum we obtain

$$\Phi_{nG}(\kappa) = \frac{\sigma_n^2}{4\pi \kappa} \frac{(5/3) B^2}{\kappa_0^2} \frac{(\kappa/\kappa_0)^{2/3}}{[1 + B (\kappa/\kappa_0)^{5/3}]^2}. \quad (1.31)$$

This function's $\kappa^{-1/3}$ low-frequency dependence yields a singularity at the origin.

To solve this problem, the Eq. 1.27 form involving a weighted sum of Υ_1 terms was used. But before proceeding, let us first compare the high-frequency behaviors of the Kaimal function and that of the Kolmogorov spectrum translated into its 1-D form in Eq. 1.25:

$$\frac{12\pi}{5} \beta C_n^2 = \sigma_n^2 \kappa_0^{2/3}. \quad (1.32.A)$$

$$\kappa_0 = \left(\frac{12\pi}{5} \frac{\beta C_n^2}{\sigma_n^2} \right)^{3/2}. \quad (1.32.B)$$

The κ_0 thus depends on turbulence strength and the form taken by the refractive index variance.

While we cannot convert the Kaimal expression into a 3-D version that behaves properly, the opposite can be performed: We can produce a 1-D version of our proposed spectrum and compare it against the 1-D Kaimal function. To perform such comparisons, we first introduce the standard normalized form used by Kaimal:

$$\Psi_{nG}(\kappa_1) = \kappa_1 F_{nG}(\kappa_1)/\sigma_n^2. \quad (1.33)$$

This form is useful because it can be transformed more easily between its temporal-frequency and spatial-frequency versions.

To compare forms, let us first evaluate σ_n^2 for the Eq. 1.27 spectrum:

$$\sigma_n^2 = \int_0^\infty \Phi_n(\kappa) 4\pi \kappa^2 d\kappa = \frac{12\pi}{5} \beta C_n^2 A_A \sum_{i=1}^3 w_i \mathcal{L}_i^{2/3}, \quad (1.34)$$

where

$$A_A = \frac{(3\pi)^{3/2}}{11 \Gamma\left(\frac{5}{6}\right) \Gamma\left(\frac{2}{3}\right)} \approx 1.7209. \quad (1.35)$$

Our spectrum can then be converted into 1-D form:

$$\frac{\Psi_{nR}(\kappa_1)}{\kappa_1} = \frac{1}{A_X} \sum_{i=1}^3 w_i \frac{\mathcal{L}_i^{5/3} \left[(\kappa_1 \mathcal{L}_i)^2 + \frac{6}{11} \right]}{\left[1 + (\kappa_1 \mathcal{L}_i)^2 \right]^{11/6}}, \quad (1.36)$$

using

$$A_X = A_A \sum_{i=1}^3 w_i \mathcal{L}_i^{2/3}. \quad (1.37)$$

From $\Psi_{nR}(\kappa_1)$ and $\Psi_{nG}(\kappa_1)$, both B and κ_0 can be evaluated. In the limit $\kappa_1 \rightarrow 0$, $\Psi_{nG} \rightarrow B/\kappa_0$. In the limit $\kappa_1 \rightarrow \infty$, $\Psi_{nG} \rightarrow \kappa_o^{2/3} \kappa_1^{-5/3}$. From the high-frequency limit a relation between κ_0 and L_o is obtained:

$$\kappa_0^{2/3} = \frac{A_A^{-1}}{\sum_i w_i \mathcal{L}_i^{2/3}} = \frac{1.72086^{-1}}{1.74015 \times L_o^{2/3}} \rightarrow \kappa_0 = \frac{0.19298}{L_o}. \quad (1.38)$$

This result also allows us to simplify the expression for the refractive variance:

$$\sigma_n^2 = \frac{12\pi}{5} \beta C_n^2 / \kappa_0^{2/3} = \frac{(12\pi/5) \beta}{0.19298^{2/3}} C_n^2 L_o^{2/3} = 0.745 C_n^2 L_o^{2/3}. \quad (1.39)$$

In the low-frequency limit we can obtain a value for B :

$$\frac{B}{\kappa_0} = \frac{\frac{6}{11} \sum_i w_i \mathcal{L}_i^{5/3}}{A_A \sum_j w_j \mathcal{L}_j^{2/3}} \rightarrow B = \frac{0.19298 \frac{6}{11}}{L_o 1.72086} \frac{5.41478 L_o^{5/3}}{1.74015 L_o^{2/3}} \approx 0.19033. \quad (1.40)$$

This result differs from the values used by Kaimal. In the original paper $B = 0.16$; more recently, Kaimal and Finnegan (1996) recommended $B = 0.164$. On the other hand, from Kaimal's data, comparison appeared to show $B \approx 0.20$ (Tofsted 2000). The 0.19 introduced here represents a compromise between these different results, though tending toward the data result.

Now, the $\Psi_{nG}(\kappa_1)$ function has a peak value that occurs at $\kappa_m = \kappa_0 (2B/3)^{-3/5}$. The Kaimal group studied this maximum, but only in terms of the related dimensionless frequency $f = \kappa z / 2\pi$. In this form, Tofsted (2000) analyzed the Kaimal et al. scatter plot showing the peak point, f_m , as a function of the dimensionless ratio $\zeta = z / L_{Ob}$, the ratio of the height z to the Monin–Obukhov scaling length L_{Ob} (Paulson 1970). Data from one of Kaimal's plots were digitized, and an equation was fitted to these digitized data. Separate fits were generated for

unstable and stable surface-layer conditions (positive and negative L_{Ob} values):

$$f_m = \begin{cases} 0.460 \sqrt{+\zeta} + 0.0014 & \zeta > 0, \\ 0.036 \sqrt{-\zeta} + 0.0014 & \zeta < 0. \end{cases} \quad (1.41)$$

The fit achieved is illustrated in Fig. 2.

Figure 3 compares different versions of the Kaimal Ψ_{nG} function based on different values of the B parameter along with the fit of the Ψ_{nR} function transformed from the proposed 3-D spectrum (the Proposed Spectrum).

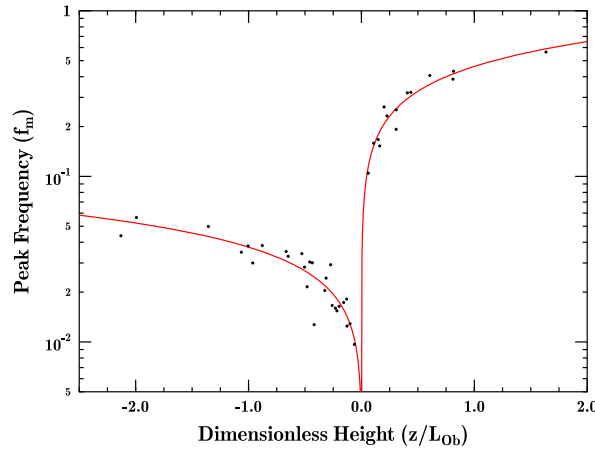


Fig. 2 Intercomparison of Kaimal-frequency maximum data (f_m) versus dimensionless height parameter $\zeta = z/L_{Ob}$ and plot of Eq. 1.41

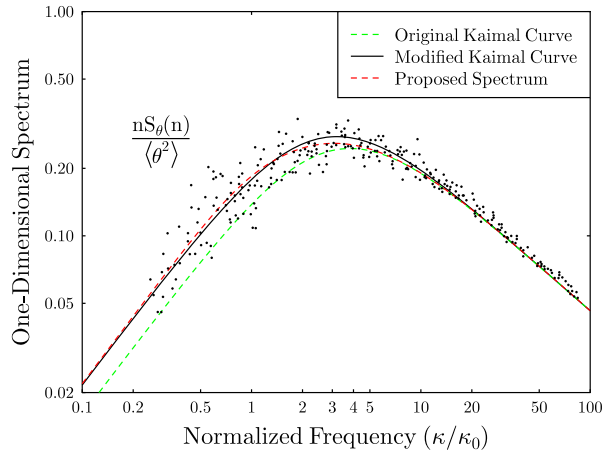


Fig. 3 Intercomparison of digitized Kaimal data with 1-D curve of Ψ_{nG} using original Kaimal $B = 0.16$ and $B = 0.19$, and Ψ_{nR} based on $B = 0.19$

Simplified means exist for evaluating the Obukhov length L_{Ob} (e.g., Tofsted et al. 2006), but these are less accurate than energy-budget-based evaluations. Calculation of L_{Ob} is a main focus of the present study, using Surface Energy Budget (SEB) methods to evaluate this parameter accurately.

Whichever means is used, for a given z and the computed L_{Ob} , f_m can be evaluated, leading to an estimate of L_o . For the proposed model's choice of $B = 0.19033$, the relation,

$$L_o = \frac{0.19298}{\kappa_0} = \frac{0.19298 z}{2\pi f_0} = \frac{0.19298 z}{2\pi f_m (2B/3)^{3/5}} = \frac{0.10599 z}{f_m}, \quad (1.42.A)$$

immediately follows.

Combining this result with the expression for f_m ,

$$L_o = \begin{cases} z/(4.34 \sqrt{+\zeta} + 0.013) & \zeta > 0, \\ z/(0.34 \sqrt{-\zeta} + 0.013) & \zeta < 0. \end{cases} \quad (1.42.B)$$

This relation reveals the distinctly different behavior of L_o under the 2 different stability regimes. During daytime conditions, $\zeta < 0$, and $L_o \approx 3\sqrt{|z L_{Ob}|}$, indicating outer-scale values often larger than the distance z to the ground.

This suggests that the daytime outer scale is driven by large-scale mixing from turbulence aloft. Even near-surface turbulence is thus seeing the influence of air mixing throughout the boundary layer. Conversely, under nocturnal stable conditions, turbulence is suppressed, such that L_o is significantly less than the distance to the ground. That is, the turbulence-suppressing nature of the inversion only permits localized small-scale mixing.

Lastly, at the neutral event ($\zeta \rightarrow 0$) the outer scale increases rapidly with height, indicative of the presence of low-frequency mixing that is not driven by fluctuations merely at the ground level. Effectively the entire boundary layer becomes involved when neutral mixing can occur. However, under such conditions our interest wanes since the effects of the turbulence will be negligible.

The above discussion of L_o evaluation is limited to the surface-layer atmosphere. Outside the surface layer alternative methods must be formulated, but available data are scarce. Notice that in arguing the Kolmogorov turbulence form we assumed that

at the outer scale the characteristic velocity was that of the wind speed. Perhaps this was because the wind speed differential would be that between the speed at height z and that at height zero. But, in general this parameter would need to be modeled using a quantity of order $L_o dU/dz$. Buoyancy effects would also need to be considered. Hence, results obtained for the surface layer do not have immediate analogs in the remainder of the boundary layer.

1.5 Inner-Scale Effects on the Refractive Index Spectrum

Inner-scale effects on the refractive index spectrum have been developed by a number of researchers, starting with Tatarski (1961). However, most of these models do not integrate easily. Therefore, some years ago the present author introduced (Tofsted 2003) a bump spectrum constructed using a transition function originally introduced by Belen’kii (1996).

The first step in describing this spectrum is to further examine the variability of the inner scale (first defined in Eq. 1.21), including its height dependence. The kinematic viscosity, ν , depends on the dynamic viscosity, μ , from Eq. 1.1 and the density, ρ_a , from Eq. 1.2. Let us combine this dependence with a surface-layer characterization of the dissipation rate, ϵ , that is (approximately) $u_*^3/(k_v z)$. Here, u_* is the friction velocity, given in its neutral stability form by

$$u_* \approx \frac{k_v u}{\ln(z/z_o)}, \quad (1.43)$$

where k_v is von Kármán’s constant, $k_v \approx 0.40$ over rough terrain, z_o is the roughness length, and u is the wind speed at height z above the displacement height. Combining terms, we have

$$\ell_o \propto [\mu/(\rho_a u_*)]^{3/4} (k_v z)^{1/4} \propto \left[\frac{T^{5/2} \ln(z/z_o)}{P(T+C) k_v u} \right]^{3/4} (k_v z)^{1/4}. \quad (1.44)$$

This formulation indicates that we can determine the inner scale as a function of height, but we must begin by knowing u and T at height z , along with P , and z_o . The apparent wind-speed dependence in this function is $u^{-3/4}$; however, data collected at Table Mountain, Colorado, by researchers from the National Oceanic and Atmospheric Administration’s Wave Propagation Laboratory at Boulder, Colorado, suggest a slightly modified dependence.

In Tofsted and Auvermann (1991) we developed the empirical relation (Eq. 33 of that paper) that I shall approximate here as

$$\ell_o \approx 0.000463 \left[\frac{T^{5/2} z^{1/3}}{P(T+C)} \ln\left(\frac{z}{z_o}\right) \right]^{3/4} \left[1 - 0.0618 u + \frac{0.515}{u} + \frac{0.268}{u^2} \right], \quad (1.45)$$

where the temperature and pressure-dependent term was appended to a modified wind-speed function and z and z_o obtained from the height of the meteorological sensors and site vegetation.

The wind-speed component of this curve is plotted in Fig. 4 along with the data set from which it was derived. In addition, we present the $u^{-3/4}$ wind-speed dependence as the blue dashed line. Only the neutral condition's log-wind profile was introduced since we did not have data-tagging to assign any specific stability condition to elements of the data set, though clearly the data set does bifurcate at inner-scale lengths above 7 mm, and this may be stability related. A more detailed study of this behavior would be possible using one or more Scintec SLS-20 scintillometers in combination with wind and temperature measurements at multiple heights to provide the data needed to characterize the vertical dependence of ℓ_o in the surface layer as well as ℓ_o 's stability dependence.

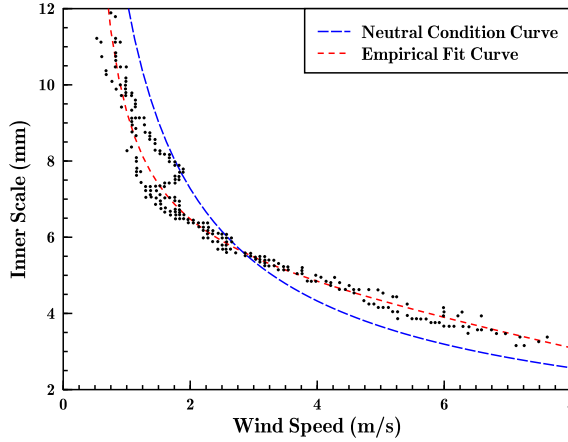


Fig. 4 Empirical inner-scale relationship to observed wind speed versus theoretical inner-scale wind dependence for neutral stability case

Knowing ℓ_o , the inner-scale effect due to dissipation can be modeled using a function suggested by Belen'kii (1996):

$$\mathcal{I}(x) = \frac{x^{11/6} K_{11/6}(x)}{2^{5/6} \Gamma(11/6)}. \quad (1.46)$$

Here, K_λ is the modified Bessel function of the third kind, order λ . This function is approximately unity at small values of argument x and trails off toward zero at large x . Belen’kii used the function in a single-mode form to approximate Tatarski’s (1961) inner-scale exponential dissipation effect. This function is plotted in Fig. 5. However, Tatarski’s form did not account for the spectral bump.

Here, Belen’kii’s form is used due to its integral properties, but where 2 copies of the function are combined to simulate the Hill bump spectrum (Hill and Clifford 1981) in the form,

$$\Phi_{nH}(\kappa, \ell_o) = \beta_n C_n^2 \kappa^{-11/3} F(\kappa \ell_o / 1.412), \quad (1.47)$$

with the envelope function,

$$F(\gamma) = 2.75 \mathcal{I}(\gamma/1.324) - 1.75 \mathcal{I}(\gamma/0.586). \quad (1.48)$$

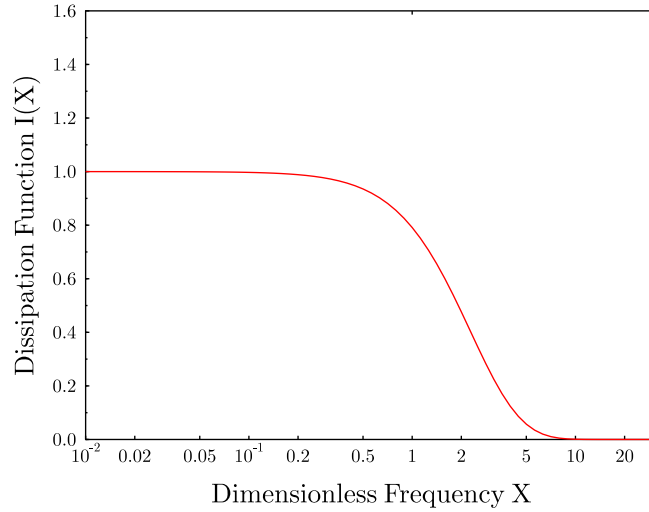


Fig. 5 Dissipation curve of Belen’kii function

The F function, being based on \mathcal{I} , behaves as $F \rightarrow 1$ for small argument, while exhibiting $F \rightarrow 0$ at large argument, and exhibiting the characteristic Hill-bump behavior near $\kappa \approx 1/\ell_o$. This curve was fitted to bump spectra of Hill (1978) and Frehlich (1992) where a compromise between the differing forms was constructed. A third bump spectrum is also available, by Churnside (1990), but the shape of this curve is approximately the same as that of Hill’s spectrum and so was not included. These bump spectra are intercompared in Fig. 6.

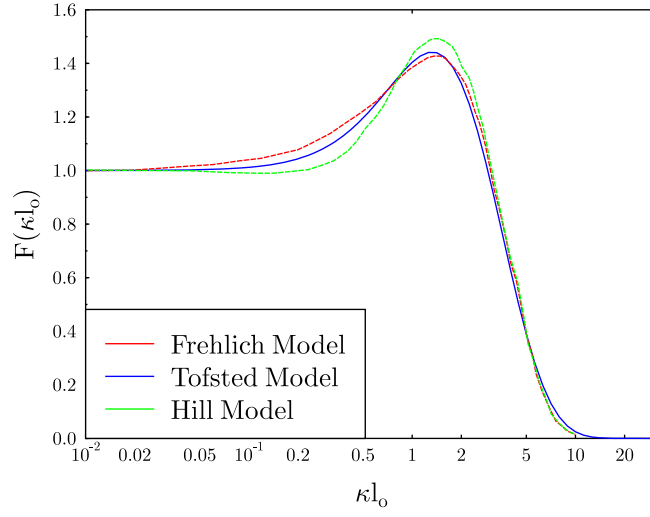


Fig. 6 Intercomparison of different inner-scale-affected bump spectra

The fitted coefficients modeled the average of the Hill spectrum and Frehlich's intermediate case ($1.324 = 10^{0.122}$; $0.586 = 10^{-0.232}$).

To conclude this development, let us note how the inner- and outer-scale modulated spectra can be combined. Inner- and outer-scale modulated forms of the original Kolmogorov spectrum, Φ_{nK} , exhibit asymptotic behaviors that match this spectrum at low- and high-frequency ranges respectively. To create a complete spectrum we simply note that under most conditions $L_o \gg \ell_o$. As such, there is little feedback between the inner- and outer-scale modulated portions of the complete spectrum. Thus, we should be able to simply write

$$\Phi_n(\kappa) = \Phi_{nR}(\kappa, L_o) + \Phi_{nH}(\kappa, \ell_o) - \Phi_{nK}(\kappa), \quad (1.49)$$

where we subtract a copy of the Kolmogorov spectrum to avoid double-counting the inertial subrange. In this way, separate integral forms can be developed to treat different portions of the spectrum separately.

Although the combined spectrum is not perfect, in that it assumes isotropic turbulence, this would not affect its properties at high frequency or within the inertial subrange, where it would be isotropic. Therefore, its properties account for the majority of the spectrum that most directly impacts optical effects. Also, at the low-frequency end of the spectrum—although the spectrum proposed is isotropic—when converted to a 1-D spectrum its properties match those of the

Kaimal group, which was viewed as the best model available at the point where the research bifurcated into the recent focus on Large Eddy Simulations and the interest of the optical community on spectral properties. It is hoped that the present work will help to re-establish these 2 divergent areas. The main question, though, is how to transform the information available with regard to anisotropic turbulence and interpret this information in terms of a useable spectrum for propagation-analysis purposes. One method might be to simply transform the 3-D spectrum down to a 2-D form and then low-pass filtered. The result could be interpreted as a low-frequency part of the complete spectrum. The equivalent high-pass filtered portion would correspond to the 3-D portion of the spectrum. We already have some concept of the range of the transition, but the full exploration of this issue is outside the scope of the current investigation.

2. Introduction to the Surface Energy Budget

In this chapter we shall discuss the connection of the turbulence strength, C_n^2 , to surface layer properties, particularly energy fluxes arising from or directed toward the surface. Recall that in Chapter 1 we discussed in general terms the connections between the energy dynamics of the surface-layer atmosphere and how those are related to properties of the turbulence spectrum. For example, the inner-scale correlation with wind speed is strong, as well as its connection to height above the surface. The outer scale is a function of height above the surface as well as the Obukhov length, L_{Ob} . It was also described how temperature differentials at the top of the surface layer enter the base of the convective boundary layer during daylight heating of the boundary layer and influence the turbulence above the surface layer. At night the situation is somewhat altered since the surface becomes a heat sink rather than a source. Nonetheless, surface-layer dynamics remain important even at night due to the process generating cooler air near the surface that is a source of temperature differentials when mixed with warmer air from above via mechanical mixing that occurs intermittently during the night.

2.1 Turbulence Prediction using Surface Energy Budget

To further establish these connections, let us review an analysis that first appeared in Tofsted et al. (2006). To begin, we introduce the Kunkel and Walters (1983) definition of C_n^2 :

$$C_n^2 = C_T^2 \frac{A^2 P^2}{T^4} \left(1 + \frac{0.03}{B}\right)^2, \quad (2.1)$$

where $A = 79 \times 10^{-6}$ K/mbar, C_T^2 is the temperature-structure parameter, P is again the pressure in mbar, T is temperature in Kelvin, and B is the Bowen ratio, the ratio of the sensible to latent heat fluxes, $B = H_S/H_L$. This is a surface-layer formulation. In most cases where turbulence is strong, B will tend to be greater than unity, and perhaps much greater than unity such that this term can be viewed as a minor perturbation.

The key variable in the above expression is therefore C_T^2 . Wyngaard (1973) recommended the function,

$$C_T^2 = T_*^2 z^{-2/3} 4.9 \times \begin{cases} \left[1 - 7.0 \left(\frac{z}{L_{Ob}}\right)\right]^{-2/3}, & L_{Ob} < 0; \\ \left[1 + 2.4 \left(\frac{z}{L_{Ob}}\right)^{+2/3}\right], & L_{Ob} > 0. \end{cases} \quad (2.2)$$

During daylight surface heating, $L_{Ob} < 0$, the C_T^2 height dependence is approximately $z^{-4/3}$, while at night the initial vertical dependence of $z^{-2/3}$ gives

way to an approximately constant C_T^2 at the top of the surface layer. What we don't see in this standard method of vertical structure are the commonly observed vertical and horizontal variations in C_T^2 .

What we do see in Eq. 2.2 is the connection from $C_n^2 \rightarrow C_T^2 \rightarrow T_*$, the scaling temperature. This latter parameter connects C_n^2 directly to measurable properties of both microscale surface-layer statistics and to surface fluxes modeled by the SEB, primarily the sensible heat flux.

The sensible heat flux is approximately constant across the surface layer. It can be expressed using the T_* parameter in the form,

$$H_S = -\rho_a C_p u_* T_* = -\rho_a C_p k u_* \theta_*, \quad (2.3)$$

where ρ_a is the air density, C_p is the specific heat of air at constant pressure, k is von Kármán's constant ($k \approx 0.4$), and u_* is the friction velocity.

Equation 2.3 highlights one of the problems of the standard literature in flux-profile theory, also known as similarity theory: the appearance of multiple instantiations of the same parameter in slightly different forms. In this case the scaling temperature, T_* , also appears in the form of the scaling potential temperature, θ_* , where $T_* = k \theta_*$.

Friction velocity and scaling temperature also appear in conjunction with the expression for the Obukhov length, L_{Ob} (e.g., Paulson 1970):

$$L_{Ob} = \frac{u_*^2 T}{k g T_*} = \frac{u_*^2 \theta}{k^2 g \theta_*}, \quad (2.4)$$

where T or θ is a characteristic temperature/potential temperature of the surface layer, and g is the acceleration due to gravity ($+9.8 \text{ m/s}^2$). (Near the surface, $T \approx \theta$.) Through the use of H_S it is possible to eliminate T_* or θ_* from the Obukhov length calculation, which results not in a solution but merely transfers the problem to that of determining the sensible heat.

Interestingly, L_{Ob} is considered a constant of the surface layer, yet θ (T) is a function of height. To resolve this we will focus on θ and use its value as extrapolated from the top of the boundary layer. Because this temperature varies little over the course of a diurnal cycle, the importance of θ is minimized, leaving u_* and θ_* as the principal unknowns in determining L_{Ob} .

Now, the problem with estimating u_* , θ_* , and L_{Ob} is becoming simpler with time due to advanced sensor technologies. Modern 3-D sonic-anemometer technologies (e.g., Climatronics' CSAT-3 or RM Young's 81000 series devices) permit direct calculation of second-order statistics for atmospheric wind and temperature fields.

After removing mean trends, the wind fluctuations can be assigned as a perturbation vector (u', v', w') where the u direction is oriented along the mean wind, v is a crosswind term in a right-hand orthonormal system, and w is the vertical wind component. To denote mean effects we will often adopt the angle-bracket symbology $\langle \cdot \rangle$, representing time-averaged quantities where the averaging time is significantly longer than the time required for an integral scale (twice the outer-scale length of turbulence) to drift past the observation point. Based on this symbolism we shall form second-order statistics denoting the Reynolds' stress tensor components,

$$R_{ij} = \langle u'_i u'_j \rangle, \quad (2.5)$$

where $u_1 = u$, $u_2 = v$, $u_3 = w$. For a properly oriented wind system, $\langle w' \rangle \equiv 0$, since there can be no net wind flow through the ground interface. Use of the Reynolds' tensor allows us to define the friction velocity in terms of the net downward-directed momentum flux. This is given by Stull (1988):

$$R_{ij} = \langle u'_i u'_j \rangle. \quad (2.6)$$

For example, a time-averaged sensible heat flux can be evaluated using

$$u_*^2 = \sqrt{R_{13}^2 + R_{23}^2}. \quad (2.7)$$

However, in general, R_{13} , $R_{23} < 0$ because winds are higher the farther one displaces from the surface. Therefore, downward-perturbed winds are usually faster than the average, while upward-perturbed winds are generally slower than the average wind speed. In the special case where the coordinate axes are aligned such that the surface stress is oriented along the u axis, $u_* = -R_{13}$.

The sensible heat flux can similarly be expressed in terms of perturbation wind and temperature fluctuations (Paulson 1970):

$$H_S = \rho_a C_p \langle w' T' \rangle = -\rho_a C_p k u_* \theta_* = -\rho_a C_p u_* T_*. \quad (2.8)$$

As regards various flux calculations, the significance of the integral scale (relative to the expectation averaging time) is that small-scale effects are isotropic and therefore decorrelated, while the large-scale perturbations are correlated and contribute to the vertical fluxes of heat, moisture, and momentum. The integral scale reflects the peak energy level in the flow. Therefore, the integration time must be sufficiently long to accurately account for the energy within the flow.

We are therefore left with the apparent paradox in the standard theory (and one to be tested) that whereas T_* is based on correlations at the integral scale, T_* can be used to predict C_n^2 , which is characteristic of inertial subrange-sized perturbations seemingly distant (frequency-wise) from the size of turbulent eddies producing fluxes.

Nonetheless, the takeaway from this analysis is that by using sonic-anemometer measurements it is possible to evaluate u_*^2 and $u_* T_*$ directly, from which u_* and T_* may be derived. Using these parameters, C_n^2 can be evaluated, along with L_{Ob} . The C_n^2 can also be derived via an analysis of a sensed-temperature spectrum (e.g., Tofsted et al. 2007). We thus have 2 means of evaluating C_n^2 and can compare the 2 methods as functions of height and/or stability conditions.

However, in lieu of direct access to sonic-anemometer data, u_* and T_* are significantly more difficult to estimate. This factor leads to the adoption of SEB techniques, which require less direct information (e.g., time and/or spatially averaged wind information as opposed to high-frequency 3-component wind data).

2.2 The Surface Energy Budget

The SEB approach involves first estimating the sensible heat flux in light of several other energy fluxes at the *surface*; then, by estimating the Obukhov length, obtaining u_* , and finally T_* , after which C_n^2 follows directly. We shall write the energy-balance equation at the surface in the following form:

$$R_{S\downarrow} + R_{L\downarrow} = H_S + H_L + R_{S\uparrow} + R_{L\uparrow} + G. \quad (2.9)$$

In each case the fluxes being measured are entering or leaving the *surface layer*, which is here distinguished from what we previously described as the surface-layer atmosphere. By *surface layer* what is intended is a layer of foliage plus the surface itself. That is, a flat ground surface that has temperature T_g at any given moment.

The R terms of Eq. 2.9 are radiative fluxes. The R_S designates shortwave-radiative fluxes (wavelength of radiation less than $2.6 \mu\text{m}$). This is radiation in the solar band. By R_L we designate terrestrial graybody radiation at wavelengths greater than $2.6 \mu\text{m}$. Arrows indicate either upward flow from the surface interface or downward toward it.

The H terms denote convective fluxes into the surface-layer atmosphere. The H_S is the sensible heat flux (warming of the air), measured as positive when the surface is heating the air, and H_L is the latent heat of vaporization of water in the soil layer or evapotranspiration from the foliated layer. The G represents the ground-heat flux, such that positive G represents heat flow into the ground, warming the soil.

In general, because the density of the foliage is not considered substantial, the net energy retained by the surface interface is assumed equal to zero.

In its Eq. 2.9 form, the surface energy budget appears rather straightforward to evaluate. However, the presence of a foliated layer introduces complications in bookkeeping aspects of the calculation. For example, in addition to tracking the surface temperature, T_g , we must also account for a bulk temperature of the mean leaf surface, characterized by T_f .

Consider Fig. 7. Here, σ_F denotes the fraction of the surface covered by plants when viewed from above. Due to the foliated layer, the sensible heat flux has been subdivided into a component due to heat from the ground (bare soil), H_{Sg} , and a component due to heat being transferred at plant surfaces, H_{Sf} . A similar subdivision occurs for the latent heat fluxes. In both cases the surfaces interact with the air near the surfaces. The carrying capacity of the air regulates the overall net fluxes.

In Fig. 7 the convective-flux arrows are directed upward. This denotes that rather than allowing the surfaces to interact with each other, due to the flux mechanism the plant and soil surfaces directly involved in the convective fluxes themselves only indirectly interact with one another.

The main influence is therefore the direct flow of energy into or out of the surface-layer atmosphere. This, in turn, will tend to heat/cool the surface layer air and result in the corresponding feedback. Conversely, when treating radiative fluxes there are direct reflection and re-emission effects that are immediate.

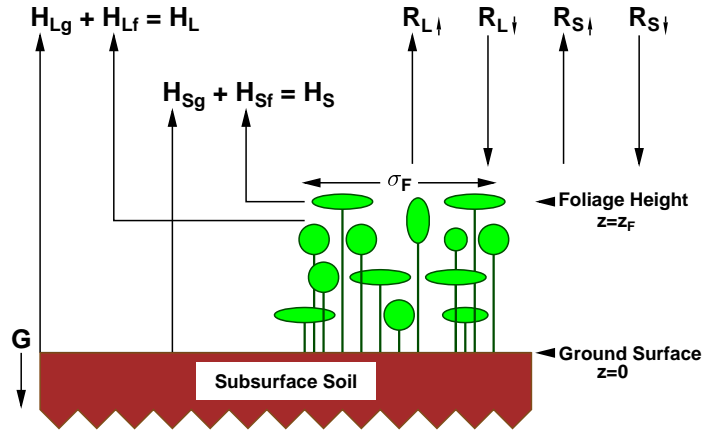


Fig. 7 Expanded decomposition of surface-energy fluxes in the presence a foliated layer

For reference, let us codify what is contained in Fig. 7 in terms of equations:

$$H_{Sg} + H_{Sf} = H_S, \quad (2.10.A)$$

$$H_{Lg} + H_{Lf} = H_L. \quad (2.10.B)$$

In other literature (e.g., Deardorff 1978; Tofsted 1993) the latent heat flux is written as the product between the latent heat of vaporization, L_v , and the vapor fluxes, E_g and E_f , corresponding to the rate of evaporation of moisture from the ground and from the leaf surfaces (evapotranspiration) in units of grams per square meter of underlying surface per unit of time increment. Here, for simplicity of presentation, all convective fluxes are denoted by the H symbology.

The primary goal of the remainder of this report is to further explain and argue for the solution of Eq. 2.9 (with 7 fluxes) or its extension in terms of Eq. 2.10, which introduces 4 new fluxes to replace 2 from the original expression. The reason for this approach can be explained when considering the alternative.

2.3 Flux-Profile Characterization of the Sensible Heat Flux

The flux-profile method becomes necessary under conditions where site data are unavailable or only known from model runs involving estimated temperature and wind-speed conditions. Under such conditions, modeled forms of the mean horizontal wind speed and temperature as functions of height must be invoked.

Paulson (1970) introduced forms for these functions of height given by

$$u_z - 0 = \frac{u_*}{k} \left[\ln \left(\frac{z}{z_o} \right) - \psi_1 \left(\frac{z}{L_{Ob}} \right) \right], \quad (2.11)$$

$$T_z - T_s = \frac{T_*}{k} \left[\ln \left(\frac{z}{z_o} \right) - \psi_2 \left(\frac{z}{L_{Ob}} \right) \right], \quad (2.12)$$

where u_z and T_z are horizontal wind-speed and temperature mean values at height z , and ψ_1 and ψ_2 are diabatic-influence functions dependent on the ratio z/L_{Ob} . The *surface*-based values of wind speed and temperature are denoted as $0 = u_s$ and T_s , respectively. However, neither of these important features is exactly as it might be portrayed at face value. That is, despite its appearance, T_s is not actually the temperature at the surface. Rather, it is an equivalent temperature at an extrapolated height somewhere within the surface layer of Fig. 7. Similarly, u_s equals zero at an extrapolated height (and perhaps a different height from the temperature profile) within the surface layer.

The diabatic-influence functions are related to dimensionless vertical wind and temperature gradient functions,

$$\phi_1(z/L_{Ob}) = \frac{kz}{u_*} \frac{\partial u}{\partial z}, \quad (2.13)$$

$$\phi_2(z/L_{Ob}) = \frac{kz}{T_*} \frac{\partial T}{\partial z}, \quad (2.14)$$

such that

$$\psi_x(\xi) = \int_0^\xi \frac{1 - \phi_x(\xi')}{\xi'} d\xi'. \quad (2.15)$$

For daytime conditions the diabatic-influence functions appear as

$$\phi_1(\xi) = (1 - 15\xi)^{-1/4}, \quad \phi_2(\xi) = (1 - 9\xi)^{-1/2} \frac{K_m}{K_h}. \quad (2.16)$$

Under nocturnal conditions these functions are modeled using

$$\phi_1(\xi) = (1 + 4.7\xi), \quad \phi_2(\xi) = (1 + 4.7\xi) \frac{K_m}{K_h}. \quad (2.17)$$

In both cases K_m/K_h is the ratio of eddy diffusivities of momentum to heat, equal to 0.74 under neutral conditions. Dyer (1974) used the constant 5 instead of 4.7 for nocturnal effects and 15 instead of 9 for the heat-related daytime relation. The coefficients included above are due to Businger et al. (1971). These are also the equations included in Stull (1988). (However, note the error in Stull's Eq. 9.7.5f where he used an exponent of $-1/4$ instead of the correct $-1/2$, as is included in Part b of his Fig. 9.9, which reproduces Businger et al's results.)

The importance of these relations is that u_* and T_* appear to be related to the vertical structures of the horizontal wind-speed and temperature profiles. If we can determine the shapes of these profiles, we can determine u_* and T_* and therefore determine H_S . But note that while the wind speed always approaches zero at *the surface*, the height of the extrapolated zero wind speed surface is not at the ground itself but, rather, at some height z_0 , termed the roughness height. Likewise, T_s is not the surface temperature, but instead is some effective temperature that causes the profile fit to match the current shape.

These functional forms also indicate that the temperature and wind speed are varying with height across the surface layer. The vertical profiles are in turn related to large-scale mixing effects that are related to the heat and momentum fluxes within the surface layer.

We also see from Eq. 2.11 that while we may know the left-hand side's (LHS) mean wind u_z , the RHS of 2.11 depends on both u_* and L_{Ob} (assuming z is a fixed observation height and the surface roughness z_o is a known, slowly varying function of time). Of course, we could combine the resolution of Eq. 2.11 with 2.12, but this equation also introduces the new unknown T_s . And, T_s is not easily obtained, given that it consists of an amalgam of effects related to both the surface and foliage temperatures.

But, we can estimate T_s (or at least get closer) if we can estimate T_g and T_f through an energy-budget computation. We can also check that work by computation of the H_S flux directly.

Given the complications of working with the rather intricate ψ and ϕ functions used in the profile methods, it is perhaps not unexpected that various flux modelers would chose simpler compound expressions to describe the sensible heat flux. For

example, Deardorff (1978) effectively approximates the sensible heat flux through use of the form,

$$H_S = \rho_a C_p c_H u (T_s - T_z), \quad (2.18)$$

where T_s is an aggregate surface temperature (see the Eq. 2.12 discussion) and T_z is again the estimate of the temperature at a specific height. This is the same height as associated with the horizontal wind speed u_z and density ρ_a (effectively, ρ_a is also a function of height but we omit the height indication). This reformulation replaces unknowns u_* and T_* by presumably measurable (or model/forecast predicted) quantities u and T_z , along with the new sensible-heat-flux efficiency factor, c_H , and modeled parameter T_s .

For composite surfaces consisting of a flat soil surface plus a vegetative layer, one must know the surface values of T_g , the soil-surface temperature, plus T_f , the aggregate foliage temperature.

Yet, perhaps inevitably, by introducing this new form, Deardorff has also introduced yet another parameter than needs to be evaluated: c_H . Thom (1972) used a slightly altered computation:

$$H_S = \rho_a C_p \frac{(T_s - T_z)}{r_H(z)}, \quad (2.19)$$

where r_H is a convective-flux resistance factor that incorporates the wind-speed effect. Let us also, here, define the specific heat of dry air at constant pressure:

$$C_p = 7R/2 = 1004.84 \frac{\text{J}}{\text{kg K}}, \quad (2.20)$$

where R is the gas constant, equal to 287.04 J/(kg K). This factor is related to the coefficient 0.34838 from the air-density equation, since $0.34838 = 100.0/287.04$, where the factor of 100 converts pressure from millibars into Pascals. (For moist air there is a slight adjustment to the Eq. 2.19 expression, but as it represents only a minor perturbation it will usually be ignored in the various derivations.)

The above assessment highlights that there are ad hoc methods for computing the sensible heat flux; that each requires knowledge of an effectiveness constant (c_H , r_H , etc.) dependent on atmospheric stability, and of a surface-equivalent temperature.

In this formulation, a method is used for mixing the temperatures of the foliage (T_f) and soil surface (T_g) that involves a weighted average of the 2 temperatures

based on their relative surface areas. Typically, a foliage layer has much greater exposed surface area than the overshadowed ground. To parameterize this effect, 2 numbers are used: σ_f , the relative fraction of the terrain covered by the foliage (the fractional, orthogonally shadowed area), and Υ_f , the single-sided area of leaves per unit of area of terrain covered. That is, for each square meter of terrain covered, Υ_f says there is Υ_f times as much leaf surface. The traditional value determined for Υ_f is 7. The value of 7 was adopted by Deardorff (1978) based on reported values by Allen and Lemon (1972) for a corn crop and by Monteith et al. (1965) for a barley crop — that for each square meter of overshadowing foliage, there are approximately 7 m² of leaf surface area. However, these studies considered mature agricultural crops. Such numbers thus refer to specific states of well-cultivated plant stands. Natural (noncultivated vegetation) would not likely exhibit this dependence. For example, short grasses simply do not have the same areal extent as significant crops of vegetables or grains.

These 2 parameters multiply to compute N_f , the square footage of single-sided plant-leaf surface per square meter of underlying surface:

$$N_f = \sigma_f \Upsilon_f, \quad (2.21.A)$$

or, more appropriately,

$$\Upsilon_f = N_f / \sigma_f. \quad (2.21.B)$$

For more general types of plants, the simple rule likely does not apply. This problem is addressed in more detail in Chapter 6.

Using the basic rule for N_F , Tofsted (1993) approximated the surface temperature as the surface-area-weighted average,

$$T_s = \frac{(T_g + 1.1 N_f T_f)}{(1 + 1.1 N_f)}. \quad (2.22)$$

The factor 1.1 was used to account (c.f., Deardorff 1978) for the difference in surface area between the leaf surface N_f and the leaf plus stems, twigs, branches, and trunks that can be involved in the sensible heat flux but would not contribute to the evaporative heat flux.

In the process, the problem has seemingly become more complex by exchanging T_s for both T_g and T_f , the ground- and foliage-surface temperatures. This is somewhat deceptive, though, since T_s was never truly the surface temperature. Technically, the logarithmic rule approaches minus infinity at exactly zero, so the process is only taken to a distance akin to the z_0 used in the wind-speed profile.

2.4 Surface and Atmospheric Inertia Effects

As we shall also explain in detail in a later chapter, there is a further consideration that affects all of our discussions, as well. That detail is first encountered when treating the surface temperature, since there is a thermal wave that passes into the surface. Therefore, there is always a resistance-type effect at the soil surface. But the same comment applies to the near-surface atmosphere, since heat that transfers into the air is distributed over a deeper zone than is associated with merely the thickness of the surface layer. These inertial effects in turn have an influence on how the model can accept measured data. By this is implied the following: Imagine the effect of inputting a measured atmospheric temperature into the model. As long as this temperature is reflective of and trails the warming or cooling surface temperature, the proper results occur: heat flows in the proper direction from the surface. However, what if our knowledge of the existing conditions is only partial? In this case the measured air temperature might lead the surface temperature, creating anomalous heat fluxes and predictions. For example, if our knowledge of solar radiation is not moment to moment — at the same data rate as the temperature, say — then under partly cloudy conditions the model might be using an incorrect radiation estimate but an accurate air-temperature value that is reflective of the moment-to-moment variations in radiation. To keep the model as consistent as possible, it is necessary to drive the vertical temperature model using the surface heat flux as its guide for warming or cooling.

This aspect will be treated in a separate section; but, we begin with a treatment of the various fluxes to develop improved models of these individual components before treating the overall coordination of the fluxes in temperature calculations.

2.5 History of Surface Energy Budget Model

The earliest attempt to produce an SEB model was an analog computer simulation by Halstead et al. (1957). As computer technology increased, the number of authors attempting such derivations has also increased, including the present author. More specifically, the derivation history closest to the present work is derived from an algorithm reported by Deardorff (1978) that was an amalgam of various techniques and empirical relations formulated to account for the different fluxes. Following Deardorff's work, researchers at the US Army Atmospheric Sciences Laboratory, Ken Kunkel and Don Walters, coded Deardorff's relations into a FORTRAN code

in the early 1980s that was used to predict turbulence conditions at what was to become the White Sands Missile Range's (WSMR's) High Energy Laser Systems Test Facility. Although this model was a direct translation, Kunkel and Walters recognized that it lacked an appropriate surface adjustment for surface-roughness effects in the sensible heat flux (Kunkel and Walters 1983).

In 1984 the present author encountered the Deardorff model as encoded by Kunkel when studying vertical structure of temperature in the surface layer and its effects on refractive path bending. Initially, the effort was merely to study the predicted vertical temperature gradients predicted by the model based on input weather data; however, this effort soon branched out to consider various alternative energy-budget factors since the model appeared to be in error under certain conditions when predicting sensible and latent heat fluxes. The most serious difficulties occurred when attempting to model effects for highly vegetated moist regions. This issue was addressed (e.g., Tofsted and Gillespie 1986) through the adoption of parametric results by Thom (1972). However, due to changing priorities this work was abandoned in the late 1980s. The final report documented the last state of the model (Tofsted 1993) that had not changed for more than 5 years. Since 1993, though, the need for a model to predict SEB effects has not diminished. If anything, such a model is more necessary today, given the proliferation of higher-powered optics and lasers, including advanced (FLIR) third-generation imaging sensors.

Moreover, while significant advances have occurred in the field of weather prediction, the standard mesoscale meteorological models still are primarily focused on generation of correct wind calculations and less so on temperature and surface properties. Indeed, the MM5 model commonly used a few years ago had its first computational level at 40+ meters above ground level (AGL). Such a level is outside or on the upper edge of the surface layer, leaving characterization of surface effects as an afterthought.

3. Surface Energy Budget Model Inputs

Up to this point we have discussed primarily the theoretical framework upon which the task of turbulence prediction is based. Now, it is appropriate to introduce the conceptual framework of the computer model itself. In so doing, the focus of this chapter to address a *use case* and the choices made with regard to user inputs within this case, since the inputs supplied will tend to drive the quality of the model's results obtained.

As such, let us consider what sort of model might be of use in a modeling environment. To begin, one must assume a user with some degree of familiarity with the problem being addressed; nonetheless, many users might only know that a problem with the optical systems exists but not know the physical basis for the effect. As such, users are only assumed to have sufficient familiarity with the environmental parameters to provide inputs to the model.

The other problem that typically arises is that for surface characterization many parameters are necessary to specify the state of the surface, subsurface soil, vegetation, moisture availability, and atmospheric conditions. Hence, if the number of parameters required to run such a model became prohibitively high, it may become unusable. Given this potential, the present effort has struggled to adopt as simple of a set of inputs as possible to supply the model with the necessary conditions, while restricting the number of inputs and the information required; this is so a relatively untrained user could successfully operate the code and obtain meaningful results quickly. In the process of discussing these inputs, we also address the means of translating between the input data and the relevant-state variables used by the model. These variables then appear in later chapters where we discuss the dynamic models used to evaluate the fluxes.

Given that this is initial version of the code is based on an initial set of assumptions with regard to user inputs, future versions can be readily envisioned in which more detailed information is supplied, thereby improving the temporal resolution of wind and temperature information. But in this first-level model, we characterize the needed inputs in terms of various elements of the environment: ground state, surface state, planetary location, temporal information, and general atmospheric conditions. In all, there are 15 variables considered necessary to run the code. Each of these variables is assigned a default value, so the code can be run with no standard inputs,

or by simply using the defaults for most inputs. The remaining inputs are entered using a standard format in a file named `SiteCond.dat`, the site conditions file. Each line of this input file contains a mnemonic 6-letter keyword followed by either a numerical value (integer or floating point depending on variable) or a second keyword (of variable length) used to select between different types of the designated variable. The use of keywords makes the input file easily understandable in terms of the input required (though in some cases the user must know the appropriate dimension to use for the input parameter). In most cases, where possible, the model inputs utilize the MKSA system. One exception is the case of air pressure where the common meteorological use of millibars is adopted over the MKSA system's use of Pascals (1 mbar equals 1 HPa). Temperatures are always in degrees Celsius or Kelvin.

This model is designed after the system developed for the Electro-Optical Systems Atmospheric Effects Library (EOSAEL) input methodology. Here, however, rather than permitting multiple entries per data-input line, only one parameter is to be input per line. While this is less efficient, it makes the input more readily legible and comprehensible.

3.1 Soil Properties

The primary soil characteristics that must be used within the SEB model are the solar-band mean albedo, or reflectivity, of the soil and the infrared band soil-surface emissivity, along with 2 of 3 of the properties: soil heat capacity C_g [J/(kg-K)], thermal diffusivity κ_g [m²/s], and thermal conductivity k_g [W/(m-K)]. In the process we also identify the soil density ρ_g [kg/m³]. Only 2 out of the 3 soil thermal properties are needed, since the third can be calculated via

$$\kappa_g = k_g / C_g.$$

Requiring a user to supply the relevant condition data needed to assign all 6 of these parameters would be difficult under most operational conditions. Hence, rather than impose this requirement on the user, we choose to parameterize the soil conditions in terms of 2 variables only. As an alternative potentially a database of values could be accessed, including information on soil conditions and moisture levels. While such an application is beyond the scope of the present effort, certain modeling environments feature just such access, permitting a table look-up to obtain the

necessary information, and in principle passing this information back to a main routine.

But for the present, we simply assign up to 3 variables: `SOILTP`, `SOILML`, and `SOILRH` — soil type, moisture level, and roughness height, respectively. For now there are only 3 possible soil-type input values permitted: `SAND`, `CLAY`, and `PEAT`. These use the canonical data sets supplied by Oke (1978, table 2.1, pg. 38). Oke supplies values of the major soil thermal parameters for dry and saturated conditions. At intermediate soil-moisture levels the model of Deardorff has been adapted to interpolate between the dry and saturated conditions to produce meaningful, intermediate moisture results. On the other hand, Oke’s Table 2.1 only supplies information for the soil thermal properties. Table 1.1 of Oke (1978) is used to augment this information to include soil albedo and emissivity ranges used for dry versus wet soils.

The initial dry soil condition data used is contained in the Table below.

Table Baseline dry-soil properties

Variable Name	Symbol	Dimensions	SAND Value	CLAY Value	PEAT Value
HeatCap	C_g	$10^{+6} \text{ J}/(\text{m}^3\text{-K})$	1.28	1.42	0.58
TherDif	κ_g	$10^{-6} \text{ m}^2/\text{s}$	0.24	0.18	0.10
WK	w_K	dimensionless	0.30	0.30	0.60
Wgmax	w_{\max}	dimensionless	0.40	0.40	0.80
Wwilt	w_{wilt}	dimensionless	0.15	0.15	0.30
Albedo	α_g	dimensionless	0.35	0.23	0.14
Emisty	ϵ_g	dimensionless	0.91	0.94	0.95

To characterize the relative moisture in the soil, the `SOILML` soil-moisture-level input is used. Moisture-level choices range from `PARCHED` `VERYDRY`, `DRYSOIL`, `WETSOIL`, and `VERYWET` to `SATUR8D`. These moisture levels correspond to numerical fill factors of water in the soil relative to a maximum fill factor possible for a particular soil type. Numerical translations are 0.02 (i.e., 2% fill), 0.10, 0.35, 0.65, 0.90, and 1.00 (100% fill). Let this input be termed m_S , such that $0 < m_S < 1$. From the previous input variable (soil type), one obtains a maximum soil-moisture fill fraction termed w_{\max} on the order of 0.25. The net soil-moisture content is then denoted by the variable w_g , the ground-moisture fill factor per unit of volume of soil:

$$w_g = m_S w_{\max}. \quad (3.1)$$

To gain some perspective on what constitutes typical conditions, Deardorff (1978, table 2) identified 2 typical soils: the O'Neill average and results from a clay pasture. In the former case, the soil-pore space was 22% ($w_{\max} = 0.22$) and of this the moisture fraction was 18% ($m_S = 0.18$). For the clay pasture the pore space was 30% ($w_{\max} = 0.30$) and of this roughly 50% was saturated ($m_S = 0.50$). As might be expected of a bottom-land pasture, the resulting soil is quite wet and of much greater heat capacity, reducing its diurnal variability.

To model the impact of soil moisture on the albedo, Deardorff's modification is used:

$$\alpha_{g,moist} = \alpha_{g,dry} (1.0 - 0.5 m_S). \quad (3.2)$$

The soil heat capacity is modified by the amount of soil moisture. To account for this we multiply the water content, w_g , by the density of water, $\rho_w = 10^3 \text{ kg/m}^3$, times the heat capacity of water, $C_w = 4184 \text{ J/(kg-K)}$:

$$C_{g,moist} = C_{g,dry} + \rho_w C_w w_g. \quad (3.3)$$

For the thermal diffusivity, Deardorff (1978, Eq. 38A) attempted to simulate the effect of moisture. However, the relationship shown by Oke (1978, Fig. 2.5.a) appears to be better accomplished by starting with the dry thermal conductivity, $k_{g,dry} = C_{g,dry} \kappa_{g,dry}$, and modifying it as

$$k_{g,moist} = k_{g,dry} + \rho_w C_w \kappa_{g,dry} \Sigma(3 w_g / w_{\max}), \quad (3.4)$$

where $\Sigma(x)$ is the sigmoidal function,

$$\Sigma(x) = \frac{[\exp(x) - \exp(-x)]}{[\exp(x) + \exp(-x)]}. \quad (3.5)$$

Then, computing

$$\kappa_{g,moist} = k_{g,moist} / C_{g,moist}. \quad (3.6)$$

For these 2 cases, soil emissivities, ϵ_g , were also reported. Values of 0.90 and 0.95, respectively, were given for the O'Neill and clay soils, and the soil albedos, α_g , were reported as 0.25 and 0.15, respectively. The O'Neill soil, being considerably drier than the pasture soil, was also significantly more reflective, while the 2 emissivities were similar.

The last soil-input category is `SOILRH`, a measure of the soil-surface-roughness element height used to evaluate the roughness length (z_{0G}) of the ground. Three input values are used: `GRANULR`, `PEBBLED`, and `ROCKY10`. These inputs correspond to numerical sizes of typical “surface roughness elements”. `GRANULR` means fine grains 1 mm in size; `PEBBLED` represents surface pebbles 1 cm in size; `ROCKY10` equates to rocky soil covered with rocks 10 cm in size. These will produce surface-based, roughness-element heights of 1 mm, 1 cm, and 10 cm that are used to compute the surface-roughness length, z_{0G} , used to evaluate the friction velocity, sensible heat model, and humidity flux. Assigning this input to the variable h_{0G} , the ground-roughness length is computed via

$$z_{0G} = 0.13 h_{0G}. \quad (3.7)$$

3.2 Foliage Properties

In the Deardorff approach to handling foliage information (although plant experts would disagree) the primary variables of interest are the height of the vegetation, which affects wind flow, and the amount, which affects the amount of shielding that the vegetation layer provides for the surface beneath. Though this is a relatively simple approach, and there are improvements that are obviously possible, for the current analysis this approach appeared to be the most accessible and easily definable.

To define these 2 inputs, 3 possible variables can be assigned. This route was taken so that users who have direct access to a ruler or other means of measuring length can easily input a more realistic number than the mnemonic choices available. The 3 variable names are `FOLTYP`, `FOLHGT`, and `FOLCVR`. The first 2 of these are 2 versions of the same input, essentially the standing height of the vegetation, z_F (as previously illustrated in Fig. 7).

The user can select the foliage-type input, `FOLTYP`, to indicate preset values of the height of the vegetation. Choices include `GREEN` (i.e., a golf green with foliage heights of 5 cm); `GRASS` measuring 15 cm (6-inches) high; `WEEDS` 25 cm high; `HEDGE` 50 cm high; and `BUSHS` 1.00 m high.

Alternatively, the user can input a `FOLHGT` involving a floating-point height (in meters) directly. The governing variable in the code is termed *FolHgt* and is set to a

default value of 0.5 m, roughly that of tall weeds (and approximately the height of the yucca plants native to the WSMR, New Mexico, area).

The second main category of input required for foliage is the fractional foliage cover, variable *FolCvr*, and use of the input keyword FOLCVR. We shall use the symbol σ_F for this parameter in equations beyond this chapter. Valid inputs range from 0.0 to 1.0. Negative values and results corresponding to a cover fraction greater than 100% are simply reset to the appropriate valid range.

It should also be mentioned that 2 constants are set to evaluate foliage radiative properties: foliage reflectivity of shortwave solar radiation (albedo), set as $\alpha_F = 0.20$, and foliage infrared radiative emissivity, $\epsilon_F = 0.95$. (These values correspond to live vegetation, but in deserts the plants spend much of the year in dormant — dead— states.) The emissivity and albedo of dead grass and weeds are obviously different, but are not available presently.

3.3 Surface-Layer Atmosphere Characteristics

To describe the most basic information needed to characterize the atmosphere (aside from clouds), we require at least one temperature, one wind-speed, and one humidity value. The governing assumption of the model is simplicity of input; and, while sophisticated temperature, wind, and humidity data could significantly improve the outputs, a user might not have access to such information, particularly if attempting to predict the turbulence levels in a forecast. In this case, a simple approach is taken: the use of persistence in prediction.

Based on this use case we simply require one temperature, measured or predicted, for dawn. The time of dawn is chosen because this should be the minimum temperature of the day or close to it. From this we should be able to assess properties of the complete boundary layer for the day. The relevant variable is *TdawnC*, with the input keyword TDAWNC. The input value is the air temperature at 4 m AGL, measured in degrees Centigrade. In many tactical settings a 6 AM weather observation is taken. From this input we calculate $T_{dawn} = T_{dawnC} + K_C$, where $K_C = 273.16$ converts the input temperature from Centigrade to Kelvin units.

Along with a dawn temperature reading, the humidity variable chosen is a relative humidity given as a fractional saturation (0.0 equals no humidity, 1.0 equals 100% relative humidity). Dawn is again chosen such that the temperature and the relative

humidity can be combined to generate an absolute humidity density (kg/m^3) in the air. The program variable is *RHdawn*, while the input keyword is *RHDAWN*. Let this variable be written, R_{dH} .

The last parameter is a 24-hr averaged horizontal wind speed (m/s) at a selected station height (*StaHgt*) in meters AGL. The value of this station height is set internally to the model but could be added as an input if desired. The wind-speed code variable is *WindSH* and the input keyword is *WINDSH*. The choice of a *station height* is necessary since temperature and wind speed are functions of height above the surface. We assign the symbol $\bar{U}_{24}(z_S)$ to this variable, where z_S is the station height.

Default conditions set for these variables are $T_{dawnC} = 15^\circ\text{C}$; $WindSH = 2.0$ m/s; $RHdawn = 0.080$ (i.e., 8% relative humidity); and $StaHgt = 2.0$ m.

3.4 Cloud-Cover Information

The next general category of inputs is the upper atmosphere, characterized by cloud properties. Three parameters are used, and the model of the clouds is rather simple. This is because for too many clouds one can simply assume the turbulence level will be suppressed sufficiently that many tactical operations will encounter limiting conditions other than turbulence (i.e., aerosol effects, precipitation, or diffraction at long ranges).

To characterize the clouds, we use 3 input types. The *FRACCC* keyword denotes input of the fractional cloud-cover amount, and the model variable *FracCC*. The valid range of this input is again 0.0 (no cloud cover) to 1.0 (overcast conditions). Let σ_C represent this parameter.

The second parameter is the cloud level, *CLDHGT*, using an index variable *CldHgt* set to 1, 2, or 3 in the model, which correspond to input keywords *LOWEST*, *MEDIUM*, and *HIGHER*.

The third parameter supplies a cloud type via keyword *CLDTYP*, using an integer variable *CldTyp* set to 1, 2, or 3, corresponding to input keywords *CUMULO*, *STRATO*, and *CIRRUS*.

The significance of these choices of keywords and characterizations is in connection with a cloud transmission model (Shapiro 1972) used to estimate the relative propagation of radiation through the cloud layers.

Default values for these 3 parameters are *FracCC* of 10% (0.1) and low-level cumulus clouds ($CldHgt = 1$; $CldTyp = 1$).

3.5 Site and Time Information

Finally, we need to set a series of variables to know the time and location of the calculation being made. Since we are performing a 24-hr simulation we only require the year, keyword `YEARAD`, and variable *YearAD*, and a date, keyword `JULDAT`, and variable *JulDat*. Both of these parameters require integer-valued input numbers.

The site of the computation is then identified based on a 3-D plot, given as latitude, longitude, and height of the site above sea level (ASL). Again, this information could be gleaned fairly easily from web resources. The mnemonics for these variables were selected as follows: `LATTNE` is latitude of the site of interest in degrees north of the equator. `LONGEG` is the longitude of the site measured in degrees east of Greenwich. Hence, WSMR, New Mexico, is assigned a positive *LattNE* code variable around 32.0, while *LongEG* is assigned a negative value of approximately -106.0 .

The vertical dimension of the position is indicated using the variable `HGTASL`, and code variable *HgtASL*, denoting the site's height ASL, but read as kilometers rather than meters. (This input breaks the paradigm of using only meters for lengths.) The main use of this variable is to assess the mean air density. Here, a simple approximation of the air density is given as a function of height ASL in kilometers in the variable *H*. Using a function empirically derived by Abel Blanco of the US Army Research Laboratory, we have the approximation,

$$\rho = 1.225 - \frac{H}{10} \left[1.176 - \frac{H}{100} \left[4.34 - 7.46 \frac{H}{100} \right] \right], \quad (3.8)$$

where ρ is given in kg/m^3 .

A final input is a height (in meters AGL) to be used in calculating the output C_n^2 values. This variable is denoted using the keyword `HGTCLC` and associated variable *CalHgt*. This parameter allows the user to input data at one height (the station's) and output results at a different height (where C_n^2 is desired to evaluate its effect on propagation). Let z_C represent this variable.

3.6 Model Execution

Following input of all data elements the input file requires an `ENDDAT` statement. This statement takes no additional parameter. Once this line is read, the model executes. Any lines following the `ENDDAT` statement are ignored. The following is a complete model-input set:

Example Input File SiteCond.dat

YEARAD	2014
JULDAT	175
LATTNE	32.00
LONGEG	-106.00
HGTASL	1.200
FRACCC	0.250
CLDHGT	MEDIUM
CLDTYP	STRATO
HGTCLC	2.000
TDAWNC	5.00
WIND4M	3.00
RHDAWN	0.20
FOLCVR	0.10
FOLTYP	WEEDS
SOILTP	SAND
SOILML	PARCHED
SOILRH	PEBBLED
ENDDAT	

4. Diurnal Ground Heat Flux Model

In this chapter we will discuss the present model's method for handling the ground heat-flux. The method developed to address this is described in detail. However, it is perhaps worthwhile to first compare this technique with methods used previously to see why it might provide a better estimate of the soil's conductive heat-flux than previous methods.

As the touchstone model of the author's experience, the reader is referred to Deardorff's (1978) model. This model applied a force-restore technique to calculating the ground heat-flux. The force-restore method was developed by Bhumralkar (1975) and Blackadar (1976). In this model a forcing term (the ground heat-flux) heats a near-surface layer of thickness d_1 (approximately 10 cm) that corresponds to the penetration depth of the diurnal heat wave. Secondly, this force is partially compensated by a restoring term associated with heat transfers between the diurnal soil layer and an even deeper layer of thickness d_2 (~ 50 cm) associated with the penetration depth of the annual thermal wave. At the time of the late 1970s this method was considered one of the most advanced available (e.g., Hoffert and Storch 1979).

A key problem with this approach is that one obtains a solution for the temperature of a layer 10 cm thick, but not a solution for the actual temperature of the soil surface. Or, perhaps in fairness one might say the technique is tuned to provide a correct temperature of a thermal wave penetrating the ground plane, but only for one wave frequency that makes one cycle per diurnal period. It is relatively easy to see where this might lead to problems. For example, frontal passages might cause variations in solar irradiation at the surface that are not periodic over 24 hr. In this case, shorter-period fluctuations carry the incident energy to different depths and can result in shorter-term ground-layer responses.

Moreover, the SEB model relies on the actual surface-skin temperature to generate the correct outgoing (upward directed) infrared radiation that is directly responsible for cooling the ground. And, if the ground heat-flux is not properly handled, the radiation model will not respond properly, either. This results in a cascading series of model errors, particularly affecting the balance of the proper energy entering the atmosphere via the sensible heat flux, and will affect the turbulence prediction. The sensible heat flux relies (again) on the actual soil temperature, not on a mean

temperature of a soil layer. To fix this problem, a means must be derived to calculate the ground heat-flux based on the surface temperature alone without relying on the nature of the penetration depth of any particular frequency of thermal perturbations.

But before considering that method, let us also mention the issue of horizontal conduction within the ground. For purposes of this calculation, the soil will be considered flat. It may, of course, be considered tipped relative to the incident sunlight. This would not affect the derivation. However, in most cases we will consider it oriented perpendicular to the vertical, though this might be addressed in future. The main point is that horizontal heat flow will be ignored. When considering the penetration depth of the diurnal thermal wave it is relatively easy to see why. In most cases our knowledge of soil properties is crude at best; and typically the approximation of horizontal homogeneity is a given. Certainly the resolution of available soil type data is no better than 10 cm, and the effects of horizontal differentials at larger scales would be minimal. Since the model described does not attempt to address such infrared-visualization effects, such flows will not be considered.

The method discussed and developed here was based on a combination of Laplace and Fourier transform techniques. Therefore, the discussion is divided into 2 sections. In Section 4.2 the Laplace transform component of the analysis is discussed as applied to a periodic boundary condition. The soil is considered a flat, semi-infinite (into the earth) slab of uniform medium of uniform thermal properties. The results of this analysis allow one to model the energy flux exactly for such a periodic surface-temperature-boundary condition. One may then proceed to decomposition of the soil-surface-temperature diurnal wave in terms of a Fourier series. This is discussed in Section 4.3, where an expression for the complete diurnal ground heat-flux wave is formulated as a summation of periodic components.

4.1 Model Assumptions Used

In Section 4.2 the surface response to a sinusoidally-perturbed temperature boundary-condition is derived. Such a derivation requires a series of assumptions be made to allow the solution to be tractable. In the process, hopefully, the assumptions made are not themselves unrealistic. These are

- 1) We assume the soil thermal properties to be constants both in time and depth within the layer of interest during the computational period.

As justification, since we are primarily interested in turbulence effects — and since turbulence issues primarily occur under relatively dry desert-climatic conditions when optical turbulence becomes a problem — the soil is usually dry, meaning its moisture content will not vary significantly with depth beneath the surface. Such conditions would also argue against the presence of rainfall and evaporation over a 24-hr period of interest. Either of these would tend to reduce the prevalence of optical turbulence as well as cause variations in the soil properties as functions of time and depth. Even without such variations, one might anticipate some changes in soil properties with increasing depth. Yet due to the shallow penetration of the diurnal wave such impacts might tend to be minimized, especially when considering only a 24-hr period. This was the same approximation used by Ren and Xue (2004).

Nonetheless, such effects could be considered under a testing regime where it might be possible to track the drying out of a soil layer over several days and consider how variations in moisture would tend to alter the resulting turbulence predictions.

2) We also assume the effects of the annual temperature wave can be ignored if we are only dealing with a day or a few days of computational time.

To assess the impact of this assumption, let us consider the average variation in annual daytime temperatures as indicative of the variations in soil temperature for the annual wave. At WSMR's locale in southern New Mexico, the average daytime high temperature varies from approximately 55 °F to 95 °F between the winter and summer months. Taking this range in combination with the results of the analysis below (further discussed in Section 4.3) we find the maximum energy flux into the soil for an average soil is approximately 3 W/m². This amount, while significant on an annual basis, is minor compared to the magnitudes of diurnal fluxes that are on the order of hundreds of Watts per meter squared. Strong turbulence conditions require strong sensible heating rates. Therefore, while the effects of the annual thermal wave should be included for longer-term (climate) studies, when considering 24-hr variations in turbulence strength this effect can be ignored.

3) Finally, we assume that the diurnal thermal wave can be treated as periodic.

For this third assumption, we note that once the annual wave effect is removed, the main influence on turbulence is due to cloud and wind effects that might be

treated as being diurnally cyclical in nature. For instance, in summer months in New Mexico a common diurnal cycle begins with relatively clear skies in the morning hours becoming perceptibly cloudier in the afternoon, then dissipating after dusk.

In many locations, in the absence of a major weather change, persistence is the dominant factor in forecasting. Beyond that, precipitation events generally disrupt the level of turbulence observed. Hence, the model developed is designed to be a best fit to study conditions where turbulence becomes a significant factor. Further, the diurnal model could also be adjusted to treat a multiday scenario to study cyclical patterns of precipitation and subsequent drying. But, this is beyond the scope of the present work.

4.2 Laplace Analysis of Ground Impulse Response Function

In this section, Laplace transforms will be used to study the flow of heat into a semi-infinite soil volume with a known, single-frequency sinusoidal temperature perturbation as the upper-boundary condition and homogeneous soil conditions throughout, based on the assumptions stated in Section 4.1. For simplicity, the variable x will denote distance measured into the semi-infinite slab volume starting at the soil boundary ($x = 0$) and extending downward into the semi-infinite region ($0 < x < +\infty$).

Based on this model and assumptions, we may ignore horizontal heat fluxes, such that we need only determine the form of a function $T(x, t)$ representing the temperature as a function of depth and time that solves the heat-transfer equation:

$$\frac{\partial T(x, t)}{\partial t} = \kappa \frac{\partial^2 T(x, t)}{\partial x^2} = a^2 \frac{\partial^2 T(x, t)}{\partial x^2}, \quad (4.1)$$

where $\kappa = a^2$ [m²/s] is the thermal diffusivity, assumed constant.

For the boundary condition, let us write

$$T(0, t) = A \sin(\omega t) + T_\infty = d(t) + T_\infty, \quad (4.2)$$

where $\omega = 2\pi/\tau$ and τ is the period of the sinusoidal oscillations.

Here, note that T_∞ was added to avoid negative temperatures, but effectively it becomes merely a background-temperature offset. That is, it represents not only the

mean temperature at the surface but also the asymptotic temperature deep beneath the surface:

$$T(\infty, t) \rightarrow T_\infty = \text{const.} \quad (4.3)$$

Once a solution is found for this case, it will be relatively simple to generalize the results in the next section, since the equation is linear in $T(x, t)$.

To solve this system, it will be easiest to Laplace transform Eq. 4.1 with respect to time. Here, we use the standard definition of the Laplace transform (e.g., Kreyszig 1972):

$$\mathcal{L}[w(t)] = \int_0^\infty e^{-st} w(t) dt = W(s). \quad (4.4)$$

Standard transform and inverse-transform tables will be used to provide the results needed to express the differential equation in terms of its Laplace-transform equivalent. First, we consider the transform of a time derivative:

$$\mathcal{L}\left[\frac{\partial w(t)}{\partial t}\right] = s W(s) - w(0). \quad (4.5)$$

This result tells us we need to know the value of the function $w(t)$ at $t = 0$, $w(0)$. However, such terms are truly necessary only if we are concerned with the effects of transients. Since our interest is only in the general periodic behavior of the solution, behavior that persists long after the transients have damped out, we ignore all such effects and simply assign all transient terms as $w(0) = 0$.

Next, since t and x derivatives acting on T_∞ must equal zero, we may always assign $T_\infty = 0$ initially, ignoring the mean-temperature offset (the zero frequency (DC) term) as well. This is consistent with the observation that $T_\infty = \overline{T(0, t)}$ is the mean background temperature throughout the solution.

The Laplace transform of Eq. 4.1 can thus be written,

$$a^2 \frac{\partial^2 \Theta(x, s)}{\partial x^2} - s \Theta(x, s) = 0, \quad (4.6)$$

except that $\Theta(x, s)$ represents the transform of $T(x, t) - T_\infty$, where the background offset has been removed.

Equation 4.6 may now be solved along the x dimension, taking the easily derived general form,

$$\Theta(x, s) = D(s) \exp\left[-\sqrt{s} x/a\right] + E(s) \exp\left[+\sqrt{s} x/a\right]. \quad (4.7)$$

One of these terms is immediately removed by applying the boundary condition. Because $T(x, t)|_{x \rightarrow +\infty}$ approaches T_∞ , $E(s)$ must be set to zero, since the exponential part of this term diverges as $x \rightarrow +\infty$. Therefore, $E(s)$ may be eliminated, leaving

$$\Theta(x, s) = D(s) \exp \left[-\sqrt{s} x/a \right]. \quad (4.8)$$

Recall that, in general, when one encounters products in various transform spaces, these products typically transform to become convolutions in the original space. Hence, the product solution, $\Theta(x, s)$, becomes a convolution upon inverse transformation into $T(x, t)$. For the Laplace transform such convolution operations are expressed as

$$\mathcal{L}^{-1} [F_1(s) F_2(s)] = \int_0^t f_1(t-v) f_2(v) dv. \quad (4.9)$$

This form is consistent with the Laplace transform's causal applications, yielding a causal integral involving 2 temporal functions.

Now it will be noted that since $\Theta(x, s)$ is the transform of $T(x, t)$, we may always set $x = 0$, in which case we have $\Theta(0, s)$ which must inverse-transform as $T(0, t)$. This implies that the boundary function, $d(t)$, is the inverse Laplace transform of $D(s)$. The remaining exponential factor in Eq. 4.8 must therefore relate to the effects of heat transfer from the surface into the conducting slab as a temporal (and causal) impulse-response function. However, it is unnecessary to actually perform the forward Laplace-transform operation needed to convert $d(t)$ into $D(s)$ since we are not interested in $D(s)$, per se, and only in the spatial-temporal solution.

The complete behavior of $T(x, t)$ will thus require convolving the known function $d(t)$ with the transform of the exponential factor of the Laplace-transformed solution. Once this convolution function is known, we may perform the convolution integral in time.

The inverse transform of the exponential term, $e^{-\sqrt{s}x/a}$, is a common look-up table function given as

$$\mathcal{L}^{-1} [e^{-\delta \sqrt{s}}] = \frac{\delta}{2 \sqrt{\pi} t^{3/2}} \exp \left(-\frac{\delta^2}{4t} \right) = g(t, \delta), \quad (4.10)$$

where $\delta = x/a$. This function can be rewritten as

$$g(t, \delta) = \frac{1}{2 \sqrt{\pi} \delta^2} \frac{\exp \left(-\frac{1}{4(t/\delta^2)} \right)}{(t/\delta^2)^{3/2}}. \quad (4.11)$$

It is perhaps not surprising that as an impulse-response function the time-integrated area beneath the function (when integrated over $t = 0 \dots + \infty$) is unity, regardless of the value of δ . And, as $\delta \rightarrow 0$ as $x \rightarrow 0$, the function obtains attributes similar to that of a Dirac delta function. This integral property is also guaranteed by the simple observation that the function's transform value at $s = 0$ is unity. One may likewise represent this function in a dimensionless form, with the property

$$\int_0^{\infty} g(t, \delta) dt = \int_0^{\infty} \frac{1}{2\sqrt{\pi}} \frac{\exp\left(-\frac{1}{4u}\right)}{u^{3/2}} du = \int_0^{\infty} G(u) du = 1, \quad (4.12)$$

using $u = t/\delta^2$.

The function $G(u)$ is plotted in Fig. 8. The unique property of this function is its ability, in the limit as $\delta \rightarrow 0$, of $G(t/\delta^2)/\delta^2$ to sift out the value of the function at $t = 0$ (as $\delta \rightarrow 0$), upon convolution. Moreover, this function behaves like a single-sided Dirac delta function. Its single-sidedness allows it to act in such a way that it avoids acausal effects. The function $g(t, \delta)$ thus exhibits all of the attributes of an impulse-response function, distributing the behavior of $T(0, t)$ downward into the volume, where the delay of the temperature flowing downward depends on the depth being assessed, parameterized by the variable δ .

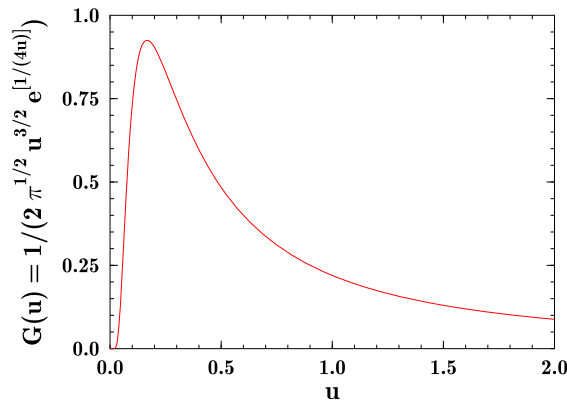


Fig. 8 Dimensionless function $G(u)$ produced from Laplace analysis of the heat equation

The convolution operation in Eq. 4.9 can now be performed. An exact form is available for the inverse Laplace transform of the exponential function, and Eq. 4.2 supplies a relation for $f_2(t) = d(t) = A \sin(\omega t)$, leading to the following expression for the temperature wave inside the soil layer:

$$T(x, t) - T_{\infty} = A \int_0^t g(t - v, x/a) \sin(\omega v) dv. \quad (4.13)$$

Since only a steady-state behavior is sought, any transients are ignored such that the lower bound of the convolution integral can be replaced by $-\infty$.

This integral can be evaluated best by converting it into a dimensionless form by introducing the substitutions: $q = \omega t$, $u = \omega v$, and $c^2 = \omega \delta^2$. Then, the integral takes the form

$$A \int_{-\infty}^q \frac{1}{\sqrt{4\pi} c^2} \frac{\exp\left(-\frac{1}{4(q-u)/c^2}\right)}{[(q-u)/c^2]^{3/2}} \sin(u) du. \quad (4.14)$$

We now proceed to manipulate this dimensionless version. First, let us rearrange the integration limits by the substitution $r = q - u$, allowing the integral to be rewritten

$$A \int_0^{+\infty} \frac{1}{2c^2 \sqrt{\pi}} \frac{\exp\left(-\frac{1}{4r/c^2}\right)}{(r/c^2)^{3/2}} \sin(q - r) dr. \quad (4.15)$$

Next, it will be advantageous to introduce yet another new integration variable, $m = r/c^2$, $dm = dr/c^2$, such that the integral can be rewritten

$$A \int_0^{+\infty} \frac{1}{2\sqrt{\pi}} \frac{\exp\left(-\frac{1}{4m}\right)}{m^{3/2}} \sin(q - c^2 m) dm. \quad (4.16)$$

In this form the sine can be expanded, using

$$\sin(q - c^2 m) = \sin(q) \cos(c^2 m) - \cos(q) \sin(c^2 m),$$

such that terms in q can be factored out of the integral, leaving 2 simplified integrals of m , that evaluate as

$$\int_0^{\infty} \frac{1}{2\sqrt{\pi}} \frac{\exp\left(-\frac{1}{4m}\right)}{m^{3/2}} \cos(c^2 m) dm = e^{-c/\sqrt{2}} \cos(c/\sqrt{2}); \quad (4.18)$$

$$\int_0^{\infty} \frac{1}{2\sqrt{\pi}} \frac{\exp\left(-\frac{1}{4m}\right)}{m^{3/2}} \sin(c^2 m) dm = e^{-c/\sqrt{2}} \sin(c/\sqrt{2}). \quad (4.19)$$

Converting these results back into the original variables used, the periodic solution for the sinusoidal-temperature wave is written

$$T(x, t) = A e^{-x/\Delta} \sin(\omega t - x/\Delta) + T_{\infty}, \quad (4.20)$$

where we introduce a new characteristic penetration depth, $\Delta = \sqrt{2\kappa/\omega}$, associated with a wave of frequency ω and soil thermal diffusivity κ .

Such a wave exhibits an increasing phase delay between the amplitude function at a depth $x > 0$ and the phase at the surface, and rapidly diminishing magnitude.

The shape of the vertical temperature profile can also be used to evaluate the ground heat-flux, G , for this simple model, as well. At any soil depth, x , G may be calculated as

$$G = -\kappa C_s \frac{dT}{dx}, \quad (4.21)$$

where C_s is the soil heat-capacity (J/m³/K). The G thus has the dimensions of a flux (W/m²). Computing this flux based on the vertical temperature gradient of the sinusoidal-temperature model at the ground surface ($x = 0$), we obtain

$$G(t) = -\kappa C_s \frac{dT(x=0, t)}{dx}. \quad (4.22)$$

After some math, the vertical gradient of the temperature at the surface ($x = 0$) can be computed as

$$\frac{dT(x=0, t)}{dx} = -\frac{\sqrt{2}A}{\Delta} \sin\left(\omega t + \frac{\pi}{4}\right). \quad (4.23)$$

The ground heat-flux can thus be written

$$G(t) = \frac{\kappa C_s \sqrt{2} A}{\Delta} \sin\left(\omega t + \frac{\pi}{4}\right) = C_s A \sqrt{\omega \kappa} \sin\left(\omega t + \frac{\pi}{4}\right), \quad (4.24)$$

where the lead constant product carries the dimensions of a flux (W/m²). The quantity $\sqrt{\omega \kappa}$ has the dimensions of a velocity (m/s). Higher-frequency waves thus penetrate into the soil layer more quickly, but because Δ is smaller, their effect is limited compared to the lower-frequency diurnal wave and even lower-frequency seasonal and yearly waves.

4.3 Fourier Analysis of a Diurnal Response

The results of the previous section are next generalized by expanding the periodic surface-boundary-condition temperature result of the previous section into a more complicated multi-frequency result based on a Fourier series decomposition of the 24-hr diurnal temperature behavior:

$$T(0, t) = \sum_1^n A_n \cos\left[\frac{2\pi n t}{\tau}\right] + \sum_1^n B_n \sin\left[\frac{2\pi n t}{\tau}\right] + T_\infty. \quad (4.25)$$

Again, τ is the 24-hr diurnal cycle period used by the model. The resulting temperature profile can be written based on the results of the previous section:

$$T(x, t) = T_\infty + \sum_1^n A_n e^{-x/\Delta_n} \cos \left[\frac{2\pi n t}{\tau} - \frac{x}{\Delta_n} \right] + \sum_1^n B_n e^{-x/\Delta_n} \sin \left[\frac{2\pi n t}{\tau} - \frac{x}{\Delta_n} \right]. \quad (4.26)$$

Here, the penetration depths, Δ_n , of each component wave of frequency $\omega_n = n\omega_1$ are expressed as

$$\Delta_n = \sqrt{\frac{2\kappa}{\omega}} = \sqrt{\frac{\kappa\tau}{\pi n}} = \frac{\Delta_1}{\sqrt{n}},$$

where $\Delta_1 = \sqrt{\kappa\tau/\pi}$ is the basic depth.

To obtain the ground heat-flux we can extend the results obtained for the single sinusoidal-boundary component in Eqs. 4.23 and 4.24. Note first that in general the single-wave component will have a gradient at any point within the volume given by

$$\begin{aligned} \frac{dT_n(x, t)}{dx} &= -\frac{A_n}{\Delta_n} e^{-x/\Delta_n} [\sin(\omega t - x/\Delta_n) + \cos(\omega t - x/\Delta_n)] \\ &= -\frac{\sqrt{2} A_n}{\Delta_n} e^{-x/\Delta_n} \sin \left(\omega t - x/\Delta_n + \frac{2\pi}{8} \right). \end{aligned} \quad (4.27)$$

At the surface, the flux for this component equals

$$G_n(t) = A_n C_s \frac{\kappa \sqrt{2}}{\Delta_n} \sin \left(\omega_n t + \frac{\pi}{4} \right) = A_n C_s \sqrt{\kappa \omega_n} \sin \left(\omega_n t + \frac{2\pi}{8} \right). \quad (4.28)$$

The peak heat flux thus always occurs 1/8th of a cycle prior to the time of the peak temperature. We will also be able to combine terms to produce a series of quantities $V_n = \sqrt{\kappa \omega_n}$ with dimensions of velocity (m/s or cm/s). These denote the velocity of penetration of heat associated with a given frequency of thermal fluctuation. Higher-frequency terms travel faster into the soil, but not as far as lower-frequency waves.

Consider, for example, the behavior of this lowest-order diurnal term, consisting of $\omega_1 = 2\pi/\tau$, with $\tau = 86,400$ s. For dry soils the soil thermal diffusivity is typically of the order $\kappa = 0.2 \times 10^{-6}$ m²/s, yielding $V_1 = 3.8 \mu\text{m/s}$, and $\Delta_1 = 7.42$ cm. Velocity V_1 equates to a speed of 1.37 cm/hr. This depth value appears typical of diurnal thermal waves of the order of several centimeters.

In contrast, a fluctuation with a period of 5 min has a wave velocity of $64.7 \mu\text{m/s}$ (significantly faster), but affects a layer whose depth is only approximately 4.4 mm.

Returning to the general expression for the soil temperature, the derivative of the complete temperature-profile function may be written in the form,

$$G(t) = C_s \sum_n^N \left[A_n V_n \cos \left(\omega_n t + \frac{2\pi}{8} \right) + B_n V_n \sin \left(\omega_n t + \frac{2\pi}{8} \right) \right]. \quad (4.29)$$

While we have focused on the nature of the diurnal wave given a boundary condition of a temperature, if, instead, we have been given a system of energy fluxes at the surface, we could equally well begin by solving for the equivalent ground heat-flux necessary to bring the energy equation into balance using Eq. 4.29 to solve for coefficients A_n and B_n , thereby determining the surface temperature.

Since the ground heat-flux reacts to temperature changes at the ground, and involves an energy-storage mechanism, the ground acts much like a capacitor in an electrical circuit, except that (unlike a capacitor) as heat is introduced into the ground (mainly due to solar irradiance) the sensible heat-flux and ground thermal-radiative-flux tend to oppose this heat transfer. Nonetheless, because of this storage capacity, it would appear that by iteratively updating the ground heat-flux, and thereby the surface temperature, one could solve iteratively for the ground temperature until the energy-budget equation relaxes to a solution.

4.4 Conclusions and Observations

This new ground-heat-flux calculation method may be described as a *Periodic Ground-Heat-Flux Model for a Semi-Infinite Uniform Medium*. The importance of the ground heat-flux is usually not significant when considering only daytime effects, since solar radiation is usually so dominant during daylight hours. However, for longer-term modeling and especially for nighttime situations, the energy stored in the soil becomes important as other fluxes grow in significance after dark or around the time of the neutral event.

As an interesting observation based on the foregoing analysis, one might ask this: What is the typical time of day when the air temperature near the ground reaches a maximum? Presumably, this is connected to the time when the ground temperature reaches its maximum. From the $+2\pi/8$ term appearing in the argument of the

ground-heat-flux equation, one can see that if the main thermal flux stimulates the lowest frequency, ω_1 , of the diurnal heat wave, the peak ground heat-flux will occur around solar noon, but the peak temperature will be one-eighth cycle or 3 hours later, equating to approximately 3 PM standard time. Since most of the United States uses daylight savings time most of the year, particularly during summer, this time adjustment indicates the local high temperature should occur around 4 PM (daylight savings time). This behavior is commonly observed under clear-sky conditions.

One might similarly consider the impact of this equation on an annual temperature wave. Peak heating in the Northern Hemisphere should occur on the summer solstice, but the peak temperature should then occur around $365/8$ days later, or around August 6 in the Northern Hemisphere. The statistically coldest day of the year would then occur approximately 46 days after the winter solstice, or on approximately February 5 in the Northern Hemisphere. It is interesting that even while not knowing this rule, the days of summer were chosen to be centered $\pm 1/8$ th of the year about the peak summer temperature and minimum winter temperature.

5. Effects of Vegetation on Convective Surface Fluxes

In this chapter, we begin to consider updated models of the various flux components constituting the surface energy budget. These fluxes fall into radiative, convective, and conductive categories. In this chapter we consider the 2 convective fluxes, the sensible heat flux and the latent heat flux, which is due to surface evaporation or dew formation and evapo-transpiration from plant surfaces. The present chapter follows the development of these fluxes based on prior work (Tofsted 1993).

5.1 General Discussion

The general theory commonly used to model convective fluxes at the earth's surface is typically based on the flux-profile method (Dyer 1974), or (which is the same thing) similarity theory. Similarity theory implies there are similarities that exist in the atmospheric properties of all *conservative passive additive properties* contained in the air flowing within the surface-layer atmosphere. We have already discussed the meaning of this concept in Chapter 1. Here, this concept is applied as we model the fluxes of sensible heat (essentially, the conservative property of temperature) and latent heat (conserved moisture) to and from the surface. According to similarity theory the functional forms of equations describing these fluxes should be *similar* in nature.

Obukhov (1946) was the first to propose that there should be similar shapes to vertical profiles of temperature, humidity, and wind speed above a surface based on parameterized relations. He developed the concept of the friction velocity, u_* , to parameterize the wind speed. Similarly, he identified a parameter termed the scaling temperature, T_* , to characterize the vertical temperature profile's shape and introduced a length scale, here called simply the Obukhov length, L_{Ob} , to characterize the curvatures of such profiles.

Let us begin by defining the 2 quantities we wish to discuss here: The sensible heat flux is denoted as H_S . The latent heat flux is denoted by H_L . Both of these might be related to more basic fluxes of temperature, F_T , and water vapor, F_Q , such that (Stull 1988),

$$H_S = \rho_a C_p F_T, \quad H_L = \rho_a L_v F_Q. \quad (5.1)$$

Here the sensible heat is obtained by multiplying $F_T = u_* T_* = \langle w' T' \rangle$ [K-m/s], by air density, ρ_a , and is proportional to the specific heat at constant pressure, C_p

(Eq. 2.20), while the latent heat flux relies on $F_Q = u_* Q_* = \langle w' Q' \rangle$ [m/s], where Q is a relative amount of water vapor present per unit quantity of total moist air (g/g). Thus, the air density, ρ_a , can be removed from the water vapor to produce an equation form that is similar to that of the sensible heat, but with the introduction of the quantity L_v , the latent heat of vaporization (e.g., $L_v = 2,465$ J/g at 15°C) (Oke 1978), that scales the amount of water vapor released into a net energy flux.

In both cases the net flux arising from the composite surface depends on the temperature(s) of the surface(s) involved; warmer surfaces feature higher saturation vapor pressure and therefore are more effective at carrying water away from the surface. However, moisture fluxes also depend on the availability of water at the surface where evaporation is evaluated.

A common variable is the Bowen ratio,

$$\beta = \frac{H_S}{H_L} = \Gamma \frac{F_T}{F_Q}, \quad (5.2)$$

where $\Gamma = C_p/L_v$ is the psychrometric constant. Stull (1988) mentions that β ranges from 5 over semiarid regions to 0.5 over grasslands to 0.2 over irrigated fields to even negative values over desert oases. However, he concludes: “Attempts to use this approach have mostly failed, because the Bowen ratio usually varies with time and weather over each site.” I.e., assigning a β value a priori is not effective.

Plants, in order to survive, carefully control their water resources by controlling *stomatal* entryways that exchange moisture and CO_2 with the outside air. The degree of difficulty of passage of moisture through the surface of plants is termed the *stomatal resistance*. Under high-humidity conditions this resistance tends to be low. Conversely, under low-humidity conditions this resistance can be high and extremely high for desert-type plants. Or, as Stull remarks, “[T]he evapotranspiration component of the latent heat flux from plants is a complex function of the age, health, temperature and water stress of the plant.”

This is, in fact, a serious enough problem that neither Stull nor Hoffert and Storch (1979) attempt to suggest complete equations for the latent heat fluxes to include plant stomatal resistance. Perhaps it is a matter of going “where angels fear to tread,” but Deardorff (1978) did suggest equations, and for that purpose we use his results.

It should also be pointed out that the current model takes a somewhat more relaxed view of humidity-flux calculations. In Tofsted (1993) it was assumed the computation of the surface fluxes could be dominated by humidity effects. However, in many locales where turbulence dominates, moisture availability can be very low. Also, in terms of a diurnal model, to have a periodic condition it is important to not permit discontinuities in the fluxes or model parameters. Allowing the soil layer to vary significantly in moisture content over the diurnal cycle would disrupt such a model, particularly if a reset event were to occur every 24 hr. Hence, the approach taken is to simply set the user's choice of moisture level at the beginning of the model scenario and leave this value constant throughout the model run. In this way, the effects of different moisture levels can be studied without permitting the soil to dry over a multiday period.

Also in the previous study, 2 distinct soil-moisture parameters were used: a near-surface soil moisture, w_g , and a deeper surface moisture, w_2 . However, the measurement of such parameters becomes problematic; further, the modeling of the effects of these and/or benchmarking their effects independently also becomes problematic. Therefore, only a single soil-moisture value is employed. This value is constant throughout any given model run, and may be thought to correspond to the w_g parameter associated with the top 10 cm of soil. This is also consistent with the new model's focus on a new method for computing the ground heat-flux discussed in Chapter 4. There, the soil thermal properties are considered constant over the model calculation period as well as constant with depth into the soil. This is consistent with keeping w_g constant throughout the model runs.

Therefore, it is hoped the reader recognizes the sensible-heat-flux calculation is somewhat simpler to formulate than the latent heat-flux. We therefore will begin by describing the sensible-heat-flux case and, once that effect has been described in detail, treat the latent heat-flux in approximately the same level of detail.

5.2 Sensible Heat Flux Calculation for a Vegetated Surface

Let us begin this section with a brief review of the material presented in Chapter 2. In that previous discussion the main point was that the sensible heat flux is closely connected with the analysis of the friction velocity, u_* , the scaling temperature, T_* , and the Obukhov length, L_{Ob} . However, we also discussed the fact that these parameters, while easily computed from modern rapid-sampling sonic-anemometer

devices, are badly poised to be computed from normal wind and temperature measurements. We then introduced a substitute relation for the sensible heat flux based on an air temperature, T_Z , a surface layer aggregate temperature, T_S , and a wind speed, u_Z , at the same height as the air temperature as Eq. 2.19:

$$H_S = \rho_a C_p c_H(z) u_Z (T_S - T_Z) = \rho_a C_p \frac{(T_S - T_Z)}{r_H(z)}. \quad (5.3)$$

Now, $r_H(z)$ is a height-dependent function of the wind speed u_Z and the current stability condition. And, this function is the main focus of attention in this section. We also introduced a definition for the surface-layer temperature being a composite of the surface temperature of the ground, T_g , and the foliage, T_f , in Eq. 2.22.

Deardorff (1978) appears to have correctly adduced that because the foliage cover generally presents a much greater surface area than the underlying surface, that the sensible heat flux from the foliage should be much greater than that of the ground. However, Deardorff's formulation was somewhat flawed in that it could result in much higher heat fluxes from the foliage than would be reasonable to assume, given the remaining terms in the energy budget. That is, Deardorff failed to consider the carrying capacity of the air. Simply because there is 7.0 times the surface area does not mean the air is capable of absorbing 7.0 times the energy. Rather, the air's carrying capacity is fixed, but the mix of how much of that capacity is reflective of the soil temperature and how much is reflective of the foliage temperature is what is in question. Hence, we use Eq. 2.22 for describing the effective surface temperature.

But, once the effective surface temperature is known via Eqs. 2.21 and 2.22, there is still an element to consider — the flux-resistance factor, r_H . Here, it will be recalled that although we compute the surface aggregate temperature as a mixture of the ground and foliage leaf temperatures, the position at which the temperature profile intercepts this actual temperature cannot be the top surface of the foliage, or the actual, exact surface height of $z = 0$. Figure 9 illustrates this same problem, but in relation to the height at which the wind-speed profile becomes zero. This height is adjusted relative to the height above the surface, z , according to 2 corrections. The first correction is the surface-roughness length, z_0 . For a flat surface with no vegetation the wind-speed profile will become zero at $z = z_0$. However, for foliated surfaces the leaf surfaces are typically elevated some distance above the ground, such that the projected zero wind-speed height occurs at $z_0 + D$, where D is termed the *displacement height* (e.g., Stull 1988, sec. 9.7.3).

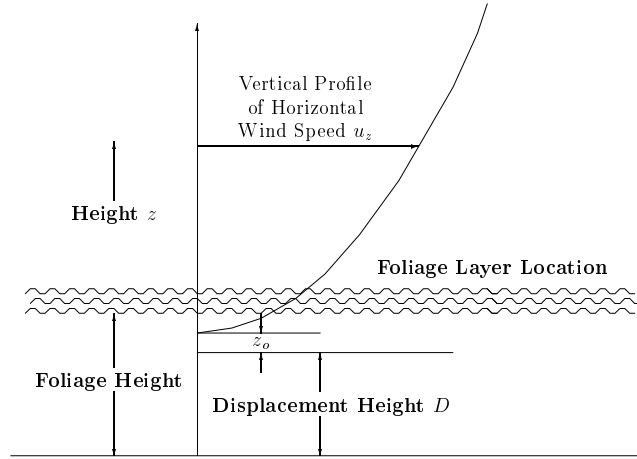


Fig. 9 Foliated layer's displacement-height and roughness-length offsets

The roughness height therefore influences the curvature of the wind profile, but the profile itself is also displaced.

Further complicating this situation is the fact that the height at which the temperature profile appears to intercept the surface layer's aggregate temperature, T_S , occurs at a different offset height than z_0 , or D , or $D + z_0$. The effect of this height difference must be accounted for in the flux calculation. Otherwise, one could simply derive a method for computing T_* based on height z , computed temperature T_S , and z_0 directly from Eq. 2.12. This would include an iterative computation of L_{Ob} , u_* , and T_* . Instead, due to these offsets, T_* can only be evaluated after estimating H_S , as influenced by a surface-resistance factor r_H (or $u c_H$) that reflects these offsets.

Stull recommends determining the value of D by studying a measured wind profile. This would require at least 3 wind sensors to determine the mean, vertical gradient, and curvature of the profile. In lieu of such available data, using Eqs. 2.21 and 2.22, the following approximations are considered:

$$z_{0F} \approx 0.13 z_F; \quad z_{0G} \approx 0.13 z_G. \quad (5.4)$$

$$D_F \approx 0.70 z_F; \quad D_G \approx 0.70 z_G. \quad (5.5)$$

Here, Frank Hansen's¹ recommendation was to estimate the roughness length z_0 as approximately 13% of the height of the typical roughness element. But instead of seeking a single, composite roughness length or displacement height, it is observed

that the wind profile never reaches zero at the base of the vegetation. Rather, a portion of the wind remains beneath the vegetation and only reaches zero at the surface. Hence, the profile is characterized twice, once for the wind curtailed by the foliage and a second time for the wind affected by the soil surface.

The resulting height of the zero wind-speed level from the foliage perspective is approximately $0.83 z_F$ for a fully vegetated surface. This result is consistent with Stull's data (1988, Fig. 9.7). Both sets are scaled in the same manner to account for the impact of surface irregularities (where z_G represents the top height of rocks, uneven ground, etc., and where z_F represents the tops of trees, shrubs, etc.).

The displacement height's importance is that one cannot correctly evaluate the friction velocity u_* from Eq. 2.11 unless the height z is first adjusted according to the displacement height in the modified form,

$$u_Z = \frac{u_*}{k} \left[\ln \left(\frac{z - D}{z_0} \right) - \psi_1 \left(\frac{z - D}{L_{Ob}} \right) \right]. \quad (5.6)$$

A similar expression applies when evaluating the scaling temperature T_* . We shall expand on this result, but only after considering the temperature profiles for barren soil and foliated surfaces.

A further height adjustment is required to evaluate r_H due to fine scale differences between the zero height of the wind versus the temperature. To do so, the research findings of Kunkel and Walters (1983), hereafter KW-83, and Thom (1972), hereafter T-72, have been investigated. The KW-83 paper examined sensible heat-flux measurements obtained under barren soil conditions at White Sands Missile Range, based on measurements at the High Energy Laser Systems Test Facility then under development. Conversely, the T-72 analysis was performed for heavily vegetated crop surfaces. These 2 research efforts produced surprisingly similar offsets expressed as $C u_*^\alpha$, where α was 0.333 for T-72 and 0.450 for KW-83.

5.3 Barren Soil's Resistance Factor

At this point a distinction should be made between the present method and that of Deardorff. While Deardorff's model included a number of interesting features involving various researchers' findings, his development of the sensible heat flux made an incorrect assumption.

Fluxes of sensible and latent heat are driven by bouyant and forced mixing of turbulence elements of different sizes. The general term "eddy" is used to describe

such elements. Klipp (2014) has shown that these fluxes are largely driven by the largest turbulence elements that are not isotropic. Isotropic turbulence tends to have no correlations between its components and therefore is inappropriate for carrying off momentum or energy where biases are required.

Many simplified models have been developed to approximate these fluxes, of which Deardorff's model was typical. Deardorff used a simplified approximation where he introduced one heat-exchange-rate coefficient, c_H , for all daytime (unstable atmospheric state) calculations, and a second exchange rate for stable (nighttime) cases. Deardorff also attempted to include the effects of a foliated layer. Knowing the expected heat flux from a nonfoliated surface, however, he simply assumed that a heavily foliated surface would transfer N_F times as much heat as the flat surface in a linear scaling. As a result, sensible heat-fluxes of up to 700 W/m² were computed based on this model, results that were completely erroneous.

In contrast, others (e.g., Hoffert and Storch 1979) have attempted to invoke the direct use of Eqs. 2.11 and 2.12 (or their equivalents) directly, without adjusting for the difference in height between the temperature and wind-speed zero-height levels. Even considering Thom's analysis versus Kunkel–Walters, one must also interpolate results between barren and foliated terrain types.

Fortunately, when this work began in 1983, we inherited Ken Kunkel's implementation of Deardorff's paper, in which Ken had already implemented his adjustment to account for the barren-soil conditions. Then, over the next few years, Thom's work was first uncovered and subsequently included as an extension of KW-83 to treat foliated surfaces.

To discuss this development, let us first examine Kunkel and Walters' method for barren soils. Kunkel and Walters adopted Deardorff's basic form for expressing the sensible heat flux as a function of a temperature difference, the mean wind-speed u_Z , and a variable c_H parameter:

$$H_{SKW} = \rho_a C_P c_H u_Z (T_S - T_Z). \quad (5.7)$$

Using the nomenclature developed here, Kunkel–Walters' c_H appears as

$$c_H = \frac{0.74^{-1} k^2}{\left[\ln \left(\frac{z-D_G}{z_{0G}} \right) - \psi_1 \left(\frac{z-D_G}{L_{Ob}} \right) \right] \left[\ln \left(\frac{z-D_G}{z_{0G}} \right) - \psi_2 \left(\frac{z-D_G}{L_{Ob}} \right) + \frac{kX}{0.74} \right]}. \quad (5.8)$$

This form is modified by $k X/0.74$ from the form that would be obtained by simply using Eqs. 2.11 and 2.12 to solve for c_H , where the ψ_1 and ψ_2 functions are those appearing in Eqs. 2.11 through 2.17. The adjustment term $k X/0.74$ appears related to the offset height of the effective zero-temperature plane. The use of the parameter D_G emphasizes that the displacement height involved here is that of a barren surface.

According to Kunkel and Walters, X was derived from the bluff-body form of Garratt and Hicks (1973), and ψ_1 and ψ_2 are the diabatic-influence functions described in Chapter 2. This method parameterized a laminar sublayer to handle the barren surface. The variable k is again von Kármán's constant (approximately 0.4 for rough surfaces); z is the height above the surface; and z_{0G} is the bare-ground roughness length. Note that KW-83 did not consider a displacement height because the flat ground and lack of vegetation did not require the consideration of one. But the use of D_G suggests that the soil offset will need to be distinguished from that associated with the vegetation, as does the use of u_{*G} suggest that the drag effects of the soil will be different from those of the foliage.

Kunkel and Walters defined X as

$$X = [0.37 (30 u_{*G} z_{0G} / \nu)^{0.45} Pr^{0.8}], \quad (5.9)$$

where $\nu = \mu / \rho_a$ is the kinematic viscosity, which we have already encountered just prior to Eqs. 1.1 and 1.2; and Pr is the Prandtl number (0.72 in our atmosphere). Simplifying, $k X$ can be expressed as

$$k X = 0.5258 (u_{*G} z_{0G} / \nu)^{0.45}. \quad (5.10)$$

One may then consider how this compares with the resistance technique:

$$c_H u \approx 1/r_H(z), \quad (5.11)$$

Multiplying c_H by u , Eq. 2.11 can be used to collapse a portion of the c_H expression into u_* . What remains is a denominator associated with the T_* equation plus the adjustment factor $k X$:

$$c_H u = \frac{k u_{*G}}{0.74 \left[\ln \left(\frac{z - D_G}{z_{0G}} \right) - \psi_2 \left(\frac{z - D_G}{L_{ob}} \right) + 0.71 (u_{*G} z_{0G} / \nu)^{0.45} \right]}. \quad (5.12)$$

Since u_* , z_0 , and ν are all positively valued and independent of the stability condition, the surface resistance to heat flux will be greater than that predicted by the basic theory based on Eqs. 2.11 and 2.12. This suggests that the interface height for the barren soil is lower than the corresponding zero-wind condition's extrapolated height — for if the height were greater it would mean the resistance was less, not greater; any positive contribution in the denominator equates to a greater resistance.

5.4 Vegetated Terrain's Resistance Factor

Thom's (1972) resistance model yields much the same conclusion as for the barren-soil condition. In his paper, Thom characterized the aerodynamic resistance to the flux of property P , calling it r_P . This is the resistance encountered at a rough surface that generally exceeds the resistance to momentum flux (r_M), just as for the previous barren-soil case. Thom expressed this difference in a nondimensional form using the parameter B_P^{-1} , given by

$$B_P^{-1} = u_* [r_P(z) - r_M(z)]. \quad (5.13)$$

This *resistance method* treated the property fluxes of heat, momentum, and humidity much like currents (I) in electrical circuits. Temperature, humidity, and kinetic-energy differentials between a material property of the air measured at station height z_s and a similar property measured at the surface are analogous to potential differences (V), such that the resistance terms (r) parameterize the fluxes.

Thom quantized the baseline atmospheric resistance (resistance to momentum flux) as

$$r_M(z) = \frac{u(z)}{u_*^2}. \quad (5.14)$$

This is *obvious* since $\rho_a u_*^2$ is just equal to the total vertical flux of horizontal momentum (Stull 1988, 67). The corresponding flux relation for momentum based on the resistance model of Eq. 5.3 would be

$$F_M = \rho_a \frac{(0 - u(z))}{r_M(z)} = -\rho_a u_*^2. \quad (5.15)$$

Both ρ_a and u_* are positive definite. Therefore, F_M is a downward-directed flux of momentum to the surface.

Thom's equation for a general property flux uses r_P written as

$$r_P(z) = \frac{1}{u_*} \left| \frac{\chi_z - \chi_s}{\chi_*} \right|_{\chi \leftarrow P}. \quad (5.16)$$

In the case of sensible heat (temperature), χ_z is the temperature at height z (i.e., T_Z); χ_s is the surface value of the parameter, in this foliated case, $T_F = T_S$, the effective mean aggregate surface temperature of the leaves; and χ_* is the scaling value of the given parameter. In this case, χ_* becomes the scaling temperature, T_* . Hence,

$$r_H(z) = \frac{1}{u_*} \left| \frac{T_Z - T_S}{T_*} \right|. \quad (5.17.A)$$

From the definition of T_* in Eq. 2.12, the ratio inside this equation's absolute-value operator is always positive. We therefore remove this symbol:

$$r_H(z) = \frac{T_Z - T_S}{u_* T_*} \longrightarrow \frac{1}{r_H(z)} = \frac{u_* T_*}{T_Z - T_S}. \quad (5.17.B)$$

The nondimensionalized excess resistance to heat (B_H^{-1} in an analog of Eq. 5.13) can then be written using Eqs. 5.14 and 5.17.B as,

$$B_H^{-1} = u_* [r_H(z) - r_M(z)] = \frac{T_Z - T_S}{T_*} - \frac{u(z)}{u_*}; \quad (5.18.A)$$

from which,

$$\frac{T_Z - T_S}{T_*} = B_H^{-1} + \frac{u(z)}{u_*}; \quad (5.18.B)$$

$$\frac{T_*}{T_Z - T_S} = \frac{u_*}{B_H^{-1} u_* + u(z)}. \quad (5.18.C)$$

Thom then completes his analysis by supplying an explicit form for B_H^{-1} :

$$B_H^{-1} = 1.35 (u'_*)^{1/3}, \quad (5.19)$$

which is explicitly dependent on his choice of dimensions of cm/s for his friction velocity, u'_* . Translating this result into the model dimensions of m/s,

$$B_H^{-1} = 6.27 u_*^{1/3}. \quad (5.20)$$

However, Thom also based his model on a bluff-body analysis and obtained the above relation assuming $\nu = 0.15 \text{ cm}^2/\text{s}$ and $z_0 = 7 \text{ cm}$ for the bean crop he studied. Thom's result can thus be cast into the same framework as Kunkel–Walters' by using his result that a typical $u'_* = 25 \text{ cm/s}$ produces a B_H^{-1} of 4.0. From this result, and using the conditions cited, one obtains the rule,

$$B_H^{-1} = 0.38 (u_* z_0 / \nu)^{1/3}. \quad (5.21)$$

Combining this new relation with Eqs. 5.17.B and 5.18.C, the transfer-coefficient product becomes

$$\begin{aligned} c_H u_F &\approx \frac{1}{r_H(z)} = \frac{u_{*F} T_*}{T_Z - T_S} = \frac{u_{*F}^2}{u_F + 0.38 u_{*F} (u_{*F} z_{0F}/\nu)^{1/3}} \\ &= \frac{k u_*}{k u_F/u_{*F} + k \times 0.38 (u_{*F} z_{0F}/\nu)^{1/3}}. \end{aligned} \quad (5.22)$$

For a rough surface $k \approx 0.40$ is used to evaluate the lead constant in the denominator's perturbation term, yielding

$$c_H u_F = \frac{k u_{*F}}{\left\{ \ln \left[\frac{(z-D_F)}{z_{0F}} \right] - \psi_1 \left[\frac{(z-D_F)}{L_{Ob}} \right] + 0.15 (u_{*F} z_{0F}/\nu)^{1/3} \right\}}, \quad (5.23)$$

where the roughness length and displacement height used are those consistent with a fully foliated layer. Yet the use of z_{0F} , u_{*F} , and D_F indicates we will need to consider separate parameters from those used to describe the bare-ground case.

5.5 Transfer Efficiency for Intermediate Cases

The previous 2 sections considered the separate effects of bare soil and a foliage layer's influence on sensible heat. Similar results were obtained for the 2 analyses. For comparison purposes both of these results are reproduced here:

$$c_{HG} u = \frac{0.74^{-1} k u_{*G}}{\left\{ \ln \left[\frac{(z-D_G)}{z_{0G}} \right] - \psi_2 \left[\frac{(z-D_G)}{L_{Ob}} \right] + 0.71 (u_{*G} z_{0G}/\nu)^{0.45} \right\}}; \quad (5.12)$$

$$c_{HF} u = \frac{k u_{*F}}{\left\{ \ln \left[\frac{(z-D_F)}{z_{0F}} \right] - \psi_1 \left[\frac{(z-D_F)}{L_{Ob}} \right] + 0.15 (u_{*F} z_{0F}/\nu)^{0.33} \right\}}. \quad (5.23)$$

Both feature similar adjustment terms in the denominator. The first offsets adjust the log-altitude $\ln(z/z_0)$ profile shapes by diabatic-influence functions (ψ_1 and ψ_2). Thom bases his correction on the wind-profile function ψ_1 , while Kunkel–Walters based theirs on the thermal term involving ψ_2 . Both also included similar intercept height adjustments based on fractal-power functions of friction-velocity variables.

Even after accepting both of these results as correct in the limit, applying Thom's solution to conditions involving fully foliated surfaces, and implementing Kunkel–Walters' analysis of barren-soil conditions, an interpolation rule still is needed under intermediate conditions ($0 < \sigma_F < 1$). Complicating this task is the means of

subdividing the wind effects on the 2, since changing the surface-roughness length, z_0 , impacts the values of the very parameters, u_* , L_{Ob} , and T_* (particularly u_*), that drive the resistance calculations.

Previously, in Tofsted (1993), the sensible heat flux was parsed by weighing the average surface-interface temperature, used when evaluating the sensible heat flux, by the relative areas of exposed ground and foliage surfaces, as in the example of Eq. 2.22. However, this method assumed that the same wind ventilated both the soil and plant surfaces. Here, a different paradigm is invoked where, instead of parsing the temperature, we parse the wind that ventilates the surface interface based on the wind-speed profile as illustrated by Thom (1972, Fig. 1).

The wind-speed profile shown in Thom's figure is similar to that of Fig. 8 above, except instead of the speed becoming zero inside the foliage canopy, a remnant of wind remains beneath the canopy that becomes zero only at height $z_{0G} + D_G$. This suggests the wind speed can be divided into a portion that influences only the foliage fluxes and another part that influences only fluxes at the ground surface. The wind-speed equation then is written as, $u_Z = u_{ZG} + u_{ZF}$, or in expanded form as,

$$u_Z = \frac{u_{*G}}{k} \left[\ln \left(\frac{Z - D_G}{z_{0G}} \right) - \psi_1 \left(\frac{Z}{L_{Ob}} \right) \right] + \frac{u_{*F}}{k} \left[\ln \left(\frac{Z - D_F}{z_{0F}} \right) - \psi_1 \left(\frac{Z}{L_{Ob}} \right) \right], \quad (5.24)$$

at heights Z significantly above the surface interface ($Z > 2 h_F, 2 h_G$).

In most cases, for substantial vegetation, the foliage layer will absorb the bulk of the wind's momentum, leaving a reduced wind profile beneath the canopy. Below the canopy, the wind profile should reflect the influence of the ground and its roughness parameter.

The main factor in this approach to be resolved is the relative values of u_{ZG} and u_{ZF} , or, equivalently, u_{*G} and u_{*F} . Previously, a weighted average was computed based on the relative areas of barren ground (1) versus leaf-surface area ($N_f = \sigma_f \Upsilon_f$). This appears approximately correct, but instead of applying it to the temperature, in this case it is applied to the wind. Still, some factors could be better resolved by comparison with measurements for different terrain/vegetation combinations. That is, while the ground is considered *flat*, and given a weighting of unity, depending on its roughness (z_{0G}), a unit area of bare ground may create more

drag than the same area of relatively smooth leaves. But since the leaves present different angles of attack to the incident wind, they may present more or less drag than the surface. Nevertheless, the model used will be to subdivide the available wind based on the relative area:

$$W_G = \frac{1}{1 + N_f}; \quad W_F = \frac{N_f}{1 + N_f}. \quad (5.25)$$

This relative-area concept will then distribute the available drag effects according to proportional amounts of the momentum being transferred to the surface via the 2 component friction velocities:

$$u_{*G} = W_G u_*; \quad u_{*F} = W_F u_*. \quad (5.26)$$

Each wind component is then modeled as exhibiting its own wind profile, consistent with the surface it interacts with. For example, the wind interacting with the soil is modeled as only experiencing drag effects due to the ground (parameterized by a separate ground roughness length z_{0G}).

Here, the 10% adjustment of the leaf index N_f to account for twigs and branches is dropped to ensure that the results obtained for the sensible heat flux are consistent with calculations made for the latent heat flux.

Subdividing the wind effect rather than the temperature influence allows the efficiency coefficients for the ground and foliage to be applied separately in resolving the impact of each of the 2 influences. Thus, one can define:

$$c_{HG}(Z) = \frac{0.74^{-1} k u_{*G} / u_{ZG}}{\left\{ \ln \left[\frac{(Z-D_G)}{z_{0G}} \right] - \psi_2 \left[\frac{(Z-D_G)}{L_{Ob}} \right] + 0.71 \left(\frac{u_{*G} z_{0G}}{\nu} \right)^{0.45} \right\}}; \quad (5.27.A)$$

$$c_{HF}(Z) = \frac{k u_{*F} / u_{ZF}}{\left\{ \ln \left[\frac{(Z-D_F)}{z_{0F}} \right] - \psi_1 \left[\frac{(Z-D_F)}{L_{Ob}} \right] + 0.15 \left(\frac{u_{*F} z_{0F}}{\nu} \right)^{0.33} \right\}}. \quad (5.27.B)$$

The net sensible heat flux can then be written as $H_{Sg} + H_{Sf}$ in the form,

$$H_S = \rho_a C_p \left[c_{HF}(Z) u_{ZF} (T_F - T_Z) + c_{HG}(Z) u_{ZG} (T_G - T_Z) \right]. \quad (5.28)$$

By performing the parsing of the drag effects on the wind via the u_* variable, we can still write that $H_S \propto u_* T_*$. This allows T_* to be evaluated from H_S , and we may iterate on the values of L_{Ob} , u_* , and $H_S(T_*)$.

In the program these relations are simplified through the use of the constants

$$A_{Hg} = \rho_a C_p c_{HG}(Z) u_{ZG}, \quad (5.29.A)$$

$$A_{Hf} = \rho_a C_p c_{HF}(Z) u_{ZF}, \quad (5.29.B)$$

such that,

$$H_{Sg} = A_{Hg} (T_G - T_Z), \quad (5.30.A)$$

$$H_{Sf} = A_{Hf} (T_F - T_Z). \quad (5.30.B)$$

In a similar manner, individual latent heat fluxes from ground and foliage are found in the next section.

5.6 Latent Heat Flux for Foliated-Terrain Conditions

Based on the results obtained for the sensible heat-flux for vegetated-terrain conditions, it is now possible to expand on these results to solve for the latent heat-flux for vegetated-terrain conditions. In doing so, we follow a modified version of the method Deardorff developed for the latent heat flux. In Deardorff's approach to the moisture flux — unlike the sensible heat flux that just depended on temperature — not every surface need be moist. Therefore, the fraction of a surface that is susceptible to evaporation must be *moist* initially. Parameters are used to designate the degree of moisture availability on both ground and vegetation surface. Variables r'' and α' characterize fractional moisture availabilities of foliage and bare ground surfaces, respectively. The weighted mean fraction of the surface susceptible to evaporation was modeled through use of the parameter,

$$A' = \frac{\alpha' + r'' N_f}{(1 + N_f)}, \quad (5.31)$$

in Tofsted (1993). The terms α' and r'' are based on Deardorff (1978), given as,

$$\alpha' = (1 - \delta_c) + \min(1, w_g/w_K) \delta_c, \quad (5.32.A)$$

$$r'' = 1 - \delta_c [r_s/(r_s + r_a)] [1 - (w_{dew}/w_{dmax})^{2/3}], \quad (5.32.B)$$

$$\delta_c = \begin{cases} 1, & \text{evaporation is occurring,} \\ 0, & \text{condensation is occurring,} \end{cases} \quad (5.32.C)$$

where w_g is the fractional moisture of the ground (by volume); w_K is the fraction of moisture the ground contains when it behaves as if it is saturated; r_s is the

stomatal resistance; r_a is the atmospheric resistance; w_{dew} is the mass of dew on the foliage per square meter of ground surface area (normally zero during the day); and w_{dmax} is the maximum dew accumulation per square meter of ground before runoff to the ground will occur. Further equations for r_s , r_a , and w_{dmax} can be found in Deardorff (1978). These equations depend on the foliage type, wilt factors, mean incident sunlight, and other coupling factors that will not be explained here. The controlling parameters are generated in the model, and no justification for the validity of Deardorff's approach will be presented. Note that evaporation is considered to be occurring if $Q_{sat}(T_G) > Q_Z$ (i.e., when the specific humidity of saturated air at the ground temperature exceeds the specific humidity of air at the station height) or $Q_{sat}(T_F) > Q_Z$, depending on whether the ground or foliage surfaces are being considered.

Using a flux-equation form similar to that in Paulson (1970), the total latent heat flux is described by the equation,

$$H_L = L_v E = -\rho_a L_v Q_* u_*, \quad (5.33)$$

where E is the evaporative flux (kg of water per square meter of underlying surface per second), and Q_* is defined in the same sense as T_* in Eq. 2.8, in that a negative Q_* is indicative of heat leaving the surface interface and entering the surface-layer air.

This equation can also be expressed in efficiency-coefficient and resistance-method forms as

$$H_L = L_v E = \rho_a L_v c_Q u_Z (Q_S - Q_Z) = \rho_a L_v \frac{(Q_S - Q_Z)}{r_Q}, \quad (5.34)$$

where r_Q is the resistance to water-vapor flux, c_Q is the efficiency of the water-vapor flux, and Q_S is an equivalent surface-specific-humidity source term. This was the approach taken in Tofsted (1993).

This approach is modified to account for the current parsing of the wind speed, instead of the surface property, according to the relative drag effects of the surface based on the properties of the foliage layer in accord with the sensible-heat-flux calculation discussed above.

This is possible because of the general assumption that $r_Q = r_H$, reflecting the *similarity* of all conservative-passive-additive transport processes. This calculation

is even more simply stated than in Tofsted (1993), since the wind-speed parsing becomes separated from the humidity-availability parsing necessary to determine separate, equivalent Q_S values for the ground and foliage surfaces.

Given the above discussion, one can readily write

$$Q_G = \alpha' Q_{sat}(T_G), \quad Q_F = r'' Q_{sat}(T_F). \quad (5.35)$$

Essentially, these quantities represent saturation water-availability as represented by the Q_{sat} components, multiplied by relative-humidity parameters represented by α' and r'' . We then write, immediately, $H_L = H_{Lg} + H_{Lf}$, such that,

$$H_L = \rho_a L_v \left[c_{QF}(Z) u_{ZF} (Q_F - Q_Z) + c_{QG}(Z) u_{ZG} (Q_G - Q_Z) \right]. \quad (5.36)$$

Here, using the property that both humidity and temperature may be considered conservative-passive-additives, we may assume

$$c_{QF} = c_{HF} \quad \text{and} \quad c_{QG} = c_{HG}. \quad (5.37)$$

This procedure allows for the same parsing of the wind into foliage and ground components as was performed in the sensible-heat-flux case.

6. Boundary-Layer Thermal Accounting

In this chapter a key deficiency of the Deardorff (1978) model is addressed. In Chapter 5 the calculation of the sensible and latent heat fluxes focused on the parsing of energy contributions to these fluxes between foliage and soil surfaces. However, one aspect of these fluxes that was not emphasized was the issue of the air temperature used, T_Z .

The issue is this: In Deardorff's model, the air temperature is simply considered to be a given and not affected by energy fluxes to or from the surface interface. Instead, the air temperature is typically updated based on measured data at some height z above the surface. But this gives rise to 2 possible problems. First, what if such data are simply unavailable? Second, what if the available data are not properly synchronized with the surface-soil and surface-foliage temperatures? In this case the measured air-temperature evolution could be out of phase with the surface interface, producing false fluxes.

To produce a suitable air-temperature evolution, the air temperature in the surface layer should lag the surface temperatures but should lead the reaction of the overall boundary-layer temperature. To address these dynamics the flux-profile relations governing the standard, vertical temperature structure are slightly modified to produce profile shapes that appropriately connect the energy states of the boundary and surface layers.

To do so we note that the general temperature profile within the boundary layer is generally characterized by some type of adiabatic lapse-rate profile, using either the moist adiabatic lapse rate of -6.4 K/km or the dry adiabatic lapse rate of -9.8 K/km. By extrapolating these profiles to the ground an intercept point may be identified, given by temperature T_G that we shall use in characterizing the energy content of the boundary-layer air. Beyond T_G , the surface-layer atmosphere is characterized by an extra amount of energy related to a height scale and the difference in temperature between T_G and the temperature at some characteristic height. In the previous chapter this temperature was called T_Z . Here, we shall substitute various variable names to be more consistent with a height (Z) and temperature (T) paradigm.

6.1 Vertical Temperature Profile Models

To begin, recall that in Eq. 5.28 we developed an expression for the sensible heat flux being a combination of fluxes from the soil and foliage surfaces, H_S . We

also introduced a length scale termed the Obukhov length, L_{Ob} . In this chapter that variable will be renamed as Z_K , consistent with other height scales that will likewise be labeled as Z -type variables.

Given that H_S is known or can be calculated knowing T_Z (T_A in this chapter), we write the Obukhov length as

$$Z_K = -\frac{U_*^3 T}{k g [H_S/(\rho_a C_p)]}. \quad (6.1)$$

The Obukhov length is considered the dominant, vertical scaling length within the surface layer according to the flux-profile theory. This characteristic vertical length-scale approximately equals the height at which mechanical and buoyant effects are balanced. Beyond $|Z_K|$ mechanical effects dominate. Using Z_K , any function of height within the surface layer can be written in a dimensionless form dependent on the ratio $\zeta = z/Z_K$.

In particular, the vertical structures of wind speed and temperature are typically written using a nondimensional function of height dependent on ζ . Paulson's (1970) nomenclature has been slightly altered to write vertical temperature and wind-speed gradients in the forms,

$$\phi_1(z/Z_K) = \frac{kz}{U_*} \frac{\partial U}{\partial z}; \quad (6.2)$$

$$\phi_2(z/Z_K) = \frac{kz}{T_*} \frac{\partial T}{\partial z}; \quad (6.3)$$

where k is von Kármán's constant (a dimensionless quantity set to 0.385), U_* is the friction velocity (m/s), and T_* is the scaling temperature (K). The U_* and T_* parameters are defined based on their relations to the vertical sensible heat flux (W/m^2),

$$H_S = -\rho_a C_p U_* T_*, \quad (6.4)$$

where ρ_a is the air density (kg/m^3) at the flux-calculation height and C_p is the specific heat of air at constant pressure ($C_p \approx 1004.84 \text{ J/kg/K}$). We assume that the sensible heat flux is a constant of the surface layer (it varies by approximately 10%, but we assume it constant), such that U_* and T_* are also constants of the layer.

We also of necessity must compute the flux at some height, call it z_{calc} . For purposes of this chapter we identify this height with the height Z_A at which the air temperature equals T_A . (And note that temperature and wind variables are actually

expectation values, $T = \langle T \rangle$, averaged such that fluctuations over several seconds, corresponding to variations within the inertial subrange, are ignored.)

Integrating the above nondimensional gradient functions ϕ_1 and ϕ_2 , one can produce integrated vertical wind-speed and temperature profile functions involving new nondimensional diabatic-influence functions ψ_1 and ψ_2 :

$$U_* = \frac{k [U_Z - U_0]}{\ln(z/z_0) - \psi_1(z/Z_K)}, \quad (6.5)$$

$$T_* = \frac{k [T_Z - T_S]}{\ln(z/z_0) - \psi_2(z/Z_K)}, \quad (6.6)$$

where z_0 is the surface-roughness length, some small fraction of the height, Z_F , of the average roughness element (Hansen¹ recommended $z_0 \approx 0.13 Z_F$), and T_S is the *effective* surface temperature.

To be consistent when using these forms, Eqs. 6.5 and 6.6 cannot be used to determine H_S , since H_S is found using the flux model of Chapter 5. Instead, since $U_0 = 0$, and assuming U_Z is known, Z_K can be computed iteratively. Then, once Z_K is known, T_* can be derived from H_S and U_* , and Eq. 6.6 then provides an estimate for

$$\Delta T_Z = T_Z - T_S = T_A - T_S. \quad (6.7)$$

Yet, notice that this analysis only yields ΔT_Z , not T_A and T_S separately. But T_A is also necessary to evaluate the downward long-wave-radiation flux. And both T_A and T_S are needed separately to account for energy contained in the surface layer.

Hence, we need at least one more equation to resolve T_A . It will also become clear that this formulation must be considered separately for different atmospheric-stability conditions. Therefore, let us begin by considering the daytime diabatic-heating case. (The nocturnal boundary-layer case will be examined later.)

For the daytime case, solar radiation warms the surface interface, which then heats the surface-layer atmosphere. The temperature T_A will therefore be elevated somewhat above the background, boundary-layer equivalent temperature T_G ($T_A > T_G$). This differential is maintained by the continuous flow of sensible heat into the atmosphere from the surface interface. But, warmed air in the surface layer is then the primary means of delivering heat into the remainder of the boundary layer through convective processes.

This secondary warming can only occur if $T_A > T_G$. Otherwise, when $T_S > T_A$ the surface layer can warm, even while no heat is transferred into the upper boundary layer. Likewise, T_A will rapidly decay toward T_G in the event the sensible heat flux from the surface is cut off, an effect often seen when clouds shade the surface and during solar eclipses.

Yet, clearly, the sensible heat only depends on ΔT , not T_G . This leads to an interesting paradox: While the sensible heat flux depends on $T_S - T_A$, the flux of heat out of the surface layer depends on $T_A - T_G$. Temperature T_A couples to both, meaning either a steady-state relation could exist or a cyclical behavior could emerge.

6.2 Decomposition of the Sensible Heat

To identify the resulting set of coupled equations to describe evolution of the boundary-layer and surface-layer atmospheres, we must be able to parse the sensible heat-flux into a portion that is heating the surface-layer air and another portion that passes through the surface layer and heats the boundary layer. We denoted these by H_{SA} and H_{SB} for the portions associated with the surface layer and boundary layer, respectively,

$$H_S = H_{SA} + H_{SB}. \quad (6.8)$$

The easiest of these to resolve is H_{SB} , which affects the value of T_G . The rate at which T_G is increasing in the boundary layer, dT_G/dt , involving temperature change, dT_G , and occurring over time step dt will be expressed simplistically (for now) as

$$\frac{dT_G}{dt} = \frac{H_{SB}}{(\rho_a C_p)} \frac{1}{Z_I} \propto \frac{T_A - T_G}{Z_I}, \quad (6.9)$$

where Z_I is the depth of the boundary layer up to the elevated inversion height. Here we assume the heat delivered is distributed evenly over the complete boundary layer. Use of H_{SB} acknowledges our need to model both a sensible heat flux flowing into the boundary layer but also a net energy flux from all sources that affect the boundary-layer temperature. We designate H_{SB} as the *boundary-layer heat flux*, but in fact the complete flux equation will be more complicated since there are several fluxes affecting the energy budget of the boundary layer. For example, there exists a downward sensible heat flux at the top of the boundary layer caused by entrainment of rising air into the elevated inversion layer that is approximately an extra quarter

of H_{SB} , according to Stull (1988). Also, the density of the air is not constant and accounting for this involves inclusion of an extra weighting factor. But the main point illustrated by Eq. 6.9 is that the change in T_G depends on the temperature difference $(T_A - T_G)$ and not $(T_S - T_G)$ or $(T_S - T_A)$.

Using the same logic as in Eq. 6.9, we can heat the surface-layer air using

$$\frac{dT_A}{dt} = \frac{H_{SA}}{(\rho_a C_p) Z_T}, \quad (6.10)$$

where Z_T is a characteristic length scale of the surface-layer atmosphere. Likely, it is of the order of magnitude as $|Z_K|$, but this is one of the elements to be resolved in this analysis. Also, this Equation presumes that T_A changes in the same proportion as the mean characteristic temperature of the full surface layer.

In the steady-state case, note that T_A becomes a constant, and $H_{SB} = H_S$, where $H_{SA} = 0$. That is, the surface layer then acts merely as a conduit for transferring energy to the boundary layer.

We thus have 2 expressions for heating the 2 layers. These must next be coupled. To see how they might be related, consider that to mix the heated air in the surface layer into the boundary layer the dynamics must rely on the relative buoyancy of the surface-layer air as it rises. The relative buoyancy is given by the characteristic air temperature (T_A) versus the local ambient (background) temperature. One can think of the temperature T_A as being associated with air heated near the surface that is rising and the background air being air that has been mixed in the boundary layer and is falling toward the surface and, therefore, is characterized by temperature T_G . Of course, as the air rises out of the surface layer, it cools along with the rest of the ambient air at the same adiabatic lapse rate as the background air characterized by temperature T_G . The relative difference should remain approximately constant as long as we can ignore the effects of entrainment. But the entrainment that occurs is part of the mixing that diffuses the heat across the layer. Hence, overall, the product $V \Delta T$ should remain a constant, where V is the volume of the rising air and $\Delta T = T_A - T_G$ is the temperature difference. This volume is associated with the unit footprint of the model (1 m^2 of surface) and the characteristic height of the air being mixed out of the surface layer (Z_T).

The initial acceleration of the rising buoyant air will be $a = g \Delta T / T_A$. This is simply Archimedes' principle applied to the buoyant air. The sense of ΔT is that

when $\Delta T > 0$ an upward displaced parcel of air will become buoyant. Let us consider a given air parcel to have an initial vertical velocity equal to zero. The parcel's acceleration is thus proportional to the density difference divided by the mean density of the air being moved (force divided by mass equals acceleration). The time of rise that we are concerned with is related not to the time it takes for the parcel to rise to the top of the boundary layer, but merely the time needed for the parcel to exit the surface layer. The distance the parcel must rise is thus only Z_T . The rise time should thus be on the order of

$$t_{rise} \geq \sqrt{2 Z_T / a} = \sqrt{2 Z_T T_A / (g \Delta T)}. \quad (6.11)$$

For typical temperature differences on the order of a few degrees, an estimate of the acceleration coefficient can be formed as $a = g \Delta T / T \approx g / 100 = 0.1 \text{ m/s}^2$. For strong daytime heating Z_T could be perhaps only 10 m thick. The time needed to rise this 10 m would be approximately 14 s, consistent with observed rapid decay of surface-turbulence conditions when clouds overshadow optical lines of sight.

Of course, this calculation focuses only on the time necessary for a warm air parcel to rise by a height equal to the surface-layer thickness. This calculation could also be used to simulate the behaviors of other organized features of the daytime atmosphere such as thermal plumes. At WSMR, desert *dust devils* are often observed that are perhaps 300 m tall (the rise time for these would be on the order of 80 s). The computed final velocity of air at the top of such a column, based on the buoyancy force, would be approximately 8 m/s. Typical dust devils expel visible material from their tops. While 8 m/s may be high, since it does not include entrainment effects, as an order-of-magnitude result it appears reasonable.

Next, we assign a quantity $\Delta E = \rho_0 C_p \Delta T Z_T \text{ (J/m}^2\text{)}$ as the amount of energy per square meter provided by the surface layer over rise time t_{rise} . We thus have an amount of energy delivered in a specific amount of time, such that,

$$H_{SB} = \Delta E / t_{rise} = \frac{\rho_0 C_p \Delta T Z_T}{\sqrt{2 Z_T / a}} = \rho_0 C_p \sqrt{\frac{g \Delta T^3 Z_T}{2 T_A}}. \quad (6.12)$$

We thus have 2 out of the 4 terms in Eq. 6.9. However, the product $\rho_a Z_I$ needs to be slightly adjusted since it actually represents an integrated mass and height product given by

$$\rho_a Z_I \longrightarrow \int_0^{Z_I} \rho_a(z) dz. \quad (6.13)$$

To integrate this expression, we replace the vertical dependence of ρ_a by a form derived from the hydrostatic equation:

$$\frac{dP}{dz} = -\rho_a g \longrightarrow \int_0^{Z_I} \rho_a dz = -\frac{1}{g} \int dP = +\frac{1}{g} [P(0) - P(Z_I)]. \quad (6.14)$$

The pressure at the surface is given as $P(0) = P_0 = P_{bottom}$ based on the height of the site ASL, while the top pressure may be approximated by an exponential decline based on Z_I and the atmospheric scale height,

$$Z_{Sc} = \frac{RT}{g} = \frac{RT}{P} \frac{P}{g} = \frac{1}{\rho_a} \frac{P}{g} \longrightarrow \frac{P_0}{g} = \rho_0 Z_{Sc}, \quad (6.15)$$

using g , the gravitational acceleration, and R , the gas constant. Hence,

$$\rho_a Z_I \longrightarrow \frac{P_0}{g} [1 - \exp(-Z_I/Z_{Sc})] \approx \rho_0 Z_I \frac{[1 - \exp(-Z_I/Z_{Sc})]}{(Z_I/Z_{Sc})}. \quad (6.16)$$

While this expression could be improved further, we will stop here. Rather, let us simplify the writing of the result by defining

$$G_1(\tau) = [1 - \exp(-\tau)]/\tau. \quad (6.17)$$

$$\rho_a Z_I \longrightarrow \rho_0 Z_I G_1(Z_I/Z_{Sc}). \quad (6.18)$$

As an example, for a boundary layer of thickness $Z_I \approx 2$ km and a scale height $Z_{Sc} \approx 8$ km, $Z_I/Z_{Sc} = 1/4$ and $G_1(1/4) = 0.885$. Thus, the error in using $\rho_0 Z_I$ is approximately 12% versus the more accurate version. (Further improvements will remove progressively less error.)

Returning now to Eq. 6.9, replacing terms with the results of Eqs. 6.12 and 6.18:

$$\frac{dT_G}{dt} \approx \frac{\rho_0 C_p \sqrt{g \Delta T^3 Z_T / (2 T_A)}}{C_p \rho_0 Z_I G_1(Z_I/Z_{Sc})} = \frac{\sqrt{g \Delta T^3 Z_T / (2 T_A Z_I^2)}}{G_1(Z_I/Z_{Sc})}. \quad (6.19)$$

Of course, this Equation supplies an answer for daytime (surface heating) conditions ($\Delta T > 0$) only, and only if T_A can be sustained over the time period of the time step involved. If t_{rise} is significantly less than the time step of the model, it could be that the heated atmosphere rises out of the surface layer leaving air of temperature T_G in its wake. Therefore, the production time is significant. For example, in the example above where the rise time was found to be approximately

14 s, a model time step of 1 min would be too long. The time step chosen should therefore be less than the rise time of the surface layer. Secondly, at night, $\Delta T < 0$ and Eq. 6.19 yields imaginary numbers, invalidating the method. Thus, a separate derivation will be needed for the nighttime case.

It would also be convenient if we could replace the surface-layer height Z_T by some other depth scale, such as $|Z_K|$; but, as we shall discover in a later section, Z_T is best treated as its own variable, as it is related to Z_A and T_A .

From the result for the energy entering the boundary layer, H_{SB} , we can combine Eqs. 6.8 and 6.10 to obtain the result,

$$\frac{dT_A}{dt} = \frac{H_S - H_{SB}}{(\rho_0 C_p)} \frac{1}{Z_T}. \quad (6.20)$$

Thus, while H_S depends on $T_S - T_A$, any energy remaining within the surface layer will tend to heat the surface layer and diminish the energy exiting to the boundary layer. This formulation also assumes Z_T remains constant as the layer is heated.

6.3 Extended Surface- and Boundary-Layer Heating Equations

In the previous section the sensible heat warming of the surface and boundary layers was considered in a simple fashion. However, now these relations are expanded to include additional terms due to radiative and convective fluxes that were previously omitted. While latent heat fluxes do not alter the temperature state, and short-wave radiative fluxes pass through the atmosphere without warming it (or so it is modeled here), long-wave radiation is partially absorbed; a sensible heat flux from the top of the boundary layer must be handled.

First, consider the long-wave infrared fluxes. The atmospheric surface layer will tend to absorb long-wave radiation emitted by the surface and re-emit radiation toward the surface and toward the boundary layer above. Likewise, the atmospheric surface layer will absorb radiation emitted downward from the boundary layer. Governing these fluxes is the atmospheric emissivity, which we consider in detail in the following chapter. Here, let us designate the emissivity as ϵ_A . The radiative fluxes are itemized as follows:

- 1) The long-wave flux from the atmospheric surface layer — both upward (from the top of the surface layer) and downward (from the bottom) directed — modeled as

$$L_{\uparrow,A} = L_{\downarrow,A} = \sigma \epsilon_A T_A^4, \quad (6.21)$$

using σ for the Stefan–Boltzmann constant.

2) The downward long-wave flux from the bottom of the boundary layer (into the top of the surface layer) is expressed by

$$L_{\downarrow,B} = \sigma \epsilon_A T_G^4. \quad (6.22.A)$$

3) Then, the upward long-wave from the *effective surface* designated as $L_{\uparrow,E}$ (also discussed at length in the next chapter). Because the atmospheric emissivity also quantifies the ability of the atmosphere to absorb infrared radiation, only a portion, $\epsilon_A L_{\uparrow,E}$, of the upward-directed long-wave energy leaving the surface interface will be absorbed by the surface layer. The remainder will pass through both the surface layer and the boundary layer and be lost to space.

4) The last 2 long-wave fluxes of note arise from the upward-directed radiative flux leaving the top of the boundary layer, denoted by

$$L_{\uparrow,B} = \sigma \epsilon_A T_T^4 = \epsilon_A L_{\uparrow,T}, \quad (6.22.B)$$

where T_T is the temperature at the top of the boundary layer, given by $T_T = T_G - \Gamma Z_I$, where Γ is the adiabatic lapse rate for dry air equal to 9.8 K/km. ($L_{\uparrow,T}$ is the equivalent blackbody radiation at the top of the boundary layer.)

5) Finally, the downward radiative flux emitted from above the boundary layer accounts for both upper air radiative emissions and cloud emissions. To model the upper-air emission we use an estimation from Stull's Figs. 3.6 and 3.8 that suggest the upper air dries out to a specific humidity value that is one-third of the value in the boundary layer. From this approximation we can compute a quantity ϵ_U that is the emissivity for this layer. We then model the downward basic radiation as

$$L_{\downarrow,U} = \sigma \epsilon_U T_T^4, \quad (6.23)$$

where T_T is the temperature of the top of the boundary layer. To this quantity we add the cloud radiation that is blackbody in nature but scaled according to the amount of cloud cover (F_C):

$$L_{\downarrow,C} = \sigma F_C T_C^4. \quad (6.24.A)$$

This is the total flux emitted downward from the cloud layer. However, only a certain fraction of this will reach the top of the boundary layer, as determined by the upper-air emissivity:

$$L_{\downarrow,C,T} = \sigma F_C (1 - \epsilon_U) T_C^4. \quad (6.24.B)$$

Of this amount, a certain fraction will then make it through the atmospheric window and reach the effective surface. This amount is expressed by

$$L_{\downarrow,C,E} = \sigma F_C (1 - \epsilon_A) T_C^4. \quad (6.24.C)$$

The difference between these 2 calculations (where $\epsilon_A > \epsilon_U$) is just that portion of the radiation that is absorbed in the boundary layer:

$$L_{\downarrow,C,B} = \sigma F_C (\epsilon_A - \epsilon_U) T_C^4. \quad (6.24.D)$$

The reason why we can represent the absorption effects in this manner is because the absorption effects of the upper air and the boundary layer are associated with the same absorption lines, so the effects overlay one another spectrally.

Throughout this discussion, T_C has represented the air temperature (K) at the cloud-base height. Following Stull we compute T_T then add 3 °C (denoting the rise in temperature of the air due to the elevated inversion) to obtain T_C for low clouds:

$$T_{C(low)} = T_T + 3 [C]. \quad (6.25.A)$$

For midlevel clouds we assume they are another 3 km up. Using the moist adiabatic lapse rate, we compute

$$T_{C(mid)} = T_{C(low)} - 3 [km] \times 6.4 [C/km]. \quad (6.25.B)$$

For high clouds, we add another 3 km of altitude:

$$T_{C(high)} = T_{C(mid)} - 3 [km] \times 6.4 [C/km] = T_{C(low)} - 6 [km] \times 6.4 [C/km]. \quad (6.25.C)$$

The factor $(\epsilon_A - \epsilon_U)$ is added to account for the absorption of the cloud radiation by the intervening upper-air layer. The difference is used because the ability of the air within the boundary layer to absorb radiation is proportional to ϵ_A , but this absorption coincides with the same spectral lines where the upper air is absorbing with efficiency ϵ_U .

Combining flux terms, the improved version of the surface-layer temperature's evolution becomes,

$$\frac{dT_A}{dt} \approx \frac{(H_{SA} - 2 L_{\uparrow,A} + L_{\downarrow,B} + \epsilon_A L_{\uparrow,E})}{\rho_0 C_p Z_T}. \quad (6.26.A)$$

Using this result, the more accurate version of the T_G evolution becomes

$$\frac{dT_G}{dt} \approx \frac{\left(\frac{5}{4} H_{SB} - L_{\uparrow,B} - L_{\downarrow,B} + L_{\uparrow,A} + L_{\downarrow,U} + L_{\downarrow,C,B}\right)}{\rho_0 C_p Z_I G_1(Z_I/Z_{Sc})}, \quad (6.26.B)$$

where the $5/4$ factor derives from the entrainment of warmer air in the elevated inversion that mixes into the boundary layer when rising plumes of air overshoot the top of the boundary layer and mix with warmer air above. This results in a downward sensible heat flux into the boundary layer. The result is a partial heat flux from the inversion layer downward into the boundary layer.

Eq. 6.26.B can also be somewhat simplified as

$$\frac{dT_G}{dt} \approx + \frac{\left[\frac{5}{4} H_{SB} - L_{\downarrow,B} + L_{\uparrow,A} + (\epsilon_A - \epsilon_U) (L_{\downarrow,C} - L_{\uparrow,T})\right]}{\rho_0 C_p Z_I G_1(Z_I/Z_{Sc})}, \quad (6.27)$$

which we may further simplify and write as

$$\frac{dT_G}{dt} \approx \frac{\left[\frac{5}{4} H_{SB} + L_{\uparrow,A} - L_{\downarrow,B} + L_{\uparrow\downarrow,T}\right]}{\rho_0 C_p Z_I G_1(Z_I/Z_{Sc})}, \quad (6.28)$$

where $L_{\uparrow\downarrow,T}$ represents the net long-wave radiation entering at the top of the boundary layer that will be absorbed within the upper regions of the boundary layer.

The key dynamical aspect of Eqs. 6.26.A and 6.28 is to note that T_A is an important term in evaluating T_* , the scaling temperature that directly influences the computation of C_n^2 . It also drives the sensible heat flux from the ground and regulates the heat flux into the boundary layer. Thus, while computation of the various surface-energy-budget fluxes is important, producing an accurate model of the dynamics of the evolution of the surface-layer temperature is critical to improving estimates of C_n^2 . To capture the dynamics of T_A it will be necessary to reduce the length of the time step used.

Along with the difference $T_S - T_A$, the resulting scaling temperature T_* will also tend to cycle, causing variability in the C_n^2 calculated. Wind-speed variations will also tend to introduce more or less heat into the surface layer, causing fluctuations. This is often observed during daytime environments. We thus appear to have a model capability that tends to mimic the observed variability of daytime near-surface C_n^2 , as long as our time step is short enough to capture the temporal frequency of these variations.

Note also that a portion of the radiation arriving from the clouds has been blocked by the upper-air absorptivity, ϵ_U . Since this absorptivity is at lower specific humidity the absorption effects will be more tightly centered about the absorption lines of the radiation. Therefore, the upper air has already absorbed this radiation.

6.4 Perturbed Daytime-Temperature Profile Function

The previous section's results appear to resolve a critical issue with regard to the handling of atmospheric temperatures. However, we did not resolve which value to use for the characteristic thickness of the surface layer, Z_T . We also did not resolve how to choose Z_A based on T_A .

Let us therefore consider a general temperature function with height, called $T(z) = T_Z$, and compare that with the *background* temperature that we associate with the general boundary-layer-temperature profile, $T_B(z)$. We model this latter profile using the function

$$T_B(z) = T_B = T_G - \Gamma z. \quad (6.29)$$

At this point we shall set Γ as the dry adiabatic lapse rate, since under most circumstances we will not be considering moist atmospheres.

In general, $T(z)$ will approach $T_B(z)$ as z increases. The difference between these 2 functions defines a profile we associate with the departure of the surface-layer temperature from the adiabatic atmosphere. The daytime version of this functional form is the subject of this section's discussion. The connection between the resulting profile and the use of T_A and Z_T , however, may be discussed now. Let us write

$$\tilde{T}(z) = \tilde{T}_Z = \begin{cases} T_B + (T_A - T_G), & z < Z_T, \\ T_B, & z > Z_T, \end{cases} \quad (6.30.A)$$

$$\tilde{T}_Z = \begin{cases} T_A - \Gamma z, & z < Z_T, \\ T_G - \Gamma z, & z > Z_T, \end{cases} \quad (6.30.B)$$

where \tilde{T}_Z is a model of the true vertical profile, but greatly simplified such that it follows T_B at large height and evaluates to approximately T_A throughout the surface layer. We then select Z_T and T_A in such a way that the above simplified model is optimized, using a least-squares approach, for the current atmospheric state.

To determine this optimization we must have a vertical structure model for the temperature as a function of the Obukhov length, Z_K , that smoothly merges into the background $T_B(z)$ vertical structure of the boundary layer.

We begin this process by considering the surface-layer-temperature difference formula, repeating Eq. 6.6 here:

$$T_Z - T_S = \frac{T_*}{k} \left[\ln \left(\frac{Z}{Z_0} \right) - \psi_2 \left(\frac{Z}{Z_K} \right) \right], \quad (6.31)$$

where $z = Z$, and $\psi_2(\zeta)$ is given by Paulson (1970) as

$$\psi_2(\zeta) = 2 \ln \left\{ \frac{[1 + X^2(\zeta)]}{2} \right\}, \quad (6.32)$$

where

$$X(\zeta) = (1 - \gamma \zeta)^{1/4}, \quad (6.33)$$

with $\gamma = 9$ and $\zeta < 0$ for the temperature profile for daytime conditions.

This profile, appropriate for the daytime diabatic-lapse atmosphere, can be rewritten by expressing the height dependence as

$$\ln \left(\frac{Z}{Z_0} \right) - \psi_2 \left(-\frac{Z}{|Z_K|} \right) = \ln \left(\frac{|Z_K|}{Z_0} \right) + \ln \left(\frac{Z}{|Z_K|} \right) - \psi_2 \left(-\frac{Z}{|Z_K|} \right), \quad (6.34)$$

where $\ln(|Z_K|/Z_0)$ is a constant of the current stability condition. This term thus has an influence on the offset of the profile dependent on the surface properties, but does not influence the vertical structure away from the surface. Essentially, this means it simply gets absorbed into any constant temperature offset and may be ignored.

The height-profile shape therefore only depends on the ratio $Z/Z_K = \zeta$. Unfortunately, the function $\ln(|\zeta|) - \psi_2(\zeta)$ is continuously increasing with no upper limit. However, for $|\zeta| > 20$, the 2 logarithms tend to cancel.

Still, to ensure a profile that approaches the adiabatic lapse-rate behavior of the boundary layer at large distances from the surface, a correction must be made to the surface-layer dependence that becomes dominant at large distances from the surface. In this way a single consistent function can be assigned to the surface/boundary layer for purposes of evaluating T_A , Z_A , and Z_T .

To perform this task, let us next rewrite the surface-layer profile based on our observations of Eq. 6.34:

$$T_Z = T_S + \frac{T_*}{k} \left[\ln \left(\frac{|Z_K|}{Z_0} \right) + P \left(\frac{Z}{|Z_K|} \right) \right]. \quad (6.35)$$

Let $\xi = |\zeta|$, such that,

$$P(\xi) = \ln(\xi) - \psi_2(-\xi). \quad (6.36)$$

The background profile we wish to adapt to is the $T_B(Z)$ function of Eq. 6.29. To do so, we must perturb $P(\xi)$ such that the modified function approaches zero at the top of the boundary layer and has zero derivative there as well. This perturbation should also approach zero effect within the surface layer. Let us denote this modified function as $Q(\xi, N_I)$ (where $N_I = Z_I/|Z_K|$ parameterizes the thickness of the boundary layer). This new function can be defined using

$$Q(\xi, N_I) = P(\xi) - P(N_I) - \frac{dP(Z/|Z_K|)}{dZ} \Big|_{Z=Z_I} |Z_K| (\xi - N_I). \quad (6.37)$$

This function satisfies the stated requirements at the top of the boundary layer but to ensure that the profile also matches the original profile in the surface layer, at $Z = Z_0$ the profile must become T_S . To satisfy this requirement we must use

$$T_Z = T_S + (T_G - T_S) \left[1 - \frac{Q(Z/|Z_K|, N_I)}{Q(Z_0/|Z_K|, N_I)} \right] - \Gamma (Z - Z_0). \quad (6.38)$$

This modified profile matches the desired temperature properties at the top and the bottom of the profile, while applying a minimal distortion in curvature to accomplish both purposes. That is, the $\Gamma = 9.8$ K/km gradient is a small perturbation at the base but produces the correct asymptotic behavior. Like the original profile of Eq. 6.35, $T_G - T_S < 0$, as is T_* .

Let us then find the explicit form of $Q(\xi)$. We already have a definition for $P(\xi)$. Taking the derivative of this function,

$$\frac{dP}{dZ} = \frac{1}{|Z_K|} \frac{dP}{d\xi} = \frac{1}{|Z_K|} \left[\frac{1}{\xi} - \frac{9}{(1 + 9\xi)^{1/2} + (1 + 9\xi)} \right]. \quad (6.39)$$

Evaluating this derivative at $\xi = Z_I/|Z_K| = N_I$, after a little math,

$$\frac{dP}{dZ} \Big|_{Z=Z_I} = \frac{1}{Z_I} \frac{1}{\sqrt{1 + 9 N_I}}. \quad (6.40)$$

Substituting this definition into Eq. 6.37, Q can be rewritten as

$$Q(\xi, N_I) = P(\xi) - P(N_I) + \frac{(N_I - \xi)}{N_I} \frac{1}{\sqrt{1 + 9 N_I}}. \quad (6.41)$$

This vertical function features a value $Q(Z_0/|Z_K|, N_I)$ that approximately equals $\ln(Z_0/|Z_K|)$, as expected. However, the form of Eq. 6.38 is rather complicated and

can be considerably simplified. This and evaluation of parameters T_A and Z_T of the step-profile function of Eq. 6.30 are the subjects of the next section.

6.5 Simplified Unstable Layer Vertical Model

In this section the calculation of the parameters T_A , Z_A , and Z_T of the step profile model of Eq. 6.30 are described. To evaluate parameters T_A and Z_T , we introduce the integrated squared error:

$$\delta^2 = \int_0^{Z_I} [T_Z - \tilde{T}(Z)]^2 dZ = \int_0^{Z_I} R^2(Z) dZ. \quad (6.42)$$

Taking the derivative of this expression with respect to T_A and Z_T , we obtain the results,

$$T_A = 2T(Z_T) - T_G, \quad (6.43)$$

$$(T_A - T_G) Z_T = \int_0^{Z_T} [T(Z) - T_G] dZ = \int_0^{Z_T} R(Z) dZ. \quad (6.44)$$

Combining these expressions, a transcendental equation emerges that must be solved:

$$[T(Z_T) - T_G] = \frac{1}{2Z_T} \int_0^{Z_T} [T(Z) - T_G] dZ. \quad (6.45)$$

From this function, the ratio $\xi_S = Z_T/|Z_K|$ is solved as a function of $N_I = Z_I/|Z_K|$, as shown by the red line in Fig. 10. This means of solving for Z_T is possible if Eq. 6.45 is rewritten using Eq. 6.38 to transform the term $T(Z) - T_G$ based on the substitution,

$$T_Z - T_G \approx (T_S - T_G) \frac{Q(Z/|Z_K|, N_I)}{Q(Z_0/|Z_K|, N_I)}. \quad (6.46)$$

This approximation is possible when considering the surface layer (i.e., ignoring the Γz term). Then, substituting the RHS of Eq. 6.46 into the integral of Eq. 6.45,

$$[T(Z_T) - T_G] = \frac{1}{2Z_T} \int_0^{Z_T} (T_S - T_G) \frac{Q(Z/|Z_K|, N_I)}{Q(Z_0/|Z_K|, N_I)} dZ \quad (6.47.A)$$

$$[T(Z_T) - T_G] = \frac{1}{2Z_T} \frac{(T_S - T_G)}{Q(Z_0/|Z_K|, N_I)} \int_0^{Z_T} Q(Z/|Z_K|, N_I) dZ. \quad (6.47.B)$$

However, we recognize that having factored $(T_S - T_G)/Q(Z_0/|Z_K|, N_I)$ out of the integral, using Eq. 6.38 a similar factor could also appear on the LHS.

Cancelling these factors out, the resulting equation appears in the form

$$Q(\xi_S, N_I) = \frac{1}{2\xi_S} \int_0^{\xi_S} Q(\xi, N_I) d\xi,$$

where ξ_S clearly appears as a function of N_I .

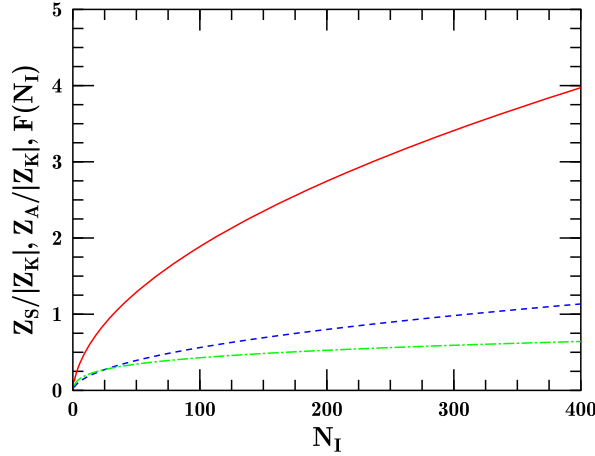


Fig. 10 Ratio $Z_T/|Z_K|$ of surface-layer characteristic thickness (Z_T) to absolute value of Obukhov length ($|Z_K|$) (red line), and ratio $Z_A/|Z_K|$ (dashed blue line), as functions of N_I

Once Z_T is known, $T(Z_T) = T_T$ can be calculated, and T_A follows immediately from Eq. 6.43. Further, because this is a daytime case, $T_T > T_G$. Similarly, $T_A > T_T$, $Z_A < Z_T$, and Z_A may be solved as a function of Z_T :

$$Q(Z_A/|Z_K|, N_I) = 2Q(Z_T/|Z_K|, N_I). \quad (6.48)$$

The function $Z_A/|Z_K|$ may also be expressed in terms of N_I , as plotted in Fig. 10. It is worth noting that while Z_A is of the same order as $|Z_K|$, this analysis and Fig. 10's blue dashed curve further justify the setting of both Z_T and Z_A as separate parameters from $|Z_K|$, since each varies in a slightly different fashion.

For daytime cases, the boundary-layer depth, Z_I , is of the order 1–4 km, and $|Z_K|$ is on the order of 10–40 m. The range of the parameter N_I is thus from 25 to 400. But while Z_T increases with N_I , Z_A remains of the order of $|Z_K|$.

The choice of T_A and Z_T permits us to write the surplus heat present in the surface layer as

$$E_S = \rho_a C_p (T_A - T_G) Z_T. \quad (6.49)$$

This product has dimensions of Joules per square meter of surface area.

The Eq. 6.38 vertical-temperature-profile expression may now be connected back to Paulson's surface-layer profile of Eq. 6.31 by associating T_* of the standard profile with its equivalent in Eq. 6.38. To do so, let us first compare the 2 profiles in their general forms:

$$\begin{aligned} T_Z &= T_S + \frac{T_*}{k} \left[\ln \left(\frac{Z}{Z_0} \right) - \psi_2(-Z/|Z_K|) \right] \\ &\approx T_S + (T_G - T_S) \left[1 - \frac{Q(\xi, N_I)}{Q(\xi_0, N_I)} \right]. \end{aligned} \quad (6.50)$$

Next, let us write the equation for the specific height $Z = |Z_K|$. (Let $T_K = T(|Z_K|)$.) Ignoring the adiabatic term,

$$\begin{aligned} T_K &= T_S + \frac{T_*}{k} \left[\ln \left(\frac{|Z_K|}{Z_0} \right) - \psi_2(-1) \right] \\ &\approx T_S + (T_G - T_S) \left[1 - \frac{Q(1, N_I)}{Q(\xi_0, N_I)} \right]. \end{aligned} \quad (6.51.A)$$

$$\frac{T_*}{k} \left[\ln \left(\frac{|Z_K|}{Z_0} \right) - \psi_2(-1) \right] \approx \frac{(T_G - T_S)}{Q(\xi_0, N_I)} [Q(\xi_0, N_I) - Q(1, N_I)]. \quad (6.51.B)$$

We can use this equation to assess a relation between T_* and the terms on the right. At this point the left and right sides appear distinctly different, but if we examine the difference of the two Q functions on the right, considerable cancellations occur:

$$\begin{aligned} Q(\xi_0, N_I) - Q(1, N_I) &= P(\xi_0) - P(N_I) + \frac{1}{\sqrt{1 + 9N_I}} \left[1 - \frac{\xi_0}{N_I} \right] \\ &\quad - P(1) + P(N_I) - \frac{1}{\sqrt{1 + 9N_I}} \left[1 - \frac{1}{N_I} \right] \\ &= P(\xi_0) - P(1) + \frac{1}{\sqrt{1 + 9N_I}} \left[\frac{1}{N_I} - \frac{\xi_0}{N_I} \right]. \end{aligned} \quad (6.52.A)$$

But $P(\xi_0) \approx \ln(\xi_0)$, since $\psi_2(0) = 0$ and $\xi_0 \ll 1 \approx 0$. And $P(1) \approx -\psi_2(-1)$, since $\ln(1) = 0$, and we assume $\xi_0/N_I \approx 0$. These transformations and approximations thus suggest

$$Q(\xi_0, N_I) - Q(1, N_I) \approx \ln \left(\frac{Z_0}{|Z_K|} \right) + \psi_2(-1) + \frac{1}{N_I \sqrt{1 + 9N_I}}. \quad (6.52.B)$$

Finally, for large N_I , the final term on the right will also be small. The Q difference on the RHS of Eq. 6.51.B is thus equal to the negative of the quantity in brackets on the LHS of 6.51.B.

Cancelling these factors out, what remains is

$$\frac{T_*}{k} \approx -\frac{(T_G - T_S)}{Q(\xi_0, N_I)}. \quad (6.53)$$

And this result allows us to rewrite Eq. 6.50 in the form,

$$T_Z = T_S - \frac{T_*}{k} [Q(\xi_0, N_I) - Q(\xi, N_I)], \quad (6.54.A)$$

or, restoring the adiabatic trend,

$$T_Z = T_S - \frac{T_*}{k} [Q(\xi_0, N_I) - Q(\xi, N_I)] - \Gamma Z. \quad (6.54.B)$$

Writing the formula in this form is important when comparing with results from the nocturnal analysis. The sign of T_* is negative during the day. On the other hand, the Q function is negative value and increasing in magnitude with height. The difference quantity in brackets is then positive, and our function is cast so that the perturbation will be positive definite during the daytime.

Now, the development of Eqs. 6.51 through 6.55 allowed us to remove one instance where T_S appeared. We can next eliminate T_S entirely by evaluating T_Z at $Z = Z_I$.

$$T(Z_I) = T_B(Z_I) = T_G - \Gamma Z_I. \quad (6.55)$$

Substituting this result into the LHS of Eq. 6.55.B and cancelling terms, we find

$$T_G - \Gamma Z_I = T_S - \frac{T_*}{k} [Q(\xi_0, N_I) - Q(N_I, N_I)] - \Gamma Z_I, \quad (6.56.A)$$

$$T_G = T_S - \frac{T_*}{k} Q(\xi_0, N_I), \quad (6.56.B)$$

where we also recognize that $Q(N_I, N_I) = 0$.

We may therefore remove the T_S term from Eq. 6.55.B, replacing it with T_G . Then, using Eq. 6.55,

$$T_Z = T_B + \frac{T_*}{k} Q(\xi, N_I). \quad (6.57)$$

Note that in this section T_* and $Q(\xi, N_I)$ are negative, such that $T_* Q$ is in every instance a positive perturbation. Further, this new profile form disconnects the profile shape from its near-surface details. This is critical since we shall find it easier to determine T_* based on the sensible heat flux than tracking the value of T_S based on a temperature estimated at a specific height within the surface layer.

Before proceeding to consider the nocturnal profile shape, let us pause and consider how we might set this profile given measured data. We see immediately that there are several parameters to consider: T_G , T_* , $\xi = Z/|Z_K|$, and $N_I = Z_I/|Z_K|$. In Tofsted et al. (2006) we estimated Z_I for the White Sands Missile Range region based on data collected locally. For other locales the height of Z_I can be estimated from the ceiling height. The model also computes and tracks this quantity. The daytime model also computes and tracks Z_K . The Obukhov length can also be estimated from measured data from a sonic anemometer. Hence, $Q(\xi, N_I)$ and T_* can be estimated. Further, from a temporal record of the sensible heat flux H_S , it is possible to identify the time of the neutral event (heating reversal). At this time $T_* = 0$ and $T_Z = T_B$ such that T_G can be established.

It is also possible to measure the temperature gradient vertically by sensing $T(Z_2) - T(Z_1)/(Z_2 - Z_1)$ and applying the result to height $\bar{Z} = (Z_2 + Z_1)/2$. The measured temperature gradient can then be assigned to the vertical gradient of Eq. 6.58. After some math, we obtain

$$\begin{aligned} \frac{dT_Z}{dZ} &= -\Gamma + \frac{T_*}{k} \frac{dQ(\xi, N_I)}{d\xi} \frac{d\xi}{dZ} \\ &= \frac{T_*}{k} \left[\frac{1}{\sqrt{1+9\xi}} - \frac{1}{\sqrt{1+9N_I}} \right] \frac{1}{|Z_K|} - \Gamma. \end{aligned} \quad (6.58)$$

Using a sample vertical gradient plus a computed Obukhov length and an evaluated T_* , this equation is actually over-specified. It could therefore be used to validate the choice of $\gamma = 9$.

6.6 Stable Layer Vertical Structure Model

The analysis of the previous section considered daytime atmospheric conditions, $Z_K < 0$. At the time when the atmosphere undergoes thermal reversal, the sign of $T_A - T_G$ reverses from positive to negative. The diabatic daytime analysis then no longer applies and new equations must be developed. As part of this metamorphosis, the temperature-evolution equations were based on buoyant mixing of heated air boiling up through the mixed layer. Stability reversal actively suppresses such buoyant motions, and this dynamic must be replaced as well.

However, the discussion of the current section will focus on the available nocturnal profile form, along with the topic of merging this form with the general adiabatic profile of the boundary layer that transforms into the residual layer after active heating of the layer ceases in the late afternoon until the following morning.

In the previous section, a bulk temperature, T_A , and a characteristic layer thickness, Z_T , were studied so that the net excess energy in the surface layer could be monitored and adjusted. We were also interested in tracking the net rate of convective heat flow into the boundary layer. The boundary layer was characterized by temperature T_G and layer thickness Z_I .

In the nocturnal environment, however, in addition to the residual layer that appears as (roughly) the replacement of the full boundary layer, a surface-based inversion layer also begins to grow. Within this inversion, the temperature is coldest at the ground and increases in temperature through the top of this layer. The inversion temperature thus features a positive temperature gradient up to the inversion top. But then the question is raised regarding the vertical shape of this element of the boundary-layer profile.

To answer this question we need to adopt a new, characteristic depth measure for the inversion layer. Let us call this depth Z_V (as Z_I is already being used to designate the height of the elevated inversion). Let us similarly identify a characteristic temperature of the inversion analogous of T_G . Call this T_V . We define T_V such that the temperature of the inversion at height $Z = 0$ extrapolates to T_V .

It should be emphasized here that the objective of these considerations is not necessarily to find *the truth*, but, rather, to find a working model that is merely an approximation of the atmosphere, not the true dynamics. Nonetheless, even an approximation can be used to supply information regarding radiative fluxes, which is one of our main objects in pursuing this concept of a vertical temperature profile.

In this section, therefore, we consider the characterization of the nocturnal boundary layer using an approach similar to that adopted in the previous section for the daytime diabatic atmosphere. That is, the standard stable flux-profile model is extrapolated to the entire boundary layer by modifying the profile functions in such a way that outside the surface layer the profile approaches the behavior of the standard adiabatic lapse rate; meanwhile, near the surface the profile structure follows that of the generally agreed-upon shape of the flux-profile theory's curves in the surface layer.

The objective, then, is to again make adjustments to the standard profile shapes that introduce only minor corrections at low altitudes, but that cause the profiles to adjust to the appropriate adiabatic behavior at high altitudes (the top of the residual layer). Such corrections leave the surface-layer characterization unchanged from the standard theory.

Unfortunately, what we shall discover is that even when this allowance is made, the standard theory must be adjusted. This is because the profile of the standard theory approaches a constant, positive vertical gradient as one rises above the surface layer. Such a behavior is inconsistent with observations of vertical temperature structure. For example, Stull's data (1988, Figs. 1.11 and 1.12) show a smoothly decreasing vertical gradient of temperature with height, unlike the linear trend of the standard profile's model.

Therefore, let us first consider the standard model, examine the parts of it that are inappropriate for merging into the complete boundary-layer model, and make adjustments as necessary.

As before, we wish to assign a general profile appropriate for the residual layer as described by the vertical function,

$$T_B(Z) = T_G - \Gamma Z. \quad (6.59)$$

The gradient of whatever perturbation function is added to this profile must produce a result that merges into this profile at some point. In particular, let us assume that the height of this merger is Z_V , a height that denotes the top of the surface-based inversion layer.

On the other hand, we have the form used for the standard vertical profile:

$$T_Z = T_S + \frac{T_*}{k} \left[\ln \left(\frac{Z_K}{Z_0} \right) + \ln \left(\frac{Z}{Z_K} \right) - \psi_2 \left(\frac{Z}{Z_K} \right) \right]. \quad (6.60)$$

The standard method for characterizing the nighttime-diabatic-influence function ψ_2 is to use

$$\psi_2(\zeta) = -\beta \zeta = -5 \frac{Z}{Z_K}, \quad (6.61)$$

such that,

$$T_Z = T_S + \frac{T_*}{k} \left[\ln \left(\frac{Z_K}{Z_0} \right) + \ln \left(\frac{Z}{Z_K} \right) + 5 \frac{Z}{Z_K} \right]. \quad (6.62)$$

Here, as for the daytime function, I have separated off the constant factor, $\ln(Z_K/Z_0)$. This offset term may again be absorbed into a general constant.

Now, the first problem with this profile shape is this choice of $\beta \zeta = 5 Z/Z_K$. Notice that if we had chosen to describe the basic inversion layer as having a vertical gradient of, say, Γ_I , that we would need to set this gradient to

$$\Gamma_I = 5 \frac{T_*}{k Z_K}. \quad (6.63)$$

That is, the properties of the surface layer would be directly linked into the properties of the surface-based inversion as a whole. Perhaps this is not a bad thing but nonetheless it means, at the least, that we lose one of our so-called free parameters, either T_* or Z_K , in fitting to the inversion-layer gradient Γ_I .

Worse, we have a constant positive gradient leaving the surface and no mechanism for turning it around to become a negative gradient once the top of the inversion layer is reached.

A second complication with using this profile form is that the daytime surface-layer profile model could be fitted into the overall boundary-layer model, linking the surface layer directly into the rest of the boundary layer. But the standard nocturnal model only links the surface layer into the bottom of the surface-based inversion, meaning a second connection would be needed to connect the result into the residual layer. This seems overly complicated.

For these reasons (and after much agonizing, given the rather widespread use of the standard forms), the original form of this expression was abandoned and a simpler alternative form was adopted, given by

$$T_Z = T_S + \frac{T_*}{k} \left[\ln \left(\frac{Z_K}{Z_0} \right) + \ln \left(\frac{Z}{Z_K} \right) \right]. \quad (6.64)$$

Now, obviously the resulting expression is just equal to an offset plus a $\ln(Z)$ function. So this function is not very interesting. The interesting aspect appears when this form is adapted to a specific height of inversion layer by introducing a \tilde{Q} function tailored to cancel the surface-layer portion not at the top of the boundary layer, but at the top of the inversion layer. In so doing, we shall retain the ability to define T_* and Z_K in the surface layer without losing the ability to model the inversion layer.

For this new form of the surface-layer temperature profile we introduce a new version of the $P(\xi)$ function (with $\xi = Z/Z_K$):

$$P(\xi) = \ln(\xi). \quad (6.65)$$

Using this form, we can now shadow the previous daytime methodology for adapting the surface-layer profile to the boundary layer. The next step is to transform the P function into an analog of the daytime's Q function. As previously, we connect this Q function into the boundary-layer-profile function T_B , but at the height Z_V , not Z_I . Let us then define a new parameter $M_I = Z_V/Z_K$ denoting the

dimensionless height of the surface-based inversion. Given this measure, the analog of Eq. 6.37 is written,

$$Q(\xi, M_I) = P(\xi) - P(M_I) - \frac{\partial P(Z/Z_K)}{\partial Z} \Big|_{Z=Z_V} Z_K (\xi - M_I). \quad (6.66)$$

The derivative of P is $(1/\xi)/Z_K$. Evaluating P at $Z = Z_V$, the derivative becomes $(1/Z_V)$. Multiplying by Z_K yields $(1/M_I)$, so Q reduces to

$$\begin{aligned} Q(\xi, M_I) &= \ln(\xi) - \ln(M_I) - (1/M_I)(\xi - M_I) \\ &= \ln(\xi/M_I) - \xi/M_I + 1. \end{aligned} \quad (6.67)$$

In this form, clearly Q can be represented as the function of a single variable:

$$Q(\xi, M_I) = \tilde{Q}(\xi/M_I); \quad \tilde{Q}(A) = \ln(A) - A + 1. \quad (6.68)$$

The function \tilde{Q} is negative throughout its range, with a maximum of zero at $A = 1$. This negative property is consistent with the Q function obtained in the daytime case. In the process, this expression has been transformed from a function of ξ and M_I to one of only $\xi/M_I = Z/Z_V$, independent of Z_K . (Perhaps this is not unexpected since in the daytime case Z_T addresses the energy characterization of the surface layer, effectively eliminating the need to track Z_K .)

As previously, this function is designed to provide a zero-function value and zero derivative at its upper limit, Z_V . And similar to the daytime version, this function diverges in a log sense as ξ approaches zero due to the $\ln(\xi)$ dependence. Therefore, also similar to the daytime case, the integral can be extended down to $Z = 0$ since $z \ln(z) \rightarrow 0$ as $z \rightarrow 0$. Thus the result will again not be sensitive to its lower bound, as in the daytime case.

The utility of this function is further justified by comparison with the curves in Stull's book (1988, Figs. 1.11 and 1.12). Rather than featuring a flat temperature structure within the inversion layer, Stull's vertical temperature profiles appear to smoothly approach a gradient of zero at the top of the inversion. Figure 11 (next page) illustrates an example of this equation.

The \tilde{Q} function can then be used in an analog of Eq. 6.38:

$$T_Z = \begin{cases} T_S + (T_G - T_S) \left[1 - \frac{\tilde{Q}(Z/Z_V)}{\tilde{Q}(Z_0/Z_V)} \right] - \Gamma (Z - Z_0) & , \quad Z < Z_V. \\ T_G - \Gamma (Z - Z_0) = T_B(Z) & , \quad Z > Z_V. \end{cases} \quad (6.69)$$

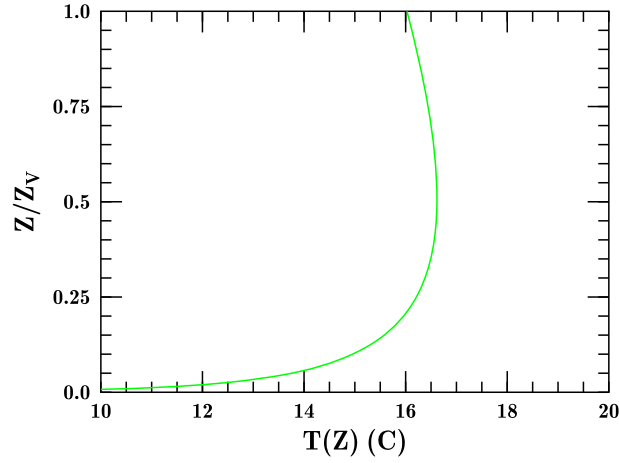


Fig. 11 Inversion-layer-temperature structure for $dT/dZ = 1^\circ\text{C/m}$ at 2 m AGL and a layer thickness of 200 m

Based on this profile, the energy deficit of the surface-based inversion can be calculated. As evident in Fig. 11, the majority of the inversion is located at less than half of the inversion height. Therefore, we shall find that the significance of T_* is such that it influences the full inversion layer.

The energy deficit of the inversion layer can now be integrated. This is determined by first evaluating

$$\int_{Z_0}^{Z_V} (T_Z - T_B) dz \approx \frac{(T_S - T_G)}{\tilde{Q}(Z_0/Z_V)} \int_0^{Z_V} \tilde{Q}(Z/Z_V) dZ. \quad (6.70)$$

Again employing the variable $\xi = Z/Z_V$ and extending the integral to zero,

$$\int_{Z_0}^{Z_V} \tilde{Q}(Z/Z_V) dZ \approx Z_V \int_0^1 \tilde{Q}(\xi) d\xi = Z_V \left[-\frac{1}{2} \right]. \quad (6.71)$$

Therefore, the energy content of the inversion becomes,

$$E_S = \rho_a C_p \int_{Z_0}^{Z_V} (T_Z - T_B) dz \approx \rho_a C_p \frac{(T_G - T_S)}{\tilde{Q}(Z_0/Z_V)} \frac{Z_V}{2}, \quad (6.72)$$

which is negative-valued because $\tilde{Q} < 0$.

Next, let us consider representing E_S using temperature T_A and height Z_T .

Using the crude temperature model of Eq. 6.30 that led to the series of relations in Eqs. 6.42 through 6.45, we can write

$$T_T - T_G = \frac{1}{2 Z_T} \int_0^{Z_T} [T(Z) - T_G] dZ. \quad (6.73)$$

Except for the upper limit of Z_T instead of Z_V , this is the same integral as in Eq. 6.71. We can thus write

$$(T_S - T_G) \frac{\tilde{Q}(Z_T/Z_V)}{\tilde{Q}(Z_0/Z_V)} = \frac{1}{2 Z_T} \int_0^{Z_T} (T_S - T_G) \frac{\tilde{Q}(Z/Z_V)}{\tilde{Q}(Z_0/Z_V)} dZ. \quad (6.74)$$

After cancelling out constant terms,

$$\tilde{Q}(Z_T/Z_V) = \frac{1}{2 Z_T} \int_0^{Z_T} \tilde{Q}(Z/Z_V) dZ. \quad (6.75)$$

Setting $\tilde{\xi} = Z/Z_V$,

$$\tilde{Q}(\xi_S) = \frac{1}{2 \xi_S} \int_0^{\xi_S} \tilde{Q}(\xi) d\xi. \quad (6.76)$$

Integrating using the Maple program,

$$\tilde{Q}(\xi_S) = \ln(\xi_S) - \xi_S + 1 = \frac{1}{2 \xi_S} \left[\xi_S \ln(\xi_S) - \frac{\xi_S^2}{2} \right]. \quad (6.77.A)$$

$$2 \xi_S \ln(\xi_S) - 2 \xi_S^2 + 2 \xi_S = \xi_S \ln(\xi_S) - \frac{\xi_S^2}{2}. \quad (6.77.B)$$

$$\xi_S \ln(\xi_S) = \frac{3 \xi_S^2}{2} - 2 \xi_S \quad \longrightarrow \quad \ln(\xi_S) + 2 = \frac{3}{2} \xi_S. \quad (6.77.C)$$

From which we find 2 roots:

$$\xi_S = 0.1763, 1.6787. \quad (6.78)$$

Selecting the lesser root, since $Z_T < Z_V$,

$$Z_T = 0.1763 Z_V. \quad (6.79)$$

The height Z_A associated with T_A may be computed using the stable layer equivalent of Eq. 6.43 that lead to Eq. 6.48:

$$\tilde{Q}(Z_A/Z_V) = 2 \tilde{Q}(Z_T/Z_V) \longrightarrow Z_A = 0.06326 Z_V, \quad (6.80)$$

For typical inversion-layer depths of 100–400 m, $Z_A = 6$ –25 m, while $Z_T = 18$ –71 m. The height range of Z_A is perhaps slightly higher than that traditionally attributed to the surface layer, but certainly occurs well within the overall inversion layer. Likewise, Z_T clearly lies outside the traditional surface layer, but since it now is being used to represent the energy deficit of the full inversion layer, it too appears reasonable.

The next step is to eliminate T_S and Z_0 from this form. Following the same approach as for the daytime case, we find that

$$\frac{T_*}{k} = \frac{(T_S - T_G)}{\tilde{Q}(Z_0/Z_V)}. \quad (6.81)$$

This result is obtained because the ratio

$$\frac{\tilde{Q}(Z_0/Z_V) - \tilde{Q}(Z/Z_V)}{\ln(Z/Z_0)} = \frac{\ln(Z/Z_0) - (Z/Z_V) + (Z_0/Z_V)}{\ln(Z/Z_0)} \approx 1, \quad (6.82)$$

as long as Z and Z_0 are much less than Z_V . This is clearly true for measurements made in the region typically associated with the surface layer; such as $Z_A \ll Z_V$.

Substituting this definition into the temperature expression,

$$T_Z = \begin{cases} T_S - (T_*/k) \left[\tilde{Q}\left(\frac{Z_0}{Z_V}\right) - \tilde{Q}\left(\frac{Z}{Z_V}\right) \right] - \Gamma(Z - Z_0) & , Z < Z_V. \\ T_G - \Gamma(Z - Z_0) = T_B(Z) & , Z > Z_V. \end{cases} \quad (6.83)$$

Both T_S and Z_0 can now be eliminated. We consider the analog of Eq. 6.56.B, expressing T_S as

$$T_S \approx T_G + \frac{T_*}{k} \tilde{Q}(Z_0/Z_V). \quad (6.84)$$

The vertical temperature-structure model from Eq. 6.83 then transforms into

$$T_Z = T_B + \frac{T_*}{k} \tilde{Q}(Z/Z_V), \quad (6.85)$$

for $Z < Z_V$, and $T_Z = T_B$ for $Z > Z_V$. Recall that $Q < 0$, while $T_* > 0$, such that a proper negative correction term occurs at night.

The Eq. 6.85 temperature formula now supports evaluation of T_A as

$$T_A \approx T_G + \frac{T_*}{k} \tilde{Q}(0.06326) = T_G + T_* \frac{(-1.82376)}{0.385} = T_G - 4.737 T_*. \quad (6.86)$$

Using T_* and Z_V the energy-deficit equation can now be written,

$$E_S = \rho_a C_p \int_{Z_0}^{Z_V} (T_Z - T_B) dz \approx -\rho_a C_p \frac{T_*}{k} \frac{Z_V}{2}. \quad (6.87)$$

An interesting aspect of this analysis is that while we have lost Z_0 , T_S , and Z_K as useful quantities to characterize the surface-based inversion and surface layer, T_* as a scaling temperature still is a meaningful quantity. It should also be emphasized that Z_K at night is often erratic, and the presence of H_S within the equation for Z_K is even more problematic at night since vertical mixing is often shut down by strong, positive vertical temperature gradients. The presence of such effects, though, does not preclude the use of T_* in characterizing the temperature structure, even if it can no longer be related to a turbulent flux of sensible heat.

Instead, assuming the height of the inversion layer, Z_V , is known or can be estimated (based on E_S , perhaps), then T_* could be directly estimated from a measured vertical temperature gradient. Taking the Z derivative of Eq. 6.86,

$$\frac{dT_Z}{dZ} = \begin{cases} (T_*/k) (Z^{-1} - Z_V^{-1}) - \Gamma, & Z < Z_V, \\ -\Gamma, & Z > Z_V, \end{cases} \quad (6.88)$$

which can be used for temperature gradients measured close to the surface in computing the parameter

$$T_* = k Z \left(\frac{dT_Z}{dZ} + \Gamma \right) \left(\frac{Z_V}{Z_V - Z} \right). \quad (6.89)$$

While this form suggests a small Z evaluation height could aid in computing T_* by reducing the Z_V influence, we note that the above has not been considered the foliage displacement-height, which tends to complicate the evaluation of Z itself.

Results of this chapter's structure models provide needed inputs for Chapter 8's long-wave radiation calculations. They also support time-evolution calculations for variables T_A and Z_T , to be discussed in Chapter 9.

7. Cloud and Surface Radiative Effects Modeling

In this chapter the equations used to model the radiative fluxes at the surface are described. To some extent this is a review of material first discussed in Tofsted (1993) with regard to Shapiro's cloud model (1972) of direct and diffuse radiation reaching the ground. Therefore, Section 7.2 is merely an overview of the Shapiro model following an overall review of the various radiation calculations included in the Deardorff (1978) model in Section 7.1. Beginning in 7.3, a new method for handling short-wave radiative reflections in a surface/foilage layer is described. This method is also considered in a slightly modified form to treat infrared fluxes within the surface interface. In the process, the methods used to describe the radiative fluxes are homogenized with the multiple surface methods inferred from the convective-flux calculations.

7.1 Review of Standard Radiation Models

In his groundbreaking 1978 paper, Deardorff brought together a series of methods developed across the research spectrum to compute the surface energy budget. It seems appropriate to review his methodology and then suggest, in follow-on sections, improvements used in the current model.

First, it should be pointed out that Deardorff (1978) provided no details regarding a shortwave solar-radiation model. This is interesting and suggests that he simply used direct measurements of incident solar-irradiation information. He simply assumed a known value for the incident solar radiation above the top of the foliage layer that is denoted by S_{\downarrow} here. He therefore wrote

$$S_{G\downarrow} = (1 - \sigma_F) S_{\downarrow}, \quad (7.1)$$

as the radiation reaching the ground, and

$$S_{G\uparrow} = \alpha_G (1 - \sigma_F) S_{\downarrow}, \quad (7.2)$$

as the radiation reflected at the ground. The difference

$$S_{G\text{net}} = S_{G\downarrow} - S_{G\uparrow} = (1 - \alpha_G) (1 - \sigma_F) S_{\downarrow}, \quad (7.3)$$

thus represents the net rate of solar shortwave radiation absorption at the ground.

Deardorff then modeled the net reflected short-wave radiation as

$$S_{\uparrow} = (1 - \sigma_F) \alpha_G S_{\downarrow} + \sigma_F \alpha_F S_{\downarrow}. \quad (7.4)$$

One might therefore infer that the net flux of short-wave radiation absorbed by the foliage layer should be expressed as

$$S_{F,\text{net}} = \sigma_F (1 - \alpha_G) S_{\downarrow}, \quad (7.5)$$

although Deardorff did not provide an exact equation describing this as such.

In so doing, Deardorff ignored the effects of all multiple reflections from soil and plant surfaces. Deardorff also discounts any reflected radiation from the surface reaching the foliage. Perhaps such assumptions could be valid for stands of cultivated crops, but for relatively uniformly mixed terrain of partial vegetation, foliage–soil interactions should not be ignored. The Tofsted (1993) SEB model simply adopted the Deardorff technique. Here, this method is updated with a more exact solution but using the same assumption of a single vegetated layer used by Deardorff.

Next, consider the method used by Deardorff (1978) to model the surface long-wave radiation flux from the atmosphere. Deardorff writes the net long-wave flux at the top of the foliage layer as

$$R_{L\downarrow} = \left[\sigma_C + (1 - \sigma_C) 0.67 (1670 q_a)^{0.08} \right] \sigma T_a^4, \quad (7.6)$$

where σ_C is the fractional cloud cover, q_a is the atmospheric specific humidity, σ is the Stefan–Boltzmann constant, and T_a is the air temperature in Kelvin. Effectively, then, Deardorff is using a relation of Staley and Jurica (1972) to express the atmospheric emissivity as

$$\epsilon_A = 0.67 (1670 q_a)^{0.08}. \quad (7.7)$$

Now Eq. 7.6 appears to be *wired* incorrectly. That is, infrared emissions from the humid atmosphere occur from molecules within a relatively short distance: Radiation reaching the ground arises from molecules within approximately only the first 10 m above ground! Beyond that distance, due to absorption effects, air molecules within the first 10 m tend to nearly completely absorb infrared energy emitted by molecules farther from the surface. Hence, it should be that

the atmospheric emissivity is the restricting factor on the near-blackbody radiation emerging from the cloud base, and not the fractional cloud cover that scales the atmospheric band emissions of the near-surface atmosphere. Thus, instead, the relation,

$$R_{L\downarrow} = \epsilon_A \sigma T_a^4 + (1 - \epsilon_A) \sigma_C \sigma T_c^4, \quad (7.8)$$

is used, whereby the effect of the near-surface air emissivity is such that it filters the incident longwave energy arising from the cloud base associated with the temperature T_c . In the process a new variable must be assessed (T_c), yet from the input parameters a reasonable guess can be obtained for this temperature based on the temperature of the top of the boundary layer plus a guess as to the height of the cloud base.

The more significant unknown to be addressed regarding the infrared radiation is the appropriate form for modeling the atmospheric emissivity, ϵ_A . One notes that the expression for ϵ_A given in Eq. 7.7 approaches zero at zero atmospheric humidity. Hence, we know that this form ignores the effects of carbon dioxide (as well as oxygen, nitrogen, and all other dry gases). This suggests at a minimum a reanalysis of atmospheric emissivity is needed. This will be developed in Section 7.6, but first a model of the radiative interactions within the surface interface will be developed in Sections 7.3–7.5. This analysis will determine the apportionment of energy between the soil and foliage surfaces, as well as consider visible direct and diffuse radiation and long-wave radiation flowing from the ground, foliage, and atmosphere.

7.2 Shapiro's Cloud Model

Shapiro (1972; 1982) constructed an empirical model based on reported radiation data from a series of ground stations along with correlated cloud condition reports. The model consisted of 3 cloud layers where absorption, transmission, and reflection coefficients were estimated for each layer along with a ground-haze effect. Each cloud layer computed the reflection (R_k), transmission (T_k), and absorption (A_k) coefficients which satisfied the condition

$$R_k + T_k + A_k = 1, \quad (7.9)$$

for the k th layer, guaranteeing conservation of energy. Shapiro's model was based on observed weather conditions and Eppley radiometer outputs of net solar radiation received under those conditions. Shapiro based his model on solar elevation to produce tabulated data sets for different clouds in each indicated cloud layer.

The choice of cloud types and layer locations has been approximated in the cloud model of the current program to simplify the input; however, the model could be expanded to accommodate increased information availability by the user since the full Shapiro model has been incorporated into the program, including the data sets of all possible cloud conditions. Currently, the user is only permitted to select a single cloud layer's elevation and a single cloud type (cumulus, stratus, or cirrus).

For a given cloud type and height the Shapiro model uses the computed solar elevation to interpolate reflectance, transmittance, and absorption information from the tabulated database. Once the layer data have been interpolated, the Shapiro method uses the equivalent surface albedo to compute the net downward radiation at the top of the surface interface, S_{\downarrow} .

As his database Shapiro used the SOLMET station network of radiation-data collected at 26 sites scattered throughout the continental United States. Shapiro's database also included precipitation impacts; however, from the standpoint of an optical turbulence evaluation, once precipitation begins it is considered a dominant effect and would either completely or effectively decrease the turbulence impacts to the level that a calculation would be unnecessary.

Shapiro considered cloud types as consisting of Thin Cirrus or Cirrostratus, Thick Cirrus or Cirrostratus, Altostratus or Altostratus, Stratocumulus or Stratus, and Cumulus or Cumulonimbus. Effects were classified according to the cosine of the zenith angle of the sun by increments of 0.10 from 0.05 to 0.95.

The Shapiro model calculated the net downward radiation flux through use of a multiple scattering computation between the different cloud layers, the haze layer, and the surface. In implementing this model, the net surface reflectance is evaluated using a multiple scattering approach described in Sections 7.4–7.6. However, the model's haze-layer parameterization has been disabled, due to complications over the maximum (10 km) visibility reported at airports. (Low humidity sites that feature high turbulence often see visibilities much higher than 10 km.)

In the model's code, the Shapiro cloud model is encapsulated in a single subroutine that is called any time the sun is above the horizon. Input cloud information is translated into formats associated with the Shapiro model, including cloud fractions and types in each layer and solar elevation.

For further details on the Shapiro model, the reader is directed to the original documentation.

7.3 Foliage Layering Model

In this and the next 2 sections the basic Deardorff method for handling the effects of a foliage layer on radiative fluxes will be examined and updated. As was pointed out in Section 7.1, the Deardorff approach does not include any feedback effects due to multiple reflectances between the foliage layer and the ground surface. There also appears to be a consistency issue with regard to this apparent contradiction: In the convective exchange model the foliage-surface area is assumed to exceed the area of underlying surface by a factor of 7.0, while the radiative model relies on a flat 2-sided, semitransparent layer whose multiplying factor is thus only 2.0. To resolve this inconsistency, several steps must be examined. The first step is to construct a consistent model of the foliage layer that produces realistic values for the surface area's multiplying factor. Once this foliage model is developed (Section 7.3), including a leaf-orientation distribution model, a foliage model can be constructed based on multiple foliage sublayers. Calculations of reflection, absorption, and transmission can then be performed for a single sublayer (Section 7.4), and then full model calculations can be performed (Section 7.5).

The main Deardorff inconsistency apparently is connected to the assumption that for a given value of σ_F , the fractional underlying surface covered by the foliage, the leaf surfaces are simply assumed to be flat and parallel to the underlying ground surface in the radiation model, but not in the convective flux model. But, in general, the leaf surfaces will exhibit random orientations to the ground. Therefore, a new model is developed in this section to account for these differences. The result is that the surface interface will exhibit different reflectance and transmission properties relative to radiation flowing through the layer in different directions. In particular, this will produce a solar-zenith-angle dependence that was not previously modeled as well as altering the diffuse scattered and transmitted radiation factors from values used previously.

To model the effect of random orientation of the leaf surfaces, we first note that each leaf has 2 surfaces for every surface oriented in the proper direction to receive incident radiative flux energy. Therefore, the relative area of leaf surface per area of underlying surface covered (σ_F) is always at least $N_F = \Upsilon_F \sigma_F \geq 2 \sigma_F$. We further recognize that there are 2 other parameters of interest: α_G , the soil albedo, and α_F , the foliage albedo, both with respect to directly incident radiation.

To develop this model, several simplifying assumptions are first made. Reflections off either the ground or leaf surfaces will be considered Lambertian: where the emerging radiance is a constant, and the resultant irradiance is proportional to the cosine of the angle due to the relative cross section of the source being reduced for directions off the normal to the surface. Second, transmittance through leaves will also be considered to emerge in a Lambertian form as well. Third, each leaf will be considered to be flat, consisting of a single normal vector associated with the appropriately directed leaf surface. Fourth, each leaf will be assumed to have a uniformly random orientation relative to the vertical axis. While this condition ignores sun-tracking (phototropic) plants, it simplifies the calculations considerably and accounts for many types of plants.

Based on this fourth assumption, it is relatively easy to visualize the probability density function of the leaf orientations. It is such that the distribution of the leaf normal vectors perpendicular to the sides of the leaves, when considering downward-flowing radiation, will be evenly distributed over the upper hemisphere. If we define as 1.0 the square area of the circle that lies underneath said hemisphere, then the total area of the upper surface of said hemisphere must equal 2.0. This is developed mathematically in the following discussion:

Let the normal vector to a given leaf be described by a unit vector whose orientation is described by variables θ (zenith angle) and ϕ (azimuth angle) oriented in the upper hemisphere.

It is common to write vectors in a Cartesian system, denoting a triplet (x, y, z) as the components of such vectors, where the $+z$ axis is oriented in the vertical direction. For unit vectors, $x^2 + y^2 + z^2 = 1$. For integration purposes the standard, spherical-polar angle system will be adopted. Let θ be the angle of a unit vector measured relative to the $+z$ axis, and let ϕ equal the azimuthal angle measured counterclockwise in the $x - y$ plane from the $+x$ axis, initially increasing toward the $+y$ axis. Then, a given unit vector can be expressed as

$$\hat{\Omega} = (\cos(\phi) \sin(\theta), \sin(\phi) \sin(\theta), \cos(\theta)). \quad (7.10)$$

The solid angle, $d\Omega$, about a unit vector $\hat{\Omega}$ is then designated by

$$d\Omega = \sin(\theta) d\theta d\phi. \quad (7.11)$$

For the uniform orientation distribution, for any given upward-directed unit vector $\hat{\Omega}$, the probability of leaves being oriented in that direction $dP = d\Omega/(2\pi)$ is equal in all directions. This is shown through the following integral:

$$\int dP = \int_H \frac{d\Omega}{2\pi} = \int_0^{2\pi} d\phi \int_0^{\pi/2} d\theta \sin(\theta) \frac{1}{2\pi} = 1, \quad (7.12)$$

where the solid-angle integral is performed over the upper hemisphere (H).

On the other hand, the overall surface area covered by such a distribution is measured by foreshortening the surface area subtended by any given leaf according to the cosine of its orientation with respect to the vertical direction. This is evaluated via the integral:

$$\int \cos(\theta) dP = \int_H \cos(\theta) \frac{d\Omega}{2\pi} = \int_0^{2\pi} d\phi \int_0^{\pi/2} d\theta \sin(\theta) \cos(\theta) \frac{1}{2\pi} = 1/2. \quad (7.13)$$

In this model there is thus twice as much upper-leaf-surface area as the underlying surface area covered, and 4 times as much surface area overall when including the lower-leaf surfaces, meaning $N_F = 4 \sigma_F$.

For this distribution Υ_F appears to equal 4.0. However, this value is obviously less than the reported nominal value $\Upsilon_F = 7$ (Monteith et al. 1965; Allen and Lemon 1972) used by Deardorff. To obtain larger values, recall first that Υ_F is defined as the ratio N_F/σ_F in Eq. 2.21.B, yet based on the immediately preceding development a single foliage layer could never produce this observed behavior.

Therefore a multilayer foliage model must be developed, but the means of describing such a model requires several further considerations. First, let us assume that leaves in different layers will not be correlated with one another. That is, the positions of individual leaves in separate layers are assumed independent. Consider a plant canopy consisting of several such independent layers, each of equal foliage density. Call this density σ_{Fm} , where there are M total layers. For example, if there were 3 layers ($M = 3$), then the total foliage-surface area per square underlying surface would be just the sum of the surface area in the 3 layers, or,

$$N_F = \sigma_{F1} \Upsilon_{F1} + \sigma_{F2} \Upsilon_{F2} + \sigma_{F3} \Upsilon_{F3}. \quad (7.14)$$

For simplicity, the orientation of the leaves can be assumed constant and equal in each layer, such that $\Upsilon_{Fi} = 4$. Also, for simplicity, the amount of foliage can be

modeled as equipartitioned between the different layers, such that $\sigma_{Fm} = \sigma_s$, a single value characterizing all of the sublayers. Hence, in this model,

$$N_F = 12 \sigma_s. \quad (7.15)$$

Next, since the leaves in each layer are distributed randomly, the overlap of the leaves between the different layers will also be random. The probability of a clear, vertically drawn line of sight through a given layer becomes $(1 - \sigma_s)$. Then, the probability of seeing through all M layers becomes $(1 - \sigma_s)^M$. So, based on the definition of σ_F ,

$$(1 - \sigma_F) = (1 - \sigma_s)^M. \quad (7.16.A)$$

$$\sigma_s = 1 - (1 - \sigma_F)^{1/M}. \quad (7.16.B)$$

Then the total foliage-surface area per unit of underlying surface becomes

$$N_F = N_F(M) = 4 M \sigma_s = 4 M \left[1 - (1 - \sigma_F)^{1/M} \right]. \quad (7.17)$$

In the limit, as the number of layers increases, the leaf fraction in each layer is reduced and a limiting behavior emerges:

$$N_{F\infty} = N_F(M)|_{\lim M \rightarrow \infty} = -4 \ln(1 - \sigma_F), \quad (7.18.A)$$

leading to a result in a familiar form,

$$1 - \sigma_F = \exp(-N_{F\infty}/4). \quad (7.18.B)$$

From this result, one may express the function,

$$\Upsilon_{F\infty} = \frac{N_{F\infty}}{\sigma_F} = -4 \frac{\ln(1 - \sigma_F)}{\sigma_F}. \quad (7.19)$$

This function begins at 4.0 for $\sigma_F = 0$ and increases steadily. Interestingly, $N_{F\infty} = 4.8$ at $\sigma_F = 0.7$, such that $\Upsilon_{F\infty} \approx 7$ at this point. Coincidentally, while Deardorff cites this factor of 7, the studies he compared to and his computations were made with $\sigma_F = 0.75$. Yet, from these relations it is clear the point $\Upsilon_F \approx 7$ is simply one point along a continuum of behavior.

In other words, it appears that using a constant Υ_F was simply a convenient approximation developed by the energy-budget-modeling community to describe

the primary behavior of the cultivated crops studied. But in more general cases, such as fallow fields and desert regions where σ_F varies significantly from the cultivated norm, the standard value would not be appropriate.

In the model developed here, N_F will be identified with $N_{F\infty}$ and Υ_F with the $\Upsilon_{F\infty}$ expression above. However, since $N_{F\infty} \rightarrow \infty$ as $\sigma_F \rightarrow 1$, σ_F will be restricted in range ($\sigma_F \leq 0.975$) to avoid these limiting cases. To check whether this is a reasonable upper limit for this variable, consider a set of circular trees that are nonoverlapping, but touching along their outer edges, whose leaves fall within cylinders of equal radius about their trunk centers. If each tree has a radial extent of 1.0, then an equilateral triangle connecting the centers of 3 adjacent trees will have sides of length 2.0, with each tree subtending $\pi/6$ of the center-to-center triangle, such that the net footprint of the 3 trees is $\pi/2$ of the full triangle of net area $\sqrt{3}$. The net foliage fraction is then $\pi/(2\sqrt{3}) \approx 0.9069$. The chosen maximum therefore exceeds this case and should be sufficient for any reasonable foliage situation.

However, an infinite-layer model is merely a mathematic construct — it cannot be implemented in software. But as illustrated in Fig. 12, low-order layer models are insufficient to account for the infinite-layer model's N_F behavior. Therefore, a 100-layer model was selected since it tracks the infinite-layer model's behavior up to large σ_F values.

Because the behavior of the infinite-layer model will be considered the standard of comparison, the nomenclature will now be simplified to remove the infinity symbols; whenever N_F and Υ_F are used hereafter, it is implied that we intend $N_{F\infty}$ and $\Upsilon_{F\infty}$.

Next, notice that from Eq. 7.16.B the quantity $(1 - \sigma_s)$ expresses the transmittance factor for radiation passing vertically through the leaf layer without intercepting one of the leaves. This transmittance expression abets the transitioning of the discussion to consideration of radiative-transfer processes involving light passing through the leaf sublayer model from zenith angles (angles relative to the vertical axis) other than zero (directly downward). Let θ_R be a zenith angle of light passing through the foliated layer. And let $\mu = \cos(\theta_R)$.

The length of the scattering path through a finite-thickness leaf layer is then longer by the factor $1/\cos(\theta_R)$ compared to radiation passing vertically through the layer.

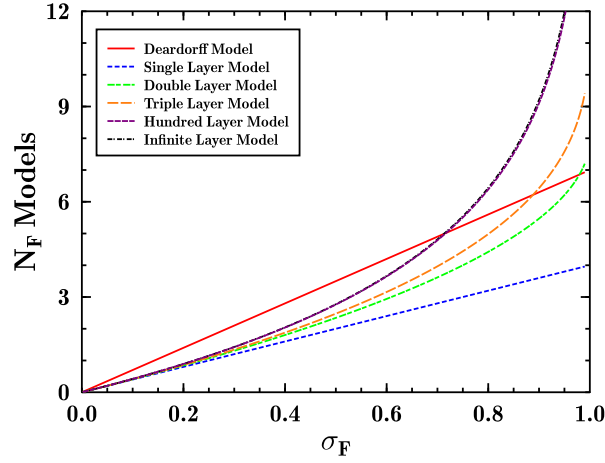


Fig. 12 Various models of N_F dependence on σ_F comparing Deardorff constant Υ_F dependence versus multilayer model dependencies and infinite-layer dependence

In this case the transmittance factor through the whole foliage layer becomes

$$T(\theta_R) = \exp[-N_F \infty / (4\mu)] = (1 - \sigma_F)^{1/\mu}. \quad (7.20)$$

Thus, even for foliage layers with low σ_F , incident direct sunlight will always become effectively cut off beyond some angle due to shadowing of the ground by the leaf layer. The greater σ_F becomes, the more rapidly the light is cut off as θ_R increases.

This transmittance term fully describes the effect of the leaf layer on the direct radiation-transmission component. What remains is a series of results involving radiation that is reflected from foliage or transmitted through the leaves. However, before engaging in these analyses, let us summarize the results of the current section.

While Deardorff's approach assumed one could fix the value of Υ_F at 7.0, regardless of the value of σ_F , the results of the current section reveal, first, that more than one layer is required to obtain this 7.0 figure and, second, that when the placement of leaves in multiple, randomized foliage layers is considered, then the value of Υ_F becomes dependent on the overall fractional foliage cover σ_F . Moreover, we have seen that σ_F also guides the overall, transmittance factor of direct radiation passing through the foliage layer, but this effect is now also a function of the solar-zenith angle.

As a consequence, we have found that both N_F and Υ_F are functions of σ_F . Or, to express this concept slightly differently, because the leaf positions in different layers are decorrelated, the net σ_{Fi} in each layer is less than σ_F , such that the leaf surface does not scale linearly with σ_F .

A single-layer model thus plots along a maximum linear relation of $4\sigma_F$, but this line is insufficient to explain observed N_F dependence. Because of this limitation, it was necessary to consider extra layers. But, these extra layers require a multilayer canopy model to describe radiative interactions much more complex than those considered by Deardorff.

This also illustrates fairly clearly that the canopy results commonly published, involving the assumed $N_F = 7\sigma_F$ behavior, would tend to overpredict the impact of foliage for thinner foliage canopies and would tend to underpredict the impacts of canopies with $\sigma_F > 0.7$.

In desert conditions normally σ_F values are relatively small ($0.1 \leq \sigma_F \leq 0.2$), producing Υ_F values close to 4. These will now predict surface effects more heavily weighted toward soil fluxes than those previously obtained. Such a model would seem to be consistent with the natural dispersion of desert plants, where the first seeds to sprout take up the available water supply. Nonetheless, certain desert vegetation, such as mesquite bushes, challenge this model and typically represent concentrations of dense, localized leaves that also can alter the shape of the very terrain itself through the accretion of hummocks of dirt at their bases, trapping the dust of many wind events.

7.4 Foliage Sublayer Reflectivity and Emissivity Model

Based on the layered foliage model posited in the previous section, a new connection can be developed between the observed additional surface area of foliage and the statistics of light propagating vertically through a multilayered foliage canopy with a uniform leaf-orientation distribution model. This process was begun in the previous section for the relatively simple calculation of the proportion of direct radiation that can pass through a layer. Still to be resolved are the details of various forms of diffuse radiation propagating through a foliage layer. In this section the first stage of that resolution process is considered by computing the reflective and transmissive properties of the randomly oriented leaf model. These results

are analyzed via integral techniques for direct scatter from the leaf-orientation distribution; then, further integration to determine the scatter/transmission of direct radiation; and, finally, the resolution of direction-averaged, *stream*-wise, upward- and downward-flowing radiation fields.

The first step in resolving these effects of reflection and transmission requires a detailed analysis of the scattering and reflective properties of a single leaf oriented in a specific direction to the direction of the incident light. Once the properties of an individual leaf have been resolved, the mean properties of a foliated layer can be evaluated through integration over the leaf-orientation distribution.

Let us designate by the unit vector $\hat{\Omega}$ the specific orientation of the upper surface of a leaf designating a vector normal to the otherwise flat surface of a leaf. If the upward direction is indicated as the positive z axis in a standard (x, y, z) Cartesian coordinate system, then the positive z axis is associated with the vector triplet $(0, 0, 1)$. For a given leaf, since the leaf distribution considered is uniform in direction, the scattering properties of a general leaf can be analyzed by selecting specific input and output directions for energy flows that exploit the symmetries of this system. Let us call $\hat{\Omega}_i$ the direction of incidence of incoming radiation, where $\hat{\Omega}_i$ points into the direction of the incoming radiation. Second, designate by $\hat{\Omega}_s$ the direction into which radiation is leaving following scattering from the leaf surface (i.e., the scattering direction).

To simplify the mathematics, let us consider for computational purposes that the incident radiation is approaching the leaf from the zenith direction $\hat{\Omega}_i = (0, 0, 1)$. Also, let us place the leaf at the origin of coordinates. This simplifies the calculation of the scattering statistics. Symmetry of the leaf-orientation distribution also guarantees that the scattering results, after integrating over the leaf distribution, will be independent of the azimuth of the outgoing radiation. Therefore, the scattering direction $\hat{\Omega}_s$ may be chosen to lie in the $x - z$ plane (the scattering azimuth is zero).

The probability that a random photon propagating vertically downward from incident direction $\hat{\Omega}_i$ will encounter a leaf whose normal vector is $\hat{\Omega}$ can then be expressed as just the uniform leaf-orientation probability $dP = d\Omega/(2\pi)$ times the foreshortened area of the leaf (proportional to $\cos(\theta)$):

$$dP_{L\theta} = \cos(\theta) d\Omega = \sin(\theta) \cos(\theta) d\theta d\phi. \quad (7.21)$$

This result is, of course, conditioned upon the event that a leaf was actually struck as the photon passed through the foliage layer.

To better understand this, let us dimensionalize the calculation: Consider an infinitesimal leaf-surface area dA . Let I represent the photon flux arriving at the leaf from the zenith incident irradiation direction $+\hat{z}$ (in photons per second per meter-squared area that would otherwise impinge upon the underlying ground surface oriented perpendicular to the direction of the streaming incident photons).

For a leaf of orientation $\hat{\Omega}$, the number of photons striking dA per second will be

$$dF = I dA \cos(\theta). \quad (7.22)$$

For underlying ground-surface area S and relative leaf-layer cover σ_{Fi} , if the leaves were removed the net flux per area S would be $I S$. But, due to the leaves, only $I S (1 - \sigma_{Fi})$ photons reach the ground unscattered per second. So, the portion of photons scattered, transmitted, or absorbed by the leaf-layer must be $I S \sigma_{Fi}$.

From the development of the previous section, we recognize that $\sigma_{Fi} S$ is just the surface under the leaves. And, due to the leaf-orientation-distribution model chosen, the total area of upper-leaf surfaces exposed to the radiation must be $\sigma_{Fi} A$, where $A = 2S$. Therefore, dA can be directly connected to $d\Omega$ or dP via

$$dA = 2S d\Omega / (2\pi) = 2S dP, \quad (7.23)$$

such that $\int dA = 2S$. That is, the integrations have been normalized so that only the radiation that strikes the foliage is being considered.

Let us assume the leaves are Lambertian reflectors. While this is not exactly true, it still provides an improvement over the Deardorff model. Let α_F be the reflectivity coefficient of the foliage. For a Lambertian reflector the radiation appears to exhibit equal radiance in all scattering directions, but the apparent area of the scattering surface is reduced according to the cosine of the scattering direction relative to the normal to the scattering surface, denoted by the angle γ . The normalization constant for this distribution of scattered energy is obtained by integrating over all scattering directions:

$$X = 2\pi \int_0^{\pi/2} \cos(\gamma) \sin(\gamma) d\gamma = \pi. \quad (7.24)$$

Hence, we divide the incoming energy by π to determine the outgoing photon flux in direction γ relative to the surface normal:

$$dR = \alpha_F I dA \cos(\theta) \cos(\gamma)/\pi, \quad (7.25)$$

where dR is the differential radiance in the outbound direction. This resulting quantity measures the rate of photon flow per second per steradian.

To better quantify this result, consider the output direction,

$$\hat{\Omega}_s = (\sin(\psi), 0, \cos(\psi)). \quad (7.26)$$

The normal to the surface dA is specified by

$$\hat{n}_{dA} = (\sin(\theta) \cos(\phi), \sin(\theta) \sin(\phi), \cos(\theta)). \quad (7.27)$$

The cosine of the angle between the outbound radiation vector and the surface normal thus becomes

$$\cos(\gamma) = \hat{n}_{dA} \cdot \hat{\Omega}_s = \sin(\psi) \sin(\theta) \cos(\phi) + \cos(\psi) \cos(\theta). \quad (7.28)$$

Only positive incident energy contributions are permitted when computing the reflected radiation, such that $\cos(\theta) > 0$, requiring $0 < \theta < \pi/2$. Second, only positive $\cos(\gamma)$ contributions are permitted for the reflected radiation, as well.

For $\psi < \pi/2$, there will be a region $0 < \theta < \theta_c$ where the entire range of ϕ produces positive cosines. This region is limited by

$$\cos(\psi) \cos(\theta_c) - \sin(\psi) \sin(\theta_c) = 0; \quad (7.29.A)$$

$$\cos(\psi - \theta_c) = \cos(\theta_c - \psi) = 0; \quad (7.29.B)$$

$$\theta_c - \psi = \pi/2; \quad \longrightarrow \quad \theta_c = \pi/2 - \psi. \quad (7.29.C)$$

Beyond the value of θ_c , for each value of θ the range of ϕ is given by $-\phi_x < \phi < +\phi_x$, where the cosine equals zero at the limits:

$$\sin(\psi) \sin(\theta) \cos(\phi_x) + \cos(\psi) \cos(\theta) = 0; \quad (7.30.A)$$

$$\cos(\pm\phi_x) = -\frac{1}{\tan(\psi) \tan(\theta)}. \quad (7.30.B)$$

Here, because $\tan(\theta)$ becomes infinite at $\theta = \pi/2$, the limits of ϕ_x always become $\pm\pi/2$ at the limiting edge of the integration region (because a leaf oriented at an angle $\theta > \pi/2$ cannot receive downward incident radiation on its upper surface). However, this result is only useful for $\psi < \pi/2$ itself. For a scattering direction in the lower hemisphere ($\psi > \pi/2$), there will exist a minimum angle θ_m below which there will be no contribution:

$$\theta_m = \psi - \pi/2. \quad (7.31)$$

Beyond this minimum, there will be a region of integration in ϕ_x beyond which the cosine will become negative:

$$\sin(\psi) \sin(\theta) \cos(\phi_x) + \cos(\psi) \cos(\theta) = 0; \quad (7.32.A)$$

$$\cos(\pm\phi_x) = -\frac{1}{\tan(\psi) \tan(\theta)}. \quad (7.32.B)$$

This is the same result as before, except that in the former case $\tan(\psi)$ was greater than zero, so $|\phi_x| > \pi/2$. Here, $\tan(\psi) < 0$, so $|\phi_x| < \pi/2$.

Let us then determine the net scattered radiation, R , arising from all possible leaf orientations that contribute (i.e., from the full surface, A , of the leaves). We then divide by the total underlying surface, $S = A/2$, as a normalization step. By further dividing by the factor α_F and the incident flux I , the resulting function will represent a probability distribution of scattering in the given direction:

$$P_{\text{scat}}(\psi) = \frac{R/S}{\alpha_F I} = \frac{1}{S} \int_A dA \cos(\theta) \cos(\gamma)/\pi; \quad (7.33.A)$$

$$P_{\text{scat}}(\psi) = \frac{1}{\pi} \iint d\theta d\phi \sin(\theta) \cos(\theta) \cos(\gamma)/\pi; \quad (7.33.B)$$

where the integration over the leaf surfaces has been replaced by an integration over the distribution of surface normals of the surface elements. The remaining step is to expand the $\cos(\gamma)$ term using the expression in Eq. 7.28, along with the integration limits described. These steps are accomplished in an implementing numerical-integration routine. Based on the geometry, we recognize that for incident radiation from above, the downward-scattered radiation, $P_{\text{scat}}(\pi)$, must equal zero. Conversely, $P_{\text{scat}}(0)$, the backscattering case, must represent a maximum return, and $\cos(\gamma)$ reduces to just $\cos(\theta)$, simplifying the math.

For the backscattering case,

$$\begin{aligned}
 P_{\text{scat}}(0) &= \frac{1}{\pi^2} \int_0^{2\pi} d\phi \int_0^{\pi/2} d\theta \sin(\theta) \cos^2(\theta); \\
 &= \frac{2}{\pi} \int_0^{\pi/2} d\theta \sin(\theta) \cos^2(\theta) = \frac{2}{3\pi} \approx 0.2122.
 \end{aligned} \tag{7.34}$$

Based on this result, the $P_{\text{scat}}(\psi)$ numerical integration results have been plotted in Fig. 13 in a normalized form by dividing through by the factor $2/(3\pi)$.

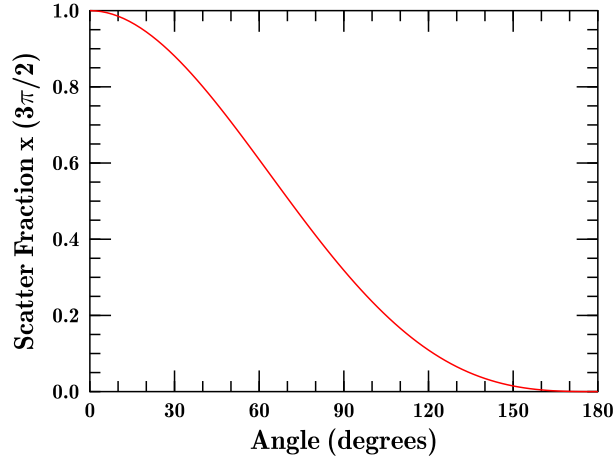


Fig. 13 Scaled and normalized reflection function $P_{\text{scat}}(\psi)/[2/(3\pi)]$

Since Eq. 7.33.B is a general rule for calculating a reflection-distribution function, like the phase functions of radiative transfer theory, this function will satisfy the normalization condition,

$$2\pi \int_0^{\pi} P_{\text{scat}}(\psi) \sin(\psi) d\psi = 1. \tag{7.35}$$

However, like a phase function, $P_{\text{scat}}(\psi)$ only characterizes scattering from a specific direction into a chosen direction. The results thus only characterize outputs evaluated as though falling onto a surface perpendicular to the direction of propagation of the scattered energy, $\hat{\Omega}_s$. To use this function in the model, this equation must be integrated out to determine the net scatter of radiation from the leaf-layer into upward- and downward-directed hemispheric radiation flow *streams*.

To do so, one applies $P_{\text{scat}}(\psi)$ in another integral over each hemisphere and weighs the contribution in each scattering direction according to the cosine of the radiation

in the corresponding direction (either $+\hat{z}$ for upward-directed radiation or $-\hat{z}$ for downward-flowing radiation).

To perform this computation, one must first define a quantity $I' = I \cos(\theta_R)$ describing the vertical component of the energy flux of incident radiation as it arrives at the scattering layer. Here θ_R is again the zenith angle of the approaching light relative to the normal axis of the scattering layer ($\pm\hat{z}$). For direct shortwave radiation this will be given by the solar-zenith angle. However, following this stage, a further step will be used to integrate over complete hemispheres of input streaming radiation to determine the scattering of diffuse radiation into upward- and downward-directed streams.

Second, to determine the net stream-wise fluxes of radiation, a small test patch of foliage is placed at the origin of coordinates and oriented so that the normal to this patch is in the $+\hat{z}$ direction. The net vertical flux returned from this patch can be evaluated by integrating over the upper hemisphere of radiation emerging from the patch and determining its contribution in the $+\hat{z}$ direction (or $-\hat{z}$ for the radiation scattered into the downward hemisphere).

Let us define a direction $\hat{\Omega}_R$ to describe the unit vector pointing into the direction of the incident direct radiation, using angles θ_R and ϕ_R in the usual sense. For radiation scattered from the surface patch into a direction designated by a scattering unit vector $\hat{\Omega}_s$ with angles θ_s and ϕ_s , let us assign the solid angle subtended about this direction as

$$d\Omega_s = \sin(\theta) d\theta d\phi. \quad (7.36)$$

The number of photons directed in the $\hat{\Omega}_s$ direction is

$$\alpha_F I' dA_F P_{\text{scat}}(\hat{\Omega}_R \cdot \hat{\Omega}_s) d\Omega_s, \quad (7.37)$$

where dA_F is the differential scattering surface area, such that $\alpha_F I' dA_F$ is the total number of scattering photons, as guaranteed by the integral over all scattering directions indicated in Eq. 7.35.

The net vertically upward directed flux is thus,

$$F_{\uparrow}(\theta_R) = \int_0^{2\pi} d\phi_s \int_0^{\pi/2} \alpha_F I' dA_F P_{\text{scat}}(\hat{\Omega}_R \cdot \hat{\Omega}_s) \cos(+\theta_s) \sin(\theta_s) d\theta_s. \quad (7.38.A)$$

The downward directed flux is,

$$F_{\downarrow}(\theta_R) = \int_0^{2\pi} d\phi_s \int_{\pi/2}^{\pi} \alpha_F I' dA_F P_{\text{scat}}(\hat{\Omega}_R \cdot \hat{\Omega}_s) \cos(-\theta_s) \sin(\theta_s) d\theta_s. \quad (7.38.B)$$

Dividing F_{\uparrow} through by $\alpha_F I' dA_F$ produces the vertical component of the relative flux of photons for the incident angle of radiation θ_R . A similar calculation can be performed for downward-directed radiation. Let these reflected-radiation terms be identified as

$$R_U(\theta_R) = F_{\uparrow}(\theta_R)/(\alpha_F I' dA_F); \quad (7.39.A)$$

$$R_D(\theta_R) = F_{\downarrow}(\theta_R)/(\alpha_F I' dA_F). \quad (7.39.B)$$

For the uniform leaf distribution described, results are plotted in Fig. 14 that divide the reflected radiation into an upward-directed stream (red line), a downward-directed stream (blue line), and a combined reflection total (green line) based on the incidence angle of the available direct radiation given by the zenith angle varying from zero (straight downward light source) to horizontal radiation (arriving from the horizon).

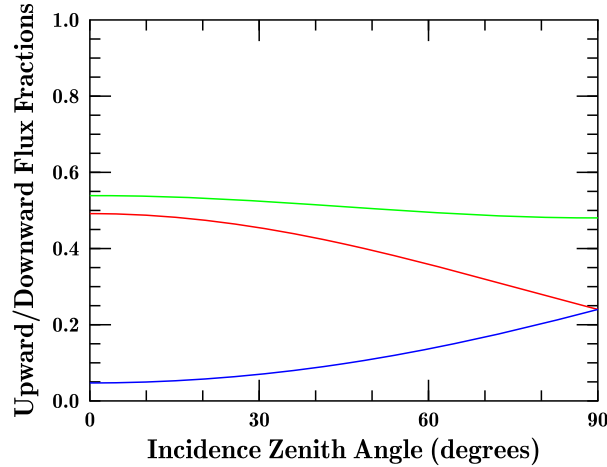


Fig. 14 Upward- and downward-integrated scattering-probability plots as functions of incident radiation's zenith angle; green line shows sum of upward and downward components.

Figure 14 provides much information. First, the flux of energy reflected upward from the leaf layer is seen to be a slowly varying function of the zenith angle up to moderate values. Hence, Deardorff's assumption that surface reflectance is independent of the radiation angle of arrival approximately holds up to moderate incident angles, but clearly fails for near-horizontal incidence.

Second, the total reflectance adds to less than 50% of the incident radiation, but this is similar to the situation with Lambertian reflectors. There, recall that if one were to integrate over the output solid angle of 2π and normalize the energy, one would obtain a normalization constant of $(2\pi)^{-1}$, as in Eq. 7.12; but, when accounting for the cosine of incidence, for the outgoing energy to be balanced against the incoming energy in the case of a 100% reflective surface the normalization coefficient must be adjusted to π^{-1} , as illustrated in Eq. 7.13. Hence, for energy-conservation purposes the results of Eqs. 7.38 and 7.39 must be normalized by the sum of the upward- and downward-directed fluxes (the green line in Fig. 14). Once this effect is accounted for, the resulting reflection curves are expressed as shown in Fig. 15. These normalized forms can be expressed as

$$\tilde{R}_U(\theta_R) = R_U(\theta_R)/[R_U(\theta_R) + R_D(\theta_R)]; \quad (7.40.A)$$

$$\tilde{R}_D(\theta_R) = R_D(\theta_R)/[R_U(\theta_R) + R_D(\theta_R)]. \quad (7.40.B)$$

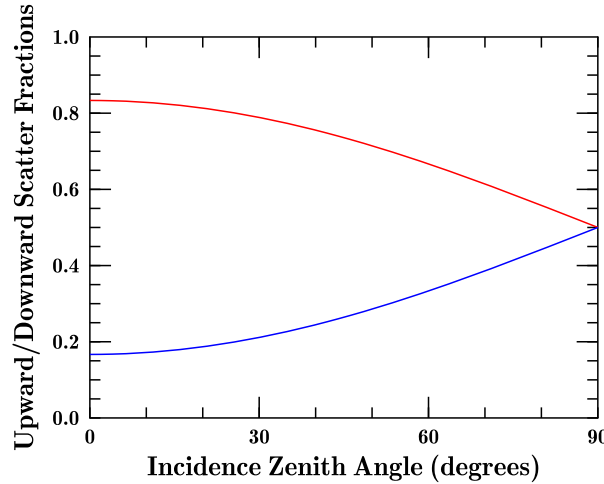


Fig. 15 Normalized hemispherical reflection curves, given scattering occurs into the upward (red) and downward (blue) hemispheres.

Now, leaves transmit as well as reflect radiation in the shortwave (solar) band. To a first order of approximation we can model such transmissions as producing outputs that are Lambertian in distribution in the same pattern as the reflected radiation. But, therefore, if it is assumed that whatever does not reflect will transmit (by ignoring absorptions), then one may immediately write transmission factors equivalent to the reflection factors, as,

$$\tilde{T}_U(\theta_R) = \tilde{R}_D(\theta_R); \quad (7.41.A)$$

$$\tilde{T}_D(\theta_R) = \tilde{R}_U(\theta_R). \quad (7.41.B)$$

The data set corresponding to the normalized reflection functions of Fig. 15 can next be used to determine the integrated mean reflectivity coefficients for incident diffuse-streaming radiation. To use the terminology of satellite radiometry, this involves determining the effects of the foliage distribution on *white sky* incident radiation. And, by reciprocity, once the backscattering statistic, R_{DB} , has been determined, the forward-hemisphere scattering statistic, R_{DF} , is immediately computed via the normalization $R_{DB} + R_{DF} = 1$.

These quantities are determined by integration over the incident radiation's solid angle, accounting for the cosine of the incident radiation, and averaging the outgoing radiation over each hemisphere.

$$R_{DB} = \frac{1}{\pi} \int_0^{\pi/2} (2\pi) \cos(\theta_i) \tilde{R}_U(\theta_i) d\theta_i = 0.7222, \quad (7.42.A)$$

$$R_{DF} = \frac{1}{\pi} \int_0^{\pi/2} (2\pi) \cos(\theta_i) \tilde{R}_D(\theta_i) d\theta_i = 0.2778. \quad (7.42.B)$$

In a similar correspondence with the transmission factors, we may also write

$$T_{DF} = R_{DB} = 0.2778; \quad (7.43.A)$$

$$T_{DB} = R_{DF} = 0.7222. \quad (7.43.B)$$

This completes the evaluation of the statistics of reflection and transmission from a single sublayer of the foliage canopy. In the next section these single-layer statistics are used to sum the aggregate behavior of a complete foliage layer using the multi-layer model described in Section 7.3.

7.5 Foliage and Surface Aggregate Radiation Properties

In the previous section a group of computations was performed to evaluate the reflective and transmissive behaviors of a thin layer of foliage characterized by a uniform leaf-orientation distribution. However, as illustrated in Fig. 12, to adequately characterize the behavior of foliage layers with surface covering fractions, σ_F , in excess of approximately 0.2, a multilayer model is necessary to achieve observed values of Υ_F exceeding 4.0 corresponding to cultivated crops (7.0) or other moderate-to-dense foliage conditions.

To handle such surfaces, the statistics of scattering/transmission from a single thin layer, as computed in the previous section, must be introduced into a scattering

model consisting of multiple plane-parallel foliage *sublayers*. Such multiple scattering techniques have been well established for radiative transfer applications. Examples such as the doubling method and discrete-ordinates techniques are generally necessary because aerosol and molecular scatterers within the atmosphere can be highly reflective. It is not the purpose of this section, however, to review, endorse, or adopt any of these techniques. Rather, since foliage and soil surfaces are moderately to highly absorbing, simplified methods can be adopted that attempt to model such reflections and transmissions using simpler techniques.

To put this issue in perspective, recall that Deardorff's (1978) model of surface reflectances ignored the issue of multiple scattering between the foliage and ground surfaces altogether. Hence, any development in this area should provide a substantive improvement in the current state of the art.

To begin the process of formulating such a reflection/transmission model for the flow of radiation within the surface interface, let us begin by focusing on shortwave radiation components. In this model, let us assume that the incident shortwave radiation can be approximated by 2 components: The first is a direct component consisting of radiation propagating through the atmosphere that appears to be streaming from the solar disk itself and arrives at the surface from an incident zenith angle θ_R measured relative to the vertical axis ($+\hat{z}$). A second component is modeled as the diffusely scattered radiation arriving from the remainder of the sky, approximated as a Lambertian source (*white sky* radiation component) produced by the scattering of solar radiation from molecular (Rayleigh scattering) and aerosol atmospheric constituents. (Components were derived from the Shapiro [1972] model.)

The white-sky diffuse-radiation component will appear as an input at the top of the layered-foliage model. The diffuse radiation then passes through the foliage layer via multiple reflections and transmissions between layer.

In contrast, direct radiation must be passed down into the sublayer model, initializing each level since the direct radiation will use the direct-to-diffuse transformation rule; on the other hand, the diffuse-to-diffuse radiation begins by using the stream rule from the outset. Following the initialization procedure, the streaming secondary radiation is multiple-scattered through the sublayer model as secondary-source terms between the model layers, plus a final surface reflection.

In either case, the model is run until all of the energy is exhausted from the system by multiple absorption events. At each iteration, the amount of energy removed by each layer is computed to determine whether the ground surface, leaf layer, or atmosphere are the ultimate recipients of the energy. Tabulated results can then be generated for each of the various energy forms passing through the interface layer. The diffuse radiation will depend only on the variables σ_F , α_F , and α_G , while the direct radiation contributions will also depend on θ_R .

Nominally, the value of α_F is set to 0.2, but this is understood to be effective layer reflectance of the foliage. Since the leaves are both forward and backward scattering, as well as transmissive, it will be necessary to perform numerical experiments to find effective leaf transmission and reflection coefficients that produce the appropriate aggregate layer reflectance of 0.2.

Complicating this process is the fact that leaves exhibit significant variations in spectral reflectivity. Below 0.80μ , in the visible band, foliage reflectance is low and focused in the green portion of the spectrum around $0.55 \mu\text{m}$. Beyond 0.80μ , the reflectivity of leaves increases dramatically, at times exceeding 0.60, depending on the sample tested. Neu et al. (1990) collected numerous sets of spectral-reflectivity data for both freshly cut and dry leaves, plotting them in great detail in their report. However, the data provided are at times contradictory and do not provide a single easily accessible result usable in the present model. Hence, equivalent leaf reflectance and transmittance had to be interpreted from the curves provided and guided by the net result expected (0.20). Certainly better models are possible, but, given the cost in time and effort to accumulate such information and account for special cases, it is outside the current scope of the work. Instead, a simplified approach was adopted. Through examination of Neu's findings, spectrally averaged values of reflectance and transmittance were inferred. Numerical experiments performed using the multilayer foliage model further confirmed these coefficients. Values selected were

$$\alpha_F \approx 0.325; \quad \gamma_F \approx 0.175. \quad (7.44)$$

where γ_F is the leaf-surface-transmittance coefficient. And, of course, these results are subject to further verification.

To model the propagation, scattering, and reflection effects in model terms, $\Phi_{\uparrow}(i)$ and $\Phi_{\downarrow}(i)$ were defined as flowing, diffuse energy streams arriving at layer i from below and above, respectively. Then, the $A(i)$'s were used to denote the net

fractional energy absorbed at each layer i . Initially, these quantities were set to zero. As the model iterated, the $A(i)$'s were updated to account for all the energy absorbed by the layer, so far, in the computation.

The model constructed to evaluate these results used 100 foliage sublayers to simulate scattering from the foliage with sufficient fidelity to model cases of σ_F up to 0.975. Let $M = 100$ denote the number of layers, indexed by i to denote the sublayers, plus a layer at $i = 0$, corresponding to the ground surface.

From Eq. 7.16.B, the foliage fraction in each sublayer is given by

$$\sigma_s = 1 - (1 - \sigma_F)^{1/100}. \quad (7.45)$$

For use in the main SEB model, direct radiation results were tabulated at a series of different incidence angles, while diffuse radiation calculations could be made for a single pass through the layer from above for each combination of σ_F and α_G .

Since it is the simpler case, let us consider the diffuse calculation first. Let the nominal incident net flux at the top of the foliage layer be given by

$$\Phi_{\downarrow}(100) = 1.$$

The remaining fluxes were initially set to zero. Following initialization, the following iterative rules were applied:

$$\begin{aligned} \Phi'_{\uparrow}(i+1) &= (\alpha_F R_{DB} + \gamma_F T_{DB}) \sigma_s \Phi_{\downarrow}(i) \\ &+ (\alpha_F R_{DF} + \gamma_F T_{DF}) \sigma_s \Phi_{\uparrow}(i) \\ &+ (1 - \sigma_s) \Phi_{\uparrow}(i), \end{aligned} \quad (7.46.A)$$

$$\begin{aligned} \Phi'_{\downarrow}(i-1) &= (\alpha_F R_{DB} + \gamma_F T_{DB}) \sigma_s \Phi_{\uparrow}(i) \\ &+ (\alpha_F R_{DF} + \gamma_F T_{DF}) \sigma_s \Phi_{\downarrow}(i) \\ &+ (1 - \sigma_s) \Phi_{\downarrow}(i). \end{aligned} \quad (7.45.B)$$

The Φ components were updated in a separate Φ' array to ensure conservation of energy. Note that α_F and the R parameters always appear together, as do the γ_F and T parameters.

A separate rule was used to update the ground-reflected energy:

$$\Phi'_\uparrow(1) = \alpha_G \Phi_\downarrow(0). \quad (7.46)$$

Following each update of the streaming-radiation components, the energies absorbed in each layer and at the ground were updated, using

$$A'(i) = A(i) + \Phi_\downarrow(i) + \Phi_\uparrow(i) - \Phi'_\downarrow(i-1) - \Phi'_\uparrow(i+1), \quad (7.47.A)$$

$$A'(0) = A(0) + \Phi_\downarrow(0) - \Phi'_\uparrow(1). \quad (7.47.B)$$

Lastly, the energy escaping back into the atmosphere at the top of the model was evaluated by accumulating the output energy via

$$E' = E + \Phi_\uparrow(101), \quad (7.48)$$

where, again, E is initialized to zero.

After each iteration of the equation set above, the updated primed values were copied into the prior flux array so the process could be iterated. Each iteration deposits energy into the absorbed-energy and escaped-energy bins while removing energy from the Φ array until it eventually becomes exhausted. At that point the calculation is finished and the energy absorbed in the foliage sublayers can be summed to determine the net energy absorbed by the foliage; the $A(0)$ value corresponds to the energy absorbed by the ground; and E corresponds to the net energy reflected back into the atmosphere. By setting the initial input energy to unity, the resulting sums are also equivalent to the net transfer coefficients of the downward-directed diffuse streaming energy into the foliage (A_F) and the ground (A_G) and the portion reflected back to the atmosphere (R_S , sky reflected).

A set of diffuse reflection results, using $\alpha_F = 0.325$ and $\gamma_F = 0.175$, for a range of surface-reflectance coefficients, α_G , from 0.05 through 0.25, are plotted in Fig. 16.

Notice that the resulting curves indicate a net foliage-layer sky reflectance of approximately 0.20 as $\sigma_F \rightarrow 1$. This occurs, even though $\alpha_F = 0.325$, because of the multiple scattering of light between the different leaf sublayers. Much of the light tends to penetrate through several layers before encountering a reflection surface. But once the light enters the canopy, it cannot directly reflect back out, due to partial blocking by vegetation above the reflection layer. A portion of the blocked light is then absorbed.

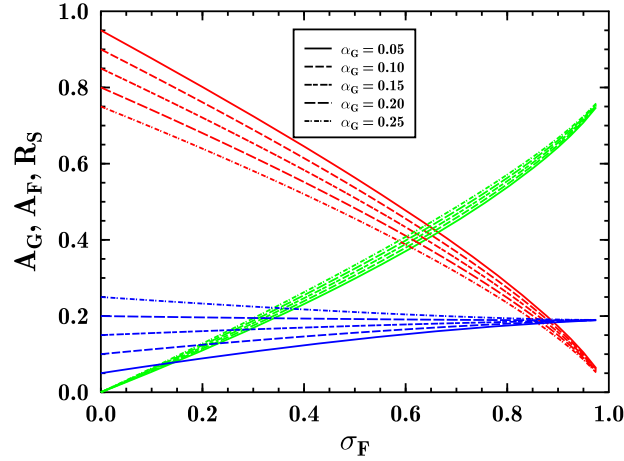


Fig. 16 Diffuse radiation absorption and reflection results obtained for varying soil albedo, α_G , and foliage fraction, σ_F , for foliage reflectivity, $\alpha_F = 0.325$, and transmissivity, $\gamma_F = 0.175$. Red curves denote fractional energy absorbed by the ground, A_G ; green curves, A_F , show fractions absorbed by foliage; blue curves, α_S , show sky-reflection fractions.

Results were calculated up to $\alpha_G = 0.95$ to support interpolation of surface conditions in the SEB model. Note also that these diffuse results, in combination with the direct-radiation results, such as the red line of Fig. 14 that exceeds 0.20, produce a net reflectivity of approximately 0.20 even though the results in Fig. 16 fall below 0.20 as $\sigma_F \rightarrow 1$.

Next, consider the case of direct radiation. The same leaf-surface reflection and transmission factors will be used for the scattered diffuse radiation. However, for initialization purposes, the direct-to-diffuse reflection/transmission results are used.

To initialize the calculations, the amount of net flux is again set to 1.0 at the top of the surface layer. This net flux is then distributed among the model sublayers and the $i = 0$ ground layer. Because 1.0 is the net flux, the solar-zenith angle cosine term's effect has been transferred outside the present calculation's results.

To perform the initialization, we must determine which fraction of the net flux is delivered to each layer for further scattering/transmission. Recall from Eq. 7.20 that the direct radiation transmittance to the surface depends on $\mu = \cos(\theta_R)$. From Eq. 7.16, the noninteracting portion of the net flux that is transmitted through the layered foliage to the top of any particular layer can be calculated as

$$T(i) = (1 - \sigma_s)^{(100-i)/\mu}. \quad (7.49)$$

Hence, for $i = 0$, the ground sees the effect of the full foliage layer, while at $i = 100$, the top layer sees no foliage-related energy loss.

Consistent with this result is use of a net transmittance for a single layer given by

$$\tau_1 = (1 - \sigma_s)^{1/\mu}. \quad (7.50)$$

We shall also use the variable $\chi_1 = (1 - \tau_1)$ to denote the net fractional energy lost as the direct beam passes through any given sublayer. If $\sigma_s/\mu \ll 1$, then Eq. 7.51 can be solved using the approximation $(1 - x)^p \approx 1 - px...$, such that $\tau_1 \approx 1 - \sigma_s/\mu$ and $\chi_1 \approx \sigma_s/\mu$. But, in general σ_s/μ may not be small, particularly as $\theta_R \rightarrow \pi/2$. Hence, we use the full equation for χ_1 .

Based on these layer results, the upward- and downward-streaming diffuse fluxes can be initialized by multiplying the radiation reaching each layer by the direct-to-diffuse scattering fraction calculations from Section 7.4. Iterating from $i = 1$ to $i = 100$, we set

$$\begin{aligned} \Phi_{\uparrow}(i+1) &\leftarrow [\alpha_F \tilde{R}_U(\theta_i) + \gamma_F \tilde{T}_U(\theta_i)] \chi_1 T(i), \\ \Phi_{\downarrow}(i-1) &\leftarrow [\alpha_F \tilde{R}_D(\theta_i) + \gamma_F \tilde{T}_D(\theta_i)] \chi_1 T(i). \\ A(i) &\leftarrow (1 - \alpha_F - \gamma_F) \chi_1 T(i). \end{aligned} \quad (7.51)$$

In addition to the internal initializing conditions, the values on the edges of the arrays were set using

$$\begin{aligned} \Phi_{\downarrow}(0) &\leftarrow \Phi_{\downarrow}(0) + T(0), \\ \Phi_{\uparrow}(0) &\leftarrow \Phi_{\uparrow}(1) \leftarrow 0, \\ A(0) &\leftarrow 0, \\ E &\leftarrow \Phi_{\uparrow}(101), \\ \Phi_{\uparrow}(101) &\leftarrow 0, \end{aligned} \quad (7.52)$$

in the order specified. A portion of the incident solar energy has thus been absorbed and the rest converted into diffuse radiation in the energy-flux *bins* of the sublayer model. Once initialized, the iteration process of Eqs. 7.44 through 7.47 is immediately applicable.

The same resolution of computations is used for each solar-zenith angle as the previous diffuse results. However, rather than stepping through zenith angles uniformly, a stepping method was developed where $\mu = \exp(-Y^2)$, and Y was stepped between 0.0 and 2.0 in increments of 0.1. The zenith angles achieved ranged from 0.0° to 88.95° , yielding a database of approximately 16,000 results.

Given the size of the resulting database it will be difficult to illustrate more than a minimal portion of the full results. Some concept of the variability produced by the model can be grasped from the following 2 graphs. Figure 17 illustrates the varying layer reflectivity (R_S) as a function of the solar altitude above the horizon for a series of ground reflectivities α_G in the common range of 0.00 to 0.20, for varying foliage fraction σ_F . The results obtained show similarities to the behaviors of measured layer reflectivities for foliage canopies, such as presented in Oke's Fig. 4.12 (1978). That figure plotted several foliage-canopy-reflectivity series for various forest types, grass, and kale as functions of increasing solar-altitude angle above the horizon. The graphs showed marked increases in reflectivity as solar altitude fell below 40° . Reasonable agreement was found between Fig. 17's $\alpha_G = 0.0$, $\sigma_F = 0.5$ curve (in this report) and Oke's oak-forest-canopy curve, and also between any of the $\alpha_G = 0.2$ cases and Oke's kale-crop curve. A good agreement with Oke's grass case should also be possible but using a higher α_G value than assigned in this model.

A second set of results plotted in Fig. 18 shows the decomposition of the fractional energy absorbed by the ground (red curves) and foliage layer (green curves) and sky reflected energy (blue curves) for varying solar-zenith angles as parameterized by Y varying from 0.0 to 2.0 in increments of 0.5. Obviously, for the $Y = 2.0$ curves the sun is very close to the horizon and the resulting curves exhibit rather extreme behaviors. For all these curves α_G has been set to 0.00 to isolate the reflection properties of the foliage.

A key observation in these graphs is that the $Y = 0.0$ and $Y = 0.5$ curves, representing overhead direct illumination and radiation arriving at a zenith angle of 52° , respectively, are shown to bracket the value 0.20, which is the expected reflectance from a foliated layer. Thus, we return to the finding that these calculations fit within the overall concept of an expected, mean layer reflectivity of 0.2 — though illustrating the variability of results when zenith angles close to the horizon are present.

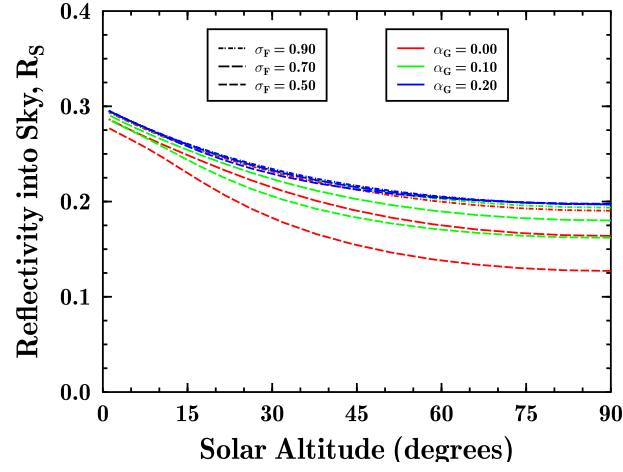


Fig. 17 Behavior of surface-layer reflectivity of foliated layers of different surface fractions σ_F as functions of ground reflectivity α_G and as a function of the solar altitude in degrees

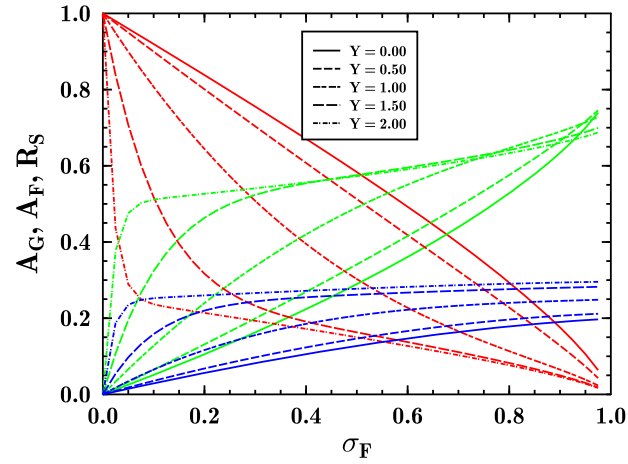


Fig. 18 Direct-radiation transmission factors to the ground (red lines), foliage (green lines), and sky-reflected (blue lines) for variable σ_F at a range of solar-zenith positions parameterized by Y , for constant $\alpha_G = 0.00$

This completes the shortwave-radiative calculations. We next consider 3 types of diffuse radiative fluxes associated with long-wave (infrared: IR) radiation. The first is downward long-wave radiation arriving at the top of the surface interface and using the same computational engine and method as previously described for the short-wave downward diffuse flux. (The only difference is the relative reflectivities used for the soil surface and the foliage.) The second is upwelling radiation emerging from the ground. The third is radiation emitted by the foliage layer in both the upwelling and downwelling directions.

The nominal IR–foliage statistic for bulk emissivity is 0.95 (layer IR albedo of 0.05). Similar to the shortwave calculations, an adjusted leaf emissivity must be introduced to produce this bulk effect. The value selected was $\epsilon_F = 0.87$. Using this value, a full set of computed results A_G , A_F , and R_S were produced for the downward long-wave case. A subset of results is plotted in Fig. 19.

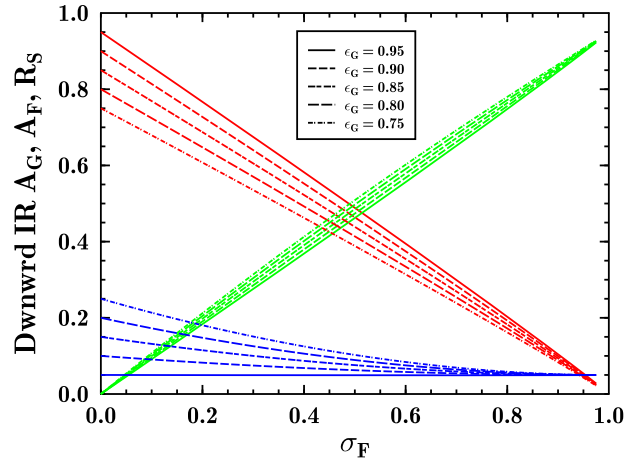


Fig. 19 Diffuse IR-radiation absorption and reflection results equivalent to the cases plotted in Fig. 16, but using altered foliage-albedo value $\alpha_{F(IR)} = 0.13$ ($\epsilon_F = 0.87$)

Next, again using $\alpha_F = 0.13$, we consider radiation emitted from the ground as the source. Setting the initial value of the upward-welling, diffuse radiation from the surface to a normalized 1.0 produced outputs corresponding to normalized multipliers that can be used to scale computed ground IR radiation given by $\epsilon_G \sigma T_G^4$ (where σ is the Stefan–Boltzmann constant). A portion of the outputs of this calculation are plotted in Fig. 20. Note that the sky-output variable has been renamed E_S corresponding to an effective surface-layer emissivity into the atmosphere, as opposed to calling it a reflectance factor, since in this case there is no incident radiation to reflect.

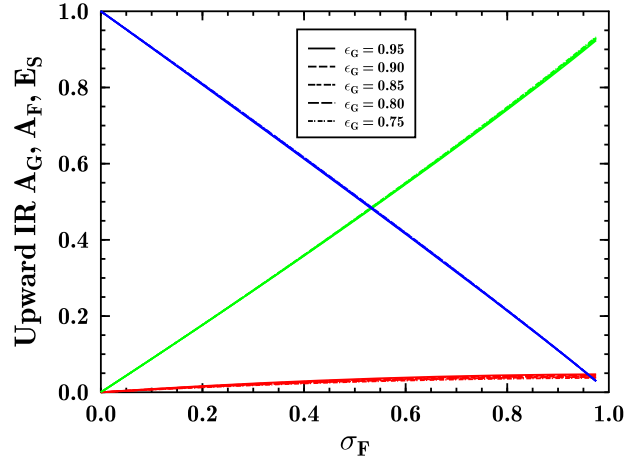


Fig. 20 Diffuse IR-radiation absorption and emission results similar to the cases plotted in Fig. 16, but using altered foliage albedo $\alpha_{F(IR)} = 0.13$ ($\epsilon_F = 0.87$) for ground-emitted radiation and plotting sky emissivity, E_S , rather than reflectivity, R_S

Finally, the foliage layer can be selected as the radiation source. Radiating energy is initialized in both upward- and downward-welling directions from each foliage layer. Each radiation component is set to σ_s , associated with the relative layer-surface-area from which the normalized radiation emerges. This choice is made such that the resulting flux fractions can be multiplied by $\epsilon_F \sigma T_F^4$, using $\epsilon_F = 0.87$, to generate the net fluxes from the layer. The results of these calculations, for a range of α_G and σ_F values, are plotted in Fig. 21.

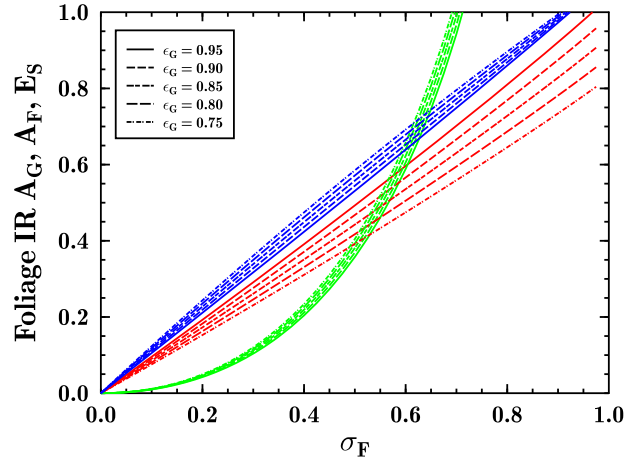


Fig. 21 Diffuse IR-radiation absorption and reflection results equivalent to cases plotted in Fig. 18, using foliage albedo $\alpha_F = 0.13$ ($\epsilon_F = 0.87$); radiation originates in foliage layer

In contrasting the results plotted in Fig. 21 with those of Figs. 19 and 20, at least 2 characteristics are self-evident. The first regards sources and sinks: In both Figs. 19 and 20 the radiation-source regions receive the least feedback of energy. This is a factor of the low reflectivity coefficients involved. This observation is also true at low σ_F values in Fig. 21. However, as σ_F increases, the foliage surface area increases rapidly. Much of the radiation then becomes self-absorbed by the foliage itself. As σ_F approaches 1 this value increases up to 5.5 times the amount of radiation that escapes from the canopy. Hence, the second unique feature is that the system is no longer normalized to unity (sum of the 3 components approximately equals 1.0), but, rather, reflects the unnormalized surface area of the foliage per square meter of underlying soil, consistent with the foliage surface area N_F . This model thus appears to be a good surrogate for modeling the microclimate of a thickly foliated layer.

Figure 21 also reveals that the sky-emitted output is greater than the one-to-one line such that the effective emissivity exceeds the 0.87 value. For example, the sky output equals 1.0 at approximately $\sigma = 0.92$. Thus, the effective emissivity at that point is $0.87/0.92 = 0.945$, close to the bulk emissivity of 0.95.

To conclude, the foliage-layer model developed produces bulk properties that correspond to various reported behaviors associated with deciduous trees, grasses, and crops, but somewhat dissimilar to behaviors of alternative leaf structures (pine forests, etc.). Hence, the model developed would be appropriate for desert grasses, low weeds, yucca, creosote, mesquite, savannas, and steppe terrains. The model would be less appropriate for desert cacti such as saguaro, agave, and ocotillo that are relatively thicker and less leaf-covered. The diffuse calculations similarly appear to have good performance using the albedos and emissivities chosen to produce the expected aggregate behaviors.

To use the results obtained, tables generated for given values of α_F and ϵ_F are combined with variable α_G , ϵ_G , and solar-zenith parameterization in an interpolation routine for the 5 scattering/transmission scenarios described. In addition, equations using N_F , Υ_F , α_F , and ϵ_F — Eqs. 2.21.A, 2.21.B, 2.22, 5.25, and 5.31 — must use the reassigned values.

8. Atmospheric Infrared Radiative Fluxes

This chapter focuses on the influence of atmospheric IR radiation on the Surface Energy Budget (SEB) as well as heating of the boundary-layer atmosphere by IR energy in general. In so doing, we attempt to avoid the general discussion of radiative fluxes within the overall atmosphere as this is the subject of many other research projects and applications. Examples include Goody and Yung (1961), Liou (1980), Stephens (1994), and Thomas and Stamnes (1999). Concurrently, models of atmospheric propagation such as LOWTRAN and MODTRAN developed by the US Air Force Research Laboratory increased in complexity from 100 cm^{-1} per channel of spectral resolution to 1 cm^{-1} spectral resolution, to a 15-component correlated-k calculation per wave-number channel.

Our focus is on the boundary layer and, more specifically, the surface layer. Since our main concern is solar loading, a simpler model will be developed as we are not interested in the detailed inner workings of the upper atmosphere. Critically, we are concerned with the surface interface where the influence of atmospheric radiation directly augments the impact of solar direct/diffuse radiation. In this model the effort was made to follow Deardorff, in the sense of providing a simple expression for the downward-longwave radiation such that one could avoid activating a complex radiative-transfer code. This is based largely on the available information, which this model assumes is minimal, but could be linked into a higher-resolution model such as the Air Force's LEEDR model (e.g., Fiorino et al. 2014). We therefore start with the expression introduced by Deardorff (1978) involving use of Staley and Jurica's (1972) atmospheric-emissivity model. We then upgrade this model through use of vertical temperature-structure models developed in Chapter 6, in combination with radiative-flux calculations performed based on atmospheric-emissivity data derived from the MODTRAN-4 code.

Using a more complete radiative-transfer model described, calculations were performed to determine the radiative flux passing downward from the base of the surface layer into the surface interface, at the top of the boundary layer upward, and both upward and downward at an interface between the boundary layer and the surface layer. In such a way the balance of energy fluxes entering and leaving the different regions of the modeled volume (boundary layer and surface layer) could be approximately tracked.

8.1 Review of Deardorff's Long-Wave Radiation Model

In his groundbreaking paper, Deardorff (1978) brought together a suite of methods developed across the research spectrum to compute the SEB. One of these was the atmospheric-emissivity model of Staley and Jurica (1972) that Deardorff used to formulate a net long-wave downward flux of IR radiation at the top of the foliage layer, expressed as

$$R_{L\downarrow} = \left[\sigma_C + (1 - \sigma_C) 0.67 (1670 q_a)^{0.08} \right] \sigma T_A^4, \quad (8.1)$$

where σ_C is the fractional cloud cover, q_a is the specific humidity, σ is the Stefan–Boltzmann constant, and T_A is the air temperature in Kelvin. The main Staley and Jurica (1972) contribution to this formulation was the atmospheric emissivity given by

$$\epsilon_A = 0.67 (1670 q_a)^{0.08}. \quad (8.2)$$

The first element to note is that Eq. 8.1 appears to be *wired* wrong. That is, experience with atmospheric IR radiation suggests that emissions from a humid atmosphere occur from molecules within a relatively short distance of the level of measurement; that IR radiation reaching the ground appears to arise from molecules within approximately the first 10 m AGL. We know this because the emissivity of the air is often greater than 80%, but the temperature used to characterize the flux is simply the air temperature T_A . Emissivity values this high could not be achieved if the energy arose from molecules much farther from the surface since then T_A would be an inappropriate temperature (too high) to use.

Given this observation, radiation from higher in the atmosphere must be heavily absorbed by the air within the first 10 m AGL, except in what are known as atmospheric window regions. Hence, it should be that the atmospheric emissivity becomes a limiting factor restricting the near-blackbody radiation arising from the cloud base; it should not restrict the near-surface atmospheric radiation from reaching the surface based on the available cloud cover, as parameterized by available cloud fraction σ_C . Thus, the first correction to the downward, long-wave radiative flux involves rewriting this function in the form,

$$R_{L\downarrow} = \epsilon_A \sigma T_A^4 + (1 - \epsilon_A) \sigma_C \sigma T_C^4. \quad (8.3)$$

In addition to filtering the incident long-wave energy arising from the cloud base, we also introduce a new temperature parameter T_C to denote the cloud temperature. To approximate the value of T_C , some simple rules are generated based on T_G , Z_I and the cloud type indicated by the user (low, medium, or high clouds).

The more significant unknown to be addressed regarding the IR radiation is the appropriate form for modeling the atmospheric emissivity, ϵ_A . One notes that the expression for ϵ_A given in Eq. 8.2 approaches zero at zero atmospheric humidity. Hence, we know that this form ignores the effects of carbon dioxide (as well as those of oxygen, nitrogen, and all other dry gases). This suggests, at minimum, a reanalysis of atmospheric emissivity is needed. In addition, we shall consider various temperature scenarios in these calculations.

8.2 Downward Long-wave Radiation Calculation Re-evaluation

In addition to the Staley and Jurica (1972) parameterization of the atmospheric emissivity, in the early 1980s a parallel study of the SEB was conducted by the US Army Waterways Experiment Station, Vicksburg, Mississippi, for the US Army Corps of Engineers. This study (Balick et al. 1981) based its long-wave atmospheric downward flux on an emissivity expression by Sellers (1965), written,

$$\epsilon_A \approx 0.61 + 0.050 \sqrt{e_a}, \quad (8.4)$$

where e_a is the water-vapor pressure in millibars.

Clearly, these 2 emissivities in Eqs. 8.2 and 8.4 will predict different behaviors, particularly based on their conflicting exponential dependence and Sellers' use of a zero-humidity offset of 0.61 versus Staley and Jurica's lack of any offset.

Therefore, a complete reanalysis was performed. Through this reanalysis we compare results obtained via a spectral integration against these 2 models. In the process we consider whether the heights we have chosen for characterizing the surface layer (Z_T or Z_A) and the characteristic temperature T_A are reasonable for modeling the long-wave fluxes to/from the atmosphere (and are characteristic of the radiative temperature, as well).

8.3 Numerical Radiative-Transfer Calculation

To make the comparison, a numerical radiative-transfer calculation can be performed for a range of initial air temperatures, pressures, and humidities. Let

us first denote by k the radiation wave number, $k = 2\pi/\lambda$. For reference purposes, most radiation calculations can be performed relative to that of a blackbody source. For such a source, the number of photons per unit wave number interval per unit volume is given by

$$n_k = \frac{k^2}{\pi^2 (e^x - 1)}; \quad x = \frac{\hbar c k}{k_B T} = \frac{1.43879 \tilde{k}}{T}, \quad (8.5)$$

where $\hbar = h/2\pi$, h is Planck's constant, c is the velocity of light in vacuum, k_B is Boltzmann's constant, and T is the absolute temperature in Kelvin (Wolfe 1989), and $\tilde{k} = k/(200\pi)$, the inverse centimeter wave number representation used by MODTRAN.

Transforming this result to energy per unit volume in spectral interval dk , we obtain

$$w_k dk = h\nu n_k dk = \hbar c k n_k dk = \frac{\hbar c k^3}{\pi^2 (e^x - 1)} dk. \quad (8.6)$$

This energy density is isotropic since it is basically the energy flowing inside a blackbody (100% emitting and absorbing) cavity. The next step is therefore to study how this emits outward by considering the energy flux in a given direction (basically, through a pinhole in the blackbody's cavity wall). Therefore, dividing by 4π , the above spectral energy is converted to an amount passing into a unit solid angle. Further, multiplying by a small solid angle, $\Delta\Omega$, one can resolve the amount of spectral energy flowing into that amount of solid angle. That is,

$$\frac{w_k dk dV \Delta\Omega}{4\pi}. \quad (8.7)$$

Now, the radiation flowing from the atmosphere toward the ground does not emerge from a blackbody cavity, but the radiation computed as arising from any volume of the atmosphere is typically evaluated as a relative fraction of the amount of energy that would arise from such a cavity. Hence, let us imagine a differential volume dV somewhere within the atmosphere above the surface, and let us imagine a finite region of the surface below, of area A . Let the region dV be located at a height z above the ground and located at an angle θ relative to the vertical direction from our test patch A , and thus at a distance $r = z/\cos(\theta)$ from the test patch. The solid angle $\Delta\Omega$ subtended by the test patch, as seen from volume element dV at distance r , would then be

$$\Delta\Omega = \frac{\cos(\theta) A}{r^2}, \quad (8.8)$$

where patch area A is foreshortened by the $\cos(\theta)$ factor in computing the surface area of the patch presented perpendicular to the vector connecting the surface patch with the volume. (We assume patch A has a normal vector in the direction of an earth-to-space path such that angle θ is a zenith angle from the vertical to the direction toward the volume element dV .)

Next, for simplicity of calculation, let us place the test patch at the origin of coordinates and orient the normal vector to the surface in the $+\hat{z}$ direction. Further, let us adopt a circular test patch of diameter D : $A = \pi D^2/4$, and assume $D \ll r$. A sample radiating volume dV can then be designated in an (r, θ, ϕ) spherical coordinate system by its volume extents dr , $r d\theta$, and $r \sin(\theta) d\phi$:

$$dV = r^2 \sin(\theta) dr d\theta d\phi. \quad (8.9)$$

From this and the previous result, we see that the r^2 dependence in the product $\Delta\Omega dV$ cancels:

$$\Delta\Omega dV = A \sin(\theta) \cos(\theta) d\theta d\phi dr. \quad (8.10)$$

The downward long-wave radiation consists of all of the energy incident on our test patch arriving in unit time, then divided by the patch area, thereby producing a statistic in Watts per meters squared.

The net spectral energy in interval dk emitted by a blackbody radiator from a volume dV in the direction of the area A is, therefore,

$$w_k dk dV \frac{\Delta\Omega}{4\pi} = \frac{\hbar c k^3 dk}{4\pi^3 (e^x - 1)} A \sin(\theta) \cos(\theta) d\theta d\phi dr. \quad (8.11)$$

This result is given as an amount of energy present inside the volume dV that is in the right spectral range and travelling in the right direction to impact on patch A , but the result sought should have the dimensions of an irradiance: power (energy per unit time) per unit area per unit spectrum. To denote this result, we recognize that the amount of energy in volume dV takes only an amount of time dr/c to pass out of said volume. Dividing by dr/c the energy quantity is transformed into a power produced by dV at A per second. Further dividing by the area A , the power delivered to patch A is transformed into a power per unit surface area:

$$dB_{\hat{\Omega}}(k, T) = w_k dk \frac{dV}{(dr/c)} \frac{\Delta\Omega}{4\pi A} = \frac{\hbar c^2 k^3 dk}{4\pi^3 (e^x - 1)} \sin(\theta) \cos(\theta) d\theta d\phi. \quad (8.12)$$

This quantity is the blackbody's spectral-radiance contribution from direction $\hat{\Omega}$ arriving at the origin of coordinates.

By integrating over the solid angle, the net spectral irradiance can be determined. Let $\mu = \cos(\theta)$, such that the integral over the upper hemisphere can be written as

$$B_B(T) = \int_0^{2\pi} d\phi \int_0^1 \mu d\mu \frac{\hbar c^2}{4\pi^3} \frac{k^3 dk}{e^x - 1} = 2\pi \int_0^1 \mu d\mu [B(k, T) dk]. \quad (8.13)$$

$$B(k, T) = \frac{k_B^3 T^3}{4\pi^3 \hbar^2 c} \times \frac{x^3}{e^x - 1}. \quad (8.14)$$

Using $2\pi \int_0^1 \mu d\mu = \pi$, a π term in $B(k, T)$'s denominator cancels.

The function with respect to x provides a universal spectral shape of the blackbody curve that scales according to the temperature of the source. For the total energy flux due to the blackbody, one would need to finally integrate as

$$B_B(T) = \frac{k_B^3 T^3}{4\pi^2 \hbar^2 c} \int_0^\infty \frac{x^3}{e^x - 1} dk = \frac{k_B^4 T^4}{4\pi^2 \hbar^3 c^2} \int_0^\infty \frac{x^3}{e^x - 1} dx. \quad (8.15)$$

The integral evaluates as

$$\int_0^\infty \frac{x^3}{e^x - 1} dx = \frac{\pi^4}{15}. \quad (8.16)$$

Inserting numerical values, $\hbar = 1.0546 \times 10^{-34}$ J/s, $k_B = 1.381 \times 10^{-23}$ J/K, and $c = 2.998 \times 10^8$ m/s, leading to

$$\sigma_{SB} = \frac{k_B^4}{\hbar^3 c^2} \frac{\pi^2}{60} = 5.67 \times 10^{-8} \left[\frac{\text{W}}{\text{m}^2 \text{K}^4} \right], \quad (8.17)$$

$$B_B(T) = \sigma_{SB} T^4 [\text{W/m}^2]. \quad (8.18)$$

This result represents the energy received from an entire plane of emitting blackbody surface, but by reciprocity it also represents the net blackbody output from a 1-square-meter surface at temperature T , where the input energy absorbed by the perfect absorber would equal the output energy radiated by the perfect emitter.

To extend this calculation to a non-blackbody problem, the first step is to replace the perfect emitter/absorber model of a blackbody, where $\epsilon = 1$, with a frequency-dependent *graybody* emitter emissivity, $\epsilon(k)$. Such graybody surfaces were encountered in the previous section, where foliage and soil surfaces were assigned emissivity coefficients ϵ_F and ϵ_G less than 1.0.

However, while solid surfaces exhibit mildly varying emissivities that can be approximately characterized by a single frequency-independent emissivity factor,

atmospheric molecular components exhibit highly variable spectral-emissivity dependence because they respond as quantum-mechanical objects with various combinations of orbital, vibrational, and rotational energy levels that produce detailed spectral line structure that is dependent on temperature, pressure, and absorbing species' density. Each atmospheric species has its own spectrum of absorption/emission, with water vapor being one of the most effective molecules due to the number of modes produced by its polar asymmetry.

To proceed we need 2 elements: We need to have a model for propagating through the atmosphere to generate the radiation that appears at the surface. We also need to know the governing statistics of the atmosphere for propagating radiation at different frequencies. First, let us consider the propagation problem. We need to have a quantity to represent the rate at which the atmosphere absorbs (extinguishes) streaming radiation as a function of a fractional quantity per unit distance propagated through the media. Let us assign this as α_k , denoting by the subscript k its wavelength dependence, but also noting that it will depend on the atmospheric state, as well.

For complete applications one considers both the impacts of scattering and absorption, designating the fraction of radiation scattered by ϖ_k , such that $\varpi_k \alpha_k$ is the scattering coefficient. However, since the calculations being made involve relatively short-range effects, and since IR scattering is minimal relative to visible-band scattering, we shall ignore scattering effects.

With that understanding, we write a radiative-transfer equation in the general form (Tofsted and O'Brien 1998),

$$\hat{\Omega} \cdot \nabla I_k(\vec{r}, \hat{\Omega}) = \alpha_k B_k - \alpha_k I_k(\vec{r}, \hat{\Omega}), \quad (8.19)$$

where I_k is a radiance field that is a function of position \vec{r} and radiation-flow direction $\hat{\Omega}$. Here we have omitted the scattering portion (effectively setting $\varpi = 0$). Here also B_k is a frequency-dependent, blackbody-radiation source term that is temperature dependent only.

The dot product of the unit vector $\hat{\Omega}$ with the gradient operator ∇ acting on the radiance field has the effect of sifting out a derivative oriented in the direction of radiation flowing in the $\hat{\Omega}$ direction. That is, $\hat{\Omega} \cdot \nabla I_k$ becomes dI_k/ds , where s is increasing in the $\hat{\Omega}$ direction.

As long as temperature is a slowly varying function of position, and α_k , the absorption/emission coefficient, operates much more quickly than B_k changes, then we may form a new variable; call it $C_k = I_k - B_k$. The above equation can thus be simplified into the form,

$$\frac{dC_k}{ds} = -\alpha_k C_k, \quad (8.20)$$

which has the rather simple solution,

$$\ln(C_k) = -\alpha_k s \longrightarrow C_k(s) = C_k(0) \exp(-\alpha_k s); \quad (8.21.A)$$

$$I_k(s) - B_k(s) = [I_k(0) - B_k(0)] \exp(-\alpha_k s). \quad (8.21.B)$$

But $B_k(s) = B_k(0) = B_k$, such that,

$$I_k(s) = I_k(0) \exp(-\alpha_k s) + B_k[1 - \exp(-\alpha_k s)], \quad (8.21.C)$$

where the altitude step must be small enough that B_k can be considered constant; that is, that atmospheric temperature and pressure are not changing markedly across the height step. We therefore designate by δs such a short path step.

To produce the full energy arriving at a given point on the ground, one must integrate downward from some height sufficient that the energy accounted for is nearly complete. One way to accomplish this is by integrating backwards from the point of interest *into* the volume. To perform this, let us recall the use of variables τ_1 and χ_1 in Eq. 7.50 of the previous chapter. In the present application we could assign

$$\tau_{\delta z, k, \mu} = \exp(+\alpha_k \delta z / \mu), \quad (8.22)$$

where $\delta z < 0$. Then,

$$\chi_{\delta z, k, \mu} = 1 - \tau_{\delta z, k, \mu}. \quad (8.23)$$

Here, δz can be constant, but α_k will depend on temperature at the height where the propagation is being computed.

To compute the output $I_k(0, \mu)$, start with $I_k(0, \mu) = 0$, and $\tilde{T}_k = 1$. Then, for $i = 0$ to n (the number of layers), let

$$I_{k, i+1}(0, \mu) \leftarrow I_{k, i}(0, \mu) + \tilde{T}_k \chi_{\delta z_i, k, \mu} B_k[T(z_i)], \quad (8.24.A)$$

$$\tilde{T}_{k, i+1} \leftarrow \tilde{T}_{k, i} \tau_{\delta z_i, k, \mu}. \quad (8.24.B)$$

In this algorithm, the radiance at height zero increases by an amount related to the source term added over each step i at height z_i , given by $\chi_{\delta z, k, \mu} B_k[T(z_i)]$, but then attenuating this amount by $\tilde{T}_{k,i}$ corresponding to the energy loss in transmitting that flux contribution to the surface. To reduce the processing overhead, it would not be necessary in many cases to integrate the result up to the top of the atmosphere since the net transmission \tilde{T}_k provides a good estimate of when the full amount of energy transfer has been accounted for. For example, the iteration process could be stopped as soon as $\tilde{T}_k < 0.00001$. The total energy flux at the ground can then be computed via

$$R_{\downarrow} = \int_0^{\infty} dk \left\{ 2\pi \int_0^1 I_k(0, \mu) \mu d\mu \right\}. \quad (8.25)$$

Written in terms of the finite-element solution of the implementing computer algorithm, this procedure is approximated by

$$R_{\downarrow} \approx \sum_{j=0}^J \delta k \left\{ 2\pi \sum_{m=0}^M I_{k(j)}[0, \mu(m)] \mu(m) \delta\mu \right\}. \quad (8.26)$$

This equation is evaluated using the quantities τ and χ from Eqs. 8.22 and 8.23, and $B_k(T)$ is effectively the spectral radiance component that is the integrand of Eq. 8.15 using the x definition from Eq. 8.5, repeated here:

$$B_k(T) = B(k, T) = \frac{k_B^3 T^3}{4 \pi^3 \hbar^2 c} \times \frac{x^3}{e^x - 1}; \quad x = \frac{\hbar c k}{k_B T}.$$

8.4 Spectral Absorptivity Data Collection

To obtain sets of data needed to characterize τ_k and χ_k , the MODTRAN-4 code was run using that code's implementation of the 1976 US Standard Atmosphere in a transmission mode where transmission coefficients were computed over the first kilometer (0–1 km) interval of the model atmosphere looking vertically through the model volume. In MODTRAN, the absorption coefficients are constant in each 1-km layer, including the 0–1 km layer. Exploiting this feature, the model was run in transmission mode, but the vertical-path transmission coefficient was intercepted prior to output from the model. Taking the negative natural logarithm of the spectral transmission produced a net layer-attenuation coefficient at 1 cm^{-1} resolution in the range of 100–5,000 cm^{-1} .

The MODTRAN output combines all significant atmospheric gases into a single attenuation coefficient. The output thus contained both dry-air and water-vapor influences. To distinguish the moist atmospheric effects from the dry-air

components, MODTRAN was run for a dry case using the baseline 1976 US Standard Atmosphere — where relative humidity is a constant 46.04% in the first kilometer — and a doubled-humidity case using MODTRAN’s humidity-scaling factor at an input value of 2.0, producing a result of 94.21% relative humidity in the first model layer. The resulting humidity levels, when expressed as specific humidities, evaluated to 0.004800 and 0.009852 (kg/kg), respectively. By intercepting the output transmission and converting it to a logarithm, MODTRAN’s 4-digit output format precision used in its transmission output was avoided, allowing attenuation coefficients to be resolved to values greater than the 9.9 optical depths per kilometer of the base model.

Using the 2 outputs in each wave-number bin, a dry-atmosphere extinction coefficient α_{kd} could be interpolated for sea-level density conditions, and a water-vapor extinction coefficient α_{kw} associated with sea-level density and 0.004800 specific humidity could be computed.

Results were obtained spanning the infrared band from wave numbers $\tilde{k} = 100$ to $5,000 \text{ cm}^{-1}$ (inverse centimeters). To translate these to wave numbers k , MODTRAN’s wave numbers $\tilde{k} = 10000/\tilde{\lambda}$ use wavelengths $\tilde{\lambda}$ expressed in microns (μm). MODTRAN 4’s available spectral resolution of $\delta\tilde{\nu} = 1 \text{ cm}^{-1}$ should be sufficient for energy-flux calculations.

Next, note that,

$$\alpha_{kd}(P_\alpha, T_\alpha) = -\ln(T_{dk}), \quad \alpha_{kw}(P_\alpha, T_\alpha, q_\alpha) = -\ln(T_{wk}), \quad (8.27)$$

where T_{dk} and T_{wk} are MODTRAN-derived transmission results, and the α values are the resulting dry-air and water-vapor extinction coefficients derived. Values obtained were categorized by the standard pressure (P_α), temperature (T_α), and specific humidity (q_α) values associated with the run.

From the basic values, analysis of MODTRAN outputs indicated variations in absorption following the relations,

$$\alpha_{kd}(P, T) = \alpha_{kd}(P_\alpha, T_\alpha) \left[\frac{P}{P_\alpha} \right]^{1/2} \left[\frac{(1-q) P/T}{(1-q_\alpha) P_\alpha/T_\alpha} \right]; \quad (8.28.A)$$

$$\alpha_{kw}(q, P, T) = \alpha_{kw}(q_\alpha, P_\alpha, T_\alpha) \left[\frac{P}{P_\alpha} \right]^{1/2} \left[\frac{q P/T}{q_\alpha P_\alpha/T_\alpha} \right]. \quad (8.28.B)$$

The pressure dependence seen here is a combination of a linear pressure dependence related to the density of the absorbers multiplied by a square-root dependence related to the pressure-broadening of absorption lines that occurs at low altitude. As altitude increases, and the pressure drops, absorption lines become narrower and therefore less absorptive. The temperature and humidity dependencies are just those factors related to the density of the absorbers.

8.5 Atmospheric Temperature and Pressure Model

To calculate the radiation emitted from a layer of the atmosphere, the previous sections of the chapter have so far laid out the radiative properties of the atmosphere. Here, the process is completed by considering the vertical profile models of temperature and pressure used to seed the absorption/emission coefficients needed by the radiative-transfer model.

In addition to knowing the temperature and pressure profiles, a water-vapor profile is critical — especially considering the dominant role of water vapor in the Staley and Jurica emissivity model. However, it is not the intent of the current text to address all conceivable temperature, humidity, and pressure profile combinations. Rather, given the temperature-profile models of Chapter 6, the concept is to add a pressure and humidity model to the temperature models and calculate the emissivities predicted by these combinations.

The series of atmospheric models features a number of variables. First, the baseline pressure is selected based on an initial height of the modeled surface above sea level (ASL). The 1976 US Standard Atmosphere is used to set the starting pressure. First, the standard air density is set using Eq. 3.8 (by ARL's Abel Blanco) using input site height ASL, H . The mean atmospheric temperature can then be set based on the 1976 US Standard Atmosphere vertical temperature function

$$T_{SA}(H) = 288.1 - 6.4 H \text{ [K]}, \quad (8.29)$$

where $T_{SL} = 288.1 \text{ K}$ is the standard sea-level temperature. The standard pressure at sea level ($P_S = P(0)$) is 1013.25 mbar. And, the standard pressure becomes

$$P_{SA}(H) = 2.87 \rho_{SA}(H) T_{SA}(H). \quad (8.30)$$

Once the surface pressure is estimated, we can compute a vertical pressure profile using the hydrostatic equation and a selected temperature profile based on

$$\frac{dP}{dz} = -g \rho_a / 100, \quad (8.31)$$

where z is the height above the surface measured in meters, and ρ_a is the atmospheric density (kg/m^3) given as

$$\rho_a = 0.34838 P/T_v. \quad (8.32)$$

Here, we could have used T'_v , the adjusted virtual temperature, in $T'_v = C T_v$, introducing the compressibility factor, C ; but, since C is within a few thousandths of 1.00, we simply use the virtual temperature, T_v , a humidity-adjusted function of the temperature:

$$T_v(Z) = T(Z) \frac{1 + r_m/\epsilon_w}{1 + r_m}, \quad (8.33)$$

where $\epsilon_w = 0.62197$ is the ratio of the molecular weight of water to the molecular weight of dry air, and r_m is the mixing ratio: the ratio of the mass of water vapor to the mass of dry air. The resulting air density varies with humidity, unlike Eq. 1.2 where humidity effects were suppressed.

The mixing ratio r_m , in turn, is a function of the specific humidity, q_a , the ratio of water vapor to total air mass (dry plus water) in a given air sample. Quantities r_m and q_a are related through

$$r_m = \frac{q_a}{1 - q_a}, \quad q_a = \frac{r_m}{1 + r_m}, \quad (8.34)$$

where q_a (kg/kg) is evaluated using

$$q_a = \epsilon_w \frac{V_p}{P - (1 - \epsilon_w) V_p}, \quad \text{or} \quad V_p = \frac{r_m P}{\epsilon_w + r_m}. \quad (8.35)$$

The V_p is the (water) vapor pressure (mbar), which is simply the saturation vapor pressure V_p^S (mbar) multiplied by the relative humidity ($0 < R_H < 1$):

$$V_p = V_p^S R_H, \quad (8.36)$$

where V_p^S is given by

$$V_p^S(T_C) = A_1 10^X, \quad X = \frac{A_2 T_C}{A_3 + T_C}. \quad (8.37)$$

The coefficient $A_1 \approx 6.13686$ (mbar). The remaining coefficients depend on whether the vapor pressure is being measured over a surface of water ($A_2 \approx 7.601$, $A_3 \approx 240.97$ °C) or ice ($A_2 \approx 9.5$, $A_3 \approx 265.5$ °C), and uses $T_C = T - 273.16$ K,

the Celsius temperature. The over-water numbers were derived from recent theory used by Li-Cor in its humidity-sensor software. The over-ice values were obtained from the Smithsonian Meteorological Tables. The over-water values were used in the numerical radiation calculations performed.

At this point, let us take stock of the equations available and the means of creating a profile.

First, given H , T_G , and Z_I .

- 1) From H we use Blanco's Eq. 3.8 to obtain ρ_{SA} .
- 2) Using Eqs. 8.29 and 8.30 we compute the surface pressure P_{SA} .
- 3) Assuming a dry adiabat up through inversion base, and assuming the air saturates at the inversion height, we compute $T_{DI} = T_G - \Gamma_d Z_I$, the dewpoint temperature at the inversion base height, using the dry adiabatic lapse rate $\Gamma_d = 9.8 \text{ K/km}$.

That is, we do not solve for T_D as a function of height. Rather, we simply assume that $T_D = T$ at the top of the boundary layer, and we assume we know the height Z_I where this crossover between the 2 temperature tracks will occur. Granted, this is a rather large assumption. Alternatively, we could model T_D as a function of height (e.g., Fiorino et al. 2014).

- 4) Given this dewpoint temperature, T_{DI} , we compute the vapor pressure at the inversion base by assuming $V_{pI} = V_{pI}^S(T_{DI} - 273.16)$, using Eqs. 8.36 and 8.37, and $R_H = 1.0$, the saturation condition. (This supplies us with a vapor pressure at the top of the boundary layer, but to find a q_a or r_m from Eqs. 8.34 and 8.35, we still need a pressure at the top of the boundary layer, $P(Z_I)$.)
- 5) Assuming the specific humidity is approximately constant throughout the boundary layer — a key assumption — then both q_a and r_m are constant with height.
- 6) From Eq. 8.35, therefore V_p/P is constant throughout the boundary layer. Unfortunately, we only know P at the bottom of the boundary layer. To obtain $P(Z_I)$ we adopt Beer's (1974) Eq. 1.2.21 (adapted to this model) based on a dry adiabatic lapse rate:

$$P(Z_I) = P(0) [(T_G - \Gamma_d Z_I)/T_G]^{\gamma/(\gamma-1)}, \quad (8.38)$$

where $\gamma = C_p/C_v = 1.4$ is the ratio of specific heats for dry air at constant pressure (C_p) to constant volume (C_v).

7) Given $V_p(Z_I)/P(Z_I)$, use Eq. 8.35 to solve for q_a and r_m .

8) Finally, Eqs. 8.31 through 8.33 can then be used, with the estimated r_m to calculation T_v given the more exact temperature profile $T(Z)$, then $\rho(Z)$, and $P(Z)$.

9) If desired, this procedure can be iterated to produce better estimates of r_m and q_a .

10) The computed profiles of temperature, pressure, and specific humidity then supply dry and moist values for Eq. 8.28 atmospheric-absorption coefficients:

$$\rho_w = \epsilon_w 0.34838 \frac{V_p}{T} = \frac{r_m}{(1 + r_m)} \rho_a = q_a \rho_a; \quad (8.39.A)$$

$$\rho_d = \frac{1}{(1 + r_m)} \rho_a = (1 - q_a) \rho_a. \quad (8.39.B)$$

11) Once the boundary layer has been established, a model of the air above is specified as follows: Using Stull's (1988) Fig. 3.8 data behavior, the specific humidity above the boundary layer is modeled as $q_u = q_a/3$. We transition to this value over a span of 250 m, representing the capping inversion's thickness. In this layer the temperature gradient reduces from the dry adiabatic profile's -9.8 K/km to the moist adiabatic rate of -6.4 K/km. Above this capping-inversion height ($Z_I + 250$) we resume the dry adiabatic lapse-rate profile.

The remaining inputs required to use Eq. 8.28 are the P_α , T_α , and q_α values corresponding to those appropriate for the tabulated extinction-data output by the MODTRAN code. These can be inferred from the metadata information contained as the preamble of MODTRAN's Tape-6 output file. This file lists values of temperature and pressure for each 1-km-thick layer. However, the information supplied appears to pertain to the lower boundary of each layer, while the output extinction information appears to relate to molecular densities averaged over each layer.

This appears to be true for both the dry-air concentration as well as the water-vapor content, though the listed relative humidity (46.04%) does appear to be the average quantity for the first-kilometer layer that is our focus. To verify this, the

MODTRAN documentation indicates the standard water-vapor content in the first kilometer is 7,750 parts per million (ppm). The code's output water-vapor content for the first km is indicated as 734 ATM CM/KM, where the dimension indicated seems to have a cryptic meaning. Similar output values for CO₂ and O₂ are also listed, as 34.6 and 19,800 ATM CM/KM, respectively, that supply us with a means of interpreting this meaning.

These values appear to be scaled relative to their sea-level values. If we interpret ATM CM/KM to indicate the number of centimeters of air at standard temperature and pressure as a portion of the first kilometer of air filled by this constituent, then the 19,800 reported for oxygen equates to 198.0 meters of sea-level pressure-temperature oxygen in the first kilometer. Since the standard nitrogen content is 78.10% of the atmosphere, oxygen is 20.90%, and most of the rest of the dry atmosphere is made up of argon (0.93%), 19,800 would correspond to 944.7 m of dry atmosphere at standard pressure and temperature, or an average density over the first kilometer that is 5.53% less than its surface value. To rescale the 734 listed for atmospheric water vapor back to its full amount, one could simply use the oxygen values at sea level and averaged over the kilometer to calculate $734 \times 209/198 = 774.78$ cm/km, or a water-vapor content of 7,748 ppm, which compares closely with the 7,750 ppm value listed in the MODTRAN manual.

Based on this result, let us assume the mean modeled temperature in the first kilometer is $T_\alpha = 288.1 - 3.2 = 284.9$ K, where half of the moist adiabatic lapse rate of 6.4 K/km has been subtracted from the mean sea-level temperature. The pressure used as the extinction baseline (P_α) can then be calculated from

$$\frac{P_\alpha}{P_{SL}} \frac{T_{SL}}{T_\alpha} = \frac{P_\alpha}{1013.252} \times \frac{288.1}{284.9} = \frac{734}{775} \rightarrow P_\alpha = 949. \quad (8.40)$$

A similar calculation performed on the 34.6 statistic given by MODTRAN for the CO₂ content produces $34.6 \times 775/734 = 36.5$ or 365 ppm. Current CO₂ levels are at roughly 402 ppm, indicating the output values of CO₂-based absorption will need to be increased by 1.101. Because of yearly increases in atmospheric CO₂ content, the dry-atmospheric term will have CO₂ extinction separately tracked.

To summarize, MODTRAN's baseline first-kilometer extinction coefficients relate to baseline pressure and temperature settings of $P_\alpha \approx 949$ mbar and $T_\alpha \approx 284.9$ K, a baseline $q_\alpha = 0.0048$ specific humidity, and atmospheric CO₂ content at 365 ppm.

However, running MODTRAN-4 using the full standard atmosphere of humidity produces high-extinction coefficients in some spectral bands, so the code was run such that the relative humidity was set to a factor of 100 less than the standard value. The results of these calculations are plotted in Fig. 22 for extinction coefficients over the first kilometer of the model atmosphere.

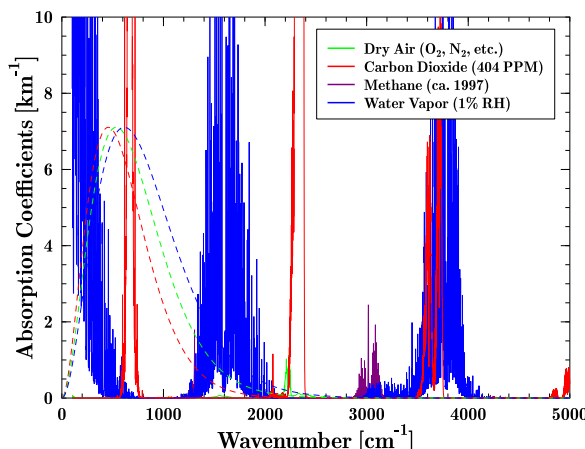


Fig. 22 Four extinction-coefficient curves based on MODTRAN output: blue curve is for water vapor at 0.46% relative humidity, red curve plots CO₂ extinction at 404 ppm, purple curve is methane, and green curve plots remaining dry-air gas effects; also, superposed are blackbody curves at 233 K (red), 273 K (green), and 313 K (blue).

Of particular interest within this Figure is the 8–12 μm “atmospheric window” occurring in the 800–1,200 wave number range. This is the main gap in the greenhouse-gas blanket that accounts for thermal radiation emitted to space. The other major gap occurs at 3–5 μm , the midwave IR (MWIR) window (wave numbers 2,000–3,000). While this window is suited to energy emitted higher in the atmosphere, the 8–12 window permits radiation emitted from the surface to escape to space. The CO₂ band at 15 μm is the main feature related to global warming, although from its appearance in the graph it clearly is already highly saturated. Contrasting with the CO₂-absorber behavior are 2 spectrally broad water-vapor bands: one extending down to 20 μm , the other extending across the 5–8 μm region.

Because the atmosphere’s water-vapor content is highly variable, its greenhouse-gas influence is also highly variable. As an illustration, Fig. 23 shows the effects of plotting water vapor at its standard humidity level of 46% versus a doubled CO₂ level (red) and unmodified dry-air and methane contents. As shown, water-vapor effects at normal levels drown out the influence of methane, while double-CO₂

content has little influence on the width of its bands. Conversely, the water-vapor bands show considerable widening, even at normal levels. Yet water-vapor content can be up to roughly 4 times the US Standard Atmosphere level in high-temperature and high-humidity conditions.

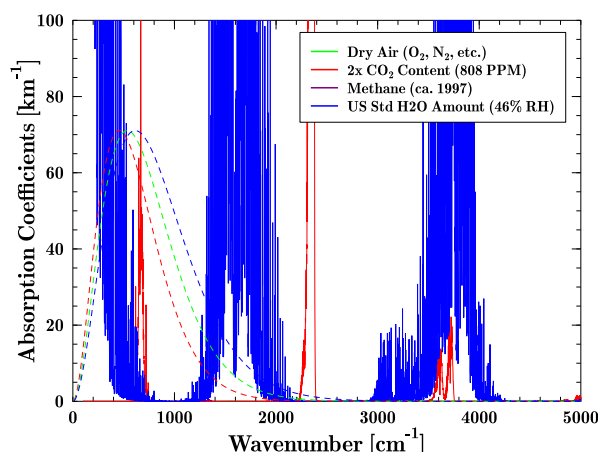


Fig. 23 Four extinction-coefficient curves based on MODTRAN output: same data as Fig. 22 shown, except water-vapor content (blue curve) is plotted as its Standard Atmosphere value, and CO₂ content (red curve) has been doubled (to 808 ppm); green plots the remaining dry-air contents and the purple line is the same methane effect as in Fig. 22, along with the same blackbody curves.

8.6 Atmospheric-Radiation Calculations

Using the outputs from a first-stage calculation of the extinction coefficients based on the MODTRAN outputs, a second-stage model was then developed to compute the net long-wave radiation reaching the surface under varying conditions using the vertical structure models of Chapter 6. The height of the surface was varied from sea level to 2,000 m. The height of the boundary layer was varied from 1,000 m to 4,000 m in 1,000-m increments. The neutral-condition temperature, T_G , was varied from -40°C to $+40^\circ\text{C}$. The thickness of the surface layer, Z_T , was varied from 5 m to 200 m; and, the vertical temperature gradient was varied from -0.5 C/m to $+2.0\text{ C/m}$. In all, some 9,000 combinations of conditions were generated for each propagation scenario. Beyond the basic question of which value to assign the atmospheric emissivity (compared to both the Staley–Jurica and Sellers formulas), an additional goal was to supply the model with a means of transferring energy between the different layers of the model’s atmosphere.

To model the atmosphere, 3 layers were considered: the surface layer positioned from 0 to Z_T , the remainder of the boundary layer located between Z_T and Z_I ,

and the upper troposphere above Z_I . The fluxes between these layers are illustrated graphically in Figs. 24 through 26.

To understand the symbology used, consider Fig. 24. Arrowheads at the tails of lines represent blackbody sources — either the undersides of clouds or the surface interface. Each flux has a four-letter label (e.g., SL SI) that denotes the radiation source (first 2 letters) and the energy destination (last 2 letters) within the model framework. The C1, C2, and C3 represent radiation flowing downward underneath low, medium, and high cloud decks. The UA represents the upper-atmosphere (troposphere) source radiation under cloudless conditions, while the C1, C2, and C3 results combine radiation emitted by the clouds plus additional radiation included in the downward-streaming radiation down to and including the base of the elevated inversion ($Z \geq Z_I$). Solid lines represent computed emissions of radiation in the atmosphere. Dashed lines correspond to radiation transmitted through a layer without further emissions in the layer passed through.

In Figs. 25 and 26 several fluxes are labeled using 5-letter combinations. This reflects the necessity of computing the related fluxes by subtracting the output from a layer from the input to the layer, assuming the remainder is the radiation absorbed by the layer. Hence,

$$C3BL = C3BL0 - C3SL0; \quad C3SL = C3SL0 - C3SI; \quad (8.41.A)$$

$$C2BL = C2BL0 - C2SL0; \quad C2SL = C2SL0 - C2SI; \quad (8.41.B)$$

$$C1BL = C1BL0 - C1SL0; \quad C1SL = C1SL0 - C1SI; \quad (8.41.C)$$

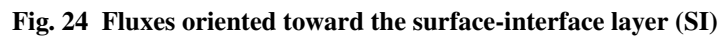
$$UABL = UABL0 - UASL0; \quad UASL = UASL0 - UASI; \quad (8.41.D)$$

$$BLSL = BLSL0 - BLSI; \quad SLBL = SLBL0 - SLUA; \quad (8.41.E)$$

$$SISL = SISL0 - SIBL0; \quad SIBL = SIBL0 - SIUA. \quad (8.41.F)$$

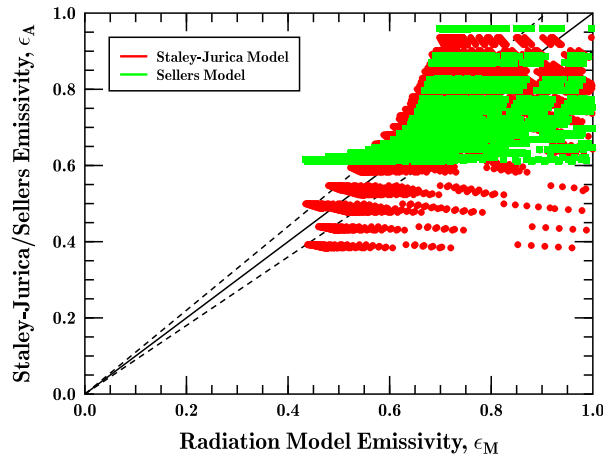
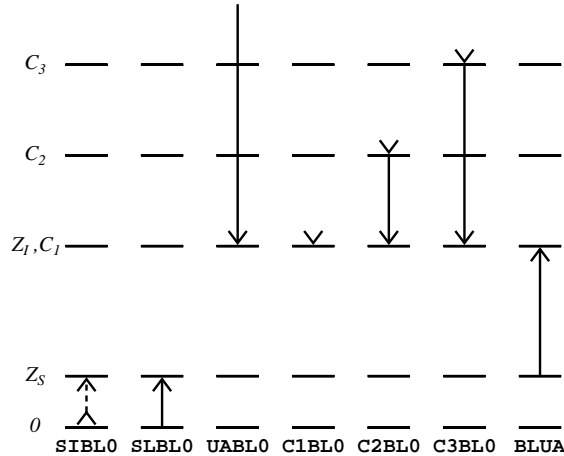
From the model's perspective, we do not care what happens to the radiation once it emerges from the boundary layer, only that it is lost, representing a cooling effect. Thus, upward-directed fluxes all stop at the elevated inversion base.

In addition to the atmospheric fluxes, the surface-interface fluxes are dependent on the temperature of the vegetation and the soil separately. And since the air temperature curve cannot connect directly to both the foliage and soil temperatures at once, the radiation calculations were performed for a range of surface temperatures, from 0 °C to 40 °C above (if $T_* < 0$) or below (if $T_* > 0$) T_G .



The statistics derived from these calculations can be compared to the results of the Staley–Jurica and Sellers formulas. The net total radiation reaching the surface is given by, effectively, the sum $\text{SLSI} + \text{BLSI} + \text{UASI}$ for the cloud-free case; in combination with C1SI, C2SI, or C3SI replacing UASI for the overcast case; or a combination of the 2 for intermediate conditions.

150



Visual inspection of these results is complicated by the fact that we required an input air temperature to compute either of the analytic models. Yet, due to the varying temperature model employed it became impossible to choose a characteristic temperature. In lieu of knowledge of a correct, effective air temperature, T_G was chosen. Obviously, neither the Staley–Jurica (SJ) model nor the Sellers (SL) model performs well when atmospheric conditions involve rapidly varying air temperatures near the surface.

Therefore, a second reduced set of results is plotted in Fig. 28. In it, only results associated with neutral conditions are plotted. These results indicate a considerably tighter dependence relative to fitting using the SJ and SL models.

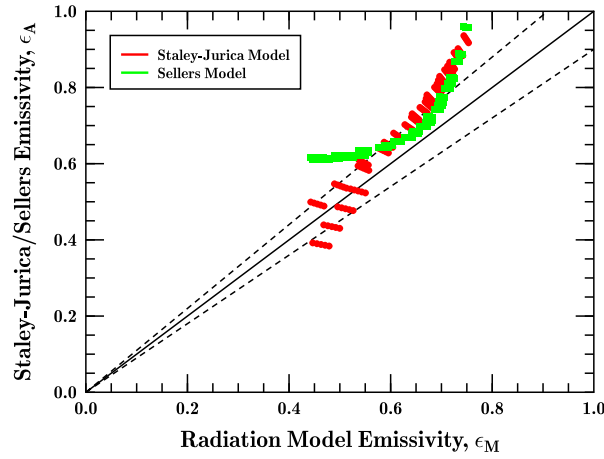


Fig. 28 Two scatterplots comparing computed emissivity values (abscissa, x-axis component) versus Staley and Jurica's (red) or Seller's (green) analytic emissivity expressions (ordinate components) for a series of neutral-atmosphere cases

In addition to the main 1-to-1 fit possible, linear lines

$$\epsilon_2 = 0.9 \epsilon_1 \quad \text{and} \quad \epsilon_2 = 1.1 \epsilon_1$$

are also plotted. The SJ curve appears to be a better fit to the numerical solutions, and perhaps could be fixed through a rescaling of its results. Yet SJ features a zero emissivity at zero humidity. In contrast, the Sellers curve appears to have a non-linear correlation to the computed results. Both appear to perform relatively poorly when near-surface temperatures are varying. This indicates the significance of near-surface radiation to the total downwelling long-wave radiation.

In these calculations, the range of humidities tested was fairly wide. Perhaps this explains why the SJ curve fell considerably at low humidity levels while the computed results did not. Perhaps the presence of CO_2 in the spectrum kept the emissivity from falling precipitously. On the other hand, at high relative humidities corresponding to high emissivities in both the SJ and SL models, the computed emissivity did not increase precipitously, either. In this sense, the computed results appear to exhibit more of the behavior expected, where a doubling of water vapor appears to have a similar effect per doubling, while the analytical curves appear to exhibit more effect than a uniform increment per doubling. Also, the computed results model the reduction in dry-air content and reduced density as the humidity level increases.

It should be relatively easy to verify the temperature and humidity aspects of the Staley and Jurica and/or computed results through measurements at a single site. More difficult would be verification of the pressure effect, which would require data campaigns at multiple sites at different heights above sea level. In any case, the relative consistency between the computationally integrated results and the Staley and Jurica expression indicates these 2 are similar. The key difference is that the Staley and Jurica results go to zero at zero humidity; the computational method does not. However, calculations were not made at exactly zero relative humidity because part of the calculations involve dividing through by the humidity level, creating an overflow situation. Given more time this calculation method can be extended to zero relative humidity.

9. Further Developments

In this final chapter of the technical portion of the report, we consider the means of modeling several aspects of the diurnal problem that can influence the transition to the nocturnal atmosphere as well as the development of the vertical perturbations of turbulence within the nocturnal boundary layer. We begin by studying/modeling the vertical structure of the daytime horizontal wind field. This is followed by a study of the low-level nocturnal jet. Through these 2 analyses we can determine from just a few inputs the general course of the wind field that is driving the turbulent fluxes at the surface. These 2 are followed by a pair of related analyses of nighttime-turbulence production. The first considers conditions supporting small-scale turbulence production. Essentially, this amounts to a reanalysis of the critical Richardson number. The second is a detailed analysis of the conditions for gravity-wave production and collapse; in the process, it develops an argument for a characteristic breaking time of such waves and how they can feed perturbation energy into the boundary layer even under seemingly stable conditions.

9.1 Diabatic Wind Modeling

In this section the standard daytime *Ekman spiral* wind profile is first discussed, and then the evolution of the nocturnal *low level jet* (Blackadar 1976) is considered. In the model developed, the user is assumed to provide minimal information. Assuming the user supplies a mean wind speed at an observation-station height the model attempts to construct a vertical profile, in particular a profile that approaches the speed of the geostrophic wind at the top of the boundary layer (the base of the elevated inversion).

The general momentum equation for horizontal wind components U_x and U_y can be written,

$$\frac{dU_x}{dt} = f_c (U_{Gy} - U_y) - f_c F_x, \quad (9.1.A)$$

$$\frac{dU_y}{dt} = f_c (U_{Gx} - U_x) - f_c F_y, \quad (9.1.B)$$

where $f_c = 2\omega \sin(\phi)$ is the Coriolis parameter (Stull 1989, 78) representing the rate of evolution of the Coriolis rotation at latitude ϕ , and $\omega = 2\pi$ radians per 24 h is the rotational rate of the earth, equal to $7.27 \times 10^{-5} \text{ s}^{-1}$. (From the Coriolis parameter, a period of rotation of the atmosphere can be defined as $T_I = 2\pi/f_c$. At most mid-latitude locations this period is approximately 17 h. This quantity is also termed the *inertial period*.)

Quantities F_x and F_y are drag terms that are expressed in dimensions of velocity.

The *geostrophic wind* (Stull 1989, sec. 3.3.3) represents a static solution to the Navier–Stokes momentum equation. In it, the wind-velocity vector's $(U_x, U_y) = (U_{Gx}, U_{Gy})$ centrifugal force in Cartesian coordinates of (x, y) is balanced against the horizontal pressure gradient due to the local synoptic weather condition. This is expressed by the equation pair,

$$f_c U_{Gx} = -\frac{1}{\rho_a} \frac{dP}{dy}; \quad f_c U_{Gy} = +\frac{1}{\rho_a} \frac{dP}{dx}. \quad (9.2)$$

Note that for most locations, T_I will be longer than the duration of the nocturnal period. Thus, typically the atmosphere cannot cycle through a complete inertial period before the night ends.

Based on the assumption that the coordinate system is oriented such that the geostrophic wind is $(U_{Gx}, U_{Gy}) = (U_G, 0)$, there is only one nonzero term:

$$U_G = -\frac{1}{f_c \rho_a} \frac{dP}{dy}, \quad (9.3)$$

since $dP/dx = 0$. Typical values of U_G are on the order of 10 m/s. The use of a geostrophic wind also assumes there is no drag effect on the wind and therefore this wind speed is applicable to the top of the boundary layer.

Below the top of the boundary layer the wind speed follows a profile commonly modeled as the Ekman spiral. To model this effect, the wind profile is assumed to approach a steady state,

$$\frac{dU_x}{dt} = 0 = f_c U_y - f_c F_x; \quad (9.4.A)$$

$$\frac{dU_y}{dt} = 0 = f_c (U_G - U_x) - f_c F_y. \quad (9.4.B)$$

The F_x and F_y drag terms are expressed in Ekman's formulation as depending on second-order derivatives of the wind components:

$$F_x = K_m \frac{\partial^2 U_x}{\partial x^2}; \quad F_y = K_m \frac{\partial^2 U_y}{\partial y^2}. \quad (9.5)$$

The solution to the differential-equation set then is written,

$$F_x = K_m \frac{\partial^2 U_x}{\partial x^2} = U_y(\text{daytime}), \quad (9.6.A)$$

$$F_x = K_m \frac{\partial^2 U_y}{\partial y^2} = U_G - U_x(\text{daytime}). \quad (9.6.B)$$

Here, K_m is the *coefficient of eddy viscosity* (e.g., Houghton 1977). If K_m is a constant of height, then this equation set may immediately be solved:

$$U_x(Z) = U_G [1 - \exp(-\gamma Z) \cos(\gamma Z)], \quad (9.7.A)$$

$$U_y(Z) = U_G \exp(-\gamma Z) \sin(\gamma Z). \quad (9.7.B)$$

Note that in the northern hemisphere the departure of U_y (due to the Coriolis force) is always to the left of the geostrophic wind and therefore in the direction of positive y , while the departure in the along-geostrophic direction is always negative, so U_x is always less than U_G . The constant γ is given as

$$\gamma = \sqrt{f_c / (2K_m)}. \quad (9.8)$$

At height $Z = \pi/\gamma$, $U_x \approx U_G$ and $U_y = 0$, which is the condition of the wind vector at the top of the boundary layer. Thus π/γ is approximately the height of the boundary layer. Since the model tracks the height of the boundary layer elsewhere, instead of requiring a separate evaluation of K_m , we can simply set

$$\gamma = \pi/Z_I. \quad (9.9)$$

However, K_m is not generally a constant of height (Houghton 1977; Stull 1989). Nonetheless, in lieu of further information the Ekman spiral provides a useful starting place for characterizing daytime winds aloft.

To correct the Ekman analysis for nonconstant K_m , one must obtain a substitute approximation for Ekman's choice, of

$$-\rho_a [\langle u' w' \rangle^2 + \langle v' w' \rangle^2]^{1/2} = \rho_a K_m \frac{\partial U}{\partial Z}. \quad (9.10)$$

Here, the quantity in angle brackets is the correlation between wind perturbations in the vertical direction (w') and in the horizontal directions (u' and v'). The quantity on the left is termed the turbulent vertical momentum flux, whereas the quantity on the right depends on the vertical gradient of the mean wind speed. Hence, this is another flux-profile relation. And, of primary interest is the behavior of this function outside the surface layer where the quantity in square brackets is a variable function

of height (as opposed to its behavior in the surface layer where it is assumed to be a constant of height within the layer).

This problem has not been solved for the model. Complicating the daytime characterization is the effect of the convective rolls mentioned elsewhere that would tend to transfer momentum into the surface layer but not through a small-scale mechanism directed by the vertical gradient.

Consider the rise time computed in Eq. 6.11. There, the time required for heated air to mix out of the surface layer into the upper portion of the boundary layer was considered. In that calculation the height used for the mixing was Z_T , the surface-layer thickness. However, a second rise time could also be inferred using Z_I that would be associated with the time required to mix air heated at the ground into the complete boundary layer. This time,

$$t_{rise,B} = \sqrt{2 Z_I / a} = \sqrt{2 Z_I T_A / (g \Delta T)}, \quad (9.11)$$

which characterizes a forcing time associated with momentum added to the boundary layer. As is frequently observed, daytime wind speeds typically increase in speed as convective rolls appear in the boundary layer. To characterize typical times and velocities involved, we could divide the rise time for the surface layer into the depth of the surface layer to characterize a velocity perturbation,

$$\Delta U \approx \frac{Z_T}{t_{rise}} = \sqrt{Z_T a / 2}. \quad (9.12)$$

Then, assuming this perturbation must propagate around the convective roll, the propagation time would equal approximately 4 times the height to the elevated inversion base, $4 t_{rise,B}$. Let us consider a boundary-layer height of $Z_I = 2,000$ m and an acceleration of $a \approx 0.1$ m/s². Then the propagation time becomes 800 s, a delay of approximately 13 min. Such perturbations in wind speed would tend to drive further fluctuations in heating that would cause further fluctuations in the wind, etc.

Ultimately, the objective would be to obtain expressions for the vertical variation of wind speed consistent with both the Ekman spiral model, similar to the approach used in modeling the temperature profile such that the wind-speed gradient approached zero at the top of the boundary layer and approached the flux-profile

form (e.g., Paulson 1970) in the surface layer, as developed in Chapter 6. But in addition to the mean wind, a fluctuating wind component would be added to account for variations in wind speed that would add perturbations to the heat production near the surface. Complicating this picture is the nature of the Ekman spiral relation that models 2 components of the wind.

9.2 Nocturnal Low-Level Jet Development

Assuming such a model is possible for the mean wind profile, a model for the nighttime evolution of the wind profile is also needed. The Ekman spiral form then provides the starting-point profile that evolves into the nocturnal *low level jet* profile. The theory of the nocturnal jet postulates that at sunset as the surface-based inversion sets up, it produces a condition where there is reduced turbulence aloft. At some elevation, $Z > Z_C$ (critical height), the wind gradient is not strong enough to maintain turbulent turnover of the air at a given level. When this occurs, the wind experiences an acceleration due to the Coriolis force.

The rationale for such accelerations is that the daytime wind profile features increased drag effects due to buoyant mixing of air from the surface layer into the boundary layer. This effect is experienced as an increased drag coefficient during the daytime, with the wind speed falling as Z decreases. Conversely, when the atmosphere becomes *stable*, cooler air near the ground suppresses vertical mixing, drag effects are reduced, and the momentum equation may be approximated by

$$dU_x/dt = f_c U_y \quad , \quad (9.13.A)$$

$$dU_y/dt = f_c (U_G - U_x), \quad (9.13.B)$$

where the drag coefficients have been set to zero. The solution to this equation set is such that the velocity vector orbits a central wind vector $(U_G, 0)$ over the inertial period $T_I = 2\pi/f_c \approx 17$ hr. Hence, the wind speed above the surface will peak at around 8.5 hr after the neutral event. Since winds near the surface start at a value less than winds aloft, a wind-speed maximum appears at an elevation close to the ground. The fact that the maximum does not occur exactly at the ground is due to the simplifying assumption made above where the drag effects were completely removed. Obviously, this procedure is not accurate close to the ground.

Assuming a layer that follows the above rules approximately, we first set the initial conditions and then evolve them. Once the daytime conditions end, the final daytime

state becomes the initial state for the nocturnal winds. We equate this condition to the winds at the neutral event:

$$U_x(0) = U_x(\text{neutral}) = U_G - F_y(\text{daytime}), \quad (9.14.A)$$

$$U_y(0) = U_y(\text{neutral}) = F_x(\text{daytime}). \quad (9.14.B)$$

This state may then be introduced in solving the nocturnal winds:

$$U_x(t) = U_G - F_y \cos(f_c t) + F_x \sin(f_c t), \quad (9.15.A)$$

$$U_y(t) = F_y \sin(f_c t) + F_x \cos(f_c t). \quad (9.15.B)$$

The maximum wind velocity is then $U_G + (F_x^2 + F_y^2)^{1/2}$ obtained in 6–8 hours.

To complete this model a near-surface drag effect consistent with the typical nocturnal profile must be postulated. Some insight into the nature of the drag variability is gained by considering a cylinder of air rotating under the influence of a vertical velocity gradient in the presence of a rotation-suppressing, negative density-gradient.

9.3 Small-Scale Nocturnal Turbulence Generation

In the next 2 sections an extended analysis of a turbulent cylinder is first presented, followed by the development of a surface-layer-based gravity-wave model under conditions of the stable surface layer. In these analyses various detailed calculations are provided, several minor errors are resolved, and methods are developed for solving the gravity-wave calculation.

An earlier analysis (Tofsted 1993, App. B) examined the criteria for the existence of turbulence in a stable flow. As is well known, the nocturnal stable atmosphere features a vertical temperature gradient that is positive (the surface-based inversion).

Under daytime *unstable* atmospheric conditions, featuring a temperature lapse rate that is negative, any motion of the air is potentially able to produce a turnover in the atmosphere leading to vertical fluxes of warm air away from the ground. This can be modeled using a simple cylinder of air featuring mean vertical gradients of both temperature and wind speed. However, at night as stable atmospheric conditions are

established the atmosphere will suppress such attempts at turnover and each layer will remain in place, resulting in near-laminar flow.

In the previous analysis (Tofsted 1993, App. B) a simple model was used to study such flow. Vertical gradients of density and wind speed were considered constant over a small cylinder. Analysis of the cylinder's rotational kinetic-energy and potential-energy states was performed. The angular momentum of the cylinder was found to be

$$L_A = (\rho_0 \dot{u} + \dot{\rho} u_0) \frac{V R^2}{4}. \quad (9.16)$$

Here, the mean density of the cylinder is given as ρ_0 , the mean wind speed is u_0 , and the vertical gradients of density and wind are given as $\dot{\rho} = d\rho/dz$ and $\dot{u} = du/dz$. The volume of the cylinder is given by $V = \pi R^2 Y$, where the wind is directed along the positive x axis, the vertical axis in which the gradients are directed is designated by z , and y is in the crosswind direction. R is the radius of the cylinder, while Y is the cylinder length along the y axis.

The cylinder's rotational inertia can be computed as $I = \rho_0 V R^2/2$. Then, the rotational kinetic energy can be computed using

$$KE_A = \frac{L_A^2}{2I} = \left(\dot{u} + \frac{\dot{\rho}}{\rho_0} u_0 \right)^2 \frac{\rho_0 V R^2}{16}. \quad (9.17)$$

Counteracting this available kinetic energy is the potential energy to be overcome. From its stable state where the densest air is considered to be at the bottom of the cylinder and the lightest air at the top, it was found that one must overcome the negative potential energy,

$$PE_A = -2 \dot{\rho} g \frac{V R^2}{4}, \quad (9.18)$$

where $g = 9.8 \text{ m/s}^2$ is the gravitational acceleration. That is, we must have

$$KE_A \geq PE_A, \quad (9.19)$$

in order to have turnover.

Introducing the expanded equation forms from Eqs. 9.17 and 9.18, Eq. 9.19 can be written as

$$\left(\dot{u} + \frac{\dot{\rho}}{\rho_0} u_0 \right)^2 \frac{\rho_0 V R^2}{16} \geq -2 \dot{\rho} g \frac{V R^2}{4}, \quad (9.20)$$

where $\dot{\rho} < 0$. However, note that we are only interested in the density gradient that is different from that achieved by normal adiabatic effects. Thus, we write the density vertical gradient as

$$\frac{\dot{\rho}}{\rho_0} = -\frac{\dot{\theta}}{\theta}, \quad (9.21)$$

adopting the potential temperature, θ , as a replacement for temperature T . Note that if we had retained the pressure-gradient term, we would have discovered that the pressure gradient effect is dominant, but only outside the boundary layer, since,

$$\frac{\dot{\rho}}{\rho_0} = -\frac{\alpha g}{\theta} - \frac{\dot{\theta}}{\theta} = -\frac{0.03414}{\theta} - \frac{\dot{\theta}}{\theta}, \quad (9.22)$$

where $\alpha = 1/R$, where $R = 287 \text{ J/kg-K}$ is the gas constant for dry air, and $g = 9.8$. Nonetheless, this form also include an adiabatic density decrease that must be cancelled out, since it does not influence buoyancy. Therefore Eq. 9.21 is the correct form. Substituting this expression into Eq. 9.20, and cancelling terms, the condition for successful turnover can be reduced to the form,

$$\dot{u} + \frac{\dot{\theta}}{\theta} u_0 > \sqrt{+\frac{8 g \dot{\theta}}{\theta}}. \quad (9.23)$$

This expression may be simplified by removing the second term on the left. Due to the presence of θ on the order of 270 K or higher in the denominator of this term, it will be small compared to both the first term on the left and the term on the right that features only a $\theta^{-1/2}$ dependence. The condition can then be written in the approximate form

$$\frac{\dot{u}^2}{8 g} > \frac{\dot{\theta}}{\theta}. \quad (9.24)$$

Further progress was achieved by introducing the nocturnal (stable layer) expressions for the wind- and temperature-gradient functions in the surface layer:

$$\dot{u} = \frac{u_*}{k z} \left(1 + \beta \frac{z}{L_{Ob}} \right), \quad (9.25)$$

$$\dot{\theta} = \frac{T_*}{k z} \left(1 + \beta \frac{z}{L_{Ob}} \right), \quad (9.26)$$

where k is von Kármán's constant (approximately equal to 0.4), z is height above the ground, L_{Ob} is the Obukhov similarity scaling height for the surface layer, u_* is the friction velocity, and T_* is the scaling temperature.

Introducing these definitions, the condition equation was reduced to the relation,

$$\frac{\theta}{g} \frac{u_*^2}{k T_*} \left(\frac{1}{z} + \frac{\beta}{L_{Ob}} \right) > 8. \quad (9.27)$$

This was the final result in the Appendix (Tofsted 1993), given in Eq. B-16. However, the definition of the Obukhov length is given as

$$L_{Ob} = \frac{u_*^2}{k g T_*/\theta}. \quad (9.28)$$

Introducing this definition on the left we obtain

$$\left(\frac{L_{Ob}}{z} + \beta \right) > 8. \quad (9.29)$$

The value of β is commonly believed to be approximately 5 (Businger gives the value as 4.7). Solving for z relative to L_{Ob} , we now find the condition reduced to

$$z < \frac{L_{Ob}}{3}. \quad (9.30)$$

Under neutral conditions the Obukhov length tends to increase toward infinity and any vertical wind gradient is sufficient to produce a turnover, leaving z unrestricted. But as stable conditions become established and the Obukhov length is reduced, the region of the air that remains turbulent is restricted to a layer close to the surface. Only within this layer are vertical wind gradients strong enough to thwart the stable, vertical density-gradient component from suppressing vertical motions that lead to laminar flow.

Hence, for even minor inversion conditions (i.e., for L_{Ob} of even moderate values: 10s to 100s of meters), there will exist a layer that becomes detached from the drag effects of the surface, in which turbulent flow is sufficiently suppressed that near-laminar-flow conditions prevail. This will cause the surface to become disconnected from the air above and lead to nocturnal wind accelerations associated with nocturnal jet flow.

Also note that this condition appears to contradict the very grounds used in defining the Obukhov length in the first place. That is, we normally associate the Obukhov length with a height scale that covers a constant stress layer. But we have just shown that for the standard vertical-structure functions given for that layer, one obtains turnover only over the first third of the layer, an apparent contradiction.

9.4 Gravity-Wave Turbulence in the Stable Surface Layer

Let us now consider a related influence on the nocturnal boundary-layer atmosphere. The state of the atmospheric surface layer at night is characterized as being *stable* in the sense that the vertical temperature gradient is generally positive (coldest air is near the surface) due to radiative cooling of the ground. As we have seen in the previous section this cooling, when applied to even small parcels of air, can cause them to be unable to turn over due to differential temperatures at the top and bottom of a cylinder. More generally, when any parcel of air in a stable atmosphere is displaced from its original height due to adiabatic warming (lowering it) or cooling (raising it), it becomes out of balance with other air at the same level. Raising it makes it denser than surrounding air and it tends to sink, while lowering it causes it to be warmer than the surrounding air and it gains buoyancy, tending to want to rise. The characterization as being *stable* thus refers to the tendency of the parcel to return to its original height.

However, due to the effect of the buoyancy, this stability is dynamic. In the absence of viscous forces, a displaced parcel will tend to oscillate about its point of origin. This means that when wind advects such stable air over certain terrain features, the terrain interaction with the advected air causes the mean flow of wind to stimulate what are termed *gravity waves*: waves that exist as transverse stability-based perturbations of the flow. Such waves remove energy from the mean flow and introduce energy into wave modes that propagate with the wind. However, while a *stable* atmosphere gives rise to such wave modes, these waves are far from stable. Rather, because the wind is vertically varying, these waves tend to disperse as they propagate. And, like waves at a beach, once a dense portion of a gravity wave has propagated out from under a less-dense portion, the wave density will become unstable where a denser portion of air lies over less dense air. As the denser air falls, this will cause mixing with air below; effectively, the layer will experience an overturning. This event will then cause air from above, characterized by faster wind speed (and presumably slightly warmer) to mix with air near the ground that is cooler and denser. The result will be an increase of the heat flux near the ground, warming the surface, but also extending the surface-based inversion to a greater depth and, at the same time, reducing the wind speed aloft due to increased dissipation rate.

Once the mixing event has sufficiently reduced the overall gradients of wind and temperature, the conditions for mixing no longer prevail. Then the atmosphere

re-establishes the disconnection between the wind and the surface, increasing gradients and the temperature gradient, but over a deeper layer, and the gravity waves reappear, repeating the process. However, the above description only provides a narrative. To produce a modeled effect we require a framework within which to produce a model. This new framework builds off the analysis of Beer's (1974) and a preliminary analysis included in Tofsted (1993).

9.5 Gravity-Wave Equation Set

First, let us define the quantity $\gamma = C_p/C_v \approx 1.4$ as the ratio of C_p , the specific heat of air per unit of mass at constant pressure, to C_v , the specific heat at constant volume.

Second, using $\rho = P/(RT)$ as the definition of density, with $R = 187$ and pressure P measured in Pascals (not millibars), let us define the quantity H as the scale height of the atmosphere. Holton (1979) expresses this quantity as

$$H = RT/g \approx 8 \text{ km.} \quad (9.31)$$

The scale height may be considered equivalent to the thickness of the atmosphere if it were considered to be of a constant density throughout. This length scale is also related the speed of sound, c , through the relation,

$$c^2 = \gamma g H. \quad (9.32)$$

These parameters basically tend to characterize static atmospheric conditions. For dynamic processes Beer (1974) introduces a discussion of Eulerian versus Lagrangian methods (point sensing versus point following) in which he provides the Stokes derivative,

$$\frac{DV}{Dt} = \frac{\partial V}{\partial t} + \mathbf{U} \cdot \nabla V. \quad (9.33)$$

Here, ∇ is a gradient operator and \mathbf{U} is the total wind vector, so that the second component represents an advection term while the first term represents just a point variation following the wind. This form applies to a scalar variable (V). For a vector quantity, \mathbf{V} , the operator becomes

$$\frac{D\mathbf{V}}{Dt} = \frac{\partial \mathbf{V}}{\partial t} + (\mathbf{U} \cdot \nabla)\mathbf{V}. \quad (9.34)$$

We are interested in the case where $\mathbf{V} \equiv \mathbf{U}$, which can be expressed (Arfken 1985) as

$$\frac{D\mathbf{U}}{Dt} = \frac{\partial \mathbf{U}}{\partial t} + \mathbf{U} \cdot \nabla \mathbf{U} = \frac{\partial \mathbf{U}}{\partial t} + \frac{1}{2}\nabla(U^2) + \mathbf{U} \times (\nabla \times \mathbf{U}). \quad (9.35)$$

But it will be just as easy to compute the result directly from the tensor form rather than invoke both the vector terms.

The Stokes derivative operator is applied to one of 4 field variables: P , ρ , U_x , and U_z , corresponding to the pressure, density, and along-wind and vertical-wind components. In general, each variable is divided into a mean component (subscript zero) and a perturbation (subscript one):

$$P = P_0 + P_1, \quad (9.36.A)$$

$$\rho = \rho_0 + \rho_1, \quad (9.36.B)$$

$$U_x = U_{x,0} + U_{x,1}, \quad (9.36.C)$$

$$U_z = U_{z,0} + U_{z,1}. \quad (9.36.D)$$

In each case (except where it is assumed zero), the zero-order variable is considered much smaller than the perturbation term.

For purposes of calculation, the perturbation quantities are all considered to exist within a framework of oscillating functions offset from one another by phase variations that remain constant, but obey the structural forms,

$$\frac{P_1}{P_0 V} = \frac{\rho_1}{\rho_0 W} = \frac{U_{x,1}}{X} = \frac{U_{y,1}}{Y} = \frac{U_{z,1}}{Z} = A_0 \exp [i (\omega t - \boldsymbol{\kappa} \cdot \mathbf{x})]. \quad (9.37)$$

Here $\mathbf{x} = (x, y, z)$, the 3-dimensional vector position, while $\boldsymbol{\kappa} = (\kappa_x, \kappa_y, \kappa_z)$ is the vector wave number and ω is the temporal radial frequency. Functions V , W , X , Y , and Z function as complex phase modifiers. However, we shall further find it useful to pick out the vertical dimension for development:

$$A(x, z, t) = A_0 \exp [i (\omega t - \boldsymbol{\kappa} \cdot \mathbf{x})] \rightarrow W(z) \exp [i (\omega t - \kappa_x x)]. \quad (9.38)$$

Beer's (1974) equations of motion for these variables consisted of the equation of motion, an energy equation accounting for the adiabatic atmosphere, and a mass continuity equation. These are expressed, respectively, as,

$$\frac{\partial \mathbf{U}}{\partial t} + \mathbf{U} \cdot \nabla \mathbf{U} = -\frac{1}{\rho} \nabla P + \mathbf{g}, \quad (9.39)$$

$$\frac{\partial P}{\partial t} + \mathbf{U} \cdot \nabla P = c^2 \left(\frac{\partial \rho}{\partial t} + \mathbf{U} \cdot \nabla \rho \right), \quad (9.40)$$

$$\frac{\partial \rho}{\partial t} + \nabla \cdot (\rho \mathbf{U}) = 0. \quad (9.41)$$

This set of equations encompasses 2 different types of solutions. The first solution is for acoustic waves. The second solution is our focus, related to gravity waves.

Some simplifications are possible when we limit the problem to just those conditions we are interested in. These include mean quantities that are time independent and mean wind quantities $U_{x,0} = A + Bz$ and $U_{z,0} = 0$. And while $U_{x,0}$ is variable with height, its vertical gradient is considered to be second order. Therefore,

$$(\nabla \times \mathbf{U}) \times \mathbf{U} \approx 0, \quad (9.42)$$

to first order (in this derivation). The Stokes operator can thus be approximated by

$$\frac{D V}{D t} \approx i(\omega - U_{x,0} \kappa_x) V = \hat{Q}(z) V. \quad (9.43)$$

This allows us to replace a main operator with a multiplicative function. In particular, the quantity $(\omega - U_{x,0} \kappa_x)$ is termed the Doppler-shifted frequency, designated Ω :

$$\Omega = \omega - U_{x,0} \kappa_x = -i \hat{Q}, \quad \hat{Q} = i \Omega. \quad (9.44)$$

First, when dealing with the mean fields, the mass continuity and energy equations are identically zero, while the momentum equation reduces to the hydrostatic equation,

$$\nabla P_0 = \rho_0 \mathbf{g}, \quad (9.45)$$

where $\mathbf{g} = -g \hat{\mathbf{k}}$. For the near-surface atmosphere treated within the boundary layer this calculation can be simplified if the temperature is constant. Using the scale height, H , the baseline density can be written as

$$\rho_0(z) = \rho_g \exp(-z/H). \quad (9.46)$$

Then, solving for the pressure,

$$P_0(z) = g H \rho_g \exp(-z/H) = P_g \exp(-z/H). \quad (9.47)$$

If, on the other hand, we are dealing with an atmosphere in which the temperature is varying linearly with height, say as $T(z) = T_g + \beta z$, then the pressure becomes

$$P_0(z) = P_g (1 + \beta z/T_g)^{-g/(R\beta)}, \quad (9.48)$$

where T_g is the ground temperature (at $z = 0$), just as ρ_g is the density at the ground and P_g is the pressure at ground level. Note that the 2 forms of pressure variation in Eqs. 9.47 and 9.48 are approximately equal when z/H is small. In this case the exponential in Eq. 9.47 approximates as $1 - z/H$, while $(1 + \beta z/T_g)^{-g/(R\beta)} \approx 1 - [gz/(RT_g)] = 1 - z/H_g$, where H_g is the H value evaluated using the ground-level temperature T_g .

Given these 2 forms, let us expand Eq. 9.41:

$$\frac{\partial \rho_1}{\partial t} + \mathbf{U}_0 \cdot \nabla \rho_1 - \rho_0 U_{z,1}/H + \rho_0 \nabla \cdot \mathbf{U}_1 = 0. \quad (9.49)$$

Simplifying, the first 2 terms on the right can be collapsed using the \hat{Q} operator. Second, the vertical derivative of ρ_0 produces only a second-order effect when multiplying the z -axis wind-perturbation component. Third, the wind-divergence term may be expressed using the term $\chi = \partial_x U_{x,1} + \partial_z U_{z,1}$. With these changes this equation appears as

$$\hat{Q} \frac{\rho_1}{\rho_0} - \frac{U_{z,1}}{H} (1 + \dot{H}) + \chi = 0. \quad (9.50)$$

This equation is equivalent to Eq. B-19d of Tofsted (1993) and to Beer's (1974) approach of using a term $-U_{z,1} \dot{H}/H$ that has been included to account for vertical variations of H .

Given the forms indicated for $U_{x,1}$ and $U_{z,1}$ in Eqs. 9.37 and 9.38, we could write out an expression for the divergence χ explicitly in expanding Eq. 9.50. However, it instead will be more effective to recognize that Eq. 9.40 and 9.41 can be combined, along with the definition of $\chi = \nabla \cdot \mathbf{U}$, to produce the relation,

$$\frac{\partial P}{\partial t} + \mathbf{U} \cdot \nabla P + c^2 \rho_0 \chi = 0. \quad (9.51)$$

The P differential term then expands, using Eq. 6.32, to produce,

$$\hat{Q} P_1 - U_{z,1} \frac{P_0}{H} + \gamma g H \rho_0 \chi = 0. \quad (9.52)$$

Dividing by P_0 , we recognize that $\rho_0 g H/P_0 = 1$, such that,

$$\hat{Q} \frac{P_1}{P_0} - \frac{U_{z,1}}{H} + \gamma \chi = 0. \quad (9.53)$$

This equation is equivalent to Eq. B-19c of Tofsted (1993).

The remaining 2 equations must be set up separately from the x and z components of Eq. 9.39. Start with the z component corresponding to Eq. B-19b of Tofsted (1993). The right side of Eq. 9.39 can be expanded as

$$-\frac{1}{\rho} (\partial_z P_0 + \partial_z P_1 + g \rho_0 + g \rho_1) \rightarrow -\frac{\partial_z P_1}{\rho_0} - g \frac{\rho_1}{\rho_0}, \quad (9.54)$$

where the P_0 gradient component balances the gravitational term ($\partial_z P_0 = -g \rho_0$). But, Beer chose (P_1/P_0) as his independent variable. Therefore, $\partial_z P_1$ must be transformed to appear as a function of only (P_1/P_0) . Consider,

$$\frac{\partial(P_1/P_0)}{\partial z} = \frac{\partial_z P_1}{P_0} - \frac{P_1}{P_0^2} \partial_z P_0. \quad (9.55)$$

From the Eq. 9.31 definition of H , we can rewrite $\rho_0 = P_0/(gH)$, such that,

$$\frac{P_1}{P_0^2} \partial_z P_0 = -\frac{g \rho_0 P_1}{P_0^2} = -\frac{1}{H} \frac{P_1}{P_0}. \quad (9.56)$$

Then, rearranging further,

$$\frac{\partial_z P_1}{P_0} = \frac{\partial(P_1/P_0)}{\partial z} + \frac{P_1}{P_0^2} \partial_z P_0 = \frac{\partial}{\partial z} \left(\frac{P_1}{P_0} \right) - \frac{1}{H} \frac{P_1}{P_0}. \quad (9.57)$$

Multiplying this equation by $RT_0 = gH$,

$$RT_0 \frac{\partial_z P_1}{P_0} = \frac{\partial_z P_1}{\rho_0} = gH \frac{\partial}{\partial z} \left(\frac{P_1}{P_0} \right) - g \frac{P_1}{P_0}. \quad (9.58)$$

Substituting this result into Eq. 9.54, the RHS of 9.39 to be rewritten,

$$-\frac{\partial_z P_1}{\rho_0} - g \frac{\rho_1}{\rho_0} = -gH \frac{\partial}{\partial z} \left(\frac{P_1}{P_0} \right) + g \frac{P_1}{P_0} - g \frac{\rho_1}{\rho_0}. \quad (9.59)$$

Now let us consider the LHS of Eq. 9.39. First, we recall (see Eq. 9.36 discussion) that $\partial_t U_{x,0} = 0$, since $U_{x,0}$ is a time-averaged mean-wind quantity. Next, from Eq. 9.37, $\partial_t U_x = i\omega U_{x,1}$, and $\partial_t U_z = i\omega U_{z,1}$. This leaves only the second divergence term to resolve. To do so, notice that the term ∇U is a second-order tensor. Luckily, most of its components are zero. This tensor can be resolved separately into its mean and perturbation components. For its mean wind portion,

$$\nabla U_0 = \begin{bmatrix} \partial_x U_{x,0} & \partial_x U_{y,0} & \partial_x U_{z,0} \\ \partial_y U_{x,0} & \partial_y U_{y,0} & \partial_y U_{z,0} \\ \partial_z U_{x,0} & \partial_z U_{y,0} & \partial_z U_{z,0} \end{bmatrix} = \begin{bmatrix} 0 & 0 & 0 \\ 0 & 0 & 0 \\ \partial_z U_{x,0} & 0 & 0 \end{bmatrix}, \quad (9.60)$$

a significant reduction occurs. For its perturbation portion,

$$\nabla \mathbf{U}_1 = \begin{bmatrix} \partial_x U_{x,1} & \partial_x U_{y,1} & \partial_x U_{z,1} \\ \partial_y U_{x,1} & \partial_y U_{y,1} & \partial_y U_{z,1} \\ \partial_z U_{x,1} & \partial_z U_{y,1} & \partial_z U_{z,1} \end{bmatrix} = \begin{bmatrix} \partial_x U_{x,1} & 0 & \partial_x U_{z,1} \\ 0 & 0 & 0 \\ \partial_z U_{x,1} & 0 & \partial_z U_{z,1} \end{bmatrix}. \quad (9.61)$$

If we assume the perturbation wind velocities are small, then $\mathbf{U}_1 \cdot \nabla \mathbf{U}_1$ will be small. And since direct calculation easily shows $\mathbf{U}_0 \cdot \nabla \mathbf{U}_0 = 0$, we need only concern ourselves with the interaction terms $\mathbf{U}_1 \cdot \nabla \mathbf{U}_0$ and $\mathbf{U}_0 \cdot \nabla \mathbf{U}_1$. The first of these interaction terms evaluates as

$$\mathbf{U}_1 \cdot \nabla \mathbf{U}_0 = U_{z,1} \partial_z U_{x,0} \hat{\mathbf{i}}. \quad (9.62)$$

For the second term,

$$\mathbf{U}_0 \cdot \nabla \mathbf{U}_1 = U_{x,0} \partial_x U_{x,1} \hat{\mathbf{i}} + U_{x,0} \partial_x U_{z,1} \hat{\mathbf{k}}. \quad (9.63)$$

The 2 terms resulting from this second term each combine with the $\partial_t = i\omega$ operator to become a \hat{Q} operator. The remaining term, $U_{z,1} \partial_z U_{x,0}$, contributes to the x -axis equation, as in Eq. B-19a of Tofsted (1993). Combining the results from Eqs. 9.54 and 9.59, the z component of the momentum equation can be written,

$$\hat{Q} U_{z,1} = -gH \frac{\partial}{\partial z} \left[\frac{P_1}{P_0} \right] + g \left(\frac{P_1}{P_0} - \frac{\rho_1}{\rho_0} \right), \quad (9.64)$$

while the x -axis component of the momentum is written,

$$\hat{Q} U_{x,1} + U_{z,1} \partial_z U_{x,0} = -\frac{1}{\rho_0} \partial_x P_1 = -gH \partial_x \left[\frac{P_1}{P_0} \right] = +i\kappa_x gH \left[\frac{P_1}{P_0} \right]. \quad (9.65)$$

This derivation thus produces 4 coupled equations:

$$\hat{Q} U_{x,1} + \mu U_{z,1} = +i\kappa_x gH \left[\frac{P_1}{P_0} \right]. \quad (9.66.A)$$

$$\hat{Q} U_{z,1} = -gH \frac{\partial}{\partial z} \left[\frac{P_1}{P_0} \right] + g \left(\frac{P_1}{P_0} - \frac{\rho_1}{\rho_0} \right). \quad (9.66.B)$$

$$\hat{Q} \left[\frac{P_1}{P_0} \right] - \frac{U_{z,1}}{H} + \gamma \chi = 0. \quad (9.66.C)$$

$$\hat{Q} \left[\frac{\rho_1}{\rho_0} \right] - \frac{U_{z,1}}{H} (1 + \dot{H}) + \chi = 0. \quad (9.66.D)$$

Here, Eq. 9.66.A has been modified to replace $\partial_z U_{x,0}$ with μ the constant wind gradient.

9.6 Vertical Wind Perturbation Equation

Let us now attempt to take the set of 4 coupled equations and derive from these a single equation that describes one of the component terms. From this solution we may then be able to determine the remaining terms by using the elimination equations in reverse. In this section we will thus focus on using mathematical elimination to obtain a single equation in a single one of the unknowns. The simplest of these to resolve will be the vertical wind perturbation term.

To solve for this term, the easiest quantity to eliminate first is the difference, $(P_1/P_0 - \rho_1/\rho_0)$, contained in Eq. 9.66.B. Multiplying 9.66.B by \hat{Q} , and using Eqs. 9.66.C and 9.66.D, we can isolate the variable \hat{Q} times this difference as

$$\hat{Q} \left[\frac{P_1}{P_0} - \frac{\rho_1}{\rho_0} \right] = (1 - \gamma) \chi - \frac{\dot{H}}{H} U_{z,1}. \quad (9.67)$$

$$\hat{Q}^2 U_{z,1} = -gH \hat{Q} \frac{\partial}{\partial z} \left[\frac{P_1}{P_0} \right] - g \left[(\gamma - 1) \chi + \frac{\dot{H}}{H} U_{z,1} \right]. \quad (9.68)$$

This can be slightly simplified by recognizing,

$$g \frac{\dot{H}}{H} = g \frac{\dot{\theta}}{\theta} = N^2, \quad (9.69)$$

the square of the Brunt–Viasala frequency. Use of this term allows us to consolidate this factor onto the LHS as

$$(\hat{Q}^2 + N^2) U_{z,1} = -gH \hat{Q} \frac{\partial}{\partial z} \left[\frac{P_1}{P_0} \right] - g(\gamma - 1) \chi. \quad (9.70)$$

Let us now reappraise the resulting equation set. We have eliminated the factor ρ_1/ρ_0 . What remains are the 3 variables, $U_{x,1}$, $U_{z,1}$, and P_1/P_0 , expressed in Eqs. 9.66.A, 9.66.C, and 9.70.

Equations 9.37 and 9.38 appeared to suggest that perhaps a single function, $W(z)$, could be used to describe the vertical structure of all of the perturbation functions. However, the appearance of Eq. 9.70 does not give us much hope this is true. That's because for $U_{z,1}$ we expect that there should exist a boundary condition at $z = 0$ such that $U_{z,1}(x, z, t)$ obeys $U_{z,1}(x, 0, t) = 0$. But dP_0/dz will not be zero at $z = 0$. Therefore P_1/P_0 cannot have the same z dependence as $U_{z,1}$.

This possibility of different vertical dependencies for the different components indicates caution is needed when performing variable transformations. That is, we should do whatever is necessary to directly solve for one of the remaining 3 components to avoid introducing phase transformations that cannot be evaluated directly. We therefore proceed to eliminate variables through direct substitution rather than through model assumptions.

The most-appropriate next candidate for elimination seems to be P_1/P_0 , but 2 courses to accomplish this are available. One method would be to substitute Eq. 9.66.A into Eqs. 9.66.C and 9.70. The other would be to use Eq. 9.66.C and insert its results into 9.66.A and 9.70. In his analysis, Beer followed the first approach, using his equivalent of our Eq. 9.66.A. In his application this approach was the obvious choice because only one component (the first term on the LHS of Eq. 9.66.A) needed to be replaced. However, in the current equation set, Eq. 9.66.A also includes a wind-gradient term. So, both 9.66.A and 9.66.C will introduce 2 terms.

However, choosing Eq. 9.66.C is still probably not preferable since 9.66.C contains χ and at the point it is introduced it will generate a second-order z derivative in Eq. 9.70. On the other hand, substituting Eq. 9.66.A into 9.66.C and 9.70 only introduces first-order z derivatives into Eq. 9.70.

We therefore begin by combining Eqs. 9.66.A and 9.66.C seeking to solve for $U_{x,1}$ in terms of $U_{z,1}$, whereby we write,

$$-\frac{i}{\kappa_x g H} \left(\hat{Q}^2 U_{x,1} + \mu \hat{Q} U_{z,1} \right) = +\frac{U_{z,1}}{H} - \gamma \left(-i \kappa_x U_{x,1} + \partial_z U_{z,1} \right). \quad (9.71)$$

Rearranging the lefthand and righthand expressions (and ignoring the central form), we attempt to isolate $U_{x,1}$ by first multiplying Eq. 9.71 by $i \kappa_x g H$:

$$+ \left(\hat{Q}^2 + \kappa_x^2 c^2 \right) U_{x,1} = +i \kappa_x \left(g - c^2 \partial_z \right) U_{z,1} - \mu \hat{Q} U_{z,1}. \quad (9.72)$$

Next, we simplify Eq. 9.72 by substituting in $\hat{Q} = i \Omega$ from Eq. 9.44,

$$\left(\kappa_x^2 c^2 - \Omega^2 \right) U_{x,1} = +i \left[-\mu \Omega + \kappa_x \left(g - c^2 \partial_z \right) \right] U_{z,1}. \quad (9.73)$$

Substituting Eq. 9.66.A into Eq. 9.70, having first reversed all signs,

$$(\Omega^2 - N^2) U_{z,1} = +gH \hat{Q} \frac{\partial}{\partial z} \left[-\frac{i}{\kappa_x gH} (\hat{Q} U_{x,1} + \mu U_{z,1}) \right] + g(\gamma - 1) (-i \kappa_x U_{x,1} + \partial_z U_{z,1}). \quad (9.74)$$

Next, we expand the first term on the right as a series of 5 parts. Let us designate vertical derivatives using $\partial_z H = \dot{H}$ and $\partial_z \hat{Q} = -i \kappa_x \mu$, where $\mu = \partial_z U_{x,0}$.

$$+gH \hat{Q} \frac{\partial}{\partial z} [\dots] = \left[-\Omega N^2 / (g \kappa_x) \right] (i \Omega U_{x,1} + \mu U_{z,1}) - i \mu \Omega U_{x,1} + i \frac{\Omega^2}{\kappa_x} \partial_z U_{x,1} + \frac{\mu \Omega}{\kappa_x} \partial_z U_{z,1}. \quad (9.75)$$

Substituting Eq. 9.75's intermediate result into Eq. 9.74 yields

$$(\Omega^2 - N^2) U_{z,1} = \left(\frac{-\Omega N^2}{g \kappa_x} \right) (i \Omega U_{x,1} + \mu U_{z,1}) - i \mu \Omega U_{x,1} + i \frac{\Omega^2}{\kappa_x} \partial_z U_{x,1} + \frac{\mu \Omega}{\kappa_x} \partial_z U_{z,1} + g(\gamma - 1) (-i \kappa_x U_{x,1} + \partial_z U_{z,1}). \quad (9.76)$$

Rearranging terms, placing the $U_{z,1}$ terms on the left,

$$\left(\frac{\mu \Omega}{\kappa_x} + g(\gamma - 1) \right) \partial_z U_{z,1} - \left[\Omega^2 + \left(\frac{\mu \Omega N^2}{g \kappa_x} \right) - N^2 \right] U_{z,1} = + \frac{i \Omega^2 N^2}{g \kappa_x} U_{x,1} + i \mu \Omega U_{x,1} - i \frac{\Omega^2}{\kappa_x} \partial_z U_{x,1} + i g(\gamma - 1) \kappa_x U_{x,1}. \quad (9.77)$$

To simplify the math, let us introduce dimensionless parameters $M = \mu \Omega / (g \kappa_x)$ and $R = M + \gamma - 1$, such that Eq. 9.77 can be written,

$$g R \partial_z U_{z,1} - \left[\Omega^2 + (M - 1) N^2 \right] U_{z,1} = - \frac{\Omega^2}{\kappa_x} \partial_z (i U_{x,1}) + g \kappa_x \left(\frac{M^2 N^2}{\mu^2} + R \right) (i U_{x,1}). \quad (9.78)$$

With this result, P_1/P_0 has been eliminated. The equation set has thus been reduced to Eqs. 9.73 and 9.78. The final step is to substitute for $(i U_{x,1})$ from Eq. 9.73 into Eq. 9.78. But before doing so, note that the new variable M allows Eq. 9.73 to be expressed in the simplified form,

$$(\kappa_x^2 c^2 - \Omega^2) (i U_{x,1}) = g \kappa_x [(M - 1) + \gamma H \partial_z] U_{z,1}. \quad (9.79)$$

The system of Eqs. 9.66.A–D has thus been reduced to Eqs. 9.78 and 9.79. To proceed we will need to remove $U_{x,1}$ from 9.78. This will require both solving Eq. 9.79 for $(i U_{x,1})$ and using this equation's derivative to eliminate $\partial_z U_{x,1}$. This latter procedure is made simpler by introducing additional new variables: Let $\beta = \kappa_x c$, and $\Gamma^2 = \beta^2 - \Omega^2$, such that Eq. 9.79 can be rewritten as

$$(i U_{x,1}) = g \kappa_x \Gamma^{-2} [(M - 1) + \gamma H \partial_z] U_{z,1}. \quad (9.80)$$

However, Eq. 9.78 also involves the derivative of Eq. 9.80, so we will need the derivative of Γ^{-2} , given by,

$$\partial_z (\Gamma^2)^{-1} = -(\Gamma^2)^{-2} \partial_z (\Gamma^2). \quad (9.81)$$

$$\begin{aligned} \partial_z (\Gamma^2) &= \partial_z (\beta^2 - \Omega^2) = +\kappa_x^2 \gamma g \dot{H} + 2 \Omega \kappa_x \mu \\ &= +\kappa_x^2 g \left(\gamma \dot{H} + 2 \frac{\mu \Omega}{g \kappa_x} \right) = +\kappa_x^2 g (\gamma \dot{H} + 2 M). \end{aligned} \quad (9.82)$$

Taking the derivative used by the middle term in Eq. 9.80,

$$\begin{aligned} \partial_z [(M - 1) + \gamma H \partial_z] &= \partial_z [\mu \Omega / (g \kappa_x)] + \partial_z [\gamma H] \partial_z \\ &= -\kappa_x \mu [\mu / (g \kappa_x)] + [\gamma \dot{H}] \partial_z \\ &= -\mu^2 / g + \frac{\gamma H}{g} (g \dot{H} / H) \partial_z \\ &= -(N^2 / g) (\mu^2 / N^2 - \gamma H \partial_z). \end{aligned} \quad (9.83)$$

Using these results, solving Eq. 9.79 for $(i U_{x,1})$, and taking the z derivative,

$$\begin{aligned} \partial_z (i U_{x,1}) &= g \kappa_x \partial_z \left\{ \Gamma^{-2} [(M - 1) + \gamma H \partial_z] U_{z,1} \right\} \\ &= -(g^2 \kappa_x^3 \Gamma^{-4}) (2 M + \gamma \dot{H}) [(M - 1) + \gamma H \partial_z] U_{z,1} \\ &\quad - \kappa_x N^2 \Gamma^{-2} [\mu^2 / N^2 - \gamma H \partial_z] U_{z,1} \\ &\quad + \kappa_x g \Gamma^{-2} [(M - 1) + \gamma H \partial_z] \partial_z U_{z,1}. \end{aligned} \quad (9.84)$$

The intermediate results given in Eqs. 9.80 and 9.84 can now be introduced into Eq. 9.78 so that we may solve for $U_{z,1}$. However, since only vertical derivatives of $U_{z,1}$ will remain, the exponential factor of Eq. 9.38 should cancel out of both sides of the resulting equation, leaving only terms in $W(z)$ and its derivatives.

Based on this reduction to the function $W(z)$, we further abbreviate these derivatives in the form $\partial_z W(z) = \dot{W}$ and $\partial_z^2 W(z) = \ddot{W}$.

With these substitutions, we can rewrite Eqs. 9.80 and 9.84 as

$$(i U_{x,1}) \propto +(g \kappa_x / \Gamma^2) \left[(M - 1) W + \gamma H \dot{W} \right]; \quad (9.85)$$

$$\begin{aligned} -(1/\kappa_x) \partial_z (i U_{x,1}) \propto & +(g^2 \kappa_x^2 / \Gamma^4) (2 M + \gamma \dot{H}) \left[(M - 1) W + \gamma H \dot{W} \right] \\ & +(N^2 / \Gamma^2) \left[(\mu^2 / N^2) W - \gamma H \dot{W} \right] \\ & -(g / \Gamma^2) \left[(M - 1) \dot{W} + \gamma H \ddot{W} \right]. \end{aligned} \quad (9.86)$$

So then, Eq. 9.78 translates into

$$\begin{aligned} g R \dot{W} - \left[\Omega^2 + (M - 1) N^2 \right] W = & -(\Omega^2 g / \Gamma^2) \left[(M - 1) \dot{W} + \gamma H \ddot{W} \right] \\ & +(g^2 \kappa_x^2 / \Gamma^2) \left(M^2 N^2 / \mu^2 + R \right) \left[(M - 1) W + \gamma H \dot{W} \right] \\ & +(\Omega^2 g^2 \kappa_x^2 / \Gamma^4) (2 M + \gamma \dot{H}) \left[(M - 1) W + \gamma H \dot{W} \right] \\ & +(\Omega^2 N^2 / \Gamma^2) \left[(\mu^2 / N^2) W - \gamma H \dot{W} \right]. \end{aligned} \quad (9.87)$$

Next, following the same procedure as in Tofsted (1993), let us isolate the \ddot{W} term and proceed to collect algebraic factors that multiply the \dot{W} and W terms. We will begin by dividing both sides by $\Omega^2 \gamma g H / \Gamma^2 = c^2 \Omega^2 / \Gamma^2$. But, let us also move all terms onto the LHS of the equation. Together, these steps lead (after some math) to

$$\begin{aligned} \ddot{W} + (g/c^2)(M - 1) \dot{W} + (g/c^2) R (\Gamma^2 / \Omega^2) \dot{W} \\ - [g^2 \kappa_x^2 / \Gamma^2] (2 M + \gamma \dot{H}) \left[((M - 1)/c^2) W + \dot{W}/g \right] \\ - \left(N^2 + \mu^2 R / M^2 \right) \left[((M - 1)/c^2) W + \dot{W}/g \right] \\ - (\Gamma^2 / c^2) \left[1 + (M - 1) (N^2 / \Omega^2) \right] W \\ - \left[(\mu^2 / c^2) W - (N^2 / g) \dot{W} \right] = 0. \end{aligned} \quad (9.88)$$

All of the coefficients related to the \dot{W} and W terms can be consolidated. Consolidating all of the \dot{W} coefficients we have, using $g/c^2 = 1/(\gamma H)$,

$$+ \left[\frac{(M - 1)}{(\gamma H)} + \frac{R}{(\gamma H)} \frac{\Gamma^2}{\Omega^2} - \frac{g \kappa_x^2}{\Gamma^2} (2 M + \gamma \dot{H}) - \mu^2 \frac{R}{g M^2} \right] \dot{W}. \quad (9.89)$$

Further consolidation is possible when we note that $\Gamma^2/\Omega^2 = \beta^2/\Omega^2 - 1$, that $g \kappa_x^2 = \beta^2/(\gamma H)$, and $M - 1 - R = -\gamma$. In addition, 2 more wave numbers may be defined: $\kappa_U = \mu^2/g$ and $\kappa_G = g/c^2$. This term then reduces to

$$+ \left[-\frac{1}{H} + \kappa_G R \frac{\beta^2}{\Omega^2} - 2 \kappa_G M \frac{\beta^2}{\Gamma^2} - \frac{N^2 \beta^2}{g \Gamma^2} - R \frac{\kappa_U}{M^2} \right] \dot{W}. \quad (9.90)$$

At this stage there are so many named coefficients that several cancellations will occur; but first, more new variables are introduced: $G = \Omega/\beta$, and $\kappa_N = (g \dot{H}/H)/g = N^2/g$.

$$+ \kappa_G \frac{\beta^2}{\Omega^2} - \frac{\kappa_U}{M^2} = \frac{g}{c^2} \frac{\kappa_x^2}{\Omega^2} - \frac{\mu^2/g}{[(\mu \Omega)/(g \kappa_x)]^2} = \frac{g \kappa_x^2}{\Omega^2} - \frac{g \kappa_x^2}{\Omega^2} = 0. \quad (9.91)$$

Using these substitutions, the \dot{W} term can be reduced to

$$+ \left[-\frac{1}{H} - \frac{\kappa_N}{(1 - G^2)} - 2 \frac{\kappa_G M}{(1 - G^2)} \right] \dot{W}. \quad (9.92)$$

This result follows that of Eq. B-22's result in Tofsted (1993), which matches Beer's (1974) $\partial_z W$ term of his Eq. 2.5.12, except for the third term, $-2 \kappa_G M/(1 - G^2)$, which accounts for the vertical wind shear, a factor that was not considered in the previous analysis.

Following the same procedure used to simplify the \dot{W} expression, the term proportional to W can be simplified to the form

$$\left\{ - \left[\frac{(M - 1)}{c^2} \right] \left[\frac{\Gamma^2 N^2}{\Omega^2} + \frac{g^2 \kappa_x^2}{\Gamma^2} (2 M + \gamma \dot{H}) + N^2 + \frac{\mu^2 R}{M^2} \right] \right\} W \\ + \left\{ - \frac{(\Gamma^2 + \mu^2)}{c^2} \right\} W. \quad (9.93)$$

Additional cancellations are also possible through the substitutions

$$\frac{\Gamma^2 N^2}{\Omega^2} + N^2 = \frac{(1 - G^2) N^2}{G^2} + N^2 = \frac{N^2}{G^2}, \text{ and,} \quad (9.94)$$

$$\frac{g^2 \kappa_x^2 \gamma \dot{H}}{\Gamma^2} = \frac{\gamma \dot{H} g^2 \kappa_x^2}{\beta^2 (1 - G^2)} = \frac{\gamma \dot{H} g^2}{\gamma g H (1 - G^2)} \\ = \frac{\dot{H} g}{H (1 - G^2)} = \frac{N^2}{(1 - G^2)}. \quad (9.95)$$

Combining terms from Eqs. 9.94 and 9.95,

$$\frac{N^2}{G^2} + \frac{N^2}{(1-G^2)} = \frac{(1-G^2)N^2}{G^2(1-G^2)} + \frac{G^2N^2}{G^2(1-G^2)} = \frac{N^2}{G^2(1-G^2)}. \quad (9.96)$$

One can also rewrite

$$\frac{\mu^2 R}{M^2} = \frac{\mu^2 R}{[\mu \Omega / (g \kappa_x)]^2} = \frac{g^2 \kappa_x^2 R}{\Omega^2} = \frac{g^2 \kappa_x^2 R}{\beta^2 G^2} = \frac{g^2 R}{c^2 G^2}, \quad (9.97)$$

and,

$$\frac{g^2 \kappa_x^2 2M}{\Gamma^2} = \frac{2M g^2 \kappa_x^2}{\beta^2 (1-G^2)} = \frac{2M g^2}{c^2 (1-G^2)}. \quad (9.98)$$

Adding these quantities, a common denominator appears:

$$\frac{g^2 R}{c^2 G^2} + \frac{2M g^2}{c^2 (1-G^2)} = \frac{g^2}{c^2} \left[\frac{R}{G^2} + \frac{2M}{(1-G^2)} \right]. \quad (9.99)$$

By collecting terms from Eqs. 9.96 and 9.99 and introducing these back into Eq. 9.93, and setting $S^2 = 1 - G^2$, the W function becomes, after some math,

$$C_T W = \left[\frac{\kappa_N \kappa_G}{G^2 S^2} + \kappa_G^2 \left(\frac{(\gamma - 1)}{G^2} + \frac{M(1 + G^2)}{G^2 S^2} \right) \right] (1 - M) W - (\kappa_x^2 S^2 + \kappa_U \kappa_G) W. \quad (9.100)$$

For comparison, let us write out Beer's W coefficient terms from his Eq. 2.5.12. The current function also contains terms related to the wind gradient, so these should appear as extra terms, but the rest should be consistent. Translating Beer's expression into the dimensionless variables used here, he obtained

$$C_B W = \left\{ \frac{\kappa_N \kappa_G}{G^2 S^2} + \kappa_G^2 \frac{(\gamma - 1)}{G^2} - \kappa_x^2 S^2 \right\} W. \quad (9.101)$$

Comparing these 2 forms we see that the 2 terms that do not match depend on M and κ_U . Both of these terms are dependent on the $\mu = \partial_z U_{x,0}$ factor through M and $\kappa_U = \mu^2/g$. Therefore, since Beer's derivation did not consider a vertical wind shear, these 2 terms would have necessarily equalled zero.

Unfortunately, this comparison highlights the many variables introduced to describe these equations in dimensionless terms, and raises the question of which dimensionless wave numbers and/or frequencies are the most *natural* for characterizing the flow modeled. This question has yet to be resolved.

As just one example, consider the product $\kappa_U \kappa_G$. Using the variables available, it can be transformed into several equivalent expressions:

$$-\kappa_U \kappa_G = -\frac{\mu^2}{g} \frac{g}{c^2} = -\frac{M^2 \beta^2 g^2}{c^4 \Omega^2} = -\frac{M^2}{G^2} \kappa_G^2. \quad (9.102)$$

One can similarly manipulate M and G variables to eliminate a few terms in the W coefficient expression:

$$\left(\frac{\kappa_G^2}{G^2} \left\{ (1 - M) \left[\frac{\kappa_N}{\kappa_G S^2} + (\gamma - 1) + \frac{2(1 + M)}{S^2} \right] - M \right\} - \kappa_x^2 S^2 \right) W. \quad (9.103)$$

Whether the resulting expression improves our understanding is debatable. What we can conclude is that generally each algebraic multiplier of W contains a product of 2 (possibly identical) wave numbers, while each \dot{W} multiplier acts like a single wave number (and $1/H = \kappa_H$ also has the dimensions of a wave number).

The complete equation is written as

$$\begin{aligned} \ddot{W} - \left[\frac{1}{H} + \frac{\kappa_N}{S^2} + 2 \frac{\kappa_G M}{S^2} \right] \dot{W} = \\ - \left(\frac{\kappa_G^2}{G^2} \left\{ (1 - M) \left[\frac{\kappa_N}{\kappa_G S^2} + (\gamma - 1) + \frac{2(1 + M)}{S^2} \right] - M \right\} - \kappa_x^2 S^2 \right) W. \end{aligned} \quad (9.104)$$

To solve this equation for $W(z)$, we have merely to introduce Dirichlet boundary conditions in which $W(z) = 0$ at $z = 0$ and $z = Z_V$, while the first derivatives of W at the boundaries remain indeterminate. Hence, setting $\dot{W}(z)|_{z=0}$ to an arbitrary constant, the solution can be integrated numerically using Euler's method or another suitable technique.

The form taken by $W(z)$ has several qualities. First, we note that the above equation could be expressed in the form,

$$0 = \ddot{W} + P(z, \kappa_x, \omega) \dot{W} + Q(z, \kappa_x, \omega) W. \quad (9.105)$$

This form is conducive to a solution using standard techniques. However, because of the boundary conditions at $z = 0$ and $z = Z_V$, the time frequency ω will become a function of these boundary conditions, as well as the choice of κ_x . One also finds that a series of solutions exists for a given atmospheric state. These different solutions each feature a zero value of $W(z)$ only at $z = 0$ and Z_V . The zeroth-order solution only contains these zeros. Higher-order solutions feature additional

zeros at an extra intermediate height for each order of the solution. Such higher-order solutions permit the boundary-layer atmosphere to dynamically *turn over* due to the effects of vertical variations of frequency ω . This is consistent with the concept of gravity waves that can break and produce intermittent turbulent episodes characteristic of nocturnal turbulence.

The next section examines various solutions to the above equation as well as the issue of breakdown of such states.

9.7 Vertical Wind Structure

According to Tofsted (1993), where several sources were cited — including Browning (1971), Miles and Howard (1964), Goldstein (1931), Lalas and Einaudi (1976), and Davis and Peltier (1976) — the wavelength of the fastest-growing gravity-wave mode is approximately 7.5 times the depth of the surface-inversion layer, Z_V .

That is, we recognize that terrain will be variable. Nighttime flow over such terrain undulations tends to induce vertical wind motions that, in turn, can generate wave energy for these waves. We also understand that such waves must be limited in their vertical wavelength and, therefore, in their vertical motions such that at the least, one-half of a wavelength must span the surface-inversion layer. Higher-frequency waves, of course, have a larger number of vertical wavelengths fitting into the inversion layer's height. Yet, higher-frequency waves are more easily absorbed by the surface layer. Hence, wavelength modes that are attuned to the terrain over which the wind is flowing are more likely to absorb more energy from the flow, while longer wavelength modes are likely to retain more of their energy, as opposed to losing their energy due to absorption in the surface layer.

Therefore, we expect to have some wavelength mode that would tend to absorb energy from the main flow more efficiently. Statistically, it is expected that that particular wavelength will produce the most rapidly growing wave mode. This reported maximum wave number is

$$\kappa_x \approx 2\pi/(7.5 Z_V). \quad (9.106)$$

We will use this as our starting point in seeking modes to drive the search for our waves.

The other criterion that must be satisfied is that the $S^2 = 1 - G^2$ parameter must be positive. Otherwise, the W solution diverges. To ensure this condition, we insist that $|G| = |\Omega/\beta| < 1$. In addition, Booker (1967) indicates a gravity wave will be absorbed at a level where frequency $\Omega = 0$. Therefore Ω must not become too small or too large. We thus begin our search for a solution with 2 boundary conditions plus 2 consistency conditions to meet.

It should be mentioned that this analysis ignores tunneling, meaning the mathematics have been simplified to ignore heating effects and viscous forces. Nevertheless, such considerations should not disturb us overmuch since the solutions we seek involve long wavelength perturbations. For such length scales the influence of viscous forces will be minimal. According to Orlanski (1973), the results obtained will be virtually identical to those of a full analysis.

The main reason we require the wave to have zero amplitude at the inversion layer's top is because the gravity waves are assumed to reflect at the top, producing a standing wave with zero amplitude at the reflection point, consisting of two equal magnitude but opposing amplitude waves that add at the top. Of course, this is just a model and the temperature structure does not feature a constant gradient up to a definitive inversion top. Nonetheless, it is hoped this model provides some *skill* in characterizing the type of waves that could exist and the resulting turbulent episodes that could be encountered.

Given that we know the inversion layer's height and the temperature- and wind-profile gradients, and given Eq. 9.104 as the governing linear-wave equation, we set $W(0) = W(Z_V) = 0$ as the boundary conditions and choose an arbitrary initial value of $\dot{W}(0) = a$. The solution is integrated from the surface using Euler's method and a given choice of κ_x . The remaining free parameter is frequency ω that must be *tuned* in such a way that $W(Z_V) = 0$ upon integration. Figure 29 illustrates 4 wave-mode solutions, $W_n(z)$, $n = 1...4$, for an atmosphere of surface temperature 288 K, surface pressure of 880 mbar, horizontal windspeed at the surface of 1 m/s, $Z_V = 200$ m, and wind and temperature gradients of 2 m/s and 3 K per 100 meters.

The resulting waves appear approximately as sinusoidal functions spanning the inversion layer. Vertical functions $W(z)$ shown are for a particular choice of horizontal wave number, κ_x , but tests with varying κ_x indicate similar forms at even widely separated, horizontal wave numbers. That is, the vertical structure appears to be insensitive to the governing horizontal wave number.

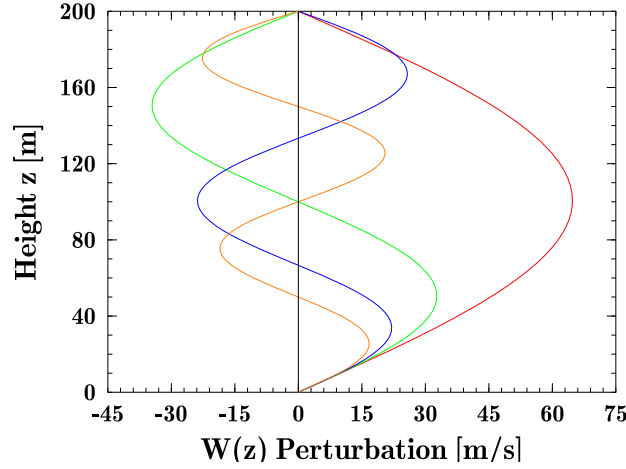


Fig. 29 First 4 vertical wind modes, $W(z)$, for typical inversion scenario

These waves also appear to exhibit group velocities, $V_{grp} = d\omega/d\kappa$, very close to their phase velocities, $V_\phi = \omega/\kappa$. This is illustrated in Fig. 30 for the first 2 computed modes ($n = 1, 2$) at a range of input horizontal wave numbers, κ_x , approximated vertical wave numbers $\kappa_z = n\pi/Z_V$, and ω obtained from the computed solution. The close approximation of the phase velocity to the group velocity is evidenced by the nearly linear relation between ω versus κ .

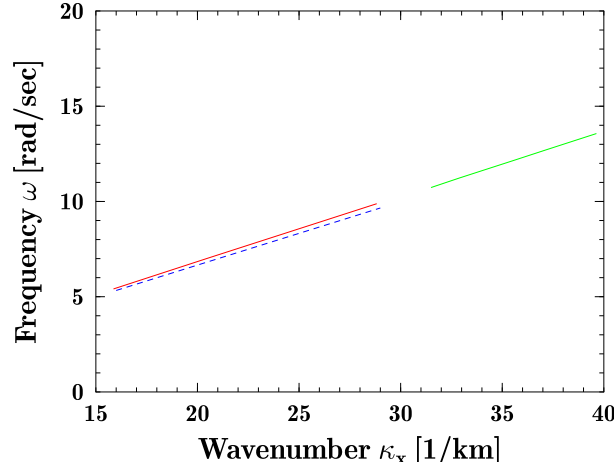


Fig. 30 Computed frequency versus wave number for first 2 modes: Mode 1 plotted in red, Mode 2 in green, dashed line is $\omega = \kappa/3$.

Due to the relative magnitudes of the horizontal and vertical wave numbers, the wave appears to primarily exist as a vertically propagating, standing wave with a small horizontal component. Indeed, this type of vertical connectivity would almost

be necessary since otherwise the waves could become entrained into the mean flow rather than riding on top of the mean flow.

In terms of the wave motions, while the z component exhibits a maximum displacement away from the boundaries, the x component exhibits a maximum displacement at the upper and lower boundaries. This occurs because the dominant term of the coupling formula in Eq. 9.79 has a major component that converts the vertical sine-like dependence of the z wave component into a cosine-like dependence in the x component. This behavior is illustrated in Fig. 31 showing the vertical dependence of $U_{x,1}$ for the same 4 modes as Fig. 29. This plot reveals that although the horizontal component is, strictly speaking, a mixed mode, because $\kappa_g \ll 1$, the derivative term proportional to $\partial_z U_{z,1}$ is dominant and the horizontal wind components appear approximately as cosine forms for their vertical dependence.

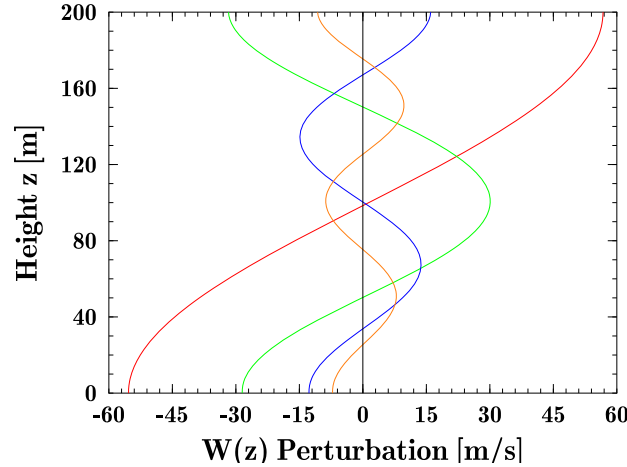


Fig. 31 First 4 horizontal wind modes, $U(z)$, for typical inversion scenario

Of course, because the equation is only an approximation, ignoring drag effects near the surface, the plot indicates maximum wind speed near the surface. While this approximation would not occur in reality, the general properties within the inversion layer, particularly for higher-frequency modes, supports the existence of such waves.

9.8 Gravity-Wave Breakdown

The analysis in the previous section constructed an approximate model of gravity waves that could exist within the surface-inversion layer at night. These waves,

moreover, could draw energy from the mean wind as it flows over undulating terrain at night. However, such waves are inherently unstable. As discussed by Whitham (1974), gravity waves are subject to collapse as a function of breakdown of the model itself as a result of variation in the phase velocity as a function of height.

To examine this behavior, we consider a nominal vertical wave number, κ_z , that can be modeled as a simple function of the height of the inversion layer, given as $n\pi/Z_V$, as was introduced in the previous section. Also, as previously stated, the wave solution sets $W(0) = W(Z_V) = 0$ at the base and top of the inversion layer. However, the actual vertical dependence of the wave function $W(z)$ is not exactly sinusoidal. Therefore, κ_z can be considered a function of height. That is, we consider the function,

$$W(z) = A \sin[\kappa_z(z) z]. \quad (9.107)$$

Assuming ω is constant for a given κ_x value, based on using up ω 's degree of freedom to ensure that $W(Z_V) = 0$, and κ_x is also fixed, then κ_z can be considered to vary.

We then find an interesting effect occurs. The wave vector $\kappa = (\kappa_x, \kappa_z)$ will point in the direction of the wave propagation. But since we are looking at a standing wave, the z component is immaterial; the only concern will be the x component. But the velocity of propagation will be $c = \omega/\kappa$, where

$$\kappa = \sqrt{\kappa_x^2 + \kappa_z^2}. \quad (9.108)$$

Hence, increases in κ_z will cause decreases in propagation speed c . An increase in κ_z could also cause the propagation vector to point more into the z direction and less in the x direction. That is, the x component of the propagation velocity will be $\alpha_x = \kappa_x/\kappa$. The horizontal velocity is thus

$$c_x = c \alpha_x = \frac{\omega \kappa_x}{\kappa^2} = \frac{\omega \kappa_x}{\kappa_x^2 + \kappa_z^2}. \quad (9.109)$$

Changes in κ_z with height have an effect on the propagation speed of the disturbance as a function of height. This can have an impact on the ability of the wave to maintain its structure over time. According to earlier analyses (Whitham 1974, 23 and 46), any disturbance that begins with propagation velocity gradients (e.g.,

$W(z)$ in this case), will, after a characteristic time, reach a point where the wave *breaks*. At this time the wave velocity gradient becomes infinite at some point. This singularity is characterized by the point where the velocity derivative is a maximum (i.e., dc_x/dz is maximized). At this location and at the characteristic time the atmosphere must become turbulent, as the rules whereby the wave itself was formed no longer exist. The characteristic *break-down time* can be expressed as

$$t_B = \frac{1}{dc_x/dz} = -\frac{\kappa^4}{2\omega \kappa_x \kappa_z} \frac{1}{\partial_z \kappa_z} = -\frac{\kappa^2}{2c_x \kappa_z} \frac{1}{\partial_z \kappa_z}. \quad (9.110)$$

For gravity waves it is possible to have multiple waves growing within the same layer at the same time. Their internal velocity structures will depend on the properties of each wave individually. The translation of Whitham's analysis to gravity waves is that eventually a spillover effect will occur where the magnitude of the wave has grown to where heavier cold air overlies less dense warm air and the less dense air below can no longer support the heavier air above. The resulting spillover or overturning of the air due to gravitational collapse then destroys the wave. The resulting mixing generates optical turbulence involving differentials of temperature throughout the boundary layer.

Based on the signs chosen for the different terms in the above equation, we would require that $\partial_z \kappa_z$ be negative, such that κ_z is a decreasing function of height.

Whitham's formulation of the t_B breakdown time corresponds to the temporal evolution of the solution in such a way that the function at some inflection point becomes multivalued. (This is akin to the case of the Tacoma Narrow Bridge that collapsed in 1940: Initially the bridge fluctuations were correlated, but as time progressed, the fluctuations in different portions became increasingly out of phase.) In the atmosphere, there being no physical connection between one portion of air and another, such discontinuities are much easier to imagine. Eventually the point of disparity becomes so marked that even at an infinite derivative the function cannot hold together.

Beyond this initial breakdown time, an increasingly larger region of the solution becomes multivalued. In the atmosphere, such discontinuities would lead to mixing of air at different temperatures (optical turbulence is produced). This mixing then induces a reduction in velocity and a restarting of the inversion-generation process, typically involving a reset of the surface temperatures and the wind speed.

As an example of this analysis, consider Fig. 32. From prior study of breakdown times (Tofsted 1993), typical periods ranged between 20 and 40 min, as observed through variations in vertical temperature gradients. This assumed mixing to the ground would destroy the integrity and intensity of the vertical temperature inversion's structure. Nighttime studies indicated significant variations in vertical temperature gradients that appear to be inversely connected to turbulence episodes in the surface layer.

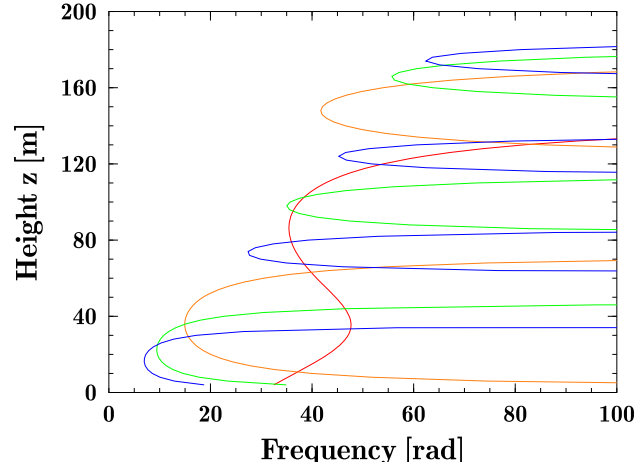


Fig. 32 Breakdown times (minutes) for a series of 4 gravity-wave modes, illustrating breakdown times from initiation of wave motion as functions of height

These breakdown plots show that the vertical structure of κ_z is such that the breakdowns typically occur first close to the surface. However, some caution is called for regarding the apparent result that the first breakdowns are caused by the highest-order wave-number cases ($n = 3, 4$), since, as Fig. 31 illustrates, the waves show maximum horizontal velocity near the ground. In fact, the model does not consider drag effects. This suggests that possibly the near-ground time scales have been overstated. Ignoring the solutions for the curves nearest to the ground, the next shortest timescale is the $n = 3$ result that peaks at approximately 80 m, and whose breakdown occurs at roughly 26 min. This result is consistent with breakdown times observed and reported (Tofsted 1993).

We thus have a conceptual framework for accounting for the mechanism causing intermittent nocturnal turbulence. However, these questions must be answered: How much energy is released upon breakdown of a given wave? What is the expected fluctuation in C_n^2 for a given breakdown as well as the duration of the

disturbance before this turbulence dissipates? Hence, while the current analysis supplies additional information, a model is still necessary, perhaps based largely on statistical inferences, as to how variations in inversion structure a) feed energy into gravity-wave modes and b) generate turbulence upon wave breakdown.

10. Conclusions

This report has discussed a series of improvements performed on a model of the Surface Energy Budget designed for the express purpose of estimating the optical-turbulence strength of the near-surface atmosphere. In the process a number of areas for improving heat-flux-calculation methods have been explored and addressed in great detail.

The primary improvements considered in the present report have focused on consistency of methods. In particular, one issue related to the surface layer was considered in Chapter 6. There, the focus was on how to produce mixed convective fluxes from surfaces of different temperatures and different relative surface fractions. The prior method in Tofsted (1993) considered only heat arising from an averaged temperature surface, but encountered mixed resistance numbers for the ground versus the foliage layer. The new method relies on a different formulation for producing these mixed fluxes.

This consideration of weighting fluxes based on a modified understanding of the relative areas of leaves and ground surface then carried over into the Chapter 7 development. The study there considered radiation scattered and absorbed within the foliage layer by multiple sublayers. In so doing, an inconsistency was resolved between the previous method of handling radiative interactions with the foliage and the convective-flux methods that assumed considerably more leaf surface than was modeled in the previous radiation model.

In the process of producing this consistent picture, a new model was developed that connects the amount of leaf surface to the foliage-cover fraction through a random leaf model. To our knowledge, the community studying such problems has mainly focused on mature agricultural crops. For immature crops, where the foliage fraction, σ_F , is significantly less than unity, or for desert areas featuring sparse vegetation, this new approach appears to be a much more realistic means of addressing vegetative impacts than the use of a constant leaf-to-area ratio. And, certainly, there are numerous areas on the planet that do not feature mature crop surfaces or high-density vegetation. For such regions the present model may be very useful.

A main additional focus was to develop tables of radiation for various atmospheric states. While such models appear to exhibit similar results as the Staley–Jurica

analytic expression under certain conditions, in general the new method presents a much broader picture of atmospheric variability than previously modeled. But to produce such calculations in Chapter 8, it first was necessary to develop consistent vertical-temperature and vertical-humidity structure concepts in Chapter 6. These equations now provide the basis for characterizing the complete boundary layer (temperature-wise) through the base of the elevated inversion.

Chapter 9 then suggested the means of extending this analysis from temperature to also handle mean wind flows, and how fluctuations in wind speed might be inserted into the model through variable daytime-wind effects. It further suggests the nocturnal boundary layer's growth and periodic dissipation are due to intermittent gravity-wave breakdowns.

With these improved flux calculations within the surface layer and the atmosphere, the resulting model is capable of much higher fidelity of fluxes above ground. The below-ground component is also improved by considering a diurnal model of ground heat-flux. This model, based on the assumption of constant soil properties, could easily be improved through a wider choice of soils along with the addition of 2 low-frequency terms (sine and cosine) to account for the annular heat wave into the soil. In this fashion the day-to-day cooling or heating that occurs seasonally could also be factored into the model.

In all, these changes represent a considerable improvement of the prior-art model of 1993 but also reflect improvements that could be used in current climate models. In particular, it is apparent that the force-restore approach commonly used to model the ground heat-flux is only truly tuned to handle the single diurnal (24 h) frequency. As such, hourly flux variations and dawn/dusk or cloud effects are not handled well. The current model is designed to include frequencies up to 5-min variations, such that cloud effects are well characterized for their influence on the diurnal variations.

The ground heat-flux model also is significant in that it models the surface skin temperature and not a vertically averaged number. Yet, the longwave radiative flux from the surface is dependent on this skin temperature rather than on a vertically averaged value. Hence, this model more accurately handles radiative cooling than most climate models.

The numerous changes introduced here represent a significant advance in the modeling of surface fluxes.

Notes

1. Private communication between the author and Frank V Hansen, then of the US Army Atmospheric Sciences Laboratory, White Sands Missile Range, New Mexico, 1990.

References

- Allen LH, Lemon ER. Net radiation frequency distribution in a corn crop. *Boundary-Layer Met.* 1972;3:246–254.
- Andrews LC, Phillips RL. *Laser beam propagation through random media*, Bellingham (WA): SPIE Optical Engineering Press; 1998.
- Arfken G. *Mathematical methods for physicists*. Orlando (FL): Academic Press; 1985.
- Balick LK, Link LE, Scoggins RK, Solomon JL. Thermal modeling of terrain surface elements. Vicksburg (MS): Waterways Experiment Station Environmental Laboratory; 1981. TR-EL-81-2.
- Beer T. *Atmospheric waves*, New York (NY): J Wiley and Sons; 1974.
- Belen’kii MS. Effect of the inner scale of turbulence on the atmospheric modulation transfer function. *J Opt Soc Amer A.* 1996;13:1078–1082.
- Bhumralkar CM. Numerical experiments on the computation of ground surface temperature in an atmospheric general circulation model. *J Appl Meteorol.* 1975;14:1246–1258.
- Blackadar AK. Modeling the nocturnal boundary layer. *Proceedings of the 3rd Symposium on Atmospheric Turbulence, Diffusion, and Air Quality*, American Meteorological Society. Boston (MA). 1976. p. 46–49.
- Booker JR, Bretherton FP. The critical layer for internal gravity waves in a shear flow. *J Fluid Mech.* 1967;27(3):513–539.
- Browning KA. Structure of the atmosphere in the vicinity of large-amplitude Kelvin-Helmholtz billows. *Q J Roy Met Soc.* 1971;97:283–299.
- Businger JA, Wyngaard JC, Izumi Y, Bradley EF. Flux profile relationships in the atmospheric surface layer. *J Atmos Sci.* 1971;28:181–189.
- Businger JA. Turbulent Transfer in the atmospheric surface layer. In: Haugen DA, editor. *Workshop on Micrometeorology*. Boston (MA): American Meteorological Society; 1973. Chapter 2.
- Churnside JH. A spectrum of refractive turbulence in the turbulent atmosphere. *J Mod Optics.* 1990;37:13–16.
- Clifford SF. The classical theory of wave propagation in a turbulent medium. In: Strohbehn JW, editor. *Laser Beam Propagation in the Atmosphere*. Berlin (Germany): Springer-Verlag, 1978. Chapter 2.
- Davis PA, Peltier WR. Resonant parallel shear instability in the stably stratified planetary boundary layer. *J Atmos Sci.* 1976;33:1287–1300.
- Deardorff JW. Efficient prediction of ground surface temperature and moisture, with inclusion of a layer of vegetation. *J Geophys Res.* 1978;83:1889–1903.
- Dyer AJ. A review of flux-profile relationships. *Boundary-Layer Met.* 1974;7:363–372.

- Fiorino ST, Randall RM, Via MF, Burley JL. Validation of a UV-to-RF high-spectral-resolution atmospheric boundary layer characterization tool. *J Appl Met and Clim*. 2014;53:136–156.
- Frehlich R. Laser scintillation measurements of the temperature spectrum in the atmospheric surface layer. *J Atmos Sci*. 1992;49:1494–1509.
- Fried DL. Optical resolution through a randomly inhomogeneous medium for very long and very short exposures. *J Opt Soc Amer*. 1966;56:1372–1379.
- Garratt JR, Hicks BB. Momentum, heat and water vapour transfer to and from natural and artificial surfaces. *Q J Roy Met Soc*. 1973;99:680–687.
- Gillespie JB, Tofsted DH. Optical refraction in the atmospheric surface layer. Nully Sur Seine (France): Remote Sensing of the Propagation Environment, Advisory Group for Aerospace Research and Development (AGARD) Conference Proceedings 502. 1992.
- Goldstein S. On the stability of superposed streams of fluids of different densities. *Proc Roy Soc A*. 1931;132:524–548.
- Goody RM, Yung YL. Atmospheric radiation. 2nd ed., New York (NY): Oxford University Press; 1961.
- Halstead MH, Richman RL, Covey W, Merryman JD. A preliminary report on the design of a computer for micrometeorology. *Amer Met Soc*. 1957;14:308–325.
- Hill RJ. Models of the scalar spectrum for turbulent advection. *J Fluid Mech*. 1978;88:541–562.
- Hill RJ, Clifford SF. Modified spectrum of atmospheric turbulence fluctuations and its application to optical propagation. *J Opt Soc Amer*. 1978;68:892–899.
- Hill RJ, Clifford SF. Theory of saturation of optical scintillation by strong turbulence for arbitrary refractive-index spectrum. *J Opt Soc Amer*. 1981;71:675–686.
- Hinze JO. Turbulence, New York (NY): McGraw-Hill; 1987.
- Hoffert MI, Storch J. A scheme for computing surface fluxes from mean flow observations. *Boundary-Layer Met*. 1979;17:429–442.
- Holst GC. Electro-optical imaging system performance. 3rd ed. Bellingham (WA): SPIE Press; 2002.
- Holton JR. An introduction to dynamic meteorology. Orlando (FL): Academic Press; 1979.
- Houghton JT. The physics of atmospheres. London (UK); Cambridge University Press; 1977.
- Hufnagel R, Stanley NR. Modulation transfer function associated with image transmission for arbitrary refractive-index spectra. *J Opt Soc Am*. 1964;54:52–61.
- Ishimaru A. Wave propagation and scattering in random media. Volumes 1 and 2. New York (NY): Academic Press; 1978.

- Kaimal JC, Wyngaard JC, Izumi Y, Coté OR. Spectral characteristics of surface-layer turbulence. *Q J Roy Met Soc.* 1972;98:563–589.
- Kaimal JC, Finnegan JJ. Atmospheric boundary layer flows, their structure and measurement. New York (NY): Oxford University Press; 1996.
- Klipp C. Turbulence anisotropy in the near-surface atmosphere and the evaluation of multiple outer length scales. *Boundary-Layer Met.* 2014;151:57–77.
- Kolmogorov AN. The local structure of turbulence in an incompressible viscous fluid for very large Reynolds numbers. *C R (Doki) Acad Sci USSR.* 1941;30:301–305.
- Kopeika NS. A system engineering approach to imaging. Bellingham (WA): SPIE; 1998.
- Kreyszig E. Advanced engineering mathematics, New York (NY): J Wiley and Sons; 1972.
- Kunkel KE, Walters DL, Ely GA. Behavior of the temperature structure parameter in a desert basin. *J Appl Met.* 1981;20:130–136.
- Kunkel KE, Walters DL. Modeling the diurnal dependence of the optical refractive index structure parameter. *J Geophys Res.* 1983;88(C15):10,999–11,004.
- Lalas DP, Einaudi F. On the characteristics of gravity waves generated by atmospheric shear layers. *J Atmos Sci.* 1976;33:1248–1259.
- Liou KN. An introduction to atmospheric radiation. New York (NY): Academic Press; 1980.
- Miles JW, Howard LN. Note on a heterogeneous shear flow. *J Fluid Mech.* 1964;20(2):331–336.
- Monteith JL, Szeicz G, Waggoner PE. The measurement of stomatal resistance in the field. *J Appl Ecol.* 1965;2:345–355.
- Neu JT, Dummer RS, Beecraft MT, McKenna PN, Robertson DC. Surface optical property measurements on bark and leaf samples. Hanover (NH 03755-1290): SWOE Program Office, CRREL; 1990. PL-TR-91-2009, SWOE Report 90-14.
- Norton C, Hoidale G. The diurnal variation of mixed layer height by month over White Sands Missile Range, NM. White Sands Missile Range (NM): US Army Electronics Command; 1975. ECOM-5579.
- Obukhov AM. Turbulence in an atmosphere with a non-uniform temperature. *Inst Theor Geophys Acad Sciences, USSR.* 1946;1:95–115.
- Orlanski I. Trapeze instability as a source of internal gravity waves. *J Atmos Sci.* 1973;30:1007–1016.
- Paulson CA. The mathematical representation of wind speed and temperature profiles in the unstable atmospheric surface layer. *J Appl Meteor.* 1970;9:857–861.
- Press WH, Teukolsky SA, Vetterling WT, Flannery BP. Numerical recipes in C. Cambridge (UK): Cambridge University Press; 1992.

- Ren D, Xue M. A revised force-restore model for land surface modeling. *J Appl Met.* 2004;43:1768–1782.
- Richardson LF. Weather prediction by numerical process. Cambridge (UK): Cambridge University Press; 1922.
- Sellers WD. Physical climatology. Chicago (IL): University of Chicago; 1965.
- Shapiro R. Solar radiative flux calculation from standard surface meteorological observations. Hanscom AFB (MA 01731): US Air Force Geophys Laboratory; 1982. AFGL-TR-82-0039.
- Shapiro, R. Simple model for the calculations of the flux of solar radiation through the atmosphere. *Appl Opt.* 1972;11:760–764.
- Staley DO, Jurica GM. Effective atmospheric emissivity under clear skies. *J Appl Meteorol.* 1972;11:349–356.
- Stark H, Woods JW. Probability, random processes, and estimation theory for engineers. Englewood Cliffs (NJ): Prentice-Hall; 1986.
- Stephens GL. Remote sensing of the lower atmosphere. New York (NY): Oxford University Press; 1994.
- Stull RB. An introduction to boundary layer meteorology. Dordrecht (The Netherlands): Kluwer Academy Publishers; 1988.
- Tatarski VI. Wave propagation in a turbulent medium. Translated by R.A. Silverman. New York (NY): McGraw-Hill; 1961.
- Thom AS. Momentum, mass, and heat exchange of vegetation. *Q J Roy Met Soc.* 1972;98:124–134.
- Thomas GE, Stamnes K. Radiative transfer in the atmosphere and ocean. Cambridge (UK): Cambridge University Press; 1999.
- Tofsted DH, Gillespie JB. Comparing results from three surface energy budget models. US Army Atmospheric Sciences Laboratory. Proceedings of the 6th Annual EOSAEL/TWI Conference. 1986. p. 401–412.
- Tofsted DH. Baseline resolution of atmosphere related FADEWS modeling issues. Volume 6: scintillation distribution, Part 1 - theoretical development. White Sands Missile Range (NM): US Army Atmospheric Sciences Laboratory; 1991. ASL-TR-0304-1.
- Tofsted DH, Auvermann HJ. Baseline resolution of atmosphere related FADEWS modeling issues. Volume 9: additional model improvements. White Sands Missile Range (NM): US Army Atmospheric Sciences Laboratory; 1991. ASL-TR-0302.
- Tofsted DH. A surface energy budget model modifying heat flow by foliage effects. White Sands Missile Range (NM): US Army Atmospheric Sciences Laboratory; 1993. ARL-TR-60.

Tofsted DH, O'Brien SG. Three-dimensional radiative transfer modeling of tropospheric atmospheres. White Sands Missile Range (NM): US Army Atmospheric Sciences Laboratory; 1998. ARL-TR-1629.

Tofsted DH. Turbulence simulation: outer scale effects on the refractive index spectrum. White Sands Missile Range (NM): U.S. Army Research Laboratory; 2000. ARL-TR-548.

Tofsted DH. Analytic improvements to the atmospheric turbulence optical transfer function. Proceedings of SPIE 5075. 2003. p. 281–292.

Tofsted DH, O'Brien SG, Vaucher GT. An atmospheric turbulence profile model for use in army wargaming applications I. White Sands Missile Range (NM): US Army Research Laboratory; 2006. ARL-TR-3748. Also available at https://www.arl.army.mil/www/default.cfm?technical_report=1262

Tofsted D, O'Brien S, Yarbrough J, Quintis D, Bustillos M. Characterization of atmospheric turbulence during the NATO RTG-40 land field trials. Proceedings of SPIE 6551. 2007. 65510J.

Tofsted D, O'Brien S, Klipp C, Yarbrough J, Quintis D, Brice R, Bustillos M, Elliott S, Creegan E. Three-dimensional turbulence measurements in the atmospheric surface layer: experimental design and initial analysis. White Sands Missile Range (NM): US Army Research Laboratory; 2009. ARL-TR-4953. Also available at https://www.arl.army.mil/www/default.cfm?technical_report=6926

Von-Kármán T. Progress in the statistical theory of turbulence. Proc Natl Acad Sci US. 1948;34:530–539.

Whitham GB. Linear and nonlinear waves. New York (NY): J Wiley and Sons; 1974.

Wolfe WL. Radiation theory. In: Wolfe WL, Zissis GJ, editors. The infrared handbook. Ann Arbor (MI): Environmental Research Institute of Michigan (ERIM); 1989. Chapter 1.

Wyngaard JC. On surface layer turbulence. In: Haugen DA, editor. Workshop on micrometeorology. Boston (MA): American Meteorological Society; 1973. Chapter 3.

List of Symbols, Abbreviations, and Acronyms

ρ	air density, in kg/m ³
P	air pressure, in millibars
C	speed of sound in air at the current thermodynamic state
T	temperature measurement in either degrees Kelvin (K) or Celsius (C)
C_n^2	refractive index structure parameter, a measure of optical turbulence strength, in dimensions of m ^{-2/3}
u or U	horizontal wind speed in m/s
H_S	sensible heat flux, in W/m ² , denoting the energy lost by the surface layer due to heating of the air in the Surface Layer atmosphere
H_L	latent heat flux, in W/m ² , denoting the energy lost by the surface layer due to evaporation of water from the soil or evapotranspiration of water vapor from the plant layer to the Surface Layer atmosphere
Z_I	depth of the Boundary Layer in meters (m)
Z_S	a characteristic depth of the Surface Layer atmosphere.
U_*	friction velocity, a characteristic windspeed for parameterizing the vertical structure of the horizontal winds near the surface.
T_*	scaling temperature, a characteristic temperature for parameterizing the vertical structure of the temperature near the surface.
AGL	above ground level
ARL	US Army Research Laboratory
ASL	above sea level
BL	boundary layer

CBL	convective boundary layer
CPA	conservative passive additive
EOSAEL	The Electro-Optical Systems Atmospheric Effects Library
FLIR	forward-looking infrared
IR	infrared
LHS	left-hand side
MKSA	meter–kilogram–second–ampere (system)
ppm	parts per million
RHS	right-hand side
SEB	Surface Energy Budget
SI	surface interface
SL	surface layer
WSMR	White Sands Missile Range

Glossary

Boundary Layer	The layer of air near the ground that is characterized by drag effects due to the surface. Typically the BL is 1–3 km deep, features a capping elevated inversion layer, and contains well-mixed aerosols.
Stable Layer	Nighttime condition where vertical air motions are opposed by a negative buoyancy force. Also termed a <i>katabatic</i> condition.
Surface Layer	The atmospheric layer just above the air–surface interface characterized by constant drag and constant sensible heat flux. A layer from 10 m to 50 m deep.
Unstable Layer	Daytime predominant condition within the earth’s boundary layer atmosphere where vertical air displacements produce a result in an acceleration force driving the parcel from its initial height location due to buoyancy forces.

1 DEFENSE TECHNICAL
(PDF) INFORMATION CTR
DTIC OCA

2 DIRECTOR
(PDF) US ARMY RESEARCH LAB
RDRL CIO LL
IMAL HRA MAIL & RECORDS
MGMT

1 GOVT PRINTG OFC
(PDF) A MALHOTRA

2 KIRTLAND AFB
(PDF) D SANCHEZ
T FARRELL

1 CERDEC NVESD
(PDF) RL ESPINOLA

1 DRDC VALCARTIER
(PDF) G POTVIN

1 SCI TECH LAB ST BARBARA
(PDF) M ONEILL

1 AF INST TECHNOLOGY
(PDF) ST FIORINO

1 UNIVERSITY MEMPHIS
(PDF) EL JACOBS

17 DIR USARL
(PDF) RDRL CIE
R BRICE
S CHANG
P CLARK
E CREEGAN
S DARCY
R DUMAIS
T FOLEY
T JAMESON
C KLIPP
D KNAPP
B MCCALL
J PASSNER
S OBRIEN
R RANDALL
J SMITH
G VAUCHER
Y WANG

INTENTIONALLY LEFT BLANK.